Elisabeth Unger

The Extremes of Neutrino Astronomy

From Fermi Bubbles with IceCube
to Ice Studies with ARIANNA

**UPPSALA
UNIVERSITET**

Abstract

Unger, E. 2019. The Extremes of Neutrino Astronomy. From Fermi Bubbles with IceCube to Ice Studies with ARIANNA. *Uppsala Dissertations from the Faculty of Science and Technology* 137. 213 pp. Uppsala: Acta Universitatis Upsaliensis. ISBN 978-91-513-0682-7.

The Fermi bubbles are extended regions of hard gamma-ray emission which were discovered with Fermi-LAT data to exist above and below the Galactic Center. In order to explain the origin of the gamma-rays, different theories are proposed. In particular, within hadronic models, highly-accelerated cosmic rays interact with interstellar matter and create the observed gamma-rays and in addition neutrinos. Data from the neutrino detector IceCube was analyzed using a maximum likelihood method. An upper limit on the possible neutrino flux from the Fermi bubbles at energies between 10 GeV and 200 GeV was determined.

While this analysis is performed with the lowest energies IceCube can reach, the ARIANNA (Antarctic Ross Ice-shelf ANtenna Neutrino Array) experiment has the goal to detect the highest energy neutrinos by measuring radio wave radiation produced by their interaction products in the ice. With ARIANNA the propagation of radio waves in the firn (packed snow) of the Ross Ice Shelf was investigated. According to the classical approach the radio waves, produced in the firn, are supposed to bend down because of the changing density, and therefore changing refractive index, an effect which is called "shadowing". Evidence that the waves can travel horizontally over a long distance will be presented. The horizontally propagating signals between two boreholes and to the ARIANNA stations were analyzed and characterized. Analyses were performed under two hypotheses to determine attenuation lengths for horizontal propagation signals. The results showed attenuation lengths between 310 m ± 83 m and 651 m ± 270 m, depending on the assumed hypothesis and performed analysis. In addition unexpected signals consistent with radio waves propagating along the firn surface, here called pre-pulses, were observed and characterized.

Elisabeth Unger, Department of Physics and Astronomy, High Energy Physics, Box 516, Uppsala University, SE-751 20 Uppsala, Sweden.

To my parents, Larissa and Johann.

Моим родителям, Ларисе и Ивану.

Contents

Acknowledgements

During my time as a PhD student at Uppsala University I have had the privilege to work with many excellent, helpful and dedicated scientists. And the work presented in this thesis reflects the collaboration with these brilliant minds. I have enjoyed the company of each and every one of you, thank you for the amazing experience. Some of you deserve a special mention.

At first I would like to show my gratitude to my supervisors Allan Hallgren and Olga Botner for giving me the opportunity to work on the amazing projects IceCube and ARIANNA. During my time as a PhD student both were supportive of my ideas, and gave me the freedom of following them, while guiding me towards making prioritized decisions. Allan was my main supervisor and always asked the kind of questions that inspired me to think about my work from different angles. Olga has the fantastic ability to turn difficult situations around and make them good or even excellent. Thank you both for being such great supervisors.

Next I would like to thank the entire IceCube group at Uppsala University in the past and the present for fruitful physics discussions, useful programming lessons, helpful explanations and wonderful and fun times outside work: David, Henric, Rickard, Carlos, Sebastian and Christoph. For funny and interesting discussions I would like to thank my office mates Martin and Miquel. A special thank you is for Leif, who thought me a lot about antenna theory. And a very special thanks goes to my office mate and friend Alex. No matter if we discussed work or life, it was always fun and helpful and despite our disagreement about the office temperature you are the best office companion I could have wished for.

I also would like to show my deep gratitude to Inger Erikson, who helped me with absolutely everything administrative. Furthermore, I would like to thank Teresa Kupsc and Alen Jadadic for great computer support.

A big thank you is for all the people in the high energy and nuclear physics departments for interesting discussions and fun time during lunch, fika and other occasions.

As a PhD student I had the amazing opportunity to visit the University of California, Irvine and work on ARIANNA with the excellent scientists Steve Barwick, Anna Nelles and Chris Persichilli. Thank you very much for all the knowledge and experience you shared with me during that time, it was

you so much for everything! Andrew, thank you for being a good friend, and the only other person in Sweden with my taste of music. Petter, I would like to thank you especially for always cheering me on, nit picking on my thesis, translating the Swedish summary, the countless fun times and just everything. I would also like to thank my friends from all over the place, which I always meet when I get the chance: Caro, Martin, Alexa, Sarah, Michi, Richard, Eva, Tobi, Barbara, Nils, Erik and all the others not mentioned here.

A very special thanks deserve my best friends which supported me and believed in me from afar, thank you that you are always there: Simi, Anna and Ghosti. We have managed to be best friends for more than a decade, no matter the distance, no matter the difficulties. Thank you for being there.

I would like to thank my family for believing in me. Especially, I would like show my deepest gratitude to my parents, Larissa and Johann, for teaching me valuable live lessons. My father thought me that life is not always easy and my mother thought me that it doesn't have to be hard. Both always supported me and my mother never doubted me. Together, they thought me that if I'm willing to work for it, I can achieve everything I dream of.

Я хочу сказать спасибо моей семье за веру в меня. Особую благодарность я бы хотела выразить моим родителям, Ларисе и Ивану, за то, что преподали мне важные жизненные уроки. Мой папа научил меня тому, что жизнь не всегда так легка. А моя мама - что жизнь не обязана быть тяжелой. Они меня всегда поддерживали и мама никогда не сомневались во мне. Вместе они вселили в меня уверенность в том, что если я буду упорно работать, я могу достичь любой цели о которой я мечтаю.

Finally I would like to thank Jerome, for being as amazing as you are, you are my superhero. Thank you for being the best vegan cook, feeding me, supporting me and understanding me. I love you.

Letzten Endes würde ich mich gerne bei Jerome bedanken, dafür dass du so unglaublich bist, du bist mein Superheld. Danke dafür, dass du der beste vegane Koch bist, dass du mich fütterst, mich unterstützt und mich verstehst. Ich liebe dich.

Acronyms

Preface

About this Thesis

This work is divided into two parts. In the first part it is investigated if a neutrino flux can be observed from the Fermi bubbles with IceCube data. The second part is engaged with the analysis of propagation of radio waves within firn (packed snow) with data collected with ARIANNA. This thesis works at the extremes of neutrino astronomy in terms of energy, because it includes the challenges of the lowest neutrino energies IceCube is able to detect and for ARIANNA it examines the presumed signal propagation, originating from neutrinos with the highest energies predicted.

The structure of this thesis is as follows:
The first chapter is a general introduction into the field of astroparticle physics.

Part I: In chapter 2 the Fermi bubbles are characterized and in chapter 3 the IceCube and DeepCore detectors are described. Chapter 4 treats the processing of data and simulation as well as the event selection to investigate the Fermi bubbles. In chapter 5 the expected neutrino flux from the Fermi bubbles is derived and the analysis method is explained. In chpater 6 the results of the analysis are described including systematic studies, and the conclusion and outlook are presented.

Part II: In chapter 7 the ARIANNA detector is described. Chapter 8 explains what horizontal propagation of radio waves in firn means, how these signals were observed and which analyses were performed to characterize these pulses. Furthermore, the observation of so-called pre-pulses is described, and also these pulses are characterized. In chapter 9 the measurements and event selection for the derivation of an attenuation length for horizontally propagating signals are explained. In chapter 10 the hypotheses, analyses and results for the horizontal propagation attenuation length are described. This chapter includes also the conclusions and the outlook.

The Author's Contribution

Uppsala University

During my time as a PhD student I was a teaching assistant on the course "Modern Physics". My work included leading the students through experiments in the laboratory and correcting their pre-exercises and reports on the experiments.

IceCube

Starting with my master thesis in 2012 about the seasonal variation of the atmospheric neutrino flux with IceCube data [204], I have also started to perform service work for the IceCube collaboration. I wrote the first version of the linear regression test to verify data quality for the monitoring system "moni2.0", which was under development at that time. Over the years I wrote helpful functions for the test and worked on further improvements of moni2.0. A large contribution was dedicated to the verification of several tests in moni2.0 with real data, in order to determine which tests perform the best. The data testing was performed for each trigger and filter and for each test it was also a task to determine appropriate thresholds to ensure data quality. Additionally, moni2.0 was compared with the old system during the transition time in order to find bugs. I have attended three moni2.0 workshops to improve my knowledge about the detector, monitoring and programming and to collaborate efficiently with the moni2.0 team. All this work was a group effort of the complete moni2.0 team, and it was very rewarding to work with them.

In 2014, 2016 and 2017 I was monitoring the detector for periods between one and two weeks. Since I was part of the moni2.0 team, I used especially the monitoring weeks to compare the old and new monitoring systems, while moni2.0 was in its beta state.

In total I have participated in eight IceCube Collaboration meetings and presented my PhD work.

ARIANNA

For the ARIANNA observatory my fellow PhD student Alex and me performed various LPDA tests in an anechoic chamber at Uppsala University. We characterized the ARIANNA LPDA antenna properties.

Furthermore, I went with my two colleagues Chris and Hans to Moore's Bay, Ross Ice Shelf, Antarctica. We built a new station dedicated for tau-neutrino detection. One station was rebuild to be a pure Cosmic Ray station. The software of several stations Battery Management Units was updated and many ice studies were performed during that season. This thesis includes analyses of these ice studies. Details regarding the studies and results can be found in the chapters 8 and 10 respectively. Part II of this thesis is partly based on the publication [62], to which I contributed a significant amount of the analyses within the ARIANNA part.

Units and Conventions

Throughout this thesis electronvolt (eV) is used as standard unit for energy. In general natural units are used, which means $c = \hbar = k_B = 1$, where c is the speed of light in vacuum, $\hbar$ represents the reduced Planck constant and k_B stands for the Boltzmann constant. Using natural units enables us to express energy, mass and momentum in eV. The meter water equivalent *mwe* is a measure of cosmic ray attenuation in underground laboratories. Laboratories at the same depth (in meters) can have greatly varied levels of cosmic ray penetration, depending on the kind of overburden, the mwe is a consistent way of comparing cosmic ray levels. The antenna gain will be expressed in decibel *dB*.

The Cover Illustration

The cover illustration shows an oversized neutrino (turquoise) interacting with the Antarctic ice resulting in a muon radiating blue Cherenkov light while passing the oversized IceCube detector at the South Pole from left to right (red to green bubbles). The red radio Cherenvkov cone, a product of the particle shower (white lines) created by the neutrino interaction is detected by an oversized ARIANNA LPDA antenna at Moore's Bay on the Ross Ice Shelf. In reality a high energy neutrino could not produce such strong signals to be observed by both detectors, at this distance, but the figure illustrates nicely the work presented in this thesis.

Illustration 1. Left: Digging out a station electronics box, barely visible behind me with cables reaching out into the snow at about 3.5 m depth, 2016-11-15. Right: This penguin, Survivor, got lost hundreds of kilometers from his group and visited us at Moore's Bay for a few days. This picture was taken when Survivor came up to me to say good bye before it left our camp in direction of the melting sea, 2016-11-13.

Illustration 2. The camp at Moore's Bay. Part of our gear is visible on the left side, in the middle is the yellow science/kitchen tent and my sleeping tent (orange) on the right, 2016-11-25.

1. Astroparticle Physics

The understanding of the universe is one of the greatest endeavors of mankind. Throughout recorded history, curious individuals have turned their gaze towards the sky to observe astronomical objects like stars or galaxies, their light and movements. The naked eye was the first tool with which such observations were made, but with the progress of technology, various new instruments have been developed for the ever ongoing exploration. Today we are able to explore a broad spectrum of electromagnetic radiation from radio to gamma-rays using radio-, optical- and Cherenkov telescopes. In addition to photons, other messengers have turned out to be useful when studying the universe: *Cosmic Rays* (CRs), neutrinos and recently also gravitational waves.

1.1 High Energy Cosmic Rays

Cosmic rays are charged particles and consist of about 90% protons, 9% helium nuclei and the rest being electrons, positrons and heavier nuclei up to iron. The exact composition depends on their energy and is subject to ongoing research. Figure 1.1 shows the all-particle high energy cosmic ray flux above 10^{13} eV as a function of energy, measured by various experiments (see references in [198]). The actual cosmic ray spectrum extends down to about 10^7 eV. At energies below 10^{10} eV cosmic rays produced by the Sun in solar flares and coronal mass ejections dominate the spectrum [106]. Above 10^{10} eV the CRs have their origins beyond our solar system and their spectrum can be approximated by a power law:

$$\frac{dN}{dE} \propto E^{-\gamma},\tag{1.1}$$

where N denotes the number of particles, E describes the energy of the cosmic rays and γ stands for the spectral index. There are three points at which the power-law changes the spectral index γ leading to a change in slope of the flux. The first steepening, known as the *knee* occurs around 3×10^{15} eV where the spectrum changes from $dN/dE \propto E^{-2.7}$ to $dN/dE \propto E^{-3.0}$. The *second knee* lies around 10^{17} eV and leads to a softer spectrum with an index of $\gamma \approx 3.3$. The last point is called the *ankle* at around 3×10^{18} eV and the transition yields a hardening of the spectrum to $dN/dE \propto E^{-2.7}$. CRs with energies above 10^{18} eV are considered to be *Ultra-High-Energy Cosmic Rays*
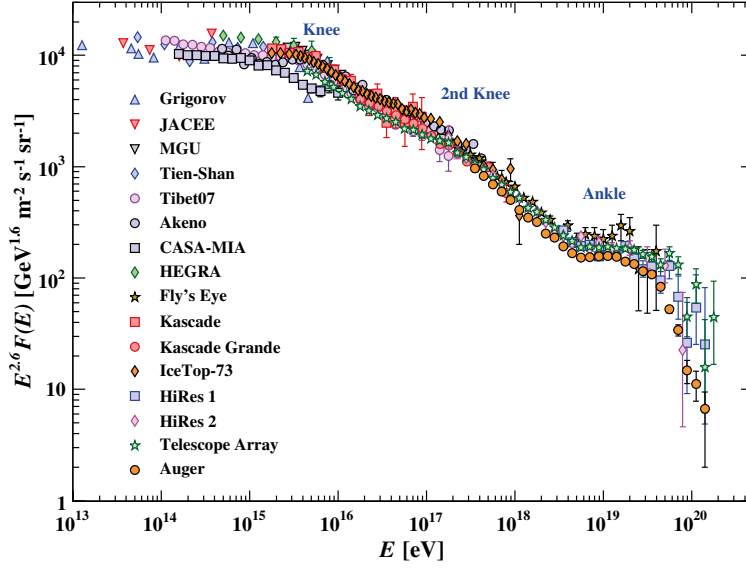
Figure 1.1. Cosmic ray spectrum measured by various experiments. The CR flux is multiplied with $E^{2.6}$ in order to enhance spectral features where the slope of the CR spectrum changes: the knee at $\sim 3 \times 10^{15}$ eV, the second knee at $\sim 1 \times 10^{17}$ eV and the ankle at $\sim 3 \times 10^{18}$ eV. Figure credit and references of shown data from experiments: [198]

.

(UHECR). At an energy of about 5×10^{19} eV the CR flux decreases rapidly and at energies beyond 3×10^{20} eV no particles have been observed, see figure 1.1. Cosmic Rays which exceed 5×10^{19} eV are called *Extreme-Energy Cosmic Rays* (EECR).

What kind of sources produce CRs, especially at the UHE end of the spectrum? Which processes cause the features in the spectrum? Which acceleration processes are able to accelerate particles to such extreme energies? What is the mass composition of the CR flux? These are the main questions of astroparticle physics, and while we are able to answer them to some degree, the complete picture is yet to be determined.

Below the knee CRs are expected to be of Galactic origin. The Galactic magnetic fields are strong enough to restrict the CRs within the Milky Way. It has been suggested that the knee could be the point at which cosmic rays reach

high enough energies to escape the Galaxy, which will be explained further below as the *Hillas criterion*. These CRs would have a gyroradius, similar to the size of the Galactic plane. Expanding shocks around *supernovae remnants* (SNR), X-Ray binaries and pulsars are possible candidates for Galactic sources with suitable acceleration processes [66]. The knee could also be a sign that the Galactic cosmic accelerators reach a maximum energy [198]. Furthermore, propagation effects like the *Hall diffusion* could also have an effect on the spectrum [180]. The Hall diffusion describes the effect of a global toroidal magnetic field in the Miky Way which disturbs the behavior of CRs in stochastic magnetic fields, leading to an additional drift on top of the usual diffusion. This effect is insignificant at lower energies but becomes dominant at energies around the knee. The knee and possible models to explain it are further discussed in [140].

The second knee could be caused by the transition from light to heavy primary CRs, as claimed by KASCADE-Grande (KArlsruhe Shower Core and Array DEtector with Grande extension), which observed the second knee first [50]. This model suggests that, at the knee, a distinct decrease of light primaries occurs and at the second knee a distinct decrease of a heavier group of primaries takes place. This implies that there might be more knees present [140]. Another approach proposes that the cosmic ray spectrum consists only of two components, of a Galactic origin ($E < 10^{17}$ eV), and of an extragalactic origin ($E > 10^{18}$ eV) and the energy range in between is the cross-over marking the second knee, which corresponds to a gradual transition [68, 161]. This model relies on the maximum energy of sources and propagation effects to explain the first knee and the ankle represents a signature of pair production.

There are several models regarding the explanation of the slope change at the ankle. The *ankle models* suggest that the ankle is the point where a steep all-nuclei Galactic spectrum and a flat extragalactic proton spectrum intersect (e.g. [72, 196, 89]). The *mixed composition model* assumes rather a transition from Galactic CRs to a variety of extragalactic nuclei (e.g. [43, 94]). The *dip model* suggests energy losses of extragalactic protons due to interactions with the *Cosmic Microwave Background* (CMB) resulting in electron-positron pair production[1] (e.g. [70, 69]): $p + \gamma_{CMB} \rightarrow p + e^+ + e^-$. A review of these and further models to explain the transition at the ankle can be found in [71].

With increasing energy of the CRs the influence of the Galactic and other magnetic fields, and therefore the deflection of CRs decreases. Hence, UHE-CRs are likely of extragalactic origin and possible sources are *Gamma-Ray-Bursts* (GRB), *Active Galactic Nuclei* (AGN), radio galaxies and galaxy clusters [136, 107].

Around an energy of 5×10^{19} eV the measured flux starts to decrease rapidly. This is called the *Greisen Zatsepin Kuzmin* (GZK) cut-off [118]. The GZK

---

[1]This process is not to be confused with the GZK mechanism, which takes place at the cutoff of the CR spectrum

mechanism describes the interaction of protons with the CMB: $p + \gamma_{CMB} \rightarrow \Delta^+ \rightarrow n(p) + \pi^+(\pi^0)$. The cutoff energy decreases and is expected to be less sharp for heavier CRs, because the interaction with the *Extragalactic Background Light* becomes important leading to photo-disintegration [45]. To observe a substantial CR flux above 10^{20} eV a UHECR source is required to be not farther than ~ 60 Mpc from Earth [190], which is close considering the universal scale. The most energetic cosmic ray ever observed, referred to as the *Oh-My-God particle* was recorded in 1991 by Fly's Eye, with an energy of 3×10^{20} eV [73]. The measurement of a significant cosmic ray proton flux above the GZK cut-off would be a hint of physics beyond the Standard Model.

The standard acceleration model for cosmic rays is the so called *Fermi acceleration of first order*, also known as *Diffuse Shock Acceleration* (DSA). This model assumes that mildly relativistic charged particles cross a moving shock-front several times and are accelerated each time by plasma moving towards them. The several crossings require that the particle direction gets randomized both downstream and upstream of the shock, for instance through elastic collisions with magnetic inhomogeneities, although the details of the magnetic fields are neglected in the model. DSA predicts a resulting power-law energy spectrum for the accelerated particles with a spectral index of $\gamma = 2$ at the source [67]. Assuming acceleration in supernova remnant shocks, this could explain the observed energy spectrum of Galactic cosmic rays. Propagation effects lead to a softening of the spectrum to $dN/dE \propto E^{-2.6}$, which is well in agreement with the observations of $\gamma = 2.7$ below the knee [203].

The original model developed by Fermi, now called *Fermi acceleration of second order* [99] is based on particles being reflected by inhomogeneities (magnetic mirrors) in magnetic clouds. The particles could gain and loose energy with each reflection but the model explained that on average energy was gained. This process is less efficient and therefore unlikely to accelerate particles to the highest energies.

In general a particle can gain more energy the longer it is able to interact with the acceleration region. However, DSA works for CR energies below 10^{18}eV and it remains a mystery how cosmic rays can get accelerated up to the measured energies of 10^{20}eV.

There is also a variety of general constraints on a cosmic ray accelerator, like the necessary power for the acceleration or the required density of particles. The geometry of the source can constrain the maximum energy a particle can reach as well. If the gyro-radius of a relativistic charged particle exceeds the size of the accelerator region, it escapes and cannot gain further energy.
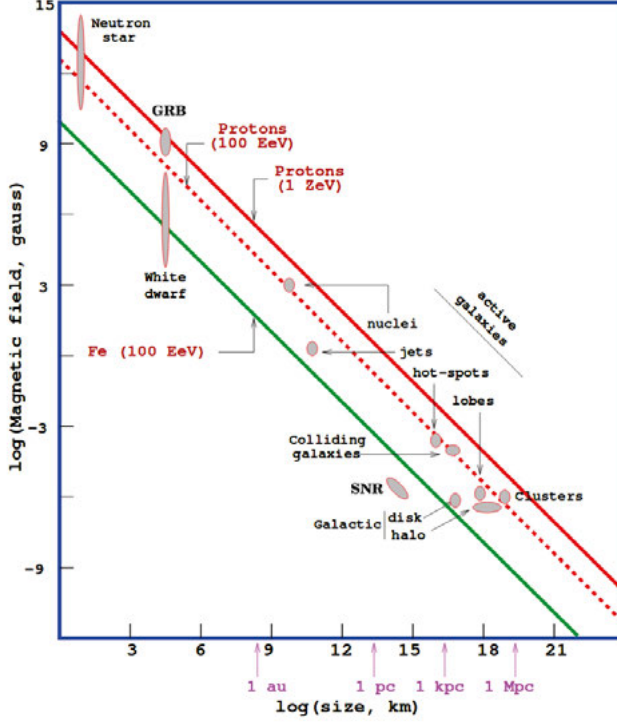
Figure 1.2. This is a modified version of the Hillas plot [48]. The original Hillas plot is shown in [135]. The three lines represent protons with energies of 10^{21} eV (solid red), 10^{20} eV (dashed red) and iron with 10^{20} eV (green) calculated with equation 1.2 for the extreme case of $\beta = 1$. Only sources on or above the lines are able to accelerate the particles to the corresponding energies.

This effect is known as the *Hillas criterion* and leads to a limit on the energy, E_{max}, the CR can gain:

$$E_{max} = ZeBr_L, \tag{1.2}$$

where Ze represents the electric charge, B is the magnetic field in the accelerator region and r_L represents its size [135]. To accelerate a cosmic ray to the highest energies a potential source needs to have either a strong magnetic field or a large size. In the so called *Hillas plot* candidates with such properties are depicted, see figure 1.2. With this criterion it is easier to understand why for example SNR are not able to accelerate CRs to the highest energies but GRBs can provide the necessary power.

Hopefully, the *multi-messenger approach* using CRs, γ-rays, neutrinos and the recently discovered gravitational waves [24] will shed light on the unanswered questions of astroparticle physics, and maybe reveal more mysteries to solve.

1.2 Multi-Messenger Astrophysics
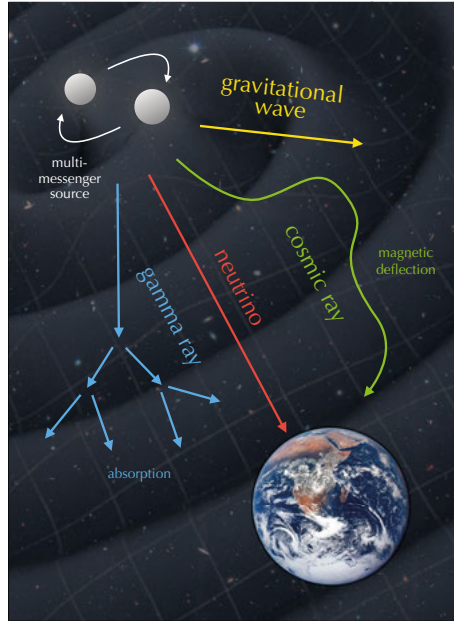
Figure 1.3. Schematic presentation of the propagation effects influencing the different messenger particles. The multi-messenger source is represented by a neutron-star merger. While gamma rays can be absorbed in e.g. intergalactic clouds and cosmic rays are deflected by magnetic fields, gravitational waves and neutrinos are not disturbed while traversing the universe. Credit: IceCube Collaboration.

In order to understand astrophysical cosmic ray source candidates and the processes involved to accelerate particles to extreme energies, it is useful to utilize the entire information these sources may provide, in particular the different particles species they may accelerate. Figure 1.3 shows a representation of all available messengers, which are predicted to be produced at the same source, and their propagation through the universe until they can be measured at Earth. Using cosmic rays, gamma-rays, gravitational waves and neutrinos together, we hope to learn more about their sources and the particle acceleration processes associated with these objects.

Cosmic rays, as charged particles, are deflected by magnetic fields and therefore their directions are scrambled and their origin cannot be determined. Although UHECR are barely influenced by magnetic fields, their flux is extremely low with about 1 particle per square kilometer per century, making it difficult to reach statistically significant conclusions.

To measure CRs it is important to know which energy range of the spectrum is to be investigated and decide on the detection technique accordingly. At low energies (below $\sim 1\,\mathrm{TeV}$), their spectrum can be sufficiently accurate

determined using direct detection techniques with baloon- or space-borne detectors. As the CR flux decreases with higher energies these instruments reach their limits. Larger detection areas are required in order to reliably measure lower fluxes. For this reason ground based experiments are advantageous, using indirect detection of secondary particles. When cosmic rays interact with the atmosphere they produce an expanding cascade of secondary particles, which are called *air showers*[2]. Ground based experiments like for example the Telescope Array [148] and the Pierre Auger Observatory (PAO) [27], which cover areas of $730\,\mathrm{km}^2$ and $3000\,\mathrm{km}^2$ respectively, are able to measure CRs at the highest energies.

Gamma Rays (γ-rays) are highly energetic photons. They are not affected by magnetic fields, and therefore can travel through space without being deflected. Their sources are thus easier to identify. While traversing the universe γ-rays can, however, interact with interstellar dust clouds, the cosmic microwave background [97], the isotropic radio background and the infrared/ optical background [190]. This reduces the detectable flux and leads to loss of information. Additionally, the Earth's atmosphere is opaque to γ-rays and ground based telescopes cannot detect them directly. However, γ-rays do interact with the atmosphere and produce *electromagnetic showers* (see section 1.4) and can be observed by Imaging Air Cherenkov telescopes like MAGIC (Major Atmospheric Gamma Imaging Cherenkov Telescopes) [41], H.E.S.S. (High Energy Stereoscopic System) [137], VERITAS (Very Energetic Radiation Imaging Telescope Array System) [156] and the yet to be built CTA (Cherenkov Telescope Array) [200], the next generation Imaging Atmospheric Cherenkov telescope. An electromagnetic shower is a cascade of *electromagnetically* (EM) interacting particles: electrons, positrons and photons. Ground based Cherenkov telescopes are able to observe showers produced by cosmic rays as well. CRs initiate *hadronic*[3] *cascades* which contain an EM component due to π^0 decay: $\pi^0 \rightarrow 2\gamma$. However, the topology differs between hadronic and electromagnetic showers, and by observing the cascades from different angles they can be differentiated. More details about the interaction of CRs and γ-rays with the atmosphere are given in section 1.4.

Gravitational waves (GWs) are the newest addition to the multi-messengers of astrophysics. They are waves within the spacetime, which are caused by accelerated masses and move with the speed of light. For the first time in human history, a gravitational wave from two merging black holes was directly observed in September 2015 by the Laser Interferometer Gravitational-Wave Observatory (LIGO) [24]. The advantage of gravitational waves is that they

---

[2]In general particle showers are also referred to as cascades. Air showers are further discussed in section 1.4.

[3]A hadron is a particle consisting of two or more quarks, like pions or protons. Hadronic air showers refer to particle showers initiated by a hadron (e.g. a nucleon).

propagate without disturbance and therefore point right back to their source. Gravitational waves open a new window to investigate accelerated cosmological objects. The LIGO and Virgo observatories are working together, e.g. on binary black hole population properties [202].

Neutrinos[4] are elementary particles with an extremely small mass, an intrinsic spin of one half and no electric charge. Due to their half-integer spin neutrinos are fermions and obey Fermi-Dirac statistics. The Standard Model, the theory which combines and describes electromagnetism and the weak and strong forces, includes three types (also called flavors) of neutrinos and three types of charged partners, which are grouped together in three generations. Neutrinos together with their chargd partners are called leptons and we distinguish between electronic, muonic and tauonic leptons. They are summarized in table 1.1. Leptons do not undergo interactions with the strong force and charged leptons do not mix outside their generations.

Table 1.1. *The three generations of leptons.*

generation	1.	2.	3.
charged	e	μ	τ
neutral	ν_e	ν_μ	ν_τ

Within the Standard Model neutrinos have mass zero, but this has been proven wrong due to the existence of neutrino oscillations. The so called *solar neutrino problem* arose as the result of a measurement of the solar neutrino flux by the Homestake Chlorine Detector [88]. The neutrino flux was smaller than theoretical predictions because electron neutrinos from the Sun oscillated into muon neutrinos. Evidence for neutrino oscillations, which was rewarded with the Nobel Prize in 2015, was provided by Super-Kamiokande and the Sudbury Neutrino Observatory (SNO). Super-Kamiokande observed a deficit of muon neutrinos in the atmospheric neutrino flux [104]. SNO reported a "non-electron flavor component" in the solar neutrino flux [38]. Neutrinos oscillate between different flavors and the oscillation probability depends on the distance they travel. Neutrino oscillations require that neutrinos have masses. However, their mass-eigenstates do not correspond to their flavor eigenstates. The measurement of neutrino masses and the neutrino mass hierarchy are subjects of current research.

Neutrinos are an excellent addition to the messengers with which to explore the universe. They travel close to the speed of light, point back to the place of their creation and the universe is basically transparent to them. However advantageous these properties are, the fact that their respective interaction

---

[4]Neutrinos were postulated by Wolfgang Pauli 1930 in order to explain the energy spectrum of electrons from the β-decay of radioactive nuclei and detected for the first time 26 years later at a nuclear reactor [83].

cross-sections are very small (see section 1.5) renders their observation quite challenging.

1.2.1 Relation between CRs, γ-rays, GWs and neutrinos

The speculations regarding astrophysical accelerators of particles are so far limited to space regions where enormous gravitational forces generate relativistic particle flows [125]. When two massive objects with rapidly rotating cores merge gravitational waves are generated. For very massive objects, these events can result in a system of a black hole, an accretion disk and two jets, which carry out relativistic high energy cosmic ray streams. Neutrinos and γ-rays are expected to be produced in interactions of accelerated protons and nuclei in or near the sources and they are therefore associated with cosmic rays (e.g. [105, 190]). Figure 1.4 displays a panorama spectrum of high-energy multi-messengers, comparing measured data of the messengers to their emission models (solid lines) and the inferred neutrino flux upper bounds (dashed lines). This figure is the visualization of the connection between CRs, γ-rays and neutrinos.

The important hadronic processes for generation of neutrinos are CRs interacting with photons, γ, and other particles in the interstellar space:

$$p + \gamma \rightarrow \Delta^+ \rightarrow \begin{cases} p + \pi^0 & (BR = 2/3) \\ n + \pi^+ & (BR = 1/3) \end{cases}. \tag{1.3}$$

The Δ^+ represents a Delta baryon, which decays further to protons (p), neutrons (n) and pions ($\pi^{0,+}$) according to the *branching ratios* (BRs)[5]. The interaction between protons is described by:

$$p + p \rightarrow \begin{cases} p + n + \pi^+ + X \\ p + p + \pi^0 + X \end{cases} \tag{1.4}$$

where X represents additional particles. The decay of neutrons and charged pions leads to neutrinos (ν):

$$n \rightarrow p + e^- + \bar{\nu}_e \qquad\qquad (BR \approx 100\%), \tag{1.5}$$

$$\pi^\pm \rightarrow \mu^\pm + \nu_\mu (\bar{\nu}_\mu) \qquad\qquad (BR \approx 100\%) \tag{1.6}$$
$$\hookrightarrow e^\pm + \nu_e (\bar{\nu}_e) + \bar{\nu}_\mu (\nu_\mu) \quad (BR \approx 100\%). \tag{1.7}$$

---

[5]The listed branching ratios can be found in [198].

High-energy multi-messenger panorama
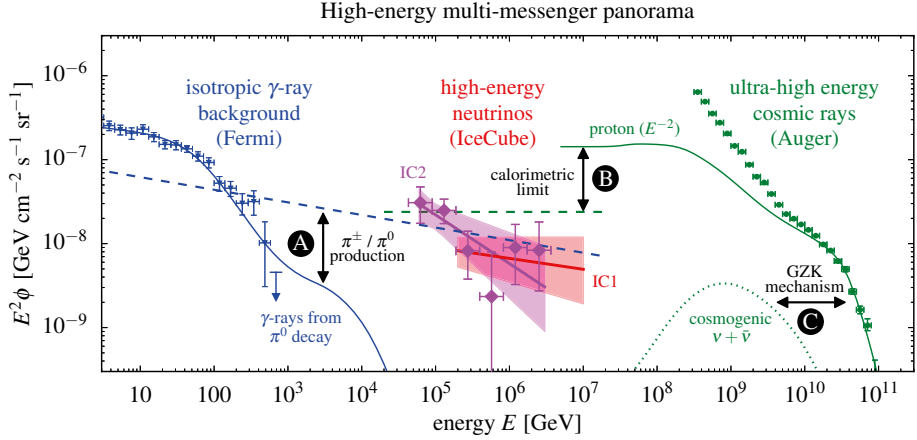
Figure 1.4. The measurements of the fluxes of extragalactic γ-rays (blue triangles) [28], neutrinos and CRs (green circles) [175] from unresolved sources are compared. The unfolded neutrino flux spectrum of *High Energy Starting Events* (HESE) is represented by the magenta rhomboids. The spectral neutrino flux is derived from the best power-law fit of the six-year HESE analysis (magenta fit, IC2) and the eight-year up-going $\nu_\mu + \bar{\nu}_\mu$ track analysis (red fit, IC1), including the 1σ uncertainty bands (shaded areas) [17]. The multi-messenger interfaces are denoted with letters. **A:** Charged and neutral pions are created together in CR interactions leading to the emission of neutrinos (dashed blue) and γ-rays (solid blue), respectively. These lines represent the upper bounds for neutrino fluxes observable at Earth. The track analysis data is consistent with the upper bound, while the HESE data show a different slope. To investigate the neutrino production mechanisms and to constrain neutrino source models more studies are required. **B:** A maximal neutrino flux (calorimetric limit, dashed green) is implied by cosmic ray emission models (solid green) of the most energetic CRs, given that both are originating from the same source. **C:** The same CR model predicts cosmogenic neutrinos (dotted green) due to the GZK mechanism. The mismatch between CR data and the CR model is explained by the chosen model, which does not account for the CR flux below 10^{10} GeV where additional models have to be considered. Details regarding the models and normalizations can be found in [36] and references therein. Details regarding the IceCube analyses are described in [17] and references therein.

On average, each of the three neutrinos created in the decays in equations 1.6 and 1.7 receives about one quarter of the energy of the pion. The pion carries typically 20% of the initial proton energy [37].

Neutral pions decay into γ-rays:

$$\pi^0 \rightarrow 2\gamma \qquad (BR = 98.8\%). \qquad (1.8)$$

Assuming equal amount and energy of neutral and charged pions at creation, the γ-rays are more energetic, because the carry 1/2 of the pion energy, but more neutrinos are generated. In pp - collisions a lot of other heavier particles can be created as well. Besides pions, kaons (K) are also often the product of such collisions. These mesons also decay further resulting in neutrinos. The corresponding decay channels will be further discussed in section 1.4.

1.3 The Neutrino Flux Spectrum
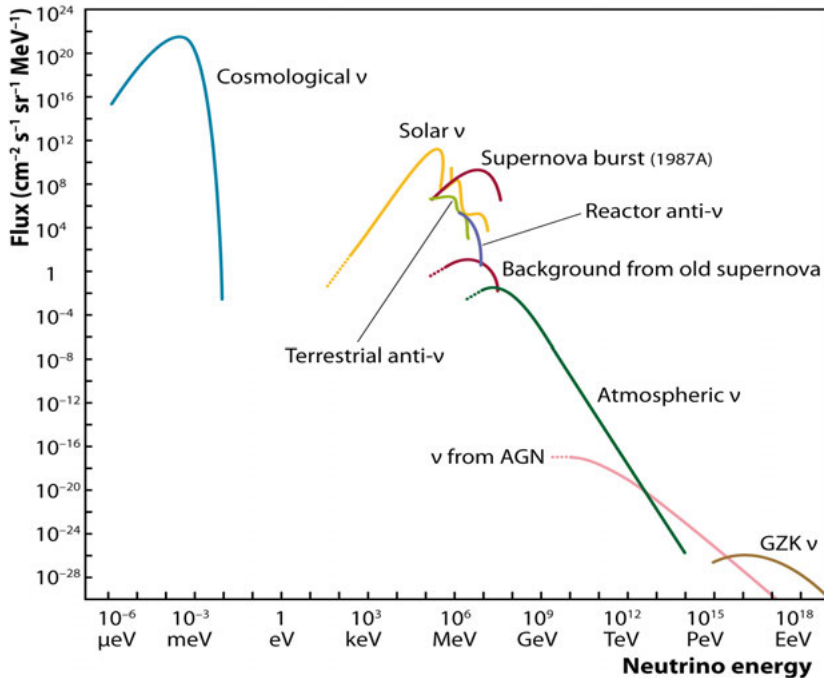
Figure 1.5. The energy spectra of neutrinos from different sources are visualized. Credit: [189].

Figure 1.5 shows the fluxes of neutrinos originating from various sources as function of energy. At the lowest energies an abundant flux of *cosmologi-*

cal neutrinos is expected. According to the *Big Bang model* these neutrinos decoupled from matter about one second after the Big Bang. Due to their vanishing interaction probability and energy transfer they have not yet been detected with present detection methods.

At higher energies (keV–MeV) neutrinos originate from the Sun, the interior of the Earth, nuclear reactors and supernovae. The supernova 1987A occurred in the Large Magellanic Cloud and due to its relatively close distance (~ 50 kpc) a flux of neutrinos was detected by three detectors: Kamiokande II, Irvine-Michigan-Brookhaven detector (IMB) and Baksan [189]. Starting at about 10^8 eV atmospheric neutrinos, created in CR interactions with the atmosphere[6] dominate the spectrum.

At energies above $\sim 10^{12}$ eV astrophysical neutrinos from sources like AGNs and GRBs are expected to exceed the flux of atmospheric neutrinos. At the end of the energy spectrum a flux of *Extreme High Energy* (EHE) cosmogenic neutrinos is predicted, originating from CR interactions with the CMB, resulting in the GZK cutoff.

The investigation of high energy neutrinos is an effort in which three experiments are currently involved: the deep underwater neutrino telescope in lake Baikal at a depth of about 1 km [56], ANTARES (Astronomy with a Neutrino Telescope and Abyss environmental RESearch) in the Mediterranean sea at about 2.5 km depth [35], and IceCube buried in the Antarctic glacier, about 1.5 km below the surface [10]. All these neutrino observatories use the same detection technique: measuring Cherenkov light[7] with photomultipliers.

Baikal-GVD is the successor detector of the Baikal Deep Underwater Neutrino Telescope and since 2015 under construction. With an instrumented volume of one cubic kilometer within the Baikal lake, Baikal-GVD is expected to detect neutrino fluxes starting at energies of a few TeV up to 10^6 TeV [56].

ANTARES is a 10 megaton-scale detector located in the Mediterranean sea off the coast of Toulon in France detecting neutrinos above $\mathscr{O}(100\,\text{GeV})$. KM3NeT (Cubic Kilometre Neutrino Telescope) [33] will replace ANTARES as a future network of deep-sea neutrino telescopes. It will include two detectors: ARCA (Astroparticle Research with Cosmics in the Abyss) to be installed offshore at Capo Passero (Italy) and ORCA (Oscillation Research with Cosmics in the Abyss) being built close to the ANTARES site [154]. As the name suggests, ARCA will be suited to observe astrophysical neutrinos in the TeV to PeV energy range [39] and ORCA will be optimized to investigate oscillations of atmospheric neutrinos below 100 GeV down to a few GeV [201, 154]. KM3NeT, which is currently under construction, will have detector volumes between one megaton, due to ORCA, and several gigatons.

---

[6]See section 1.4 for details regarding CR interactions with the atmosphere.

[7]See section 1.5 for details regarding Cherenkov light.

ARCA will have the ability of monitoring the water volume between the two different sites for extremely high energetic events.

IceCube is currently the largest neutrino observatory with one cubic kilometer instrumented volume and uses the clear South Pole ice as detection material. IceCube will be upgraded as well and the details can be found in the outlook section 6.3.

While extragalactic neutrinos were first observed by IceCube in 2013 [142] and the estimate of the astrophysical neutrino flux has been improving [12, 123], the so called GZK-neutrinos have not yet been detected. IceCube is too small to be able to measure the GZK-neutrino flux with large significance within a reasonable timespan, but limits have been set on this neutrino flux constraining models which assume a proton-dominated mass composition of UHECR [14].

To observe neutrinos at the highest energies is the aim of radio-neutrino observatories. These telescopes are designed to detect neutrinos using the Askaryan effect[8], in which radio waves with a distinct signature are created by neutrino interactions. Different approaches are chosen to detect the radio signals from the highest energy neutrinos. The ANtarctic Impulsive Transient Antenna (ANITA) [112] is a balloon-borne experiment circling Antarctica at elevations of about 37 km. The Askaryan Radio Array (ARA) [167] consists of dipole antennas deep below the snow surface down to 200 m depth at the South Pole. The Antarctic Ross Iceshelf ANtenna Neutrino Array ARIANNA has shallow antenna stations right beneath the snow surface [60]. All these experiments are monitoring the ice for the predicted radio signals from UHE neutrino interactions. The ground-based experiments ARIANNA and ARA are both in early stages of development, and the future for both is under discussion. ARIANNA and the investigations performed with the detector will be described in Part II of this thesis starting with chapter 7.

1.4 Atmospheric Background

When searching for astrophysical neutrinos, atmospheric neutrinos and muons are the main sources of background events within the IceCube detector. When cosmic- or γ-rays enter the atmosphere they interact with the molecules and produce extensive air showers of secondary particles [105], see figure 1.6. Depending on the initial energy, these particle cascades can reach the surface of the Earth. Like the primary cosmic rays, the charged particles generated in the showers have relativistic energies and thus emit Cherenkov radiation.

Interactions induced by high-energy γ-rays, electrons or positrons lead to *electromagnetic showers*, where γ-rays interact due to e^+e^- pair production and

---

[8]The Askaryan effect is described in section 7.2.1.
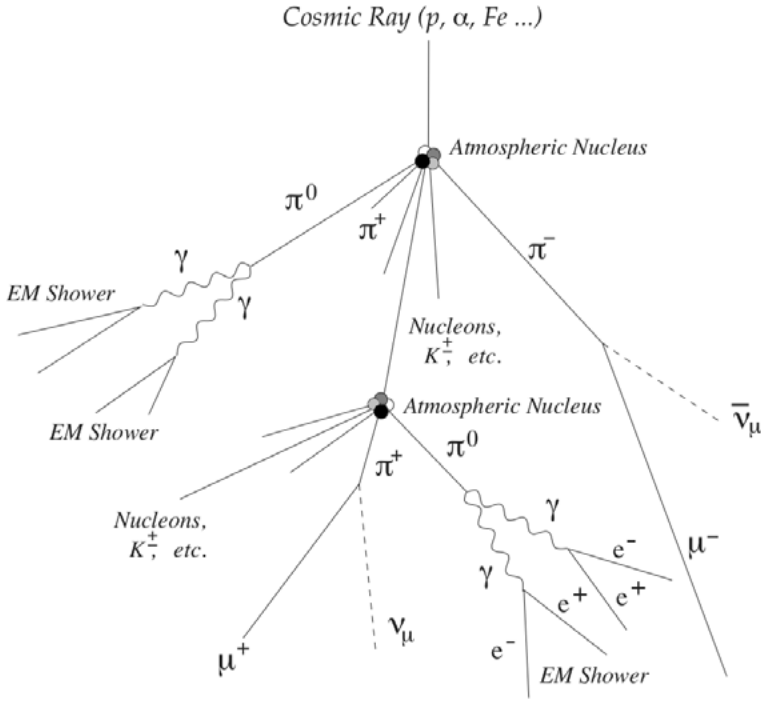
Figure 1.6. Development of an air shower created by a CR interaction with an atmospheric nucleus ($N, O, ...$). A hadronic shower of secondary particles ($\pi^{\pm,0}, K^{\pm,0}$, other particles) is generated. These particles either interact again, or decay. When a π^0 decays it creates an EM shower, charged pions lead to (atmospheric) muons and neutrinos. Figure adapted from: [173, 208].

$e^{\pm}$ emit γ-rays due to bremsstrahlung. These processes are repeated until the γ-rays do not have enough energy for pair-production anymore. Compton scattering and ionization become the dominant processes while the EM particles propagate towards the ground.

Cosmic ray interactions lead to *hadronic showers* in which different types of particles are generated, mostly pions and kaons [139]. These particles can either interact further or decay. The interaction length depends on the density of the atmosphere and the cross section of the particle, which increases with higher energy [59]. The incident zenith angle of the primary cosmic ray determines how much atmosphere the particle shower has to cross before reaching Earth. The probability of interaction depends on the density in the atmosphere. It is higher than the decay probability as long as the decay length, which depends on the particle energy and lifetime, is longer than the interaction length.

The *conventional muon and neutrino flux* represents atmospheric muons and neutrinos generated in kaon and pion decays. Kaons have several decay channels. The most important ones are:

$$K^{\pm} \rightarrow \begin{cases} \mu^{\pm} + \nu_{\mu}(\bar{\nu}_{\mu}) & (BR = 63.6\%) \\ \pi^{\pm} + \pi^0 & (BR = 20.7\%). \end{cases} \qquad (1.9)$$

The remaining decay channels are combinations of pions, muons, electrons and γ-rays and have branching ratios below 6% [198]. The most dominant decay channels for neutral Kaons[9] are:

$$K_S^0 \rightarrow \begin{cases} \pi^+ + \pi^- & (BR = 69.2\%) \\ \pi^0 + \pi^0 & (BR = 30.7\%), \end{cases} \qquad (1.10)$$

$$K_L^0 \rightarrow \begin{cases} \pi^{\pm} + e^{\mp} + \bar{\nu}_e(\nu_e) & (BR = 40.6\%) \\ \pi^{\pm} + \mu^{\mp} + \bar{\nu}_{\mu}(\nu_{\mu}) & (BR = 27.0\%) \\ \pi^0 + \pi^0 + \pi^0 & (BR = 19.5\%) \\ \pi^+ + \pi^- + \pi^0 & (BR = 12.5\%) \end{cases} \qquad (1.11)$$

Pions decay according to the equations 1.6 and 1.8. The γ-rays from the π^0 decay lead to cascades, which are denoted as the *electromagnetic component* of the hadronic shower. The ratio of kaons to pions depends on the primary CR energy and atmospheric density [105, 117].

Critical energies for kaons and pions are defined at which the probability to interact equals the probability to decay, assuming an isothermal atmosphere. Below the critical energy the particles decay rather than interact and lead to conventional muon and neutrino fluxes with the same spectral index as the parent CR. Above the critical energy the conventional spectra become steeper (softer) by about one order of magnitude ($dN/dE \propto E^{-3.7}$) compared to the primary CR spectrum ($dN/dE \propto E^{-2.7}$).

At energies higher than $\sim 100\,\text{GeV}$ muons and neutrinos from heavier charmed hadrons like D-mesons or Λ_c-baryons should contribute to the spectrum [95, 105, 187]. These hadrons have short lifetimes of about $10^{-13}\,\text{s}$ - $10^{-12}\,\text{s}$ [198], and therefore decay within short distance from their creation point. The particles generated in this process are called *prompt* contributions. The resulting prompt muon and neutrino fluxes are expected to have the same energy spectrum as the primary cosmic rays. Such decays have not yet been

---

[9]The states K^0 and $\bar{K}^0$ created in the CR interactions are mixtures of the *weak eigenstates* K_S^0 and K_L^0, denoted according to their relatively short and long lifetime. The reader is referred to [119] for details.

identified, which implies low flux. Limits on the prompt neutrino flux were set by IceCube [123].

Muons have a lifetime of about 2.2 µs [198] and depending on their energy they can reach the Earth surface and penetrate further through kilometers of water, ice or even rock. When muons are produced in the atmosphere by the decay of pions and kaons they usually have relativistic velocities and are not stopped by the overburden of ice. Therefore many muons reach the detector from above. IceCube detects about 10^{11} atmospheric muons per year, despite being buried 1.5 km below the ice. Muons induced by atmospheric neutrinos can arrive from all directions because neutrinos can traverse the Earth before interacting with the ice or bedrock. The number of neutrino induced leptons sums up to about 10^5 per year. Therefore atmospheric muons and atmospheric neutrinos represent the largest background for analyses searching for astro-physical neutrinos with IceCube.

ARIANNA has the aim to detect neutrinos at the highest predicted ener-gies and atmospheric muons and neutrinos do not have the required energy to represent background for this detector. The backgrounds for ARIANNA are discussed in section 7.2.2 and 7.3.2

1.5 Neutrino Interaction and Particle Detection

Neutrinos are hard to detect because they undergo only weak interactions, ne-glecting the vanishing influence of gravitation. In IceCube neutrino detection is carried out indirectly by the observation of the Cherenkov light emitted by their charged leptonic partners or secondary particles, created in the hadronic cascade, when the neutrino interacts with the ice or bedrock. At high ener-gies (> multi-GeV) deep inelastic scattering becomes the dominant process for neutrino nucleon interactions [144].

There are two types of interactions, the *Charged-Current* (CC) interaction via a W-boson and *Neutral-Current* (NC) interaction via the Z-boson. The inter-actions can be described as follows:

$$
\begin{aligned}
\nu_l(\bar{\nu}_l) + N &\to l^{\mp} + X &\qquad (CC) \\
\nu_l(\bar{\nu}_l) + N &\to \nu_l(\bar{\nu}_l) + X &\qquad (NC).
\end{aligned}
\tag{1.12}
$$

The l represents the flavors (e, μ, τ) of the leptons, the N stands for a nucleon and the X for a hadronic cascade. The corresponding Feynman diagrams are shown in figure 1.7. Every charged lepton, created by a CC interaction leaves characteristic signatures in the detector, which will be discussed in section 3.7. The interactions of neutrinos with electrons can be neglected at the energies at which IceCube operates. The only exception is the Glashow resonance [109],

see figure 1.8 for the cross-section. The Glashow resonance describes the interaction of anti-electron neutrinos $\bar{\nu}_e$ with electrons e^- creating a W^--boson, which happens when the $\bar{\nu}_e$ reach a threshold energy of 6.3 PeV.
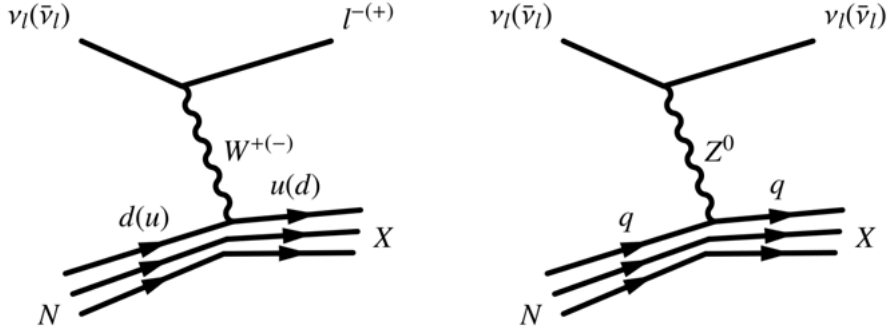
Figure 1.7. Feynman diagram for the CC neutrino-nucleon interaction (left) and NC-interaction (right). Credit: [194]

The cross-section for a neutrino-nucleon interaction in general increases with the neutrino energy. In figure 1.8 the neutrino-nucleon cross-sections for neutrinos and anti-neutrinos are shown for their CC and NC interactions. The peak shows the cross-section for the Glashow resonance. At the highest scales two models are used to extrapolate the structure functions, the *Hard Pomeron* (HP) and a smooth power law extrapolation (pQCD), see [108] and references therein.

Both CC and NC interactions produce a hadronic particle shower of neutral and charged particles. In addition the CC interaction will produce a charged leptonic particle.

In general charged particles moving faster than the speed of light in a medium, here ice, will give rise to Cherenkov light. They polarize the adjacent atoms along their way. When the atoms fall back into equilibrium they emit dipole radiation. Usually this radiation undergoes destructive interference and can therefore not be detected, but if the particle velocity is larger than the speed of light in a medium, the radiation interferes constructively and forms a cone shaped wave front, see figure 1.9.

The characteristic angle θ_c of the Cherenkov cone is given by

$$\cos\theta_c = \frac{1}{n\beta},\tag{1.13}$$

where n is the refractive index and $\beta = v/c$ the speed of the particle. When the velocity reaches a limit of $\beta \approx 1$, the Cherenkov angle becomes $\theta_c \approx 41°$ in ice with the refractive index $n \approx 1.33$. With equation 1.13 it is possible to
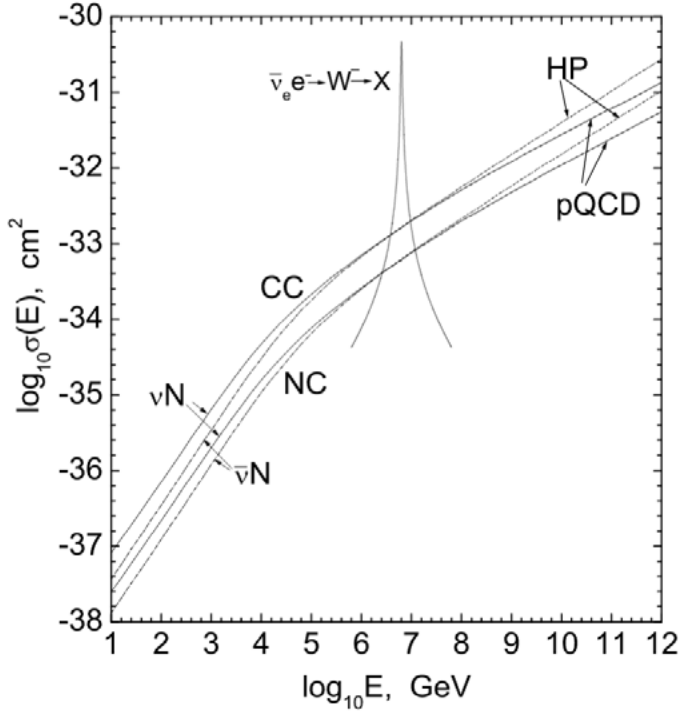
Figure 1.8. Neutrino-nucleon cross-section as a function of energy for ν and $\bar{\nu}$, their CC and NC interaction and at higher energies the extrapolation models HP and pQCD are shown. Figure credit: [108]
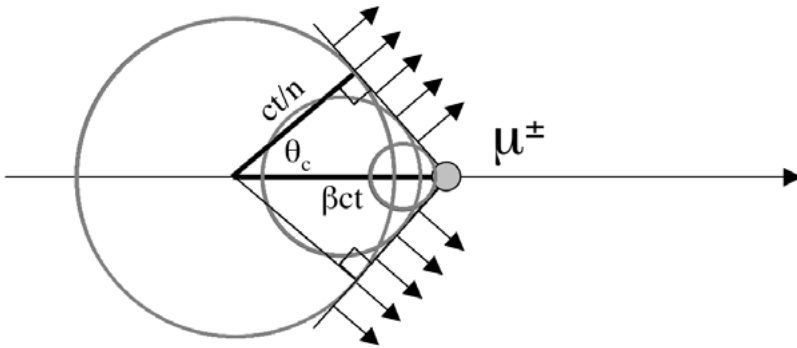
Figure 1.9. Depicted is the generation of a Cherenkov cone by a relativistic muon moving through a medium. Figure from [149]

determine the total energy E_{tot} a charged particle with mass m needs to radiate Cherenkov light:

$$\frac{1}{n\beta} \leqslant 1 \Leftrightarrow E_{tot} \geqslant \frac{m}{\sqrt{1 - \frac{1}{n^2}}} \qquad (1.14)$$

The Frank-Tamm formula describes the number of photons N produced per unit path length x and wavelength λ:

$$\frac{dN^2}{dxd\lambda} = \frac{2\pi\alpha z^2}{\lambda^2}\left(1 - \frac{1}{\beta^2 n^2(\lambda)}\right), \qquad (1.15)$$

where α represents the fine-structure constant, z is the particle's charge number and $n(\lambda)$ is the wavelength dependent refractive index. How the Cherenkov light is captured in IceCube is described in section 3.3.

1.6 Energy Losses of Charged Leptons

This section is rather important for IceCube. The charged leptons produced in a neutrino-nucleon interaction, e, μ, τ, experience energy losses while traversing the ice. The energy loss, caused by the Cherenkov effect, is small in comparison to other energy loss mechanisms which are described below. Therefore it can be neglected.

1.6.1 Electrons

The main process through which high-energy electrons (above 79 MeV in ice) loose energy is bremsstrahlung [121]. The photons created by the bremsstrahlung will undergo electron-positron pair production, which will create further bremsstrahlung photons. This process creates an electromagnetic shower and repeats until the photons do not have enough energy for pair production. The average energy loss per unit path of the involved electrons can be described as:

$$-\left\langle\frac{dE_e}{dx}\right\rangle = \frac{E_e}{X_0}, \qquad (1.16)$$

where X_0 represents the radiation length of the electron, which equals to $X_0 = 36.08$ g/cm^2 for ice [198]. The radiation length is a characteristic of the material related to energy loss and and is usually measured in g/cm^2.

1.6.2 Muons

Ionization dominates the muon energy losses at energies of order GeV and with higher energies $\mathcal{O}(\text{TeV})$ radiation processes start to dominate. The ionization losses are continuous along the trajectory of the muon and are a result of many interactions with small energy transfers. The radiation processes are usually stochastic and involve bremsstrahlung, pair production and inelastic photo-nuclear interactions. The average loss rate for all losses can be described by:

$$-\left\langle \frac{dE_\mu}{dx} \right\rangle = a + bE_\mu. \tag{1.17}$$

The coefficient a is approximated with $a = 0.268\,\text{GeV mwe}^{-1}$ and represents the ionization, and the coefficient $b = 0.47 \cdot 10^{-3}\,\text{mwe}^{-1}$ summarizes all radiative energy losses[10]. These approximations are valid for muons with energies between $20\,\text{GeV}$ and $10^{11}\,\text{GeV}$ in ice [82].

1.6.3 Tau Leptons

The tau leptons are the heaviest leptons, with a mass of $1777\,\text{MeV}$. They have a short lifetime of about $2.9 \cdot 10^{-13}\text{s}$ [198] when they are at rest. Because they decay almost immediately after production, it is much more likely to observe the decay products than the τ itself. The main decay channel with a branching fraction of about 65% is hadronic and the decay products are mostly kaons, pions and a tau neutrino. The leptonic decay channels are split almost evenly between electrons and muons:

$$\begin{aligned}
\tau^\pm &\rightarrow e^\pm + \nu_e(\bar{\nu}_e) + \bar{\nu}_\tau(\nu_\tau) && (17.8\%) \\
\tau^\pm &\rightarrow \mu^\pm + \nu_\mu(\bar{\nu}_\mu) + \bar{\nu}_\tau(\nu_\tau) && (17.4\%)
\end{aligned} \tag{1.18}$$

In the case of a leptonic decay the resulting leptons undergo the energy losses described above. The event signatures of these particles in IceCube are described in section 3.7

---

[10]The unit mwe stands for *meter water equivalent* and is described in the Preface under the section 'Units and Conventions'.

Part I:

Investigation of Neutrinos from the Fermi Bubbles with IceCube
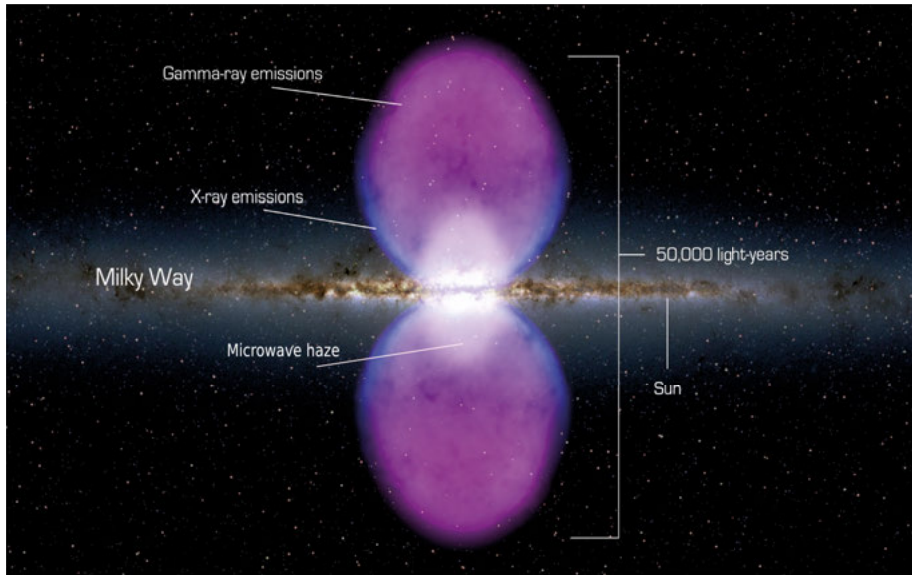
Illustration I. Artistic representation of the Fermi bubbles (violet) above and below the Galactic plane in Galactic coordinates. The figure also shows the X-ray radiation surrounding the Fermi bubbles (blue) and the microwave haze (white). Figure adapted from: [171].

2. The Fermi Bubbles

The *Fermi Bubbles* (FB) are extended regions of γ-rays located above and below the *Galactic Center* (GC), each stretching about $76\,650$ pc across, see Part I front page illustration I. They were discovered with data from the Fermi-Large Area Telescope (Fermi-LAT) [54], an instrument on the Fermi Gamma Ray Space Telescope spacecraft. The FB were initially discovered in 2010 [93, 193].
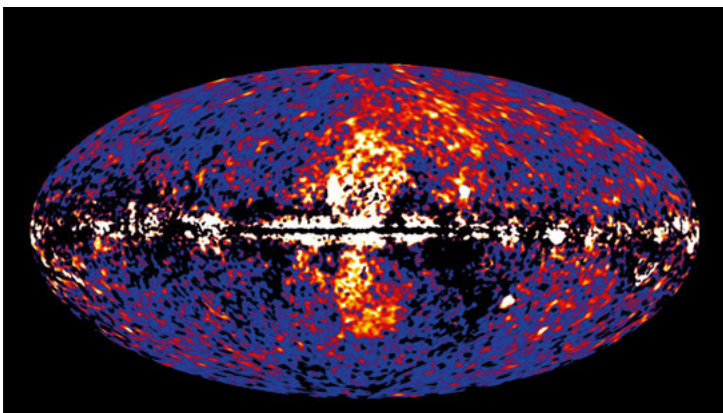
Figure 2.1. Residual all-sky map showing the Fermi bubbles (bright orange bubbles) stretching out of the Galaxy perpendicular to the Galactic plane (horizontal black line) in Galactic coordinates. This figure shows the radiation observed between 1 GeV and 10 GeV. The brighter the color the higher the energy of the gamma radiation. The Galactic foreground radiation was subtracted. Credit: [87]

In Galactic coordinates each bubble spreads from $0°$ to $|l| \approx 50°$ in longitude and $|b| \approx 40°$ in latitude. The Fermi bubbles have a mainly uniform intensity distribution with a smooth surface and sharp edges. The total luminosity of both bubbles is about 4×10^{37} erg /s which corresponds to about 2.5×10^{40} GeV /s [193]. Features within the Fermi bubbles were found in 2012: a γ-ray cocoon surrounding a jet in the southern bubble and a jet in the northern bubble [192]. The cocoon in the southern bubble was confirmed by Fermi-LAT in 2014, but no significant evidence for the jets was observed [30]. In 2018 the γ-ray sky around the Fermi bubbles was investigated with Fermi-LAT data [57]. Amongst other results, a cocoon in the northern Fermi bubble was identified. The northern cocoon is dimmer than its southern counterpart.
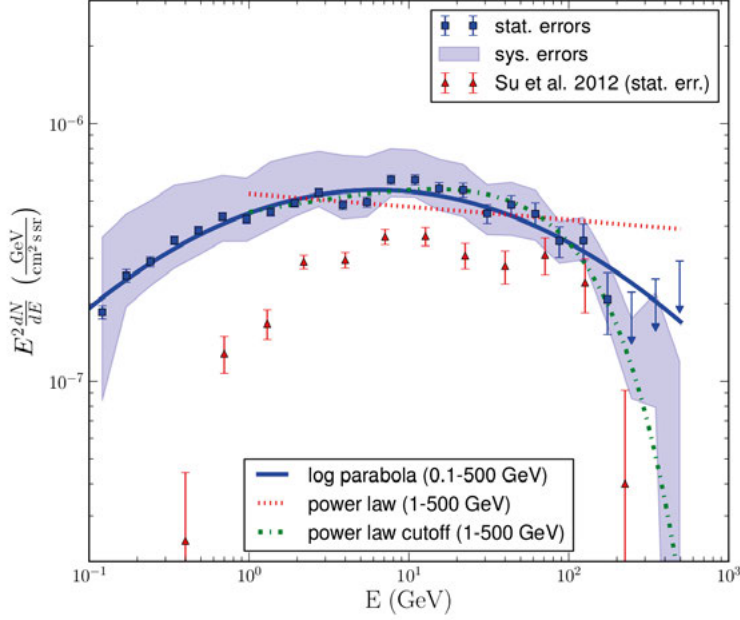
Figure 2.2. The observed Fermi bubble spectrum from Fermi-LAT combined for both bubbles. The red triangles show the spectrum analyzed by Su et. al. in 2012 [192]. The blue squares are the data analyzed by Fermi-LAT in 2014 [30].Three fits were performed by the Fermi-LAT collaboration, a log-parabola fit (solid blue), a power law (red dashed) and a power law with cutoff (green dashed-dotted). The data was analyzed from 100 MeV to 500 GeV and is consistent with an exponential cutoff at $\sim$ 100 GeV. The Fermi-LAT collaboration explains the difference between the observations in 2012 and 2014 as due to different analysis methods. A different foreground radiation modeling, definition of the FB shape template and Galactic plane mask was used. Credit: Fermi-LAT [30].

It was believed that the Fermi bubbles emit a hard E^{-2} γ-ray spectrum but the results from the Fermi-LAT collaboration in 2014 suggest that their spectrum fits better to a log parabola when considering the entire emission spectrum (100 MeV - 500 GeV) [30], see figure 2.2. In another paper analyzing the FB in 2014 an appreciable drop of the γ-ray flux was observed in the southern bubble, at low latitudes ($< -47.5°$) and low energies (< 10 GeV) [215]. The structure of the Fermi bubbles showed to be more extended to the Galactic south and west at higher energies.

The High Altitude Water Cherenkov detector (HAWC) [25] investigated the Fermi bubble γ-ray flux of the northern bubble at higher energies than Fermi-LAT, setting upper limits above 1 TeV [26].

In order to observe the Fermi bubbles in the first place the Galactic plane had to be masked out in [193, 192, 30]. The base of the Fermi bubbles was investigated separately in various aspects. It has been suggested, that the *Galactic Center excess* (e.g. [111, 19]), a spherical diffuse γ-ray emission around the Galactic Center exceeding the astrophysical background, either connects smoothly to the Fermi bubbles, or that the FB brighten significantly below $15°$ in latitude [57]. An investigation of the Galactic Center excess by the Fermi-LAT collaboration analyzed the Fermi bubble base below $|b| < 10°$, assuming the same hard spectrum as observed at high latitudes. The conclusion was that the origin of the excess is likely due to the Fermi bubble radiation at the base and a another contribution. This contribution could be due to interactions of CRs from unresolved point sources in the vicinity of the GC or due annihilation of dark matter particles [29]. Another investigation of the Fermi bubbles base was performed ($|l| < 10°, |b| < 6°$) in 2019 [130]. In order to be sensitive to the γ-rays from this region known γ-ray sources were masked out. The result shows that this region has a higher intensity than the FB emission at high latitudes. Furthermore, comparing the spectra in west (negative longitudes) and east (positive longitudes), a hard E^{-2} spectrum is observed in the west, while a softer spectrum is seen in the east [130].

2.1 Features in Other Wavelengths

Not only γ-rays were observed in the region of the Fermi bubbles. Co-located with the FBs are structures in other wavelengths, ranging from X-ray to radio emission.

Many investigations using X-rays (e.g. [166], [40], [195], [168]) and Ultra-Violet absorption lines (e.g. [76, 146]) in the vicinity of the FB were used in order to set constraints on the Fermi bubble's and the Galactic Halo's thermal and kinematic gas structure. Here, we will mention the most likely feature to be connected to the FB, and refer to [213] for a broader overview. X-ray maps from ROSAT [188] were investigated with regard to the FB, revealing biconical X-ray structures at $1.5 \, \text{keV}$ at the edges of the Fermi bubbles towards the Galactic Center (below latitudes of $l < 20°$) [74, 193], see illustration I. More recent results show an extension of the X-ray structures to high latitudes with decreasing intensity, but associated with the FB edges [150].

Ultraviolet absorption-line spectra from the Hubble Space Telescope were used in [101] to constrain the velocity of the outflowing gas near the base of the northern Fermi Bubble. Simple kinematic biconical outflow models were developed to explain the observations resulting in an outflow velocity of $\gtrsim 900 \, \text{km/s}$.

The *microwave haze* was discovered in 2004 by the Wilkinson Microwave Anisotropy Probe (WMAP) and extends from the Galactic Center to $|b| \approx 30°$ with a radius of about 4 kpc [100], see illustration I. In 2013 the observations were confirmed by the Planck satellite [176] and since then the haze was also referred to as *WMAP-Planck haze*. Technically the discovery of the Fermi bubbles was a result of the search for a counterpart of the microwave haze in γ-rays. Before the bubbles were discovered, the so-called Fermi haze was observed in 2010 with Fermi-LAT gamma ray data [93]. The Fermi haze showed similar morphology to the microwave haze and a correlation was suggested. The Fermi bubbles are believed to be a major component of the Fermi haze. However, while the Fermi haze was believed to be described by Gaussian fall-off in intensity, the Fermi bubbles show sharp edges [193] and therefore dominate at high latitudes. It has been further investigated if the microwave haze and the Fermi bubbles are correlated [93, 92]. Due to the hard spectrum of both the WMAP-Planck haze and the Fermi bubbles, and the comparable spatial locations a common origin is suspected. The latest results are confirming this suspicion, but no certain evidence has been found yet [184].

The S-Band Polarization All Sky Survey (S-PASS) has observed two linearly polarized radio lobes at 2.3 GHz co-located with the FB in 2013. The lobes are extending to higher latitudes than the Fermi bubbles ($\sim \pm 60°$) and are assumed to be counterparts to the Fermi bubbles [79].

Due to their spatial coexistence, all features discussed in the preceding few paragraphs are assumed to be counterparts of the Fermi bubbles and a common physical origin for these signals is hypothesized.

2.2 Comparison to Other Galaxies

Studies have shown an indication that similar structures to the Fermi bubbles also exist in other galaxies, here we will mention a few. The most famous example which shows extended γ-ray radiation is the galaxy *Centaurus A* [120], with an extend of about 521 222 pc. This galaxy has an active galactic nucleus and therefore shows features in a large range of wavelengths.

NGC 3079 is also an active Galaxy which shows bubbles in radio, Hα and X-ray. The south-west bubble shows a hard X-ray spectrum, similar to that of the FBs. These bubbles are assumed to be analogs to the Fermi bubbles [162]. It is rather common to observe multi-wavelength outflows in active galaxies, which is why it was fascinating to find features like the Fermi bubbles also in our Galaxy.

However, the Milky Way is not the only inactive galaxy showing multi-wavelength features. The galaxy M31 shows signs of γ-ray bubbles [179] and a microwave haze [90]. It is believed, that these features are remains of an active period of the corresponding galactic nuclei in the past.

2.3 Origin of the Fermi Bubbles

Many models were developed to explain the formation of the Fermi bubbles. Amongst others there are leptonic and hadronic models, which explain the radiation processes, in-situ models, which are focused on the acceleration processes, and inflation models which are involved with the transport of particles and inflation of the FB shape. Here, we will give a short summary of the most probable models, divided by leptonic models, hadronic models and their combination. Within those models questions like which cosmic rays are involved, how they could be transported into the Fermi bubbles and different ways of their acceleration will be addressed. A more detailed review of the FB is provided in [213].

2.3.1 Leptonic Models

Leptonic models are based on the idea that high energy cosmic-ray electrons and positrons (CRe) scatter off the *Interstellar Radiation Field* (ISRF) or CMB and create the observed γ-rays by *Inverse Compton* (IC) radiation. Most models suggest that the CRe were accelerated by previous AGN jets emerging from the GC (e.g. [122, 212, 211]). The challenge with leptonic jet models is that fast AGN jets with velocities of the order of thousands[1] of km/s would be required to transport the CRe to a sufficient distance, maintaining the hard spectrum, before they rapidly cool down due to IC scattering and synchrotron radiation. The fast expansion should also lead to stray jets, which were not observed. Furthermore, a very strict FB age constraint of a few million years is set due to cooling. These models can explain the microwave haze and the polarization features due to synchrotron radiation (e.g. [212]), but it remains unclear if the X-ray structures can be explained with the assumption of fast jets [213].

Alternative models surmounting these difficulties are provided with in-situ acceleration. An example is stochastic acceleration of CRe by isotropic, large-scale turbulence in magneto-sonic waves [165]. With in-situ models more simulations are needed to assess if they are consistent with the spatial and spectral data of the observations in other wavelengths [213].

---

[1]Usual jets have velocities of hundreds of km/s.

2.3.2 Hadronic Models

In Hadronic models cosmic-ray protons (and heavier nuclei) interact with the *InterStellar Medium* (ISM) in the Fermi bubbles resulting in the γ-rays and neutrinos as final products. In most models the CR were created and accelerated close to the Galactic Center, either by *Nuclear Star Formation* (NSF) or by the AGN. Afterwards the cosmic rays were carried by the Galactic winds into the region of the Fermi bubbles. Especially new born high-mass stars radiate strong winds and due to Supernova explosions even more extreme winds are emitted.

Hydrodynamical numerical three-dimensional simulations have shown that winds originating from a time when the supermassive black hole *Sagittarius A** (Sgr A*) in the center of the Milky Way was active could have produced the morphology of the Fermi bubbles [169]. In this model, the active phase lasted for 10^7 years and was quenched only 0.2×10^6 years ago. The X-ray features are explained by bremsstrahlung of the shocked, and therefore heated gas.

Another hadronic model treats the Fermi bubbles as scaled-up SNR [102]. With this model the scaled-up SNR could be created by either AGN activity or starbursts at the GC, but the model does not depend on the initial event. The CRs are accelerated at the strong forward shock-front, and the interaction between the CRs and the gas behind the shock develops over time into the Fermi bubble shape, including the flat brightness and sharp edges.

2.3.3 Combination of Leptonic and Hadronic Models

Although hadronic models reproduce the FB γ-ray spectrum, they fail to reproduce the microwave haze using only secondary electrons and positrons. Hence, populations of primary CRe were introduced in follow-up papers (e.g. [170, 103]).

Another model suggests that the CRs (p and e) are carried into the Fermi bubbles by winds launched by the Galaxy, and the CRs are accelerated by termination shocks. When the winds reach the gas in the Galactic halo they are slowed down and lead to the termination shocks. With this assumption the acceleration process is not localized (in-situ) and the Fermi bubbles remain in a steady-state as long as the GC star formation region is active. With this acceleration model, the Fermi bubble age has no constraints and the sharp edges are reproduced, however the spatial and spectral properties cannot easily be explained and need further investigation [157].

2.3.4 Chosen Hadronic Model

In [85] cosmic rays are produced and accelerated in the NSF region close to the Galactic Center. The Galactic winds carry the CRs into the FB region,

where they are trapped by magnetic fields for about 10^{10} years. For simplicity and because of their dominant number only protons (p) are assumed as CRs, which interact with the ambient matter according to equations 1.3 and 1.4, creating mesons, γ-rays, leptons and neutrinos. Neutral pions decay into γ-rays (eq. 1.8), which create the observed Fermi bubbles. Charged pions deliver neutrinos (eq. 1.6 & 1.7), which could be observed with IceCube.

In this model the X-rays are explained by a plasma injected at the base of the winds, which radiates X-rays in form of bremsstrahlung. The microwave haze is realized by the synchrotron radiation of secondary electrons and positrons. However, also in this model the secondary e^- and e^+ fail to explain the hard microwave spectrum.

In a follow-up work the model was improved introducing a reverse shock, the re-accelerating properties of which are used to explain the γ-ray bubbles, the microwave haze and the polarized radio-lobes. Synchrotron radiation from re-boosted CRe explain the structure and spectrum of the WMAP-Planck haze. As these electrons gain distance they lose energy, and form the observed polarized S-PASS radio lobes. Also the CRs are re-accelerated contributing to the FB γ-ray radiation. However, another generation of primary CRe (10% - 30%) is needed to describe the γ-radiation due to Inverse Compton emission[2]. Including these effects the timescale of the FB formation reduces to a few times 10^8 years [86].

The goal of the analysis presented in this thesis is to investigate a potential neutrino flux at the energies at which the Fermi bubble γ-ray flux was measured, between $10\,\mathrm{GeV}$ and up to $200\,\mathrm{GeV}$.

---

[2]When the analysis of this work was started this model was not published, hence, this analysis does not account for the new leptonic part of the model.

3. The IceCube Observatory
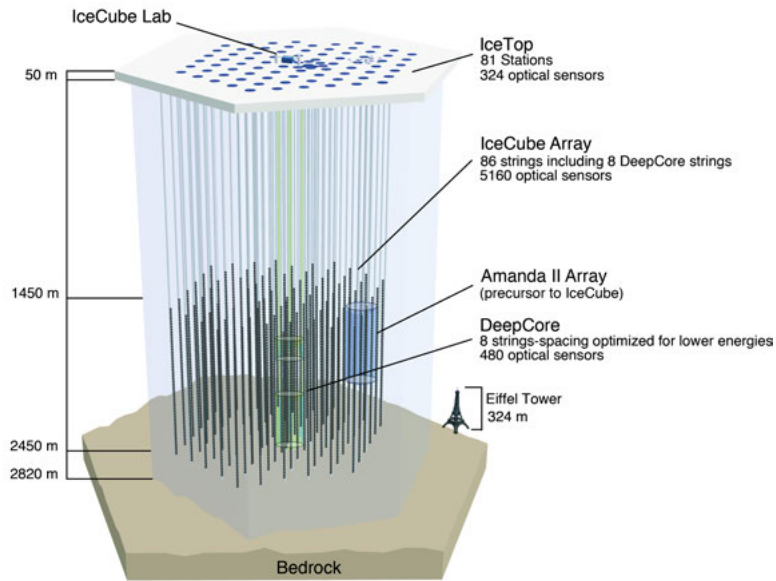
Figure 3.1. Schematic illustration of the complete IceCube neutrino observatory. Also shown, the precursor of IceCube, which is not in use anymore: AMANDA. Credit: IceCube collaboration.

In order to detect neutrinos arriving from sources outside our solar system a large neutrino telescope is needed. The IceCube Neutrino Observatory [126] is a neutrino detector in Antarctica close to the geographical South Pole. IceCube consists of an in-ice array, with strings of *Digital Optical Modules* (DOMs) positioned in one cubic kilometer of the extremely clear glacial ice at depths between 1.45 km and 2.45 km, and a surface air-shower array covering an area of one square kilometer. The construction started in 2005 and was completed in 2011, but data was already taken with the first string. For the deployment of each string a hole was drilled in the ice using hot water. The string was then rapidly put in place within the drill hole, and the water would re-freeze. It takes a couple of weeks until a hole freezes completely, starting at the surface and moving slowly down the hole. After the string of DOMs is locked into place by the surrounding ice it is commissioned into the data acquisition system and is ready to detect Cherenkov light.

3.1 The In-Ice Array

This volume of ice is monitored by 5160 CRs secured to 86 strings, cables which connect the DOMs to the *IceCube Laboratory* (ICL) and transmit power to the DOMs and signals from the DOMs to the ICL. The part of the in-ice array which is referred to as "IceCube strings" consists of 78 strings on a hexagonal grid with 60 DOMs attached and 125 meters spacing. The vertical spacing between the DOMs is 17 meters. With this configuration a neutrino energy threshold of about 100 GeV is achieved [126].

3.1.1 DeepCore
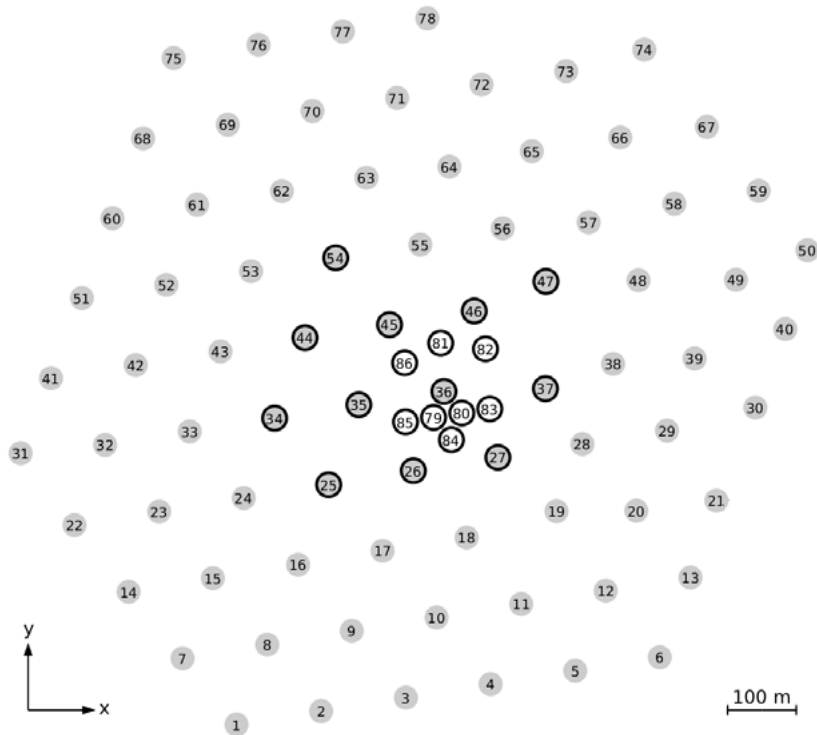
Figure 3.2. Top view of the positions of IceCube strings (gray) and DeepCore strings (white with black border). The gray strings with black border are IceCube strings which are used as extension for DeepCore. The gray strings without edge are the strings used for the IceCube veto. The numbers indicate the identification number of each string. The indicated coordinate system refers to the local coordinate system shown in figure 4.1. The local coordinate system has its origin in the center of the array. Credit: [194].

The eight remaining strings are distributed between the central IceCube strings and have a denser string- and DOM spacing of 72 m and 7 m respectively. The majority of the DOMs (50 per string) are located in the bottom part of the Ice-Cube volume below a dust layer between the depths of 1950 m and 2150 m. The remaining 10 DOMs of each DeepCore string are distributed with a 10 m spacing right above the dust layer, providing an additional veto against atmospheric events. These eight strings together with the neighboring IceCube strings form the sub detector *DeepCore*. With the denser DOM spacing in DeepCore the energy threshold is lowered to 10 GeV allowing the investigation of neutrino oscillations and astrophysical neutrino fluxes at low energies [207].

3.2 IceTop

IceTop is a cosmic-ray air-shower array with an area of $1 \, \text{km}^2$ on the surface, 1.5 km above IceCube [22]. In total 81 stations are deployed above 81 IceCube strings. Each station is comprised of two $3 \, \text{m}^3$ tanks filled with frozen water, with two DOMs within each. Besides the detection of CR, IceTop is used as veto for IceCube to distinguish atmospheric muons from neutrino induced muons, although the solid angle is very limited [197, 22].

3.3 Digital Optical Modules

The DOM is a fully self-contained optical detector and holds the equipment needed to observe single Cherenkov photons [23]. The electronics are protected by a 13 mm thick glass sphere, which can tolerate the pressure and the cold temperatures ($-20 \, °\text{C}$ to $-40 \, °\text{C}$) increasing with depth. Figure 3.3 shows a sketch of a DOM with its different components.

The Hamamatsu *Photo Multiplier Tube* (PMT), which has a diameter of 25 cm, is used for Cherenkov light detection. Due to the photoelectric effect a Cherenkov photon that hits the photocathode of the PMT knocks out an electron, referred to as a *photoelectron* (PE). The PE gets accelerated by a high-voltage field towards the first dynode, where multiplication takes place due to secondary emission. Each of these electrons emitted are then accelerated towards the next dynode. The electrons collide with the dynode material and for each incident electron a few new electrons are emitted. The process is repeated in each dynode step. In total the used PMT has 10 dynodes. The gain of the PMT is 10^7, which enables it to detect single photons.

The quantum efficiency of the PMT describes the ratio between the number of photons and knocked out electrons. It reaches a maximum of 25% at a wavelength of 390 nm [21]. It should be noted that DeepCore DOMs have
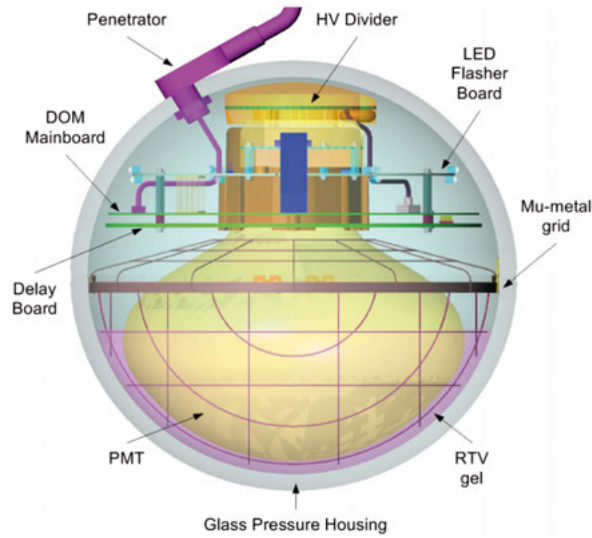
Figure 3.3. A schematic overview over the electronics within a Digital Optical Module. Credit [23]

.

a 35% higher quantum efficiency than IceCube DOMs [20]. The PMT efficiency is optimized to observe photons with wavelengths between 300 nm and 650 nm. However, the PMT is embedded in a optical *Room Temperature Vulcanization* (RTV) silicone gel [23] which provides optical coupling to the glass housing. The glass and gel limit the observable wavelengths to 350 nm and 650 nm. In order to protect the PMT from the magnetic field of the Earth it is surrounded by a mu-metal grid.

To prevent all the electronics from corrosion the DOM is filled with nitrogen gas. To keep the two glass hemispheres together and provide an active compressive force, the pressure inside the CR is approximately 0.5 atmospheres. With an on-board pressure sensor it is possible to discover potential leaks in the seal as well as an impaired vacuum of the PMT. Close to the top of the sphere the cables, which are needed for communication and power supply, intrude into the glass with a penetrator [23].

When a signal is detected by the PMT it needs to be digitized. There are two digitizer systems on the mainboard: two *Analog Transient Waveform Digitizer* (ATWD) and one *fast Analog-to-Digital Converter* (fADC). Two ATWDs are in use to reduce the dead time of the DOM, so that one ATDW can record while the other one is digitizing. The signal from the PMT is first routed through a 11.2 m long strip on the delay board, where it gets delayed by 75 ns before it reaches the ATWD. This delay is necessary because the ATWD needs

50

to be triggered in order to start the readout of the signal and the delay allows the ATWD to capture the start of the waveform. The triggering mechanism of the PMT starts when the output voltage exceeds 25% of the average voltage produced by a PE. The trigger gets a time stamp from the clock circuit. At a sampling rate of 300 MHz, 128 samples are saved by the ATWD, which leads to a sampling time of about 3.3 ns/sample and hence a sample length of 422 ns [23].

In contrast to the ATWD the fADC digitizes the signal from the PMT continuously with the trade off of a lower sampling rate of 40 MHz, collecting 256 samples. This leads to a longer (6.4 μs) but coarser record of the signal with 25 ns bins. The advantage of the fADC is that it can capture waveforms which are significantly longer than the ATWDs are able to record.

The dark noise detected by the PMT arises mainly due to thermal emission of the photocathode and dynodes, and from radioactive decays within the protecting glass sphere. At the cold temperatures that the DOMs are exposed to, the total rate of the dark noise is determined to be 600 Hz [21]. The dark noise rate in DeepCore DOMs is about 700 Hz, an effect of the higher quantum efficiency [20]. Occasionally the radioactive decays lead to scintillation in the glass, which in turn can lead to correlated "bursts" of noise. If these bursts happen within the right time frame in several DOMs, they can cause a noise-induced trigger [159].

In order to record relevant hits and to avoid saving noise induced hits the DOMs communicate with the neighboring DOMs on a string. When a DOM receives a potential photon hit it starts the PMT readout and sends out a *Local Coincidence* (LC) signal to the nearby DOMs. The type of readout is then determined by coincidence conditions. When the readout of the sending DOM has started and a neighboring DOM observes a signal within 1 μs they are in coincidence, and a complete readout of the PMT is performed. This case is called *Hard Local Coincidence* (HLC). If no LC signal is received within this time frame the DOM is in what is called *Soft Local Coinicidence* (SLC, in spite of that no local coincidence was seen). The full readout is aborted and a compact form of the fADC record, called the "coarse charge stamp" is saved. This is determined by taking the first 16 fADC samples and saving the highest bin and its adjacent bins. The coarse charge stamp is recorded for every triggered DOM.

For calibration of the position of distant DOMs and ice studies each DOM contains a flasher board with *Light Emitting Diodes* (LEDs). There is also a LED on the main board to calibrate the time, which the PMT needs from a photon hit until readout (transit time) and to evaluate the PMT response function for a single photo-electron [23].

3.4 Data Acquisition System

The ICL is located at the center of the IceTop array, see figure 3.1 for the overview of IceCube. This is the place where the *Data Acquisition System* (DAQ) is housed. All cables from the IceCube- and DeepCore strings as well as the cables from the IceTop tanks are laid out on the surface and connect to the DAQ. A detector-global DAQ is used in IceCube to identify potential signal events and to prepare the data for processing and transfer to the North via NASA's satellites for analysis.

3.4.1 Triggering

The DOMs send data packages to the ICL. These data packages are called DOM launches and contain in addition to the coarse charge stamp, the locally generated timestamps and, if the LC condition is fulfilled, the complete fADC waveform and at least one ATWD waveform. All DOMs on one string are communicating with a DOMHub computer which is connected to the string. The DOM launches arriving at the DOMHubs are sorted corresponding to their time order. Then a global, time ordered stream of DOM launches is created from all strings. This global stream is sent to all trigger evaluation scripts.

The most fundamental trigger is called the *Simple Multiplicity Trigger* (SMT) and is based on the number of HLC DOM launches within a certain time window. In particular the SMT-8 trigger condition is used, where eight HLC launches occur within a $5\,\mu s$ window.

Each trigger communicates with the Global Trigger, that creates a trigger hierarchy which reflects the time overlaps of all triggers. The trigger hierarchy is then sent to an event builder which determines the start and end time of an event and collects all DOM launches in the event time range.

The complete event also includes the information from $4\,\mu s$ before and $6\,\mu s$ after the first/last trigger condition is fulfilled. The data is then stored in an IceCube specific file type called i3, where each event is saved within its own frame. Then the i3 files are sent to the *Processing and Filtering* (PnF) system.

3.4.2 Processing and Filtering

Downgoing muons created by CRs in the atmosphere cause a summed trigger rate of more than $3\,kHz$. Due to this high rate of background events, the data needs to be processed and filtered before it can be sent to the North via satellite, which has a limited bandwidth. Full information within limited time frames is sent only for specific analyses, e.g. in case of an Supernova alert. In addition, all triggered events are saved to data tapes which are shipped once per year to the northern hemisphere repositories.

The processing includes calibrating the waveforms extracted from DOM launches, finding pulses from the waveforms and cleaning them from noise. Furthermore, some general observables and basic event reconstructions are applied, which are needed by the filtering algorithms.

The filters are optimized to discriminate possible physics event candidates from background events. Each filter focuses on certain types of conditions, for example event topology or a certain energy range. Each event frame created by the DAQ is passed through initial reconstructions. The reconstructions lead to parameters, like total collected charge, trajectory and quality of the reconstruction, which are used in order to decide if the events are physics candidates. The filters are applied to every event and when an event passes at least one filter, the complete information regarding the candidate is sent to the North.

Triggering, processing and filtering are referred to as "online" treatment of the data, while the processing and analysis in the North are called "offline" treatment.

3.4.3 Detector Monitoring

A large detector like IceCube needs monitoring for stable operation, reducing downtime and verifying the goodness of the data. The data is usually taken in eight hour periods which are called runs. The runs usually arrive at the North a day after they were recorded due to the satellite coverage of only a couple of hours per day at the South Pole.

The run data is then stored in an IceCube internal database, *IceCube Live*, where it can be monitored. Basic information like the run status, its duration and the event count are visible in an overview. Detailed information like the rates of all triggers and filters as well as the rates of the DOM launches is available in corresponding registers. In order to ease the monitoring, which is performed by assigned shifters, the data undergoes several quality tests within IceCube's monitoring system *moni2.0*[1].

The shifter's work is to examine the continuity of trigger, filter and DOM launch rates. For each run, each trigger and filter rate plots are displayed and quality test results are calculated using the last good run for comparison. For the DOM launch rates a complete map with individual quality plots and tests is available, where the color indicates if there is an issue with a specific DOM. The monitoring system makes it easier to solve operational problems fast. Runs, which pass all quality tests and are confirmed as qualitative good runs by a shifter and the run coordinator, are summarized in a *good run list*.

---

[1] As the name suggests moni2.0 is a new monitoring system which replaced the old one with the first run of the season 2017/2018 in May 2017. In the 'Preface', subsection 'IceCube' a short summary of the work the author contributed to moni2.0 can be found.

They are considered as reliable for physics analysis. Runs where issues occurred and calibration runs are excluded from this list. However, not all data from a "bad" run is unusable. For certain analyses, like the investigation of transients like Gamma Ray Bursts, the good data from a run can still be used, and is therefore also saved. Furthermore, the monitoring system is able to cut out the "bad" parts of a run, for example in the case of a power outage. These runs can be added back to the "good" data set.

In order to keep the detector running 24/7 and to solve problems without delay, specially trained shifters stay at the South Pole station. They are called *Winterovers* because they stay for a complete year including the Austral winter. The Winterovers can be reached at any moment to solve problems like crashed computing nodes or failing runs, when remote resolving does not solve the issue.

3.5 The South Pole Ice
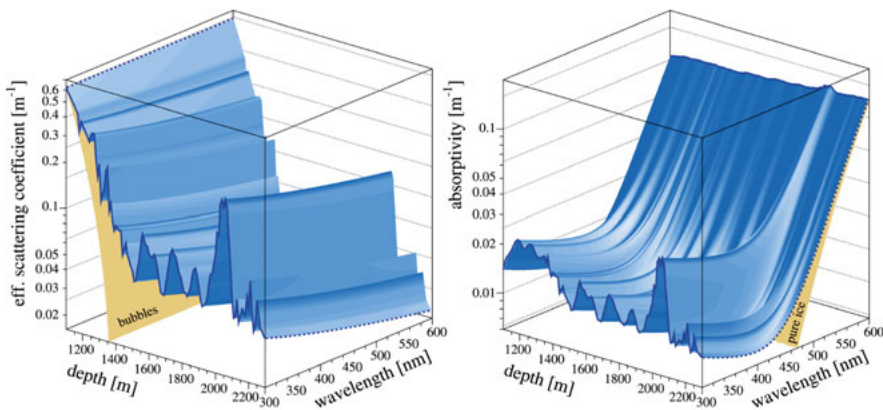
Figure 3.4. The effective scattering coefficient (left) and absorptivity (right) maps. The inverse of the coefficients are the scattering length and the absorption length, respectively. Around the depth of 2 km both have a large feature which is referred to as the main dust layer. The smaller features also represent dust layers. Credit: [31]

The ultra-clear glacial South Pole ice, which has formed over thousands of years from compressed snow, has a higher purity than laboratory ice [31]. However, the ice does show impurities and it is not completely homogeneous. At depths above 1.4 km air bubbles cause short scattering lengths for the desired wavelengths (300 nm - 650 nm) [210]. To be able to detect the faint

Cherenkov light IceCube was built 1.45 km below the surface. This also provides an overburden contributing to the reduction of the atmospheric muon background.

It is of high importance to understand the optical properties of the ice in order to simulate and reconstruct the events which IceCube detects. The most important characteristics are the absorption and scattering lengths. The LED flashers in the DOMs are frequently used in so called "flasher runs" for calibration and also investigation of the ice properties.

After drilling the holes, dust loggers [77] were used to measure the absorption and scattering properties directly. Furthermore, the ice properties were studied with the LEDs on the flasher boards of the CRs. These studies resulted in absorption and scattering coefficient models, see figure 3.4. The absorption and scattering lengths are mainly determined by the dust concentration and are therefore also correlated with each other. The features are believed to originate from climatic events which lead to different dust concentrations in the air. At depths between 1950 m and 2150 m the light transmission is poor. This feature is also visible in figure 3.4 and is referred to as the *main dust layer*. Most probably dust from the atmosphere, accumulated during an ice age[2], caused such an elevated level of pollution [2]. The absorption and scattering lengths within the dust layer are 18 m and 5 m respectively. However, below the dust layer the ice reaches its highest purity, and the absorption and scattering lengths in this region reach average values of 53 m and 172 m respectively [31].

The depth-dependent absorption and scattering coefficients are parametrized in a table that is used to describe the South Pole ice, amongst other parameters which are described in [7]. Research has shown a slight anisotropy of light propagation depending on direction. These findings are also included in the ice model used in this thesis: *SPICE LEA* [80].

3.6 IceCube Monte Carlo Simulation Chain

In order to understand the physical processes and detector response it is essential to have reliable *Monte Carlo* (MC) simulations. IceCube uses a chain of different simulations starting with the primary particle interactions, the propagation of the particles within the ice, the generation and propagation of the Cherenkov light and the detector response to the light. There are several MC simulations codes used in IceCube. Only those which are relevant for the presented work are described below.

---

[2]The ice age was probably induced by a change in the inclination of the Earths axis with respect to the Ecliptic [2].

3.6.1 Particle Generators

CORSIKA (*COsmic Ray SImulations for KAskade*) [129] is used to simulate atmospheric muons in IceCube. Primary cosmic ray particles such as nuclei, electrons and photons are injected at the top of the atmosphere and propagated towards the Earths' surface until they interact with a nucleon in the air. This collision creates either a leptonic or a hadronic particle air shower, depending on the primary[3]. CORSIKA then tracks all the particles in the shower and simulates their interactions and decays, until their energy falls below a chosen threshold. For the hadronic showers the interaction model SIBYLL is used [185].

Since IceCube is only interested in the muons, a modified implementation of CORSIKA is used. It has adjustments which make it compatible with Ice-Cube software. The events are usually generated with a 5-component model where five primary types of nuclei are injected: hydrogen, helium, nickel, aluminum, and iron. The spectra can be specified individually for each type and can be re-weighted. CORSIKA tracks all interactions which may lead to muons, and saves only those which actually result in muons. Depending on if and when the air shower hits the Earth's surface, all remaining particles except for the saved muons are stopped [141]. The muons are then transmitted to the particle propagator simulation, which will track the muon paths through the ice down to the detector.

The neutrino signals used for this work are based on simulations with GE-NIE (*Generates Events for Neutrino Interaction Experiments*) [49]. When neutrinos interact with the ice they produce secondary particles as described in section 1.5. GENIE contains information about these interactions and the corresponding neutrino-nucleon cross sections in the energy range between $10\,\mathrm{GeV}$ and $1\,\mathrm{TeV}$. Events are created using a power law energy spectrum with a certain spectral index, which is different depending on energy range and neutrino flavor. Using the relevant cross section for each neutrino flavor it is determined what kind of interaction is taking place at the given energy. The cross section model comprises resonant, elastic, quasi-elastic and deep-inelastic interactions. All particles are propagated to their final state [110].

Simulation Weights

Each generated neutrino is forced to interact close to IceCube in order to save computing time. The "detectability" of the neutrino is then handled using weights called *OneWeight*. These weights include the neutrino propagation and interaction probability (P), the generation area and solid angle, A_{gen} and Ω.

---

[3]See section 1.4 for details regarding the air shower types.

$$OneWeight = \left(\frac{P}{E^{-\gamma}} \right) \cdot \int_{E_{min}}^{E_{max}} E^{-\gamma} dE \cdot A_{gen} \Omega \qquad (3.1)$$

The generation spectrum is represented by $E^{-\gamma}$. A more detailed derivation of this equation can be found in [191]. *OneWeight* has the units GeV cm^2 sr and is applied to every event individually.

Since the generation spectrum usually does not correspond to the expected particle flux, the events can be re-weighted using *OneWeight*:

$$w_i = \frac{OneWeight_i}{N_{gen}} \cdot T_{live} \cdot \frac{d\Phi_\nu(E,\Omega)}{dE \, d\Omega}. \qquad (3.2)$$

Here i stands for an individual event, N_{gen} represents the generated number of events, T_{live} is the integrated livetime and $d\Phi_\nu(E,\Omega)/(dE \, d\Omega)$ the desired differential particle flux, which has to have the units GeV^{-1} cm^{-2} sr^{-1} s^{-1}.

3.6.2 Particle Propagator

PROPOSAL (*PRopagator with Optimal Precision and Optimized Speed for All Leptons*) [153] propagates charged particles through the ice and bedrock. It simulates energy losses along the trajectory of the particle using parameterizations as functions of particle energy. The parameterizations of energy losses like decay, ionization, bremsstrahlung, pair-production, and photo-nuclear interactions are included in PROPOSAL.

3.6.3 Photon Propagator

PPC (*Photon Propagation Code*) [81] is chosen for the propagation of the Cherenkov light of the charged particles traveling through the ice. It tracks every photon created and is therefore very expensive in terms of computing power. To speed up the process, splined tables of local ice properties from the ice model SPICE LEA are used [80]. Furthermore, the process is parallelized because the photons do not depend on each other. PPC runs on Graphics Processing Units (GPUs), which are able to process a large amount of independent parallel computations.

3.6.4 Detector Response

When at least one Cherenkov photon reaches a DOM, MCHits (*Monte Carlo Hits*) creates PMT hits. Since noise cannot be avoided in the detector, the noise simulation module Vuvuzela generates noise hits, including dark noise, pre-pulses and after-pulses. Pre-pulses occur when a photoelectron bypasses the first dynode of the PMT, leading to a pulse which precedes the main signal

pulse. After-pulses occur due to the ionization of residual gases within the vacuum of the PMT.

The PMTResponseSimulator takes all hits, including noise hits, and models the amplification of the PMT, with the result in form of a waveform. The waveforms created are then passed to the DOMLauncher, which simulates the local coincidence logic, the DOM clock, the fADC and ATWD. After the DOM-Launcher, the resulting output has the same form as real data and therefore further steps like triggering and filtering can be applied in the same way.

3.7 Event Signatures

Different event signatures are observed in IceCube and categorized as *tracks* and *cascades*. All neutrino flavors (ν_e, ν_μ, ν_τ) give rise to an initial hadronic particle shower, due the break-up of the involved nucleon, see equation 1.12. This is independent of weather they interact via CC or NC. The charged particles of the hadronic shower give rise to Cherenkov radiation and neutral pion decay leads to electromagnetic showers. The photons of both components can be registered in the detector.
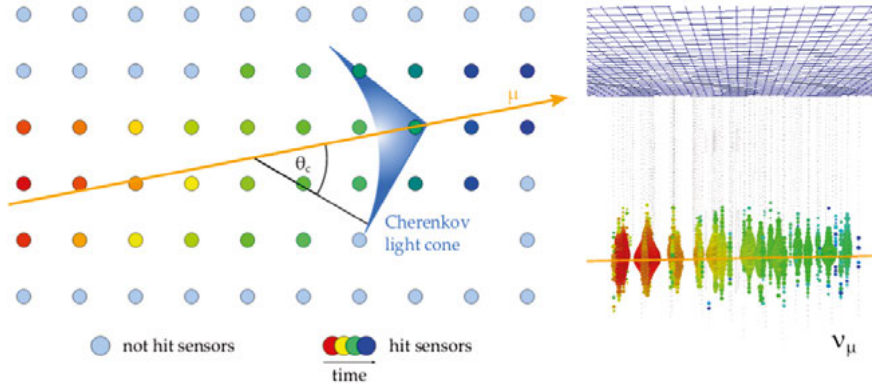
Figure 3.5. Left: schematic view of a track left by a muon passing a grid of DOMs indicating the Cherenkov light cone and Cherenkov angle. The color code shows which DOMs were hit first (red) and which were hit last (blue), indicating the travel direction of the muon. Right: An actual observed event with IceCube, displayed in the IceCube event viewer. The created muon had an energy of about 400 TeV [11]. The size of the light bubbles indicates how much energy was deposited in a certain DOM. Figure credit: [96].

In a CC interaction a lepton is produced, corresponding to the neutrino flavor of the interacting neutrino. In case of a ν_μ, a muon is created, which leaves a trace of Cherenkov light in the detector while traversing it, see figure 3.5. This event topology is called a *track*. Muons produced in the atmosphere by CRs

also reach the detector, producing track signatures, see section 1.4.

Electrons produced in CC interactions of ν_e loose their energy rapidly in an electromagnetic shower, leaving an almost spherical light pattern in the detector, see figure 3.6. Hadronic showers from NC ν interactions leave a similar spherical topology. These signatures are referred to as *cascades*. Both kinds of showers have some elongation, but due to the large DOM spacing in comparison to the shower, their light patterns appear rather spherical. However, the Cherenkov light intensity is slightly larger in the neutrino travel direction. This provides some possibility for directional reconstruction.
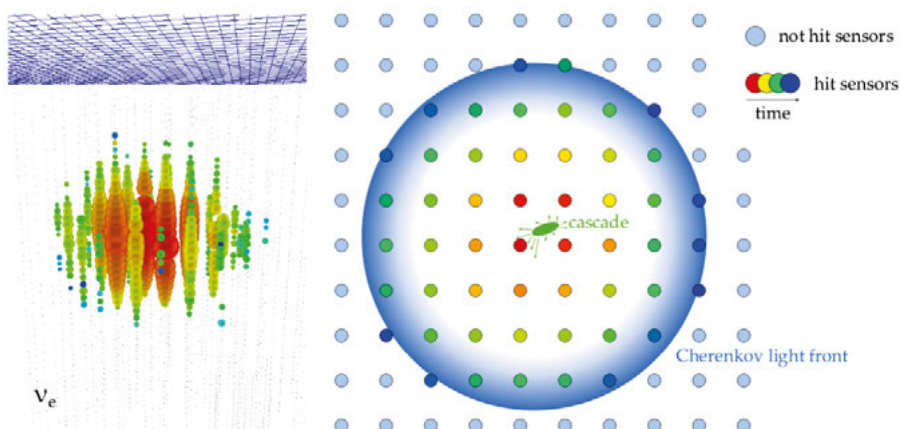
Figure 3.6. Left: Observed electron neutrino with $\sim 100\,\mathrm{TeV}$ deposited energy [143]. Right: Schematic view of the development of the Cherenkov light of a cascade in a grid of light sensors. Figure credit: [96].

Tau leptons have a very short lifetime and therefore decay very quickly, see section 1.6. The CC ν_τ signatures above 1 PeV have in most cases two cascades with a track in between. The first cascade is due to the initial interaction which results in a hadronic shower and a tau lepton. Like the muon the tau lepton leaves a track of Cherenkov light along its trajectory, but due to the short lifetime it has a higher probability decaying within the detector resulting in a second cascade, see figure 3.7. Below 1 PeV the two cascades overlap, they cannot be resolved anymore and appear as one cascade. The τ can decay hadronically or leptonically due to its high mass, see equation 1.18, leading to either a hadronic shower, an electromagnetic shower, or a muon track[4], depending on the decay channel. These signatures could be partially detected, depending on the location of the first interaction, but the limited size of the detector volume plays a role. So far these signatures have not been observed in IceCube, but the search for tau neutrinos is ongoing.

---

[4]The branching ratio of a τ decaying in to a muon is about 17%, see section 1.6.
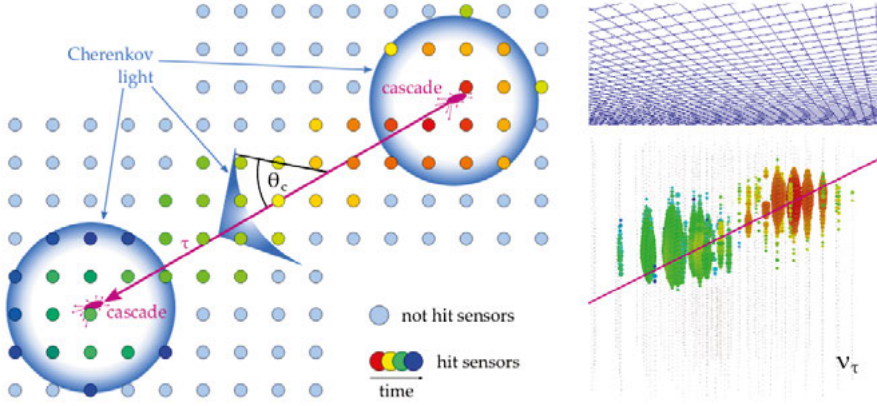
Figure 3.7. Left: Schematic view of a ν_τ signature in a grid of optical modules. Right: Simulated ν_τ signature above 1 PeV presented in the IceCube event viewer. Figure credit: [96].

3.7.1 Event Signatures at Low Energies
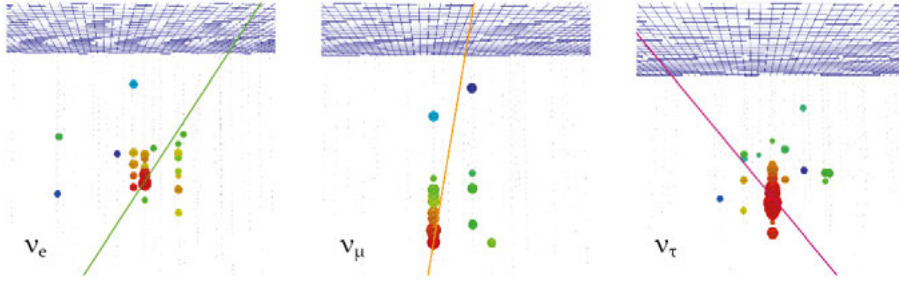
Figure 3.8. Topologies of ν_e (left), ν_μ (middle) and ν_τ (right) with energies around 50 GeV are shown in the IceCube event viewer. Figure credit: [96].

The lower the energy of the interacting neutrinos the more difficult it becomes to separate their flavor signatures. Figure 3.8 shows the signatures of all three neutrino flavors at energies of about 50 GeV. They can be separated broadly into cascade-like and track-like events. At low energy, like 50 GeV, many of the muons produced in ν_μ interactions give short tracks and may therefore also appear cascade-like. The analysis presented in this thesis uses events in energy ranges between 10 GeV and 200 GeV, hence the events have topologies similar to the ones presented in figure 3.8.

4. Data Processing

At energies below $200\,\text{GeV}$ cascades are very suitable to search for the potential Fermi bubble neutrino flux signal. Cascades have less *BackGround* (BG) compared to tracks, because the main BGs are generated by atmospheric muons and muon neutrinos, which give rise to tracks in the detector at higher energies. The tracks become rather similar to cascade-like signatures the lower the particle energy is, see section 3.7.1. We will estimate the amount of atmospheric muons and neutrinos with simulations, see section 4.2.5.

Another advantage of cascades is that all neutrino flavors can be used (see table 4.1), due to similar signatures at the low energies of this analysis. Therefore, the chosen event sample for this analysis contains cascades at the lowest energies that IceCube is able to detect with DeepCore, between $10\,\text{GeV}$ and $200\,\text{GeV}$.

4.1 Data and Simulation Selection

IceCube is to date the only neutrino detector which is able to search for neutrinos from the FBs in this energy range, which is impressive because it is built and optimized for the detection of neutrinos with much higher energy, up to the PeV range.

Table 4.1. *Neutrino signatures in IceCube for neutral (NC) and charged current (CC) events for all three neutrino flavors. The stars (*) symbolize the cascade-like signature of muon tracks and the indistinguishability of typical ν_τ signatures from cascades at low energies.*

	ν_e	ν_μ	ν_τ
CC	cascade	track*	cascade(s) with track*
NC	cascade	cascade	cascade

The data sample used was originally optimized for an all-flavor search for neutrinos from dark matter annihilations in the Milky Way Halo [9]. This analysis, referred to as the *Galactic Halo WIMP analysis*, was performed on a one-year sample (IC86-I: May 2011- May 2012). The analysis presented in this thesis is performed using the same optimization and almost six years of data: IC86-I to IC86-VI, corresponding to 2085 days, see table 4.2 for details.

Table 4.2. *Data sets, livetime and number of events are presented for each year respectively. Note that the number of events is on the final level after the event selection which will be described in this chapter.*

Dataset	Livetime [s]	events
IC86-I 2011	28 434 240	7426
IC86-II 2012	28 272 940	6918
IC86-III 2013	30 674 072	7612
IC86-IV 2014	31 511 811	7682
IC86-V 2015	31 150 852	7777
IC86-VI 2016	30 059 465	7607
TOTAL	180 103 380	45 022

The processing code originally used for the IC86-I sample was rewritten to be compatible with the latest IceCube software version. New MC simulation sets, including systematical uncertainties sets, needed to be processed because of improved ice- and noise models. While the observed data of the experimental data sets IC86-II to IC86-VI were consistent, IC86-I showed at the outset significant differences in rate and distribution shapes when viewing certain variables[1]. The differences were shown to be due to several software updates on the detector level during 2011. For this analysis, it was of high importance to ensure that the data is consistent between the samples and with the background MC sets resulting from the CORSIKA simulations [129]. Moreover, a lot of effort was made to ensure the quality and similarity between the previous[2] and the new processed simulation sets used for this analysis, on each processing level. It was tested and validated that the new simulation sets did not differ from the previous sets beyond what can be expected from systematic and statistical effects. Although 2011 showed differences in rate on level 2, they disappeared after the level 3 cuts were applied. It turned out that, with the very strict cuts used, no significant differences appeared at the final level.

4.1.1 Background Simulation

IceCube captures about 10^{11} atmospheric muons and 10^5 atmospheric neutrinos every year. Compared to the handful diffuse astrophysical neutrinos per year, this is a huge amount of background events.

The CORSIKA atmospheric muon simulation is used to simulate background data, see section 3.6.1. Before background reduction, CORSIKA and real data

---

[1]Here, variables represent characteristics of the events, and are calculated from observables. The variables for this event selection can be viewed in section 4.2.3.
[2]Previous data and simulation were used for the Galactic Halo WIMP analysis.

should be in a good agreement with each other. At the higher analysis levels, described in section 4.2.4, the data samples should contain a substantial amount of neutrinos and, therefore, the CORSIKA simulation cannot fit the sample. Comparison of CORSIKA and real data confirms the correctness of the detector simulation, year by year.

In the analysis presented here real scrambled data and not CORSIKA is used as background expectation. This reduces systematic uncertainties, and is further described in section 5.2.2. The amount of atmospheric neutrinos in the data after the event selection was determined using all three neutrino flavors provided by GENIE simulation and weighted to an atmospheric neutrino energy spectrum with the Honda et al. model [138], see section 3.6.1 for the weighting procedure.

4.1.2 Signal Simulation

For the signal estimation GENIE MC simulations were used [49], see section 3.6.1. These sets provide the neutrino events in the energy range between $10\,\mathrm{GeV}$ and $200\,\mathrm{GeV}$ which corresponds to the region of interest for the Fermi bubble flux. The events from these simulation sets were weighted according to equation 3.2 using the neutrino flux expectation from equation 5.2. Details regarding the signal expectation flux can be found in section 5.2.1.

4.1.3 Blindness of Real Data

Most analyses in IceCube are developed without access to the full data set. This *blindness* routine is performed to avoid unintentional bias[3]. Many analyses are based on a *burnsample*, a collection of runs (about 10% of the complete data) distributed over a year for testing. These burnsamples are then excluded ("burned") from the *unblinding* of the data for final results. The unblinding has to be approved by the collaboration. Within a certain time period every member of the collaboration has the opportunity to review the analysis. The internal review process helps the collaboration to understand the methods and the analysis and helps the analyzer to improve the work and cross-check the techniques and results. After the unblinding the results are presented and discussed within the collaboration, before they can be published.

---

[3]Although this analysis used the complete data set for BG estimation, the true directions of the events were scrambled and hence, the blindness was preserved.

4.2 Event Selection

The event selection for real data and all simulation sets is performed in the same way and described below. The event selection is identical to the Galactic Halo WIMP (*Weakly interacting massive particles*) analysis, which is why this section is designed in the same manner as the original event selection described in [194]. The WIMP selection can be used for the Fermi bubble analysis because in both cases the signal expectation relies on low energy cascades, and this event selection is optimized to select those. We will show below that although the cuts are not optimized for the FB flux they show good separation power.

4.2.1 Data Reduction

The first two levels of data reduction are performed at the South Pole in the IceCube Laboratory and they represent the triggering and filtering of the data. IceCube uses several triggers and filters in order to select appropriate events for the various analyses performed by the IceCube collaboration. For the present work, the DeepCore trigger and filter are used and described below.

Level 1 - The DeepCore Trigger
The SMT mentioned in section 3.4.1 is used as DeepCore trigger, but with different conditions compared to the IceCube-wide SMT. Instead of at least eight HLC[4] hits, only three HLC hits are required for DeepCore, since DeepCore is a smaller detector. The hits have to arrive no more than $2.5\,\mu s$ apart from each other. All hits (HLC and SLC) within the complete in-ice-array and IceTop are read out in a time window of $10\,\mu s$ before and $10\,\mu s$ after the first of the hits and stored as one event [20]. The arrival time of the first hit defines the trigger time. In the following analysis IceTop hits are not considered and IceCube hits outside DeepCore are used as a veto. If another trigger records hits during this time frame and if the readout window is larger than the one of the SMT3 trigger, these hits can be added to the event. The DeepCore trigger has an average rate of $260\,Hz$.

Level 2 - The DeepCore Filter
All events collected by the DeepCore trigger are handed over to the DeepCore filter. The filter reduces the amount of events originated by atmospheric muons by choosing only events which seemingly start within the DeepCore fiducial volume. In order to distinguish starting events from through-going and incoming events, the outer IceCube strings are used, see figure 3.2. The filter uses an algorithm which calculates the *Center Of Gravity* (COG) using all DeepCore HLC hits, but instead of masses the measured amplitudes in the DOMs are used, which are treated as "virtual masses" m_i:

---

[4]See section 3.3 for description of HLC and SLC hits.

$$\vec{x}_{COG} = \frac{\sum_{i=1}^{N_{Ch}} m_i \vec{x}_i}{\sum_{i=1}^{N_{Ch}} m_i}. \tag{4.1}$$

The $\vec{x}_i$ represent the positions of the DOMs and N_{Ch} is the number of fired DOMs. A corresponding mean time t_{COG} is determined including all HLC hits used for the COG calculation. All HLC hits outside the DeepCore fiducial volume, that means in the IceCube veto region, are then used in order to calculate speed parameters of the event by comparing their position and hit time to the COG position and time. A through-going muon would have its first hit in IceCube outside DeepCore and move trough DeepCore with approximately the speed of light in vacuum. Hence, if the speed parameters turn out to be close to the speed of light, the event is considered an incoming muon and is therefore rejected. Low energy neutrino events are required to begin in Deep-Core. Hits inside the fiducial volume are followed by hits outside in IceCube. As calculated the speed parameters become negative for such events. The cut on the speed parameters is set to remove through-going events. It reduces the event rate for the selected data to about 32 Hz while retaining 99.4% of neutrino events starting in DeepCore [20].

4.2.2 Level 2'

In order to avoid having noise hits as part of the event, which reduces the quality of the event reconstructions, two different noise hit-cleaning algorithms are applied. Furthermore quality cuts are made to exclude events which are difficult to reconstruct.

The *Static Time Window* (STW) cleaning uses for this analysis a time window of 5 µs before the trigger time to 4 µs after the trigger time to remove all hits, which do not fall within the window.

The *Seeded Radius-Time* (SRT) cleaning is applied afterwards. This procedure takes all hits remaining after the STW cleaning and examines them for coincidence. It starts with the HLC hits and determines for each HLC hit if there is another HLC hit within a 150 m radius and a time window of 1000 ns. This condition has to be met by at least two other HLC hits in order for the original hit to be accepted. The HLC hits which pass these criteria are stored in a list and used as seed hits for the next iteration of the SRT cleaning. In the case that no HLC hits pass, all of them are added to the list and used as seed hits.

In the next iteration, the algorithm is again applied to every HLC hit in the list, with the difference that now also SLC hits can pass the radius and time conditions, and be added to the list. The third iteration uses every hit in the list as a new seed, regardless of HLC or SLC. This provides the possibility to

reintroduce previously rejected HLC hits due to the causality connection with a SLC hit. The iterations are repeated no more than three times or until no more new hits are added to the list. This method removes most hits which are not causally connected to the event, especially isolated HLC hit pairs.

Quality cuts

After the event cleaning, basic quality cuts were applied in order to exclude events which would be difficult to reconstruct. The first cut was applied to the number of DOMs which were hit with the condition $N_{Ch} \geq 8$. The second cut was executed on the number of involved strings: $N_{str} \geq 4$. This reduces the data rate to $\sim 23\,\mathrm{Hz}$.

4.2.3 Level 3

In order to go from level 2' to level 3 straight cuts on variables with good background and signal separation were performed. Even though the cuts were initially optimized for the neutrino spectra from WIMP annihilations in the Galactic Halo [194], they nevertheless show very good separation for the Fermi bubbles as well, as we will present in this section.
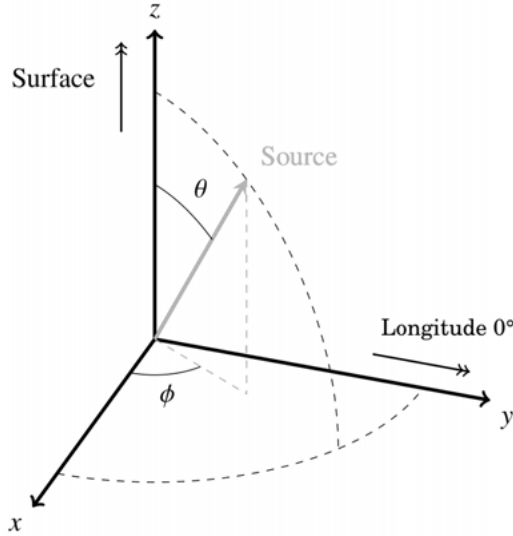
Figure 4.1. The origin of the local coordinate system in the center of the in-ice array. The z axis is pointing up towards the ice surface and the y axis is pointing towards longitude 0°. The zenith angle is represented by θ and the azimuth is shown with ϕ. Adopted from: [194].

All following variables were calculated using the cleaned event hit map. The variables can be calculated for all events in IceCube and DeepCore. The de-

scriptions here refer to events which passed the DeepCore Filter, unless stated otherwise. In total ten variables were chosen to cut the large sample at level 2' down while maintaining a high signal efficiency. The cuts were identical to those used for the earlier Galactic Halo WIMP analysis. Due to the similarity of the possible FB signal to that for low mass WIMPs the FB-signal efficiency is maintained at a high level. The main purpose is to reduce the sample in view of the following time consuming event reconstructions. For the new simulation sets and further years of data, the shapes and cuts of these variables were compared and validated at every level. Some variables are explained with reference to the IceCube local coordinate system, which is presented in figure 4.1. After the cuts on the variables (described below), the data rate was reduced to about 0.08 Hz. On every level and for every year (2011-2016), burnsamples were used to validate that the data was comparable to CORSIKA simulation. In addition every year was compared to every other year.

LineFit Speed

This variable is calculated using the improved LineFit reconstruction [8], which is one of the fast standard reconstruction methods applied to all triggered events at the South Pole. The primary purpose of the improved LineFit is to reconstruct muon tracks, but it is also suited to distinguish track-like events from cascade-like events. The improved LineFit algorithm uses the positions of all hit DOMs of one event, the corresponding times and a speed parameter to minimize the sum of the squares of the distances between the track and the hits. It disregards the effect of the Cherenkov angle, instead a speed different from that of the particle is found for the track. Outliers, hits at greater distance from the central track, are down-weighted. How the improved LineFit reconstruction works in detail can be found in [8]. The LineFit speed for track-like events has a value close to the speed of light in vacuum, while a cascade-like event has a value closer to zero. The cut on this variable is set to 0.22 m/ns, excluding all events with a higher speed, see figure 4.2a.

Tensor of Inertia Eigenvalue Ratio

The Tensor of Inertia reconstruction uses the center of gravity with the hit amplitudes as virtual masses described in the DeepCore Filter section 4.2.1. These virtual masses and their positions are then employed to calculate the eigenvalues I_1, I_2, I_3 of the tensor of inertia for the "virtual body" consisting of hit DOMs. The resulting three eigenvalues represent the principal axes of the ellipsoid created by the virtual body, where the smallest eigenvalue represents the longest principal axis. The hit positions are projected onto this axis in order to determine from which direction the particle most likely arrived. This variable is not very suitable to calculate the arrival direction of a cascade-like event, because all three axes have approximately the same eigenvalues. However, the tensor of inertia can be used to differentiate tracks from cascades.
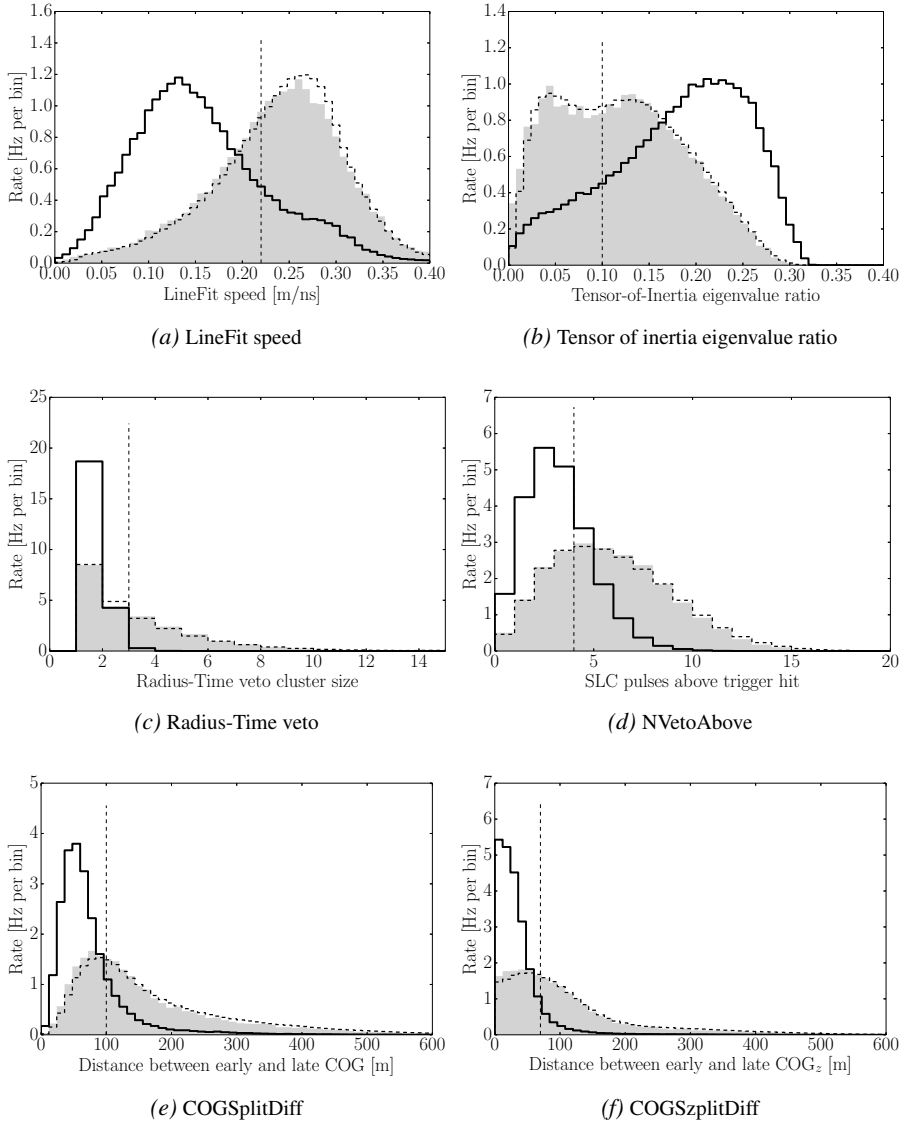
Figure 4.2. Level 3 variable distributions and cuts are displayed. CORSIKA simulation (gray shaded) and the burnsample of experimental data for 2012 (dashed), together with the Fermi bubbles signal expectation (solid) determined with GENIE simulation. The signal expectation was calculated with the neutrino spectrum derived in section 5.1. The vertical thin dashed line indicates the cut value. The simulated data is normalized to the experimental data rate.

(a) | FirstHit - COG |

(b) ZFirst

(c) QR6

(d) FillRatio
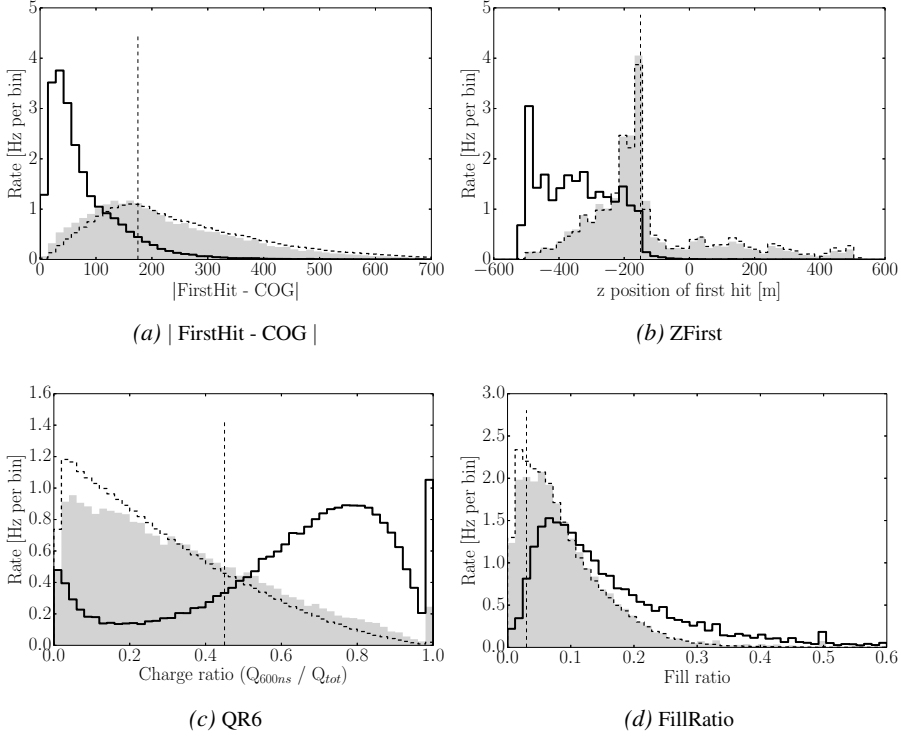
Figure 4.3. Level 3 variable distributions and cuts are displayed. CORSIKA simulation (gray shaded) and the burnsample of experimental data for 2012 (dashed), together with the Fermi bubbles signal expectation (solid) determined with GENIE simulation. The signal expectation was calculated with the neutrino spectrum derived in section 5.1. The vertical thin dashed line indicates the cut value. The simulated data is normalized to the experimental data rate.

The Tensor of Inertia Eigenvalue Ratio variable is constructed by dividing the smallest eigenvalue by the sum of all three:

$$R_{ToI} = \frac{min([I_1, I_2, I_3])}{\sum_{i=1}^{3} I_i}.$$

(4.2)

This leads to values of $R_{ToI} = 0.33$ for spherical cascades and a value closer to 0 for tracks. For this event selection all events with values above $R_{ToI} \geq 0.10$ are kept, see figure 4.2b.

Radius-Time Veto (RTVeto)
This parameter represents the maximum number of causally connected hit DOMs outside the DeepCore region, which means in the three outer layers of IceCube, see figure 3.2. Only hits before the first hit in the cleaned hitmap are considered. The higher the number of causally connected hits, the higher

the probability of the event being an atmospheric muon. Therefore, a cut value allows no more than two causally connected hits, see figure 4.2c.

NVetoAbove

This parameter represents the number of hits in the veto region above the first trigger hit. Also hits before the trigger time are considered. Four or less hits are allowed for this event selection, see figure 4.2d.

COGSplitDiff

This variable calculates the distance (in space) between the early and late hits of an event by dividing the hits in two halves. The hits are sorted by time and in case of an odd number of hits, the late hits get the additional hit. The center of gravity is then calculated for each half-event and the distance between the two COGs is obtained. For track-like events this distance is large and for cascade-like events comparatively small. The cut does not allow the distance to be larger than 100 m, see figure 4.2e.

COGzSplitDiff

The definition of this variable is the same as the COGSplitDiff parameter with the difference that only the vertical (z) component is taken into account. In IceCube coordinates the vertical axis z is defined as the one which points from the center of the in-ice array towards the surface, see figure 4.1. Also COGzSplitDiff is smaller for cascades than for tracks and the cut value is set to 70 m, see figure 4.2f.

| FirstHit - COG |

As the name suggests this variable represents the distance between the first hit and the COG of the event with the cut value of 175 m, keeping all events shorter than this distance, see figure 4.3a.

ZFirst

This parameter shows the position of the first hit, and if the hit happens to be above the DeepCore fiducial volume it is considered an atmospheric muon. All events with Zfirst below -150 m are kept in the sample, see figure 4.3b.

QR6

This is the representation of the ratio between the charge accumulated by all DOMs within the first 600 ns and the complete collected charge of the event:

$$QR6 = \frac{\sum_{t < 600 \text{ ns}} Q}{Q_{tot}} \tag{4.3}$$

For this variable cascades usually have larger values of $QR6$ as compared to tracks and events with a $QR6 > 0.45$ are kept for this selection, see figure 4.3c.

FillRatio

The smallest possible sphere is created around the event - meaning - around all hit DOMs of the cleaned hitmap belonging to the event. The FillRatio variable describes the ratio between these hit DOMs and all the DOMs within that sphere. The higher the value of the ratio the more likely the event is a cascade-like event. All events which fulfill the condition with the Fillratio higher than 0.03 are saved, see figure 4.3d.

4.2.4 Level 4

To reach level 4, three likelihood reconstructions were applied to the remaining events and then a machine learning method, namely a *Boosted Decision Tree* (BDT), was used to discriminate between signal- and background-like events.

Likelihood Reconstruction Algorithms

The advanced likelihood reconstructions take a significant amount of computing time and power and therefore, it is useful to apply them to a significantly reduced data sample. They use log-likelihood fits in order to determine the following set of unknown parameters:

$$\vec{a} = (\vec{x}_0, t_0, \hat{\theta}, E_0), \tag{4.4}$$

where $\vec{x}_0$ is a point chosen somewhere along the track in case of a track-like event and for a cascade-like event $\vec{x}_0$ is the vertex position. The corresponding time at $\vec{x}_0$ is denoted with t_0. The incoming particle direction is represented by $\hat{\theta}$ and E_0 is the deposited event energy.

One algorithm uses an infinite track hypothesis: TrackLLH (LLH stands for *Log LikeliHood*) or SPE32 (*Single Photo Electron* 32). The SPE32 name is hinting at the fact that the reconstruction uses only the first hit in every DOM and it runs 32 iterations of the algorithm to avoid converging into a local minimum.

The other two algorithms, CascadeLLH and Monopod work under the cascade hypothesis. CascadeLLH and TrackLLH use a simplified version of the ice model to fit the parameters. Monopod is more advanced, it uses the currently best ice model and CascadeLLH as a seed to perform the fits. All reconstructions return the parameters for the best-fit along with the corresponding negative log-likelihood values: $(-\log\mathscr{L})_{min}$. Another useful parameter calculated by each likelihood algorithm is the reduced likelihood:

$$(\log\mathscr{L})_r = \frac{(-\log\mathscr{L})_{min}}{N_{Ch} - N_{DoF}}, \tag{4.5}$$

where N_{Ch} is the number of hit DOMs and N_{DoF} is the number of degrees of freedom in the fit. This parameter will be used in order to calculate several of the variables needed at this level. A more detailed description about how the log-likelihood algorithms work can be found in [194].

Boosted Decision Tree Classification

To reach the final level 4 a machine learning algorithm was used, namely a BDT ensemble. The project `pybdt` was used, which is implemented into Ice-Cubes internal software and can easily be used as part of the processing. A detailed description on how the `pybdt` works can be found in [182], and a short summary is given below.

A *decision tree* is a binary tree, starting at a root and branching out with cuts on given variables. The tree first determines the variable with the best separation power and uses it as root. The cut value is the point at which the highest separation power is achieved. At this point the data is split into two categories - signal-like and background-like events - and we refer to a split node. The data is then split into sub categories again, using the next best variable at each split node. The final nodes are referred to as leaf nodes. Each leaf node corresponds corresponds to either a signal or a background sample. This process can stop for several reasons:
- when the specified maximum tree depth is reached,
- when 100% purity in a node is reached (meaning only signal or only background events are left),
- when the best split would lead to a node with less events than the specified minimum number.

Events, especially when they are less typical, can be misclassified. In order to determine if an event was misclassified the training needs to be performed on known data sets, called the *training sets*. The training set is a combination of background and signal events and can contain either MC sets or known real events, or both. After training the first tree, the misclassified events are given a higher weight and correctly classified events receive a lower weight. The weighted data is then handed over to the next tree, where the training and weighting is repeated. By re-weighting the data, the next tree has a higher probability of classifying the misclassified events correctly. This procedure is called *boosting*. With every additional tree the classification improves due to the boosting. This procedure is repeated for hundreds of decision trees in order to learn to differentiate between signal- and background-like events. Combined, these boosted decision trees are called a BDT ensemble or BDT for short.

However, if too many trees are used, the trees at the end of this chain can learn to recognize features which are specific for the training sets, but cannot be applied for the general data. This effect is called *overtraining*. After

training a BDT, a score between -1 (for background) and +1 (for signal) is returned for every event. This results in a distribution on which a final cut can be performed depending on the desired signal efficiency and/or background rejection.

In order to validate the performance and to avoid overtraining of the BDT, a second data set, the *testing set* is used. The trained BDT is applied to the testing set and then the scores of both sets are compared with each other. The BDT can be validated by comparing the distributions, which should look very similar when the BDT is not overtrained. A quantitative measure on overtraining can be obtained by applying a *Kolmogorov-Smirnov test*.

For the event selection in this thesis the training and testing sets were given by GENIE MC simulation for signal and real scrambled data for background. The BDTs were trained on the signal from the Galactic Halo WIMP analysis, but as already mentioned the signal expectation for the FB is similar and the signal efficiency is maintained.

Level 4 variables
The selected variables given to the BDTs[5] are described below. Further details about how the variables were selected and narrowed down by the BDTs are described in [194].

QR6
This variable was already described in the level 3 section 4.2.3 and still shows strong separation power after the level 3 cuts, see figure 4.4a. Therefore, it is also reused for the BDTs.

RatioLH
The logarithm of the ratio between the CascadeLLH and the TrackLLH reconstruction likelihoods is represented by this variable:

$$R_{LH} = \log\left(\frac{\mathscr{L}_{\text{CascadeLLH}}}{\mathscr{L}_{\text{TrackLLH}}}\right) \tag{4.6}$$

See figure 4.4b for distribution.

RatioRLogL
This variable represents the ratio between the reduced log-likelihoods:

$$R_{rLLH} = \frac{(\log\mathscr{L})_{r,\text{CascadeLLH}}}{(\log\mathscr{L})_{r,\text{TrackLLH}}} \tag{4.7}$$

See figure 4.4c for distribution and equation 4.5 for the definition of $(\log\mathscr{L})_r$.

---

[5]Two BDTs were trained, which will be further explained in section 4.2.4
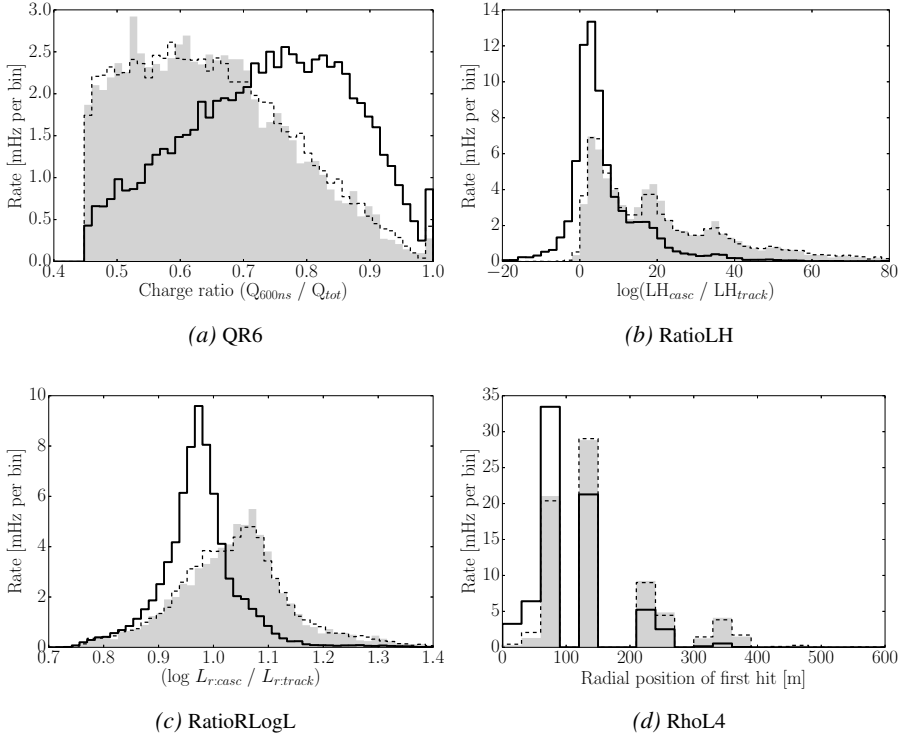
Figure 4.4. Level 4 variable distributions are displayed. CORSIKA simulation (gray shaded) and the burnsample of experimental data for 2012 (dashed), together with the Fermi bubbles signal expectation (solid) determined with GENIE simulation. The signal expectation was calculated with the neutrino spectrum derived in section 5.1. The simulated data is normalized to the experimental data rate.

RhoL4 (ρL4)

RhoL4 is the shortest distance in the x-y plane between the central string (string 36, see figure 3.2) and the first hit of the cleaned hitmap, see figure 4.4d for distribution.

TrackRLogL

TrackRLogL is the reduced log-likelihood returned by the track likelihood reconstruction, see equation 4.5. This is one of the variables that gains separation power in combination with other variable cuts. See figure 4.5a for distribution.

DeltaCOGz

For this variable all hits of one event are split in two, but in comparison to COGSplitDiff (see level 3 section 4.2.3) they are split by a plane, which is perpendicular to the improved LineFit reconstruction (see 4.2.3, LineFit Speed).

(a) TrackLogL

(b) DeltaCOGz

(c) ZFirst
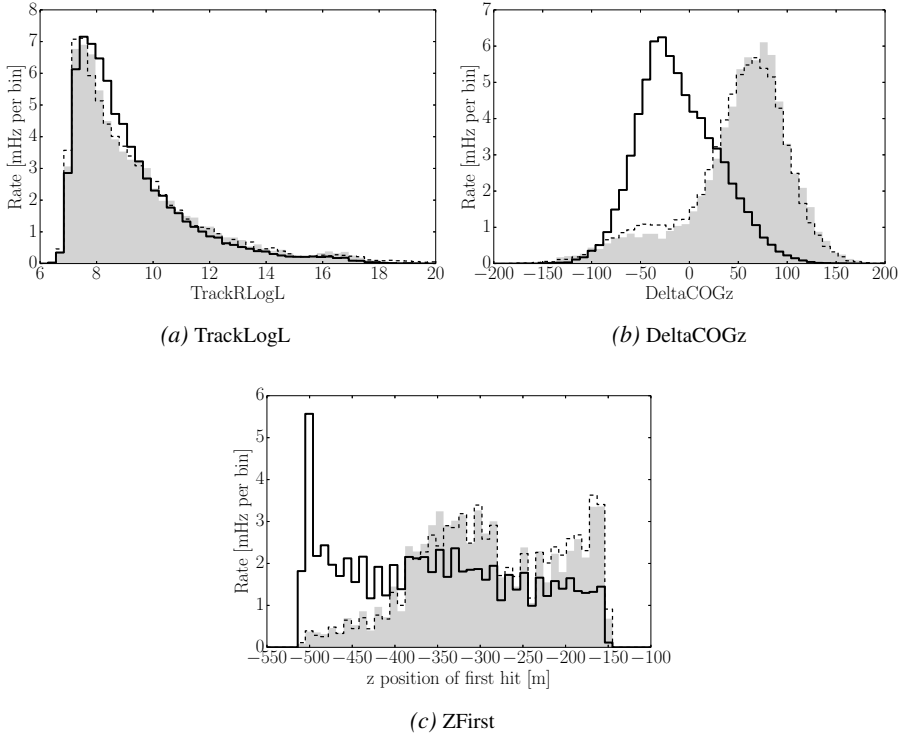
Figure 4.5. Level 4 variable distributions are displayed. CORSIKA simulation (gray shaded) and the burnsample of experimental data for 2012 (dashed), together with the Fermi bubbles signal expectation (solid) determined with GENIE simulation. The signal expectation was calculated with the neutrino spectrum derived in section 5.1. The simulated data is normalized to the experimental data rate.

This plane is then placed at the COG of all hits, and the COG of each half is calculated. DeltaCOGz represents the vertical component between the early and the late COG: $z_e - z_l$. See figure 4.5b for distribution.

ZFirst
This variable was already used for a level 3 cut (see 4.2.3), and still shows good separation. See figure 4.5c for distribution.

BDTs Results
Two different BDTs were used for this analysis. The BDTs had been originally designed fot the Galactic Halo WIMP analysis and were trained using a *Low Energy* (LE) and *High Energy* (HE) WIMP signal expectation. The resulting distributions of the BDT scores can be viewed in figure 4.6 for the LE BDT (a) and HE BDT (b). The cut values lay at 0.25 and 0.35 respectively,
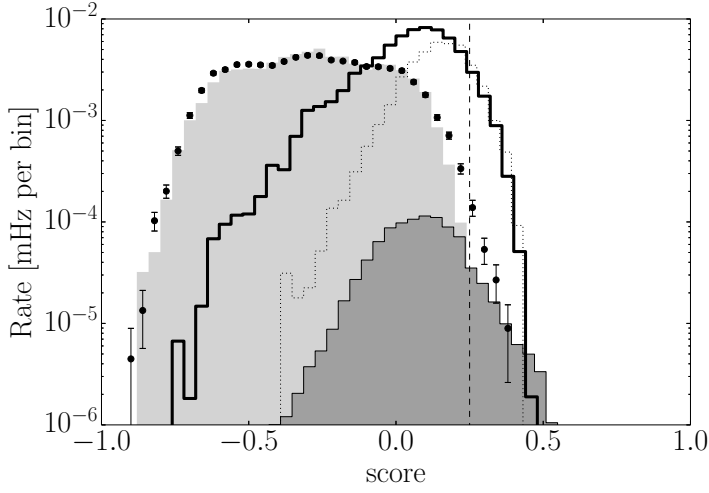
(a) LE BDT
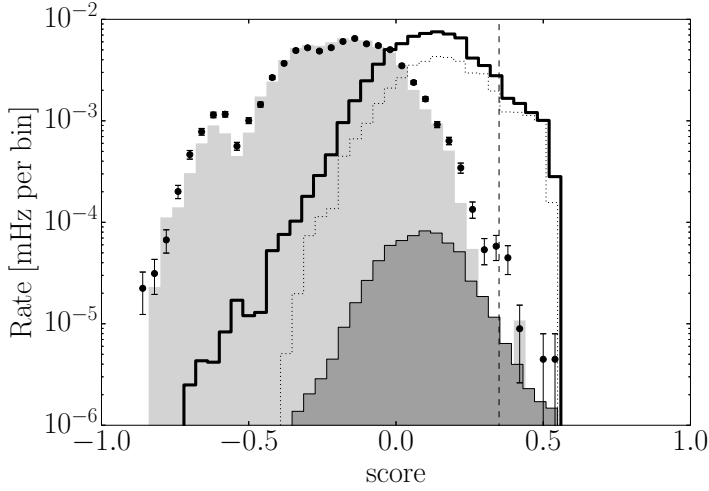
(b) HE BDT

Figure 4.6. The score distribution for the Fermi bubble signal (thick solid) for the LE (a) and HE (b) BDTs trained on the LE & HE WIMP signals from the Galactic Halo analysis [194]. It is compared to CORSIKA simulation (light gray shaded), the burnsample of experimental data for 2012 (circles with error bars) and the atmospheric neutrino background (dark gray shaded). The latter is like CORSIKA displayed for comparison only. The simulated data are normalized to the experimental data rate. Indicated with the dotted line are the original LE & HE WIMP signals from [194], which have an arbitrary normalization. The vertical dashed line indicates the cut value, keeping all events above 0.25 for the LE BDT and above 0.35 for the HE BDT.

keeping all events above these values. The shapes of the signal distributions for WIMPs and FBs are reasonably similar, especially beyond the cut values. Since there is no physical reason why the FB signal should be divided in two energy dependent subsets, the samples passing the two BDTs were combined. Every event which passed one of the BDT cuts was included. Events passing both cuts were included without double counting.

4.2.5 The Final Sample
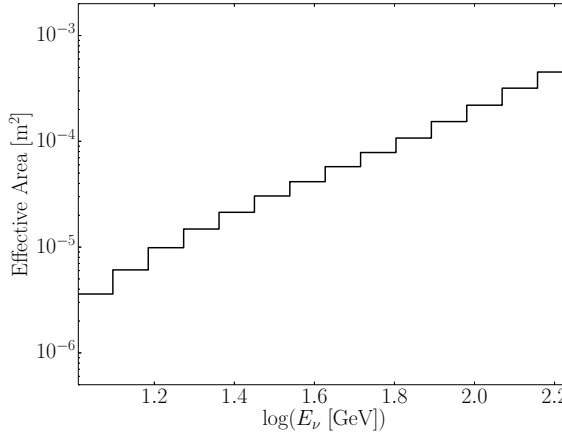
Figure 4.7. Presented is the effective area for the final combined event sample.

As can be seen in figure 4.6, the BDTs with their final cut values, 0.25 (LE) and 0.35 (HE), provide excellent background reduction of over 99%. The combined final sample has a signal efficiency of 5% for the FB signal, compared to the efficiency on level L2'[6]. The experimental data rate equals to 2.5×10^{-4} Hz. GENIE simulation was used to estimate the atmospheric neutrino background, which equals to 1.1×10^{-4} Hz and corresponds to 44% of the data rate. The atmospheric muon background was estimated using CORSIKA simulation[7] and is less than 10^{-4} Hz.

In figure 4.7 the effective area for the final combined analysis is shown and it represents the efficiency of DeepCore for this event selection. This effective area is an average over all Fermi bubble declination angles. Effective areas were calculated for five degree declination bands and compared in each energy

---

[6]For comparison: the WIMP signal efficiency was 8% for the LE- and 6% for the HE sample.
[7]Due to extremely low statistics of remaining simulated atmospheric muons L4 an upper limit is given. The prediction for the rate reduction of atmospheric muons using Corsika is not believed to be so exact that this rate discrepancy corresponds to an additional component. It rather motivates the use of data for the background estimate.

bin. The effective areas were equal within 15% with the largest deviations in the lowest energy bin. Furthermore, the combined effective area was validated on the old and new simulation sets[8] and compared to the two original effective areas from [194]. The difference between the old and new simulation is less than 5% in each bin.
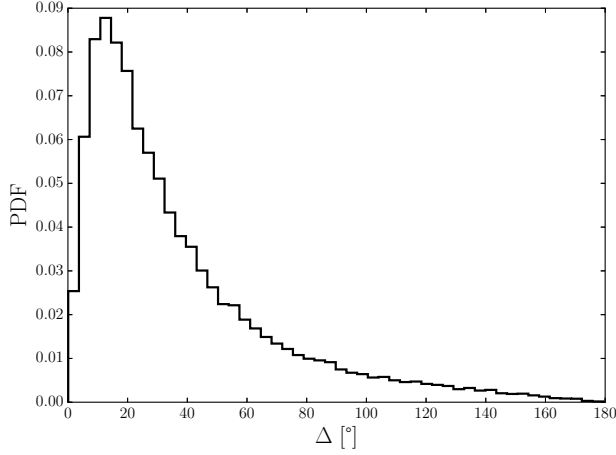
Figure 4.8. The angular resolution distribution of the simulated event sample with the FB energy spectrum. The x-axis represents the distance between reconstructed and true direction: $\Delta\Psi = \Psi_{reco} - \Psi_{true}$.

The median angular resolution of the sample is $26.5°$, see figure 4.8. The 90 percentile angular resolution lies at $83°$. At low energies the shower size is short compared to the scattering length, hence the reconstruction of the direction is challenging.

---

[8]Old simulation means the sets which were used for the Galactic Halo WIMP analysis, the new sets were used for the FB analysis presented here.

5. Investigating the Fermi Bubbles with Respect to Neutrinos

Published IceCube data was previously taken and compared spatially to the location of the Fermi bubbles, assuming hadronic models predicting neutrinos above 1 PeV (e.g. [163, 214]). There are events coincident with the Fermi bubble location, however no statements can be made whether these events actually originated from the Fermi bubbles.

With this analysis we want to use rather sophisticated tools to investigate the potential Fermi bubble neutrino flux at the energies at which the FB γ-ray flux was measured and at the lowest energies IceCube is able to detect.

5.1 The Expected Fermi Bubble Neutrino Flux

As described in chapter 2 a log-parabola function represents the best fit for the Fermi bubble γ-ray flux in the complete energy range between 100 MeV and 500 GeV (including upper limits) for the measured data presented by the Fermi-LAT collaboration [30]:

$$\frac{dN}{dE} = \Phi_\gamma(E) = I \left(\frac{E}{1\text{GeV}} \right)^{-\alpha - \beta \cdot \ln(E/1\text{GeV})}, \tag{5.1}$$

where $I = 4.6 \times 10^{-7}$, $\alpha = 1.77$ and $\beta = 0.063$ represent the fit parameters. The fit parameters are taken from [30]. The scaling parameter I was not specified in the paper and hence fitted here to the values from table 2 in [30] in column "$E^2 F$".

The method used is based on the prescription from [206] describing how the γ-ray data itself can be used as input flux in order to determine a neutrino flux expectation. The beauty of this technique is that it does not require any preliminary parametrization of the photon flux. The theory behind this method is that CR-protons interact with an ambient hydrogen cloud and the resulting mesons decay in γ-rays or leptons (including neutrinos), depending on the meson type[1]. It is assumed that the fluxes of γ-rays and neutrinos depend linearly

---

[1]The interactions (eq. 1.4 & 1.3) and pion decay channels (eq. 1.6 & 1.8) can be viewed in section 1.2.1 and the main kaon decay channels (eq.1.9, 1.10 & 1.11) are shown in section 1.4.

on the primary CR flux, and hence, they also have a linear relation between each other [206].

The prescription leads to the following expression for the muon neutrino flux at a given energy E at Earth[2], using the γ-ray flux:

$$\Phi_i(E) = c_{\pi_i} \cdot \Phi_\gamma(E/x_\pi) + c_{K_i} \cdot \Phi_\gamma(E/x_K) + \int_0^1 \frac{dx_E}{x_E} k_i(x_E)\Phi_\gamma(E/x_E) \quad (5.2)$$

with $i = \nu_\mu, \bar{\nu}_\mu$. The flux expectations are different for ν and $\bar{\nu}$ because of the production rates of various mesons. They are rescaled to the production rate of neutral pions from *proton-proton* (pp) interactions and are calculated from hadronic interaction models.

According to [206] this equation and the evaluated constants and kernels are generally applicable to transparent sources. We will summarize the terms, evaluations and numbers below, and the reader is referred to [206] for the derivation.

The first term of equation 5.2 describes neutrinos produced in pion decays, the second term describes neutrinos created in kaon decays and the third term accounts for neutrinos generated in muon decay. In expression 5.2 x_π and x_K stand for:

$$x_\pi = 1 - (m_\mu/m_\pi)^2 \text{ and } x_K = 1 - (m_\mu/m_K)^2,$$

with m_μ, m_π, m_K being the masses of the muon, pion and kaon respectively. The x_E represents the ratio between the energy E_i of the neutrinos produced in the decay chain and the input energy E:

$$x_E = E_i/E.$$

The constants c_{π_i}, c_{K_i} equal to the following numbers for neutrinos:

$$c_{\pi_{\nu_\mu}} = 0.380$$
$$c_{K_{\nu_\mu}} = 0.013$$

and for anti-neutrinos:

$$c_{\pi_{\bar{\nu}_\mu}} = 0.278$$
$$c_{K_{\bar{\nu}_\mu}} = 0.009$$

The kernels $k_i(x)$ are integrated over the energy ratio x_E in order to include neutrinos from muons which are produced by pion- and kaon-decays. Depending on x_E, the kernel integration differs in the following way for neutrinos:

---

[2]Neutrino oscillations are already included in this expression with a flavor ratio of [1:1:1].

$$k_{\nu_\mu}(x) = x^2(15.34 - 28.93x) \qquad x \le (m_\mu/m_K)^2 = 0.0458$$
$$= 0.0165 + 0.1193x + 3.747x^2 - 3.981x^3 \qquad (m_\mu/m_K)^2 < x < (m_\mu/m_\pi)^2$$
$$= (1-x)^2(-0.6698 + 6.588x) \qquad x \ge (m_\mu/m_\pi)^2 = 0.573$$

$$(5.3)$$

and similar but with different constants for anti-neutrinos:

$$k_{\bar{\nu}_\mu}(x) = x^2(18.48 - 25.33x) \qquad x \le (m_\mu/m_K)^2 = 0.0458$$
$$= 0.0251 + 0.0826x + 3.697x^2 - 3.548x^3 \qquad (m_\mu/m_K)^2 < x < (m_\mu/m_\pi)^2$$
$$= (1-x)^2(0.0351 + 5.864x) \qquad x \ge (m_\mu/m_\pi)^2 = 0.573$$

$$(5.4)$$

The neutrino flux in equation 5.2 leads then to the following equation for the log-parabola assumption:

$$\Phi_i(E) = c_{\pi_i} \cdot I \left(\frac{E}{x_\pi} \right)^{-\alpha - \beta \cdot \ln(E/x_\pi)}$$
$$+ c_{K_i} \cdot I \left(\frac{E}{x_K} \right)^{-\alpha - \beta \cdot \ln(E/x_K)} \qquad (5.5)$$
$$+ \int_0^1 \frac{dx_E}{x_E} k_i(x_E) I \left(\frac{E}{x_E} \right)^{-\alpha - \beta \cdot \ln(E/x_E)}$$

With equation 5.5 it is possible to obtain the muon neutrino flux at Earth. The fit for the gamma rays, and the resulting neutrino, anti-neutrino and total ν expectation flux are depicted in figure 5.1.

Due to the large distance between the Fermi bubbles and Earth, the neutrino flavor ratio is assumed to be [1:1:1] due to oscillations, even if the initial ratio at the source was different. All three neutrino flavors are used in the following analysis, therefore, the neutrino flux expectation is assumed to be three times larger than the total muon-neutrino flux presented in figure 5.1.
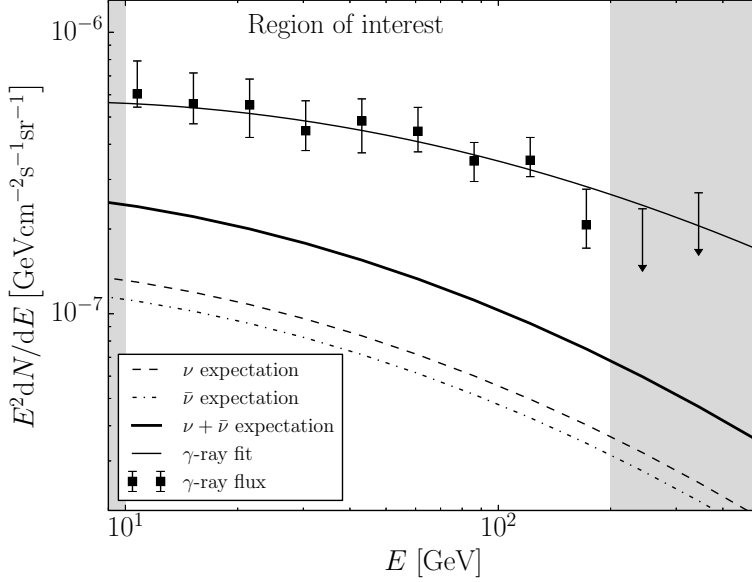
Figure 5.1. The squares represent the Fermi-LAT data for the Fermi bubbles [30]. The dashed-dotted line is the expectation for anti-neutrinos and the dashed line shows the expectation for neutrinos. The thick solid line represents the total neutrino flux ($\nu + \bar{\nu}$) which is used for this analysis for each neutrino flavor. The white region shows the energy range in which this analysis is performed.

5.2 Construction of Probability Density Functions

We want to perform an all-sky analysis, this means we need to construct *Probability Density Functions* (PDFs) which accept neutrinos from the whole sky. The angular resolution is $26.5°$, which is the reason the reason why reconstructed events can be far away from the true direction, see section 4.2.5. Due to this fact it is useful to perform an all-sky analysis.

In order to test the signal hypothesis against the background-only hypothesis a maximum likelihood method was chosen, which will be discussed in section 5.3. The hypotheses are represented by PDFs in the form of *healpy* skymaps. The Python[3] package *healpy* is designed to handle pixelated data on a sphere. Healpy is based on the *Hierarchical Equal Area isoLatitude Pixelization* (HEALPix) scheme [116]. As the name suggests it divides a sphere in pixels (further referred to as healpy bins), which all have the same surface area.

---

[3]Python is a programming language.

5.2.1 Signal Expectation

At the energies at which this analysis is performed it is not beneficial to use the detailed template shape which is published by the Fermi-LAT collaboration [30], because of the angular resolution for neutrinos. The detailed features as seen in figure 5.2 cannot be resolved. Instead, the Fermi bubble region was defined as two circles in galactic coordinates with a radius of $25°$ as shown in figure 5.3.
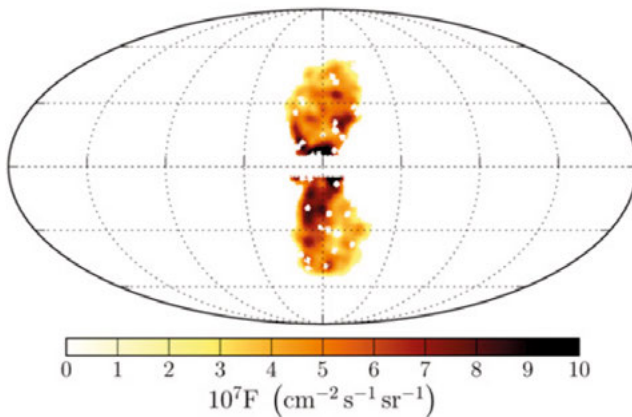
Figure 5.2. The Fermi bubble template published by Fermi-LAT in [30]. This template is a residual map after removing all other radiation sources.
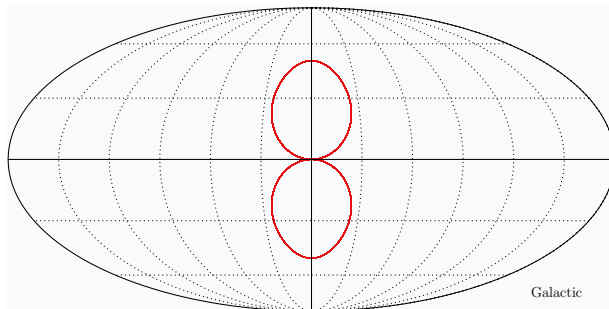
Figure 5.3. The Fermi bubble template shape for the analysis presented in this thesis, in Galactic coordinates.

The FB shape was then converted into equatorial coordinates, see figure 5.4. Simulated Monte Carlo events were weighted with the expected neutrino or anti-neutrino flux from the Fermi bubbles (equation 5.5) per neutrino flavor

according to equation 3.2, see section 3.6.1. The weighted events, which were distributed over the entire sky were cut in declination to the upper and lower Fermi bubble declinations. The remaining events were assigned a random azimuthal rotation such that they ended up in the FB signal region (within the thin red lines). The declination position of the events was not changed, because the detector acceptance is declination dependent. The resulting signal skymap PDF is presented in figure 5.4, showing a uniform signal expectation with small statistical fluctuations, due to the random assignment of the events.
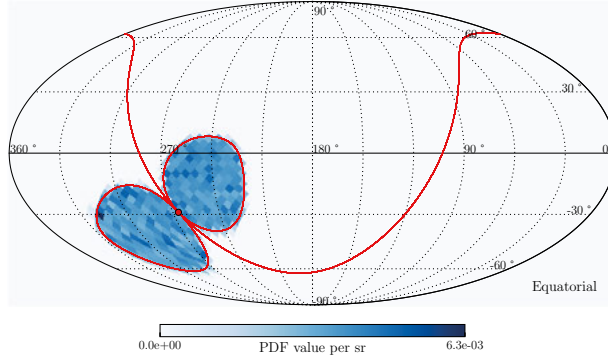
Figure 5.4. The simulated signal skymap PDF before reconstruction. The red lines indicate the galactic plane and the FB shape and the red dot represents the Galactic Center position.
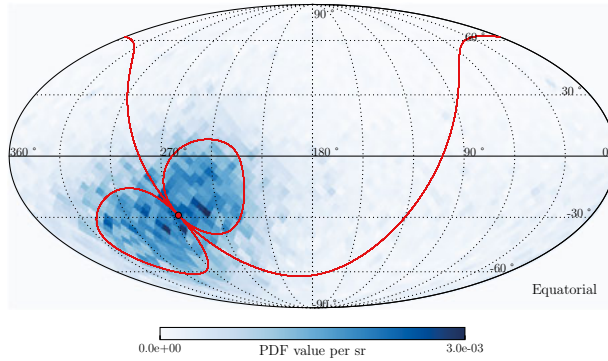
Figure 5.5. The FB signal PDF after event reconstruction.

These events were then reconstructed in direction and energy, resulting in a skymap PDF which corresponds to how the detector would see the signal, as depicted in figure 5.5. In this reconstructed signal PDF the spread of the events indicates the extent of the angular resolution, and shows that small fea-
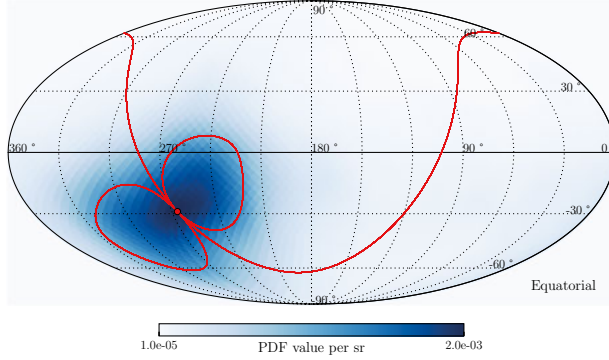
Figure 5.6. The final FB signal PDF, $f_S(b)$, after smoothing the reconstructed signal.

tures cannot be resolved. Furthermore, the skymap PDF shows now much larger statistical fluctuations, which are not realistic features. These fluctuations are the result of reconstructed events falling into certain bins. The intensity of the Fermi bubble flux is a uniform distribution, hence, this PDF has been smoothed as depicted in figure 5.6. For the smoothing the function *healpy.sphtfunc.smoothing*, which is provided by healpy [116], is used. This function applies a symmetrical Gaussian beam to the skymap resulting in the final signal PDF. The sigma of the Gaussian beam, further referred to as smoothing degree, of $7°$ was chosen, because it was the lowest value giving stable results in the confidence interval calculation leading to a sensitivity for the potential FB neutrino flux. At lower smoothing degrees, the procedure became unstable, because the statistical fluctuations in the PDFs were dominating. The effect of smoothing is smaller than the uncertainty of the reconstruction of the events, comparing the smoothing degree with the angular resolution ($26.5°$).

5.2.2 Background Expectation

Real data, see table 4.2, was scrambled in right ascension to preserve blindness regarding the true directions of the events. Scrambling becomes ineffective at the poles because of the limited solid angle. Hence, five degrees in declination were cut away at each pole. In order to get a realistic background (BG) the skymap PDF was smoothed with the smoothing function mentioned in section 5.2.1 [116], using the same smoothing degree.

5.2.3 Scrambled Signal

The advantage of using real data as BG expectation is the reduction of systematic uncertainties. The disadvantage is that the BG PDF could be contaminated
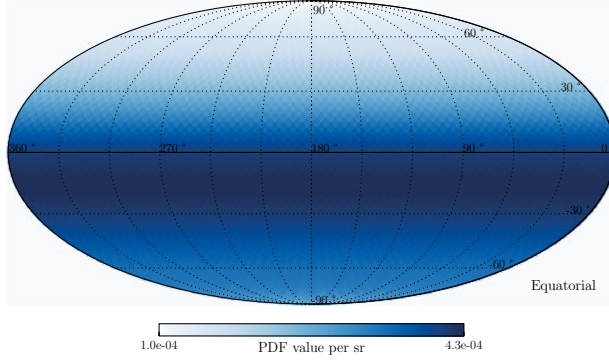
Figure 5.7. Smoothened scrambled data background PDF, $f_{sd}(b)$.
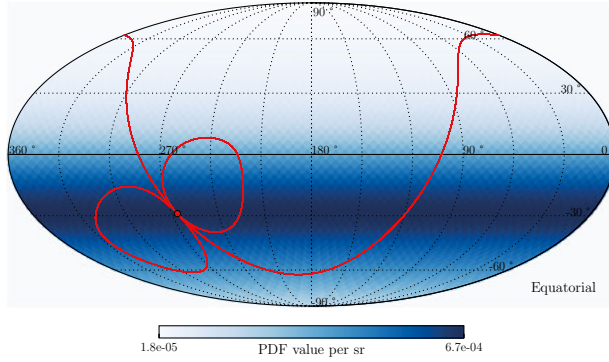
Figure 5.8. Scrambled reconstructed signal PDF, $f_{ss}(b)$, based on simulations .

with possible signal events. In order to account for the potential signal events, a scrambled signal PDF was needed (figure 5.8). The signal events in figure 5.5 were treated in the same way as the real data events, scrambled in right ascension only, and then smoothed.

5.2.4 Probability Density Function

The real scrambled data PDF $f_{sd}(b)$ is potentially contaminated with signal, therefore it has two components, the scrambled signal PDF $f_{ss}(b)$ and the unknown true background PDF $f_B(b)$:

$$f_{sd}(b) = \frac{\mu}{n_{\text{obs}}} f_{ss}(b) + \left(1 - \frac{\mu}{n_{\text{obs}}}\right) f_B(b), \tag{5.6}$$

where μ represents the number of signal events, n_{obs} is the total number of observed events and b is the bin number. The combined PDF usually consists

of a signal PDF $f_S(b)$ and a background PDF, which we can replace using equation 5.6:

$$
\begin{aligned}
f(b|\mu) &= \frac{\mu}{n_{\text{obs}}} f_S(b) + \left(1 - \frac{\mu}{n_{\text{obs}}}\right) f_B(b) \\
&= \frac{\mu}{n_{\text{obs}}} f_S(b) + f_{sd}(b) - \frac{\mu}{n_{\text{obs}}} f_{ss}(b).
\end{aligned}
\tag{5.7}
$$

The PDFs for signal, scrambled signal and scrambled background are shown in the figures 5.6, 5.8 and 5.7 respectively.

5.3 The Analysis Method

The number of signal events, μ, among the observed events, n_{obs}, is unknown and we want to construct *Confidence Intervals* (CIs) to determine it or obtain an upper limit. The method suggested by Feldman & Cousins [98], which is a frequentist approach, has the advantage that it will be determined by the data if the CI quoted should be single sided, giving an upper limit, or double sided, indicating a signal. Below we will describe how to construct the CIs according to this method.

5.3.1 Confidence Intervals and Sensitivity

In practice we modified the Feldman & Cousins method to avoid unnecessary and time-consuming calculations. The procedure used in this analysis is henceforth still called Feldman & Cousins.

1. A number of predicted signal events, μ, in the interval $[0, 0.3n_{\text{obs}}]$ was chosen[4]. This was repeated 100 times with a step size $\Delta\mu$ of $(0.3n_{\text{obs}})/100$.

   > In this analysis $n_{\text{obs}} = 45022$, see table 4.2. For every chosen μ, 10^4 *pseudo-experiments* were performed. A pseudo-experiment is a statistically independent trial to determine a test statistic.

   a) For each pseudo-experiment, $k = 1 ... 10^4$, the following steps were performed:

---

[4]The decision to assume a maximum of 30% signal in the observed data is an educated guess. If this number would be not adequate, the calculations would produce unstable (strongly fluctuating and decreasing) ranks with increasing signal events.

i. Selecting randomly a sample of n_{obs} healpy bins, $\{b_i\}$, $i = 1, ..., n_{\text{obs}}$ using the PDF in equation 5.7.

ii. Obtaining the corresponding likelihood $\mathscr{L}(\mu)$.

The likelihood is defined as a product of the corresponding PDFs:

$$\mathscr{L}(\mu) = \prod_{i=1}^{n_{\text{obs}}} f(b_i|\mu). \qquad (5.8)$$

iii. Finding the best fit, $\hat{\mu}$, for the likelihood.

The best fit is the number of events which maximizes the likelihood $\mathscr{L}(\hat{\mu})$.

iv. Calculating the logarithm of the *rank* $\ln R(\mu)$.

The *rank* is defined as:

$$R(\mu) = \frac{\mathscr{L}(\mu)}{\mathscr{L}(\hat{\mu})}, \qquad (5.9)$$

By construction $\mathscr{L}(\hat{\mu}) \geq \mathscr{L}(\mu)$, leading to $R(\mu) \leq 1$. Here, the logarithm of the rank is used as test statistic.

b) Constructing the acceptance interval for the test statistic $\ln R(\mu)$, $[\ln R_{crit}^{CL}(\mu), 0]$.

The critical rank $\ln R_{crit}^{CL}(\mu)$ represents the value of $\ln R(\mu)$ for which a fraction $(1 - \alpha)$ of all 10^4 pseudo-experiments satisfies $\ln R(\mu) \geq \ln R_{crit}^{CL}(\mu)$. The fraction $CL = 1 - \alpha$ represents the *Confidence Level*, and for this analysis the $CL = 90\%$. Since $R(\mu) \leq 1$, the acceptance interval is defined as $[\ln R_{crit}^{CL}(\mu), 0]$. Values of $\ln R(\mu)$ are added to the acceptance interval until the critical $\ln R_{crit}^{CL}(\mu)$ is the reached. We start with the highest rank, since $\ln R(\mu)$ is closer to 0 the closer the best fit $\hat{\mu}$ is to the true value of μ. This procedure is called the *ordering principle* [98].

c) Determining a confidence interval $[\mu_l, \mu_u]$.

Every value of μ which fulfills the condition:

$$\ln R(\mu) \geq \ln R_{crit}^{CL}(\mu) \qquad (5.10)$$

is included in the CI. The lowest value is represented with μ_l and the highest with μ_u.

2. The $\ln R_{crit}^{CL}(\mu)$ distribution was smoothed.

> Since $\ln R_{crit}^{CL}(\mu)$ was calculated in steps for μ the $\ln R_{crit}^{CL}(\mu)$ distribution is discrete, and therefore it is smoothed by fitting a spline to achieve continuity.

3. The sensitivity $\tilde{\mu}_{90}$ was determined.

   a) Constructing Confidence Intervals under the null-hypothesis.

   > To determine the CI, steps 1a), 1b) and 1c) were repeated for $\mu = 0$. This means the background-only hypothesis was used, with no signal present.

   b) Calculating the median upper limit.

   > The lower and upper values of the 10^4 CIs (μ_{l_k}, μ_{u_k}) can be plotted against μ, resulting in a lower and upper limit distribution. The sensitivity is defined as the median of the upper limit distribution. A sensitivity of e.g $\tilde{\mu}_{90} = 100$ means that at least 100 events are needed to be able to observe a signal at 90% CL with a 50% probability.

4. The unblinded limits μ_{90} were determined.

   > To determine the CI using the skymap with the true event directions (*unblinded skymap*) the following steps were executed:

   a) Point 1aii) Instead of the likelihood, the unblinded skymap is used.

   b) Point 1aiii) The best fit is determined.

   c) Point 1aiv) $\ln R(\mu)$ for the unblinded skymap is calculated.

   d) Point 1c) Using the previously determined and smoothed $\ln R_{crit}^{CL}(\mu)$ distribution the condition in point 1c) was applied. The μ_l and μ_u correspond to the unblinded lower and upper limits $\mu_{90,l}$, $\mu_{90,u}$.

As mentioned above, the advantage of this method is that the outcome is determined by the data, which results in a two-sided CI in case of a measurement and in an upper limit in case of a non-observation.

5.3.2 Expected Events

As mentioned in section 3.6.1 all generated events N_{gen} are forced to inter-act and the actual probability of their interaction and detection is taken into account with weights *OneWeight*. These weights, together with the neutrino flux spectrum expectation are also used in order to determine the expected number of events N_{exp}:

$$N_{exp} = T_{live} \cdot \sum \frac{OneWeight}{N_{gen}} \cdot \frac{\Phi_\nu(E,\Omega)}{dE\ d\Omega} \cdot \frac{1}{\Omega_{frac}} \tag{5.11}$$

where the livetime T_{live} corresponds to 2085 days. The weight $OneWeight/N_{gen}$ for every event is weighted with the FB neutrino flux expectation $\Phi_\nu(E,\Omega)/(dE\ d\Omega)$, which corresponds to the neutrino flux in equation 5.5, for every (anti-)neutrino flavor respectively. The variables E and Ω represent the neutrino energy and the solid angle it was generated in respectively.

The factor $1/\Omega_{frac}$ is compensating for the fact that only a fraction of the events for the whole sky were used in order to form the signal. It corresponds to

$$\Omega_{frac} = \frac{\Omega_{FB_{dec}}}{\Omega_{dec}}, \tag{5.12}$$

where Ω_{dec} corresponds to a $1°$ declination band and $\Omega_{FB_{dec}}$ stands for the FB region within that declination band. The Ω_{frac} factor allows us to use the IceCube standard simulations which generate neutrinos isotropically. The detector efficiency depends on declination but not on right ascension when a long exposure is analyzed, therefore Ω_{frac} depends also only on declination. From the simulations we expect to observe 5.3 events for the complete livetime of 2085 days for all neutrino flavors combined.

5.3.3 The Sensitivity Flux

In order to convert the sensitivity $\tilde{\mu}_{90}$ into a sensitivity flux $\tilde{\Phi}_{90}$ the *model rejection factor* is used [134]:

$$\tilde{\Phi}_{90} = \frac{\tilde{\mu}_{90}}{N_{exp}} \cdot \Phi_{exp}. \tag{5.13}$$

The expected number of events N_{exp} was determined in equation 5.11 and Φ_{exp} is three times the expected neutrino flux Φ_{ν_μ} from equation 5.5, assuming three neutrino flavors. Due to neutrino oscillations they have the same flux at Earth:

$$\Phi_{exp} = 3 \cdot \Phi_{\nu_\mu}. \tag{5.14}$$

The sensitivity flux and the median upper limit $\tilde{\mu}_{90}$ are then used to calculate the resulting flux after unblinding:

$$\Phi_{90} = \frac{\mu_{90}}{\tilde{\mu}_{90}} \cdot \tilde{\Phi}_{90}, \tag{5.15}$$

where μ_{90} represents both the lower and upper limit $\mu_{90,l}$, $\mu_{90,u}$. For the unblinding the method of Feldman & Cousins [98], as described in section 5.3.1, is used to determine confidence intervals using the skymap with the true directions of the data events, which will be revealed in the next chapter.

6. Fermi Bubble Analysis Results

After the IceCube collaboration reviewed the analysis and approved it for un-blinding, the true event directions were revealed and can be seen in figure 6.1.
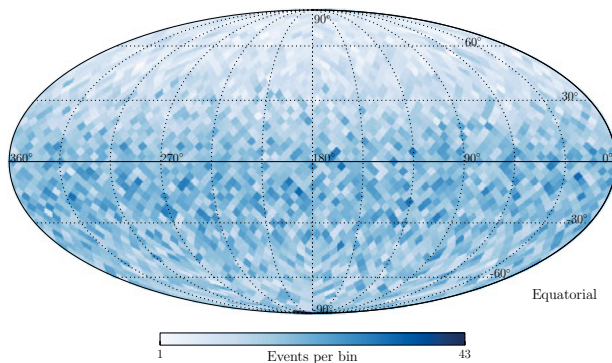
Figure 6.1. The skymap with the true event directions.

This skymap was used to determine the confidence interval for the Fermi bub-ble neutrino flux with the method of Feldman & Cousins [98], resulting in a confidence interval containing zero. Therefore, an upper limit on the Fermi bubble neutrino flux was set using equation 5.15, see figure 6.2. The sensi-tivity was determined to be $\tilde{\mu}_{90} = 279$ events and the unblinded upper limit resulted in $\mu_{90} = 471$ events. The FB ν upper limit flux for 2085 days of data is represented as a solid line and is 0.86σ above the sensitivity flux $\tilde{\Phi}_{90}$ corresponding to a p-value of 0.19. The p-value was calculated according to

$$p = 1 - \frac{u}{k},\tag{6.1}$$

where k is the total number of pseudo-experiments and u represents the num-ber of pseudo-experiments needed to reach the unblinded upper limit. The sen-sitivity is represented as a dashed line with 1σ (green) and 2σ (yellow) statis-tical uncertainty bands. For the statistical uncertainty bands the corresponding percentiles of the upper limit distribution from the pseudo-experiments for the sensitivity calculation are computed. The sensitivity lies almost two orders of magnitude above the expected FB neutrino flux Φ_{exp} (red dash-dotted), based on the FB γ-ray flux, see section 5.1.
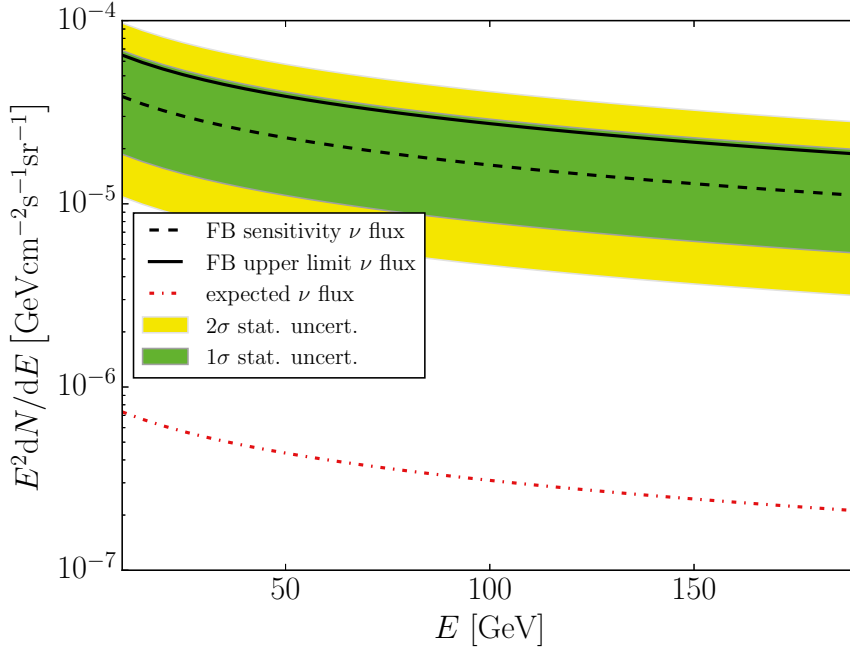
Figure 6.2. The result is presented as upper limit Φ_{90} (solid line) for all 3 neutrino flavors, together with the the Fermi Bubble sensitivity flux $\tilde{\Phi}_{90}$ (dashed line) and the 1σ (green) and 2σ (yellow) uncertainty bands. For comparison the expected flux from the FB, Φ_{exp}, is shown as well (red dash-dotted line).

6.1 Systematics Uncertainties

Different systematic effects are investigated in order to estimate the contributions to the sensitivity. This is done by producing a GENIE MC simulation for each systematic effect separately, varying one parameter at a time in comparison to the baseline MC set, on which the analysis was performed and the sensitivity determined.

The systematic uncertainties were calculated by using the systematic MC PDF to sample events and calculate the likelihood according to equation 5.8. However, the baseline MC PDF was used in order to calculate the best fit of the likelihood, which is used to determine the rank, see equation 5.9. The sensitivity for every systematic set was calculated using this method.

DOM-efficiency
The DOM-efficiency accounts for the efficiency of the DOMs to transform the detected Cherenkov light into an electrical signal. This property was measured in the laboratory as well as after implementation in the ice. For the systematic simulation sets the DOM-efficiency was changed by $\pm 10\%$, which corresponds to about 1σ on the measured value. For this analysis the effect

on the sensitivity results in an 11% worse outcome for a 10% smaller DOM-efficiency and an 8% improvement for the opposite case.

Hole ice

The "hole ice" is the ice close to the DOMs. This ice is different from the bulk ice, because it was melted when the holes were drilled and after the installation of the strings it refroze. Due to this process the hole ice contains air bubbles, which result in a shorter scattering length. The baseline GENIE settings assume a scattering length of 50 cm for the hole ice, while the systematic sets fix the value to 30 cm or 100 cm. The impact on the sensitivity is quite small, increasing it by 5% and decreasing it by 6%, corresponding to 30 cm and 100 cm respectively.

Ice model

The ice model characterizes the properties of the bulk ice. The model used for this analysis is called SPICE LEA [80], see section 3.5. To determine the ice model systematics we compare to an earlier ice model SPICE MIE [7]. SPICE LEA takes the azimuthal anisotropy of light propagation into account, and is hence more precise. The comparison resulted in an 9% impact on the sensitivity using SPICE MIE.

Noise model

The noise model describes the noise measured by DOMs. In this work, the *Vuvuzela low-dt* model is used as the baseline, and for the systematic set the previous *Vuvuzela standard* code is implemented. The difference between the two models lies in the extension of the noise model to shorter time scales, improving the data-MC agreement. Details of the models can be found in [160]. The impact on the sensitivity was about 10%.

Table 6.1. *The systematic uncertainties on the sensitivity. A negative number indicates a worse sensitivity and a positive a better sensitivity.*

systematic uncertainty	influence
DOM efficiency -10%	-11%
DOM efficiency +10%	8%
Hole ice 30 cm	5%
Hole ice 100 cm	-6%
Ice model (SPICE MIE)	9%
Noise model (Vuvuzela std.)	10%
Total	18%
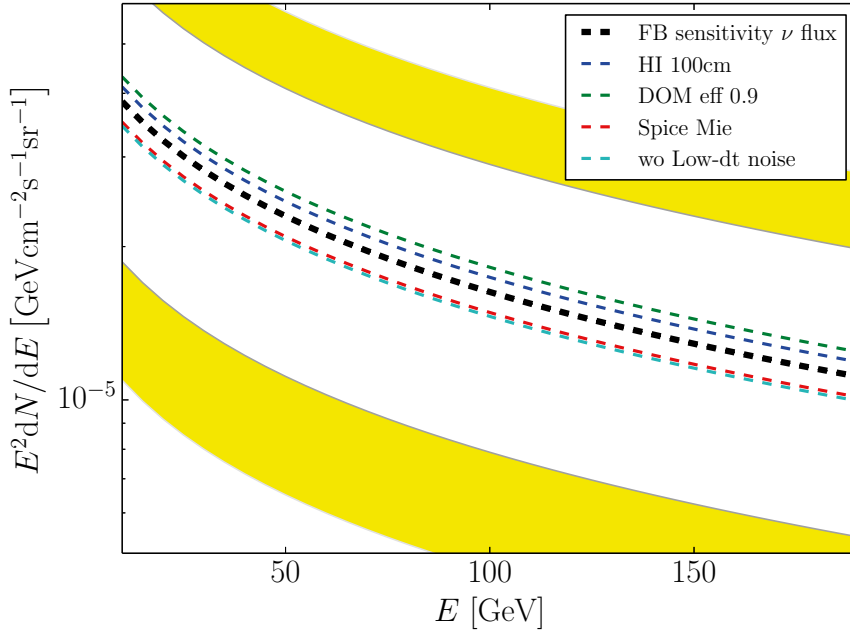
Figure 6.3. The largest contribution of systematic uncertainties determined by MC compared with statistical uncertainties. The 2σ statistical uncertainty band is shown in yellow, surrounding the 1σ band (white).

A summary of the impact by systematic effects is shown in table 6.1. The total effect is obtained taking the square root of the quadratic sum of the largest contribution within each systematic category and amounts to 18%. Figure 6.3 shows the largest systematic uncertainties on the sensitivity for each MC set. The systematic effects are smaller than the statistical uncertainties.

Table 6.2. *The systematic uncertainties on the sensitivity due to the smoothing degree. A negative number indicates a worse sensitivity and a positive a better sensitivity.*

smoothing	FB
7	0%
14	-7%
20	-15%

Systematic effects due to the smoothing degree have not been included above, because it is a systematic uncertainty on analysis level. As explained in section 5.2.1 a smoothing degree of 7° was chosen since it was the smallest value resulting in a stable analysis procedure. This was especially noticeable when

analyzing the systematic uncertainty MC sets. The influence of higher smoothing degrees on the sensitivity was determined using the baseline data set and it is summarized in table 6.2.
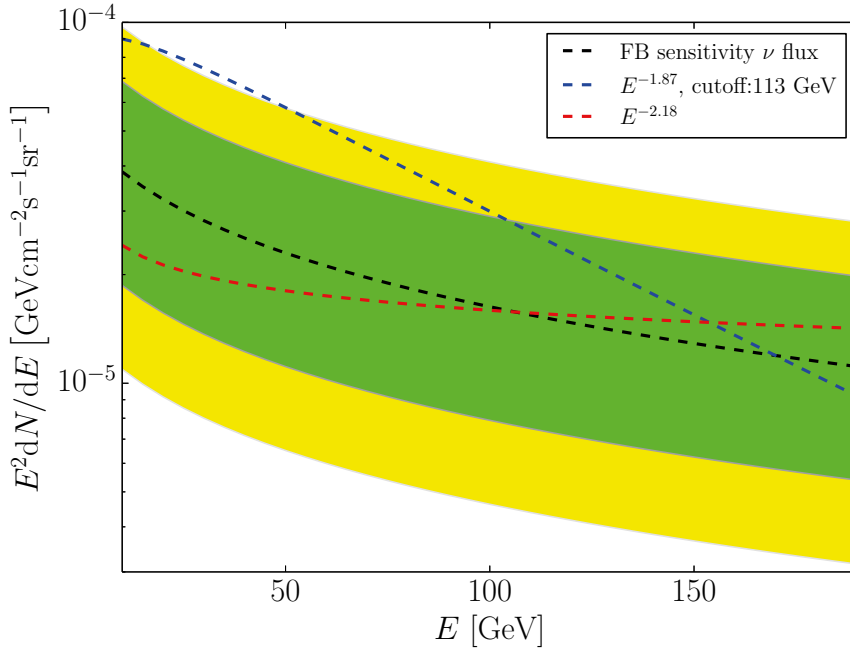
Figure 6.4. Comparison of the log-parabola FB ν flux sensitivity (black dashed) compared to sensitivities resulting from other FB ν flux expectations. The blue dashed line represents the sensitivity for an $E^{-1.87}$ spectrum with an exponential cutoff at 113 GeV. The red dashed line shows a power law of $E^{-2.18}$ without cutoffs in the investigated energy range.

Finally, the systematic uncertainty due to the parametrization of the γ-ray flux from the Fermi bubbles was investigated. For this analysis a log parabola fit was chosen because it fits the observed data best. The best fit for a power law spectrum performed by the Fermi-LAT collaboration and the best fit for the analysis from the neutrino observatory ANTARES [35] are used to investigate the impact.

In addition to the log-parabola fit, the Fermi-LAT collaboration published a power law with a spectral index of 1.87 and an exponential cutoff at 113 GeV [30], see figure 2.2. A power law through the γ-ray data with a spectral index of 2.18 was fitted by ANTARES. The fit was extrapolated to higher energies beyond the energy range measured by the Fermi-LAT collaboration. The effect on the ANTARES sensitivity was investigated for neutrinos under a few hypothetical assumptions for cutoffs in the γ-spectrum and ν-spectrum [124].

A comparison between the IceCube and ANTARES results is discussed in the next section 6.1.1. In order to get the neutrino flux expectations, equation 5.2 was used and $\Phi_\gamma(E)$ was replaced with:

$$\Phi_{\gamma,FL} = 4.6 \times 10^{-7} \left(\frac{E}{1\mathrm{GeV}} \right)^{-1.87} e^{-E/113\mathrm{GeV}} \; \mathrm{GeV}^{-1}\mathrm{cm}^{-2}\mathrm{s}^{-1}\mathrm{sr}^{-1} \quad (6.2)$$

for the Fermi-LAT γ-ray fit and

$$\Phi_{\gamma,ANT} = 5 \times 10^{-7} \left(\frac{E}{1\mathrm{GeV}} \right)^{-2.18} \; \mathrm{GeV}^{-1}\mathrm{cm}^{-2}\mathrm{s}^{-1}\mathrm{sr}^{-1} \quad (6.3)$$

for the ANTARES γ-ray fit. The power law indices and the cutoff energy are taken from the respective publications, however, the normalization factors were fitted for the energy interval relevant for this analysis[1]. The events of the GENIE baseline simulation set were weighted with the resulting neutrino flux expectations derived from these γ-ray fits, see section 3.6.1. The complete analysis was performed on these sets and the sensitivity fluxes are compared in figure 6.4.

Using the model rejection factor[2] as comparison quantity, the log-parabola sensitivity is 30% better than the $E^{-2.18}$ power law sensitivity and 60% better than the $E^{-1.87}$ power law sensitivity with cutoff. Due to the different flux expectations the flux sensitivities depend on energy, see figure 6.4.

6.1.1 Comparison with ANTARES Upper Limits

The neutrino telescope ANTARES is also looking for neutrinos from the Fermi bubbles [124]. Figure 6.5 shows a comparison between the upper limit obtained in this work and that of ANTARES for one neutrino flavor. Note that the analysis methods were very different and valid for different energy ranges in the two cases. ANTARES performed a *cut-and-count* analysis based on off- and on-zones using a livetime of 2096 days. The results for tracks and cascades were then combined using the method of Feldman & Cousins [98]. Details can be found in [124]. This thesis presents a maximum likelihood analysis for all three neutrino flavors and data collected in a livetime of 2085 days.

The shaded bands (blue and gray) represent the extrapolated neutrino flux expectations from ANTARES, where a power law with a $\Phi_\gamma(E) = I \cdot E^{-2.18}$

---

[1]The fitting of the normalization factor is necessary because the Fermi-LAT collaboration did not specify it and ANTARES defined a normalization range.
[2]See section 5.3.3.
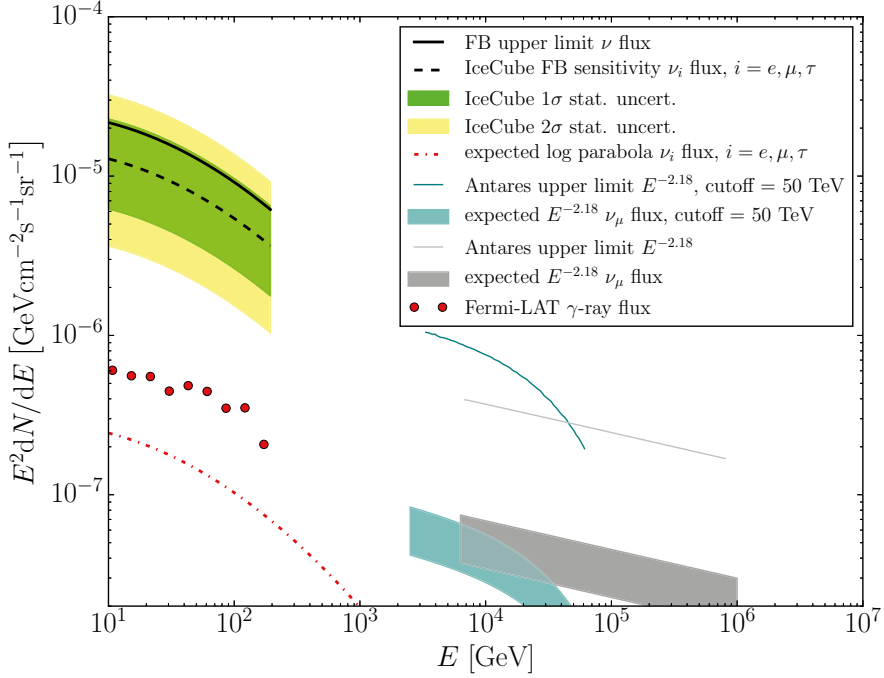
Figure 6.5. A comparison between upper limits on the neutrino flux from the Fermi bubbles obtained by ANTARES and the results of this analysis (divided by 3). The red circles represent the original γ-ray data from the Fermi-LAT collaboration and the red dash-dotted line shows the expectation for one neutrino flavor assuming the log-parabola flux. The black solid line shows the IceCube upper limit, the black dashed line is the sensitivity, together with the 1σ (green) and 2σ uncertainty bands. The shaded gray and blue bands are the extrapolated neutrino expectations for one neutrino flavor used by ANTARES. The solid lines in the same colors present the upper limits for the Fermi bubble neutrino flux for ANTARES.

spectrum was fitted to the gamma ray data and then the neutrino flux expectation was calculated using the same model as in this work [206], see section 5.1. Because of the power law expectation, equation 5.2 becomes simpler. The γ-ray flux can be extracted from all terms and the constants and kernel terms can be calculated separately leading to scaling factors to account for neutrinos (first term) and anti-neutrinos (second term). This results in a total neutrino flux for one flavor:

$$\Phi_{\nu'_\mu}(E) = \Phi_{\nu_\mu}(E) + \Phi_{\bar{\nu}_\mu}(E) = (0.188 + 0.175)\Phi_\gamma(E), \qquad (6.4)$$

The reason why the expected flux extrapolated by ANTARES is shown as a band is because this fit was normalized to the lowest and highest measurement

points of the γ-ray data and therefore results in a band instead of a single line. Several cutoff scenarios were analyzed by ANTARES with $E_{cut} = 50\,\text{TeV}$ being the lowest and 500 TeV the highest cutoff. The upper limits in figure 6.5 show the extreme cases of no cutoff (gray line) and 50 TeV cutoff (blue line). The sensitivity of ANTARES worsens significantly for lower energy cutoffs than 50 TeV [124], which does not allow ANTARES to investigate the FB neutrino flux at lower energies. Energy cuts were applied in order to optimize the data for the 50 TeV cutoff scenario. Events with energies above 2.29 TeV and 10 TeV for cascades and tracks respectively were accepted. The reader is referred to the proceeding [124] for more details .

6.2 Conclusion

This analysis was the first IceCube analysis probing for neutrinos from the Fermi bubbles, and the first analysis setting upper limits on the FB ν-flux at such low energies, below 200 GeV. Based on the described event selection a maximum likelihood analysis was performed. For a livetime of 2085 days the results were consistent with the background-only hypothesis. Upper limits for the neutrino flux expectation from the Fermi bubbles at energies between 11 GeV and 150 GeV have been determined. This range represents the true energy of 90% of the simulated events. The analysis presented is optimized to investigate the flux at the lowest energies IceCube's DeepCore can measure.

The neutrino observatory ANTARES presented upper limits on the FB ν-flux at higher energies, in the TeV to PeV energy range [124]. A direct comparison between the upper limits of ANTARES and IceCube is presented in figure 6.5 for one neutrino flavor.

6.3 Outlook

This analysis was performed using an existing event selection optimized for low energy cascades. The event selection could be improved, by setting appropriate cuts for the FB signal on every level. An investigation regarding the last two BDT cuts was performed, where the FB sensitivity was calculated for various BDT cut values. Figure 6.6 shows the FB flux sensitivity at 100 GeV as a function of the low energy BDT cut value. In comparison to the chosen cut values at 0.25 for the LE BDT and 0.35 for the HE BDT, the flux sensitivity could be improved by 5% if choosing the value 0.2 for the LE BDT (and 0.3 for the HE BDT).

Further improvements on the sensitivity of this analysis require adding more years of data. A power law flux parametrization could be used to extend the
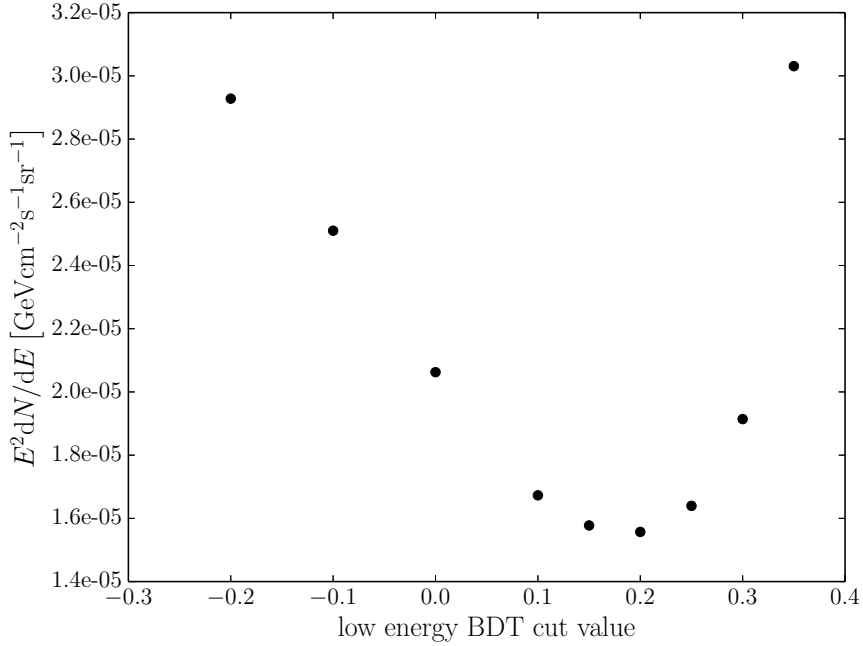
Figure 6.6. The FB flux sensitivity at $100\,\mathrm{GeV}$ at various LE BDT cuts. The high energy cut value was always set to the LE cut value increased by 0.1.

analysis to higher energies, which could lead to an improvement due to better precision of the reconstructions, because of a better angular resolution. At a certain energy threshold the analysis would need to be separated in tracks and cascades, because they would have significantly different signatures in the detector. On the other hand there is no detected excess of γ-rays from the FB in this energy region, thus a flux of neutrinos is less likely to be present. An improvement of the analysis would be to account for the potentially reduced neutrino flux from the FB due to a primary CR-electron population contributing to the measured γ-ray spectrum, see section 2.3.4.

The analysis method used in this thesis can be used to explore other extended sources in the low energy range as well, like the Galactic Ridge or the Galactic Plane.

The IceCube Upgrade, with seven denser strings, will allow more accurate low energy neutrino measurements, which will improve the energy and angular reconstructions. This is not only important for this analysis but also for investigations of neutrino oscillations and *Beyond Standard Model* (BSM) phenomena[3]. The long term goal is IceCube-Gen2 [16, 5], the next generation

---

[3]BSM includes all physics which are not explained by the Standard Model, like dark matter, sterile neutrinos or monopoles.

neutrino observatory for the South Pole. IceCube-Gen2 is supposed to consist of an in-ice High Energy Array (HEA), the Precision IceCube Next Generation Upgrade (PINGU) [18, 13], a surface array, and a potentially shallow sub-surface array of radio antennas [16, 5, 75]. The IceCube Upgrade is planed to start deployment in 2023 and might be a first step towards PINGU. The Ice-Cube Upgrade will be able to improve the detector sensitivity below 50 GeV and PINGU would bring the energy threshold below 1 GeV [75]. The surface array will be used for measuring CRs and as veto for IceCube. The high-energy in-ice extension, which is planed to be 10 times bigger than IceCube, will increase the probability for detection of astrophysical neutrinos in the PeV energy range. The radio array aims to detect neutrinos using the Askaryan effect[4], through which radio waves with a distinct signature are created by neutrino interactions. Therefore, the radio array would enable IceCube-Gen2 to detect cosmogenic neutrinos in the EeV energy range [75].

---

[4]The Askaryan effect is described in section 7.2.1.

Part II:

Investigation of Ice Properties with Radio Waves for ARIANNA

Illustration II. One ARIANNA station (X). On the right tower two solar panels are attached to power the station. The LPDA antennas and the electronics box are below the snow, and their positions are indicated by the blue flags and red flags respectively. On the left side is a tower with the prototype for the wind generator, which was deployed in season 2016/2017 for testing. In the background Mount discovery (left, North) and the Minna Bluff mountains (right) are visible.

7. ARIANNA

The Antarctic Ross Ice shelf ANtenna Neutrino Array (ARIANNA) is designed to detect the highest energy neutrinos, between 10^{17} eV and 10^{20} eV. At these *Extremely High Energies* (EHE) the Earth is not transparent to neutrinos anymore, therefore they are expected to be mostly detectable near or above the horizon. These EHE neutrinos interact with the ice and due to the Askaryan effect produce radio emission [51, 52, 53], which can be measured by ARIANNA.

At the moment ARIANNA is in the proof-of-concept phase including twelve autonomous stations (season 2018/2019). Originally it was planned to distribute 1296 stations over an area of 36 km $\times$ 36 km on the Ross Ice Shelf, Moore's Bay, with a separation of one kilometer between stations. Information about the future can be found in the outlook section 10.3. In the next pages we will describe the ARIANNA project in more detail.

ARIANNA consists of twelve stations, ten at the Ross Ice Shelf and two at the South Pole. Seven of the ten stations form the so-called Hexagonal Radio Array (HRA), which consist of four downward-pointing *Log Periodic Dipole Array* (LPDA) antennas arranged in a square and connected with cables to an electronics box, see figure 7.1 for a schematic view of the components of one station (and a potential ARIANNA detector). See illustration II for a view of one station at Moore's Bay. The electronics box includes the hardware to monitor and control the antenna operations, the solar panels and communication with a server in the Northern hemisphere. The box and the antennas are buried at a shallow depth under the snow surface, while the solar panel is attached to a tower. The remaining three stations have a different antenna configuration. Two additional stations are located at the South Pole. The various station configurations are discussed in section 7.1 and the hardware is described in more detail in section 7.3.

The Ross Ice Shelf provides an excellent environment for this project, because of its vast amount of ice and only few sources of radio frequency background. The radio signals from the McMurdo station are shielded by the Mina Bluff mountains[1] to the north and in the west by the Transantarctic Mountains. The remaining background signals arrive from above and are either due to aviation, or have natural causes, like radiation from the Galactic plane, auroras or CRs.

---

[1] Minna Bluff is visible in the background of illustration II.
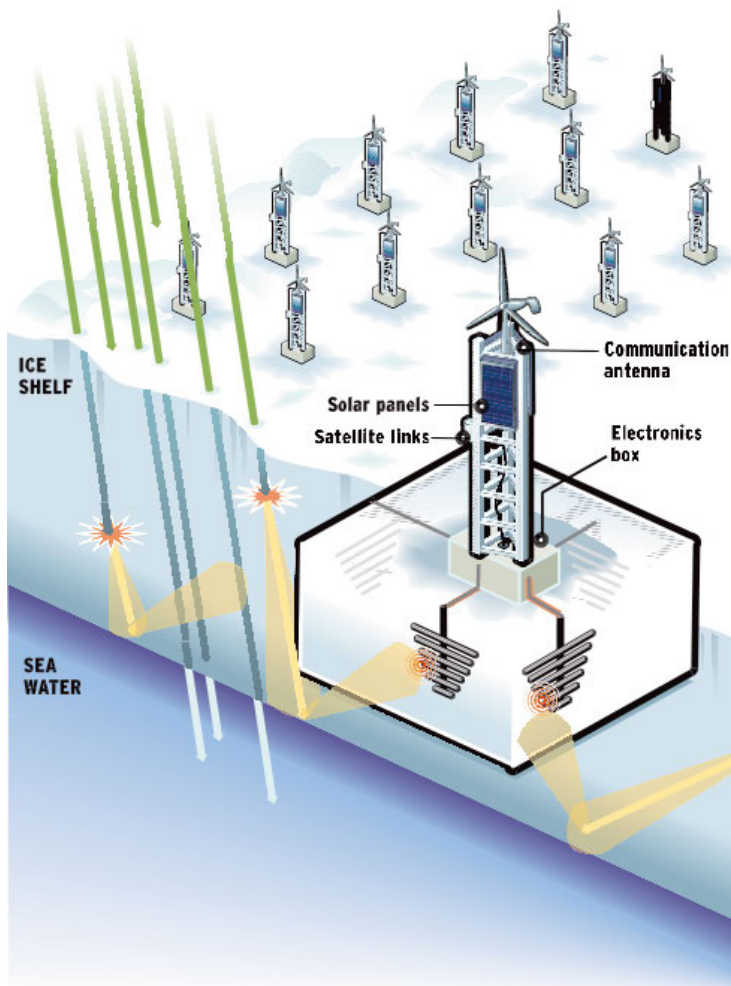
Figure 7.1. Schematic view of a potential ARIANNA detector. Depicted are the antenna stations, separated by 1 km distance. Each autonomous station has four down-facing LPDA antennas connected to an electronics box. The power supply is arranged on a tower above the surface including solar panels and wind generators. The latter are currently being tested and the actual setup is shown in illustration II. Indicated by colored lines are the neutrinos which interact with the ice and produce radio waves, shown as yellow cones. The radiation reflects off the ice/water interface and is then detected by the ARIANNA stations. Credit: Orange County Register 2012.
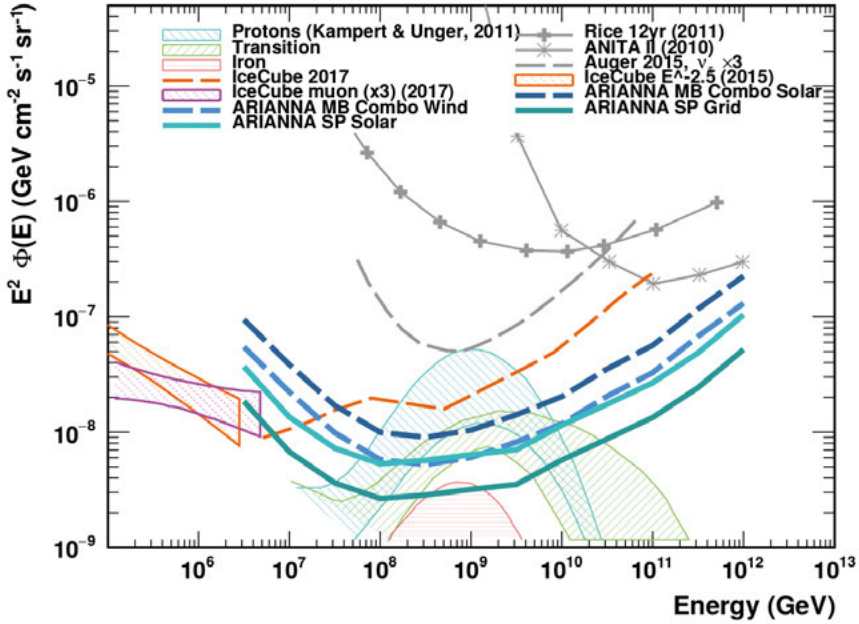
Figure 7.2. The projected sensitivities of ARIANNA for 300 stations with 12 channels each and 5 years of operation are presented [174]. The dark blue dashed line represents ARIANNA at Moore's Bay using only solar power. The light blue dashed line takes also wind power for the winter into account, expanding the lifetime. The solid light turquoise line shows ARIANNA at the South Pole with only solar power and the solid dark turquoise line represents the sensitivity when ARIANNA would be connected to the South Pole power Grid. The calculations for these sensitivities can be found in [174]. For comparison the measured astrophysical neutrino fluxes and 90% upper limits for GZK neutrinos of other experiments are shown. The blue, green and red shaded areas represent selected models of the GZK UHE neutrino flux. They take different primary CR compositions, high energy CR cutoffs and various source evolution models into account [145]. The orange shaded area represents the best fit for the measured all flavor diffuse neutrino flux by IceCube [12]. The pink shaded area shows the best fit for the observed IceCube muon flux only [123] (times three). The orange upper limit line represents the upper limit for IceCube on cosmogenic neutrinos for all flavors [15]. This upper limit has been updated using nine years of data and the astrophysical neutrino flux as background, yielding a consistent result [14]. Currently this is the best constraint on the GZK neutrino flux from 10^{17}eV to $\sim 10^{20}$eV. Figure adapted from: [174].

The data taking of HRA began in 2014 [65], with the aim to derive a sensitivity for the cosmogenic neutrino flux [60]. Estimates of the sensitivities that ARIANNA would be able to reach with 300 stations at Moore's Bay and the South Pole can be viewed in figure 7.2.

One of the stations with a special configuration has two upward pointing antennas[2] and was used to detect radio signals from CR showers [63]. At an average energy of $E \approx 6.5 \times 10^{17}$ eV the measured cosmic ray flux was $\sim 1 \times 10^{-16}$ eV^{-1} km^{-2} sr^{-1}yr^{-1} which is comparable with the observations by other experiments. This not only proves that ARIANNAs response is well understood but is also important for estimation of the background for EHE neutrino signals.

Besides ARIANNA two other experiments with different detection setup use the Askaryan effect to search for EHE neutrinos: The balloon-borne experiment ANITA and in-ice dipole array ARA, the successor of the Radio Ice Cherenkov Experiment (RICE) [155]. ANITA flew at heights between 35 km and 40 km, circling Antarctica and monitoring the ice for neutrino interactions. RICE consisted of 17 dipoles deployed in the South Pole ice between 100 m and 350 m depth. ARA currently consists of three antenna stations deployed at 200 m depth. The original plan was to have 37 stations separated by 2 km in a hexagonal grid [44]. The future is discussed in the outlook.

Exploratory work has been performed within the last few years at Summit, Greenland to evaluate suitability of the site for a potential radio neutrino experiment: the Greenland Neutrino Observatory (GNO) [55]. Other experiments with the purpose of detecting neutrinos using radio waves have been proposed like the ExaVolt Antenna EVA [113, 3] or the Giant Radio Array for Neutrino Detection GRAND [47]. The EUSO-SPB2 (Extreme Universe Space Observatory (EUSO) on a Super-Pressure Balloon (SPB)) has the goal to observe cosmic rays, gamma rays and Earth skimming neutrinos at high altitudes [32].

7.1 Detector Setup

In the season 2016/2017 ARIANNA consisted of 10 stations. The station locations are shown in figure 7.3. Seven stations (A-G) had a standard configuration, meaning all four antennas pointing down. Two stations (X and Y) were considered cosmic ray stations. Station X had two antennas pointing up at an angle of 45° relative to the surface in direction North and West, respectively, while the other two LPDAs were pointing straight down. Station Y had all four antennas pointing straight up. Station Z also has a special configuration and is called *Horizontal Cosmic Ray* station (HCR). It is devoted to detect showers

---

[2]This station (X) is one of two so called *cosmic ray stations* in season 2016/2017, see illustration II. The antennas are pointing up at 45° relative to the surface. More details regarding station X are given in section 7.1.
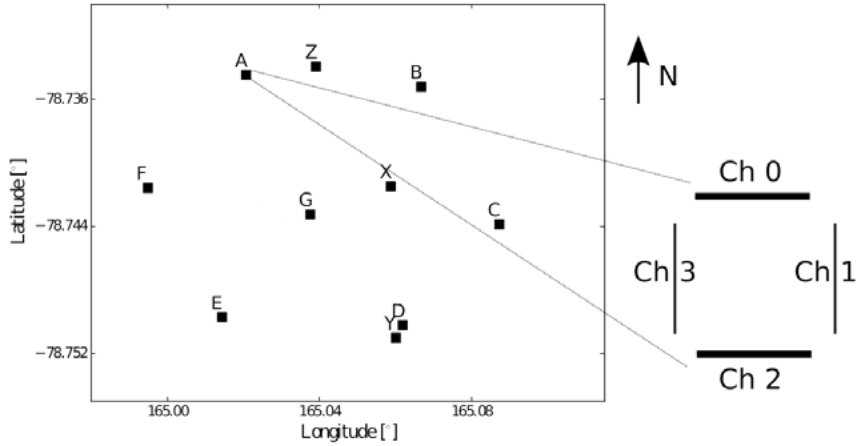
Figure 7.3. The detector layout in the season 2016/2017. Indicated with the squares and the zoom out of station A are also the LPDA positions, which are arranged in a square with 6 m distance between two pairs. The pairs are placed to be parallel with North-South (ch0 & ch2) and East-West directions (ch1 & ch3), where North points up. This means that the northern and southern antennas have their tines parallel to the East-West line and accordingly the tines of the Eastern and Western LPDAs are aligned with the North-South line.

from Earth-skimming neutrinos. Therefore, all four LPDAs are mounted on the station towers above the snow surface. The antennas are pointing in direction of Mount Discovery[3] with the tines perpendicular and parallel to the ground accounting for horizontal and vertical polarization respectively. When a τ-neutrino interacts with the mountain it would generate a tau lepton τ. The τ which escapes the rock decays in air and this leads to an air shower. The radio contribution of the air shower[4] can be detected as indicated in figure 7.4.

In the 2017/2018 season, station Y became the first station with four upward and four dipoles. Station Z was extended with two additional towers, resulting in 8 LPDAs pointing at Mount Discovery in total. Furthermore, one AR-IANNA station was deployed at the South Pole in order to investigate the suitability of the location and for performing signal propagation tests. In the

---

[3]Mount Discovery is visible in the background of illustration II.
[4]The radio contribution of an air shower is partly caused by the Askaryan effect but is mainly dominated by the charge separation caused by the Earths magnetic field.
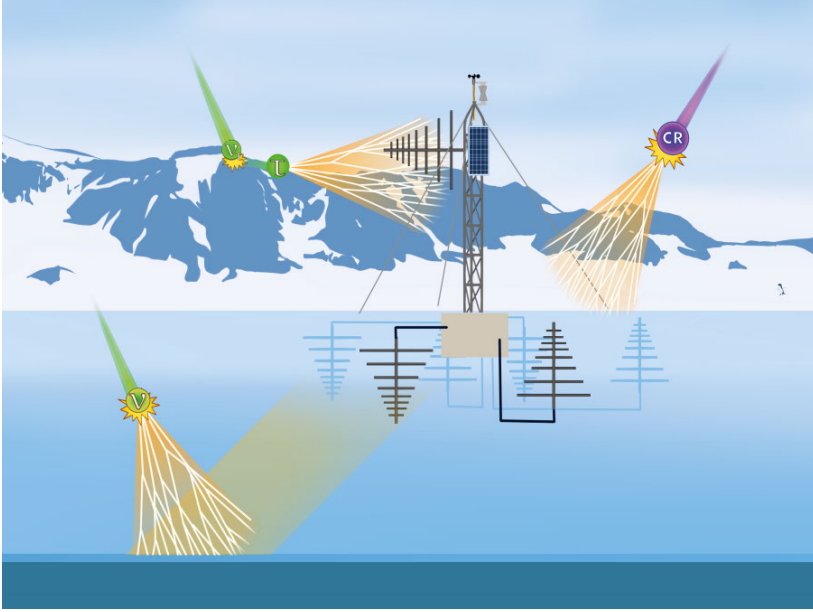
Figure 7.4. Different configurations of ARIANNA are sketched in one station. Radio signals from neutrinos interacting with the ice, and bouncing off the ice/water interface will be observed with downward-facing LPDAs. CRs are detected with upward-facing antennas, and Earth skimming v_τ could be discovered with LPDAs facing the mountain. The solar panel, the wind generator, and the electronics box are also shown. This illustration was designed by Savannah Rose Shively (UCI Irvine) for the ARIANNA collaboration.

2018/2019 season the LPDAs of station X were repositioned and now all four antennas are pointing up. Station C was decommissioned. However, an additional station was deployed at the South Pole. The two South Pole stations have eight channels each. One has four downward pointing LPDAs and four dipoles and the second station has four downward pointing LPDAs, two upward LPDAs and two dipoles. The analyses described in this thesis were performed with the 2016/2017 HRA setup.

7.2 How to Detect Neutrinos with ARIANNA?

In order to answer this question we need to understand how the Askaryan effect works and how ARIANNA is arranged to take advantage of this effect.

7.2.1 The Askaryan Effect

Similar to the phenomenon of Cherenkov radiation, which is used in IceCube and was described in section 1.5, the Askaryan effect describes the coherent emission of radio waves from particle showers developing in a dielectric medium. This effect was suggested by Gurgen Askaryan in 1961 [51, 52] and was later named after him. It has been observed in silica sand [186], rock salt [115] and ice [114] at the Stanford Linear Accelerator Center (SLAC). These targets were irradiated with beams containing billions of highly energetic electrons ($\sim 28\,\mathrm{GeV}$). The energy, frequency and angular profiles of the coherent radio emission were measured.

In case of a neutrino interacting with ice, a particle shower develops with an electromagnetic and hadronic component. The electromagnetic component contains electrons and positrons and as the shower develops, a negative charge excess of about 20% arises. The reason is that atomic electrons are drawn into the shower by a combination of Compton scattering and the production of δ electrons while positrons are absorbed when they become slow enough. The traveling charge excess leads to the emission of a cone of coherent radio or microwave radiation [51, 52, 53]. The charge excess scales linearly with the shower energy, while the radiated power P_{RF}, scales with the square of the charge excess N, and the square of the primary particle energy: $P_{RF} \propto N^2 \propto E_{prim}^2$. The radio emission is characterized by coherence, broadband frequencies and radial polarization.

7.2.2 Why Radio and not Optical?

The advantage for neutrino detection of using the radio frequency spectrum rather than the optical spectrum is that the attenuation length is longer, which means that the instrumentation of very large detector volumes becomes economically feasible. The attenuation length ranges between $\sim 300\,\mathrm{m}$ and $\sim 500\,\mathrm{m}$ for the relevant frequency range (between $\sim 100\,\mathrm{MHz}$ and $\sim 1\,\mathrm{GHz}$) in the Ross Ice Shelf [58], comparable to the average thickness of the ice shelf. The attenuation length depends on the frequency of the radio waves and also on the density and temperature of the medium. That is the reason why even longer attenuation lengths are measured at the South Pole, notably $1450\,\mathrm{m}$ at a frequency of $380\,\mathrm{MHz}$ at $-50\,^{\circ}\mathrm{C}$ [64]. Hence, radio waves can travel several kilometers and still be detectable as opposed to Cherenkov photons which at the South Pole are absorbed within less than $200\,\mathrm{m}$. Therefore, each antenna

station can monitor a large volume of ice and still be efficient in detecting EHE neutrinos. A disadvantage compared to optical detection is that the ambient thermal background noise is quite large. Therefore, the threshold energy a neutrino signal needs to exceed the background is rather high, of the order PeV. In ARIANNA, thermal noise is caused by random electron movement within the ice. Furthermore, thermal noise fluctuations in the amplifier cannot be avoided and are therefore also considered as thermal background. The anthropogenic noise caused by e.g. air planes or naturally caused radiation (auroras, Galactic plane,...) are not considered important for the neutrino energy threshold.

7.2.3 The ARIANNA Neutrino Detection Concept

The detection of EHE neutrinos is difficult partly because the predicted interaction rate is less than one neutrino per century per cubic kilometer. ARIANNA relies on the signature of the neutrino interaction in the ice due to the Askaryan effect. When a neutrino interacts with the ice it generates a short[5], broadband radio-frequency pulse. The signal will propagate and eventually reach the ice/water interface and reflect back to the surface, where the ARIANNA stations are able to detect it, see figure 7.1. Due to the smoothness of the interface the coherent and linearly polarized signal will preserve its polarization, which allows for the reconstruction of the neutrino interaction vertex from the direction of the incoming radio waves. ARIANNA has proven in ice studies to be sensitive to radio signals reflected from the ice/water interface [174]. ARIANNA is also able to detect direct signals, if the neutrino arrival direction is close to the horizon.

ARIANNA is designed to operate in a frequency range between 0.1 GHz and 1 GHz, since the high frequency components of an event (1 GHz - 5 GHz) are quickly absorbed by the ice. LPDA antennas are used in order to observe the linearly polarized signals in this frequency range. The lower frequency boundary is determined by noise, notably due to Milky Way radiation and by the dimensions of the antenna which would need to increase dramatically for lower frequencies.

7.2.4 Ice Properties

The Ross Ice Shelf is the biggest ice shelf in the world and sits on top of the Ross Sea. The thickness of the ice shelf varies between 300 m and 800 m. At the ARIANNA site, the shelf thickness was measured in four different seasons resulting in an average of 576 m $\pm$ 8 m [199]. The top $\sim$ 75 m are *firn* (packed

---

[5]The simulation of a 1 PeV shows a pulse of $O(1)$ns [46]. This pulse is a superposition of various frequencies.

snow), which transitions to ice with depth. The shelf provides a large amount of target material for the EHE neutrinos to interact with. Below the ice, there is the Antarctic ocean.

To model the propagation of the expected Askaryan pulse, measurements of the polarization, the vertical attenuation length[6] and the reflection coefficient over the range from the desired frequencies (0.1 GHz to 1 GHz) were performed [127]. The measurements were made using a transmitter antenna (Tx) to emit a signal through the ice, let it bounce off the ice/water interface and return back to the surface to be detected by the receiver antenna (Rx). Depending on the measured property, different antennas and configurations of the Tx/Rx setup were used. The returning pulse arrived at a time consistent with traveling twice the thickness of the ice and the absorption could be determined from the amplitude relation of the emitted and the observed pulse. These reflection tests are referred to as *bounce tests* [127, 58].

The results show a vertical attenuation length between 300 m and 500 m for frequencies between 75 MHz and 1.25 GHz [58]. The polarization was found to be largely preserved for frequencies between 100 MHz and 450 MHz. Above 450 MHz it is believed that not enough power was transmitted over the path length to observe the cross-polarized signal above the thermal noise threshold. Therefore, the polarization could not be measured reliably. The obtained reflection coefficient of the ice/water interface was consistent with that for a perfect mirror [172, 127]. No evidence of brine layers[7] was found when performing radio reflection tests [127]. The area where HRA is located was searched beforehand for crevasses and none were found.

While properties in the main volume of the ice at the Ross Shelf are well understood, propagation at shallow depths is more complex and measurements are needed for improved characterization. This thesis describes in chapter 8 the results from such measurements of propagation close to the surface.

7.3 The ARIANNA Detector Hardware

ARIANNA is currently powered by solar panels and cold-resistant batteries (LiFePO$_4$), which allow a run time during the Antarctic summer from sunrise (mid-September) until sunset (mid-April) [6]. The power consumption of a station is about 4 W [151]. The configuration of and data-transfer to and

---

[6]We differentiate between vertical and horizontal attenuation length, because in this thesis unexpected results regarding the horizontal attenuation length will be presented. The vertical attenuation length refers to the length previously determined in reflection or bounce tests.

[7]Brine could interfere with the radio signals due to the different density and permittivity, compared to the surrounding firn.

from the stations takes place in two different ways, both allowing real-time communication: either over long-range wifi via a relay station on the nearby Mount Discovery or by using the Iridium satellite network via *Short Burst Data* (SBD) messages [65]. For data-transfer to a server in the United States the stations must enter a communication window, during which data-taking is stopped. The stations are usually configured to communicate every half-hour and the communications window lasts a couple of minutes.

7.3.1 The LPDA Antenna
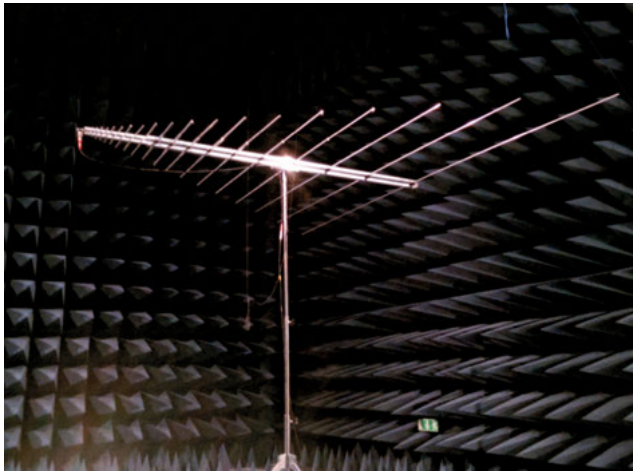
Figure 7.5. LPDA antenna used for the ARIANNA experiment in the anechoic chamber of Uppsala University.

The essential instrument for radio detection is the antenna. ARIANNA uses high-gain, linearly polarized LPDA antennas which are suitable for frequencies between 100 MHz and 1300 MHz [84] and have an excellent response between 100 MHz and 900 MHz. The boom length of the LPDA is 1.4 m, the maximum element length is 1.3 m and the minimum element length is 7.2 cm. The gain of the antennas was measured at Uppsala University to be between 6 dB and 13 dB, depending on frequency [42]. Figure 7.6 shows the relative variation of the radiated power of a LPDA antenna versus the azimuthal angle. The LPDAs are primarily sensitive to linearly polarized signals parallel to the antenna tines and have a 50 Ω impedance and a *Voltage Standing Wave Ratio* (VSWR) of 2:1 or better, also depending on the frequency range. The VSWR describes to what degree a standing wave is produced in the antenna due to reflections, and can therefore be used as a measure of the quality of the antenna for any given frequency.
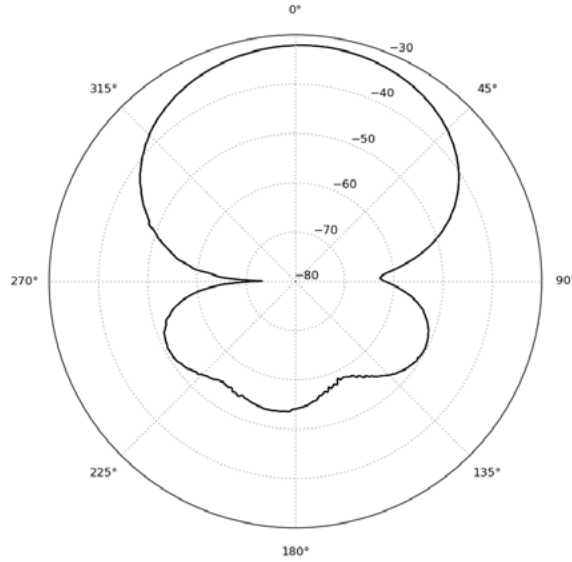
Figure 7.6. This is a polar plot of the relative power radiation pattern at 250 MHz of an ARIANNA LPDA antenna in the E-plane. The negative numbers reaching from the center of the plot outwards represent the power in dB. For a linearly polarized antenna the E-plane, which contains the electrical field vector, depends on the position of the transmitter and receiver antenna. In this measurement the E-plane of the LPDA was in horizontal position as shown in figure 7.5. The LPDAs nose was positioned to point at the transmitter antenna (0°) and then the LPDA was rotated from 0° to 360°. The transmitter was an LPDA optimized for frequencies between 200 MHz and 2 GHz and the receiver antenna was an ARIANNA LPDA antenna . The received power is represented by the black line. The direction of maximum radiation is at 0 degrees which corresponds to the nose of the antenna, as expected. It is also visible that the LPDA is sensitive to radiation arriving from the front and sides ($< \sim 60°$ and $> \sim 300°$) due to the broad *main lobe*. The three *back lobes* show less received power by ~ 20 dB. The asymmetric features are due to the binning of the data points (feature at 270°) and imperfections in the antenna (no antenna is 100% symmetric). This measurement was performed in the anechoic chamber at Uppsala University.

It is defined by the following formula:

$$VSWR = \frac{1+\Gamma}{1-\Gamma},\tag{7.1}$$

where Γ is the reflection coefficient, which describes the power reflected from the antenna. The smaller the VSWR, the better the antenna is matched to the

113

transmission line[8] and the more power is delivered to the antenna. The smallest VSWR corresponds to 1.0 and represents the ideal case when no power is reflected from the antenna. An antenna with a VSWR value around or below 2 is considered to be of good quality. Since the index of refraction in firn and ice is different from that in air, an antenna buried in these elements has a different frequency response and impedance, which normally leads to an impedance mismatch[9] with the preamplifier it is connected to. Measurements of the LPDA have been performed to study this effect and shown that the VSWR is always less than 2.5 in the relevant frequency range [199].

For each station, the antennas are connected to the electronics box and are buried just below the snow surface. In the short term this provides easy access for updates and repair if needed. However, due to the accumulation of snow, the antennas are each year about 0.7 m deeper below the surface.

The polarization of an electromagnetic field refers to the direction of the electric component of the wave and is therefore measured in the E-plane of the antenna, see figure 7.6 for the E-plane radiation pattern[10]. Considering the setup of an ARIANNA station (see figure 7.3) we can describe the signal polarization with three components, vertical, East-West (EW) and North-South (NS). The horizontal components (EW and NS) are measured with the LPDA pair with the corresponding orientation of the tines. The vertical component of the polarization can be determined from the angle of incidence with respect to the antennas[11].

For the monitoring of a station, a fifth LPDA (a so called "heartbeat" antenna) is used. When a new station is built the heartbeat LPDA is placed horizontally beneath the snow surface at a $45°$ angle with respect to the four other antennas. The heartbeat antenna sends out a calibrated pulse at regular intervals, which is received by the station antennas. With this method it can be determined if the station performs as expected.

---

[8]A transmission line is a cable connecting the antenna to a receiver or transmitter. Here we assume that the receiver or transmitter are matched to the transmission line.

[9]In air the impedance of the preamplifier is matched with the antenna. Although it is possible to modify the impedance of the preamplifier to match the antenna impedance in firn, it is a temporary solution. The stations are buried gradually deeper in the firn and hence the index of refraction increases with depth.

[10]The H-plane contains the magnetic field vector, and the receiver antenna needs to be rotated by $90°$ along the centerline.

[11]Recently suggested improved station designs include direct measurement of the vertical polarization by adding either dipoles or LPDAs with tines in the vertical plane.

7.3.2 Electronics Box

The electronics box contains all the necessary components to control the station. This includes an MBED micro-controller [164], batteries, a *Battery Management Unit* (BMU), an AFAR wireless system [34], an Iridium SBD modem, amplifiers and a *Data-AcQuisition* board (DAQ). The MBED micro-controller manages the DAQ, storage systems, communications and monitors temperature, voltage and power consumption. The BMU regulates the charging and discharging of the batteries, which are connected to the solar panels. The AFAR is a long-range wireless system and used for communication. The SBD modem which communicates over the Iridium satellite system is used as a backup method of communication. The amplifiers, the DAQ board and the trigger system will be discussed in more detail below.

Amplifiers
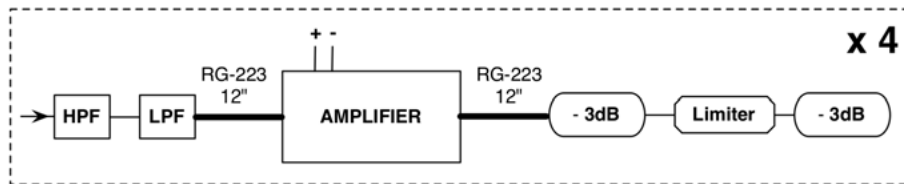
Figure 7.7. The schematic view of an ARIANNA amplifier system including filters attenuators and limiter. Credit: [199].

A schematic view of an ARIANNA amplifier system is shown in figure 7.7. A signal that is picked up by an antenna is passed through a 100 MHz high-pass and a 1 GHz low-pass filter to ensure signal measurement in the desired frequency range, and therefore reducing background. The amplifiers are broadband from 50 MHz to 1 GHz with an average gain of about 65 dB and they require low power, have low noise and run on 3.3 V. In order to prevent coupling and feedback, each amplifier is shielded individually. After the signal is amplified, it is sent through 3 dB attenuators and a limiter, which limits the amplitude to 1 V in order to prevent damage to the data-acquisition electronics. In total four amplifiers are mounted in every electronics box, one for each antenna.

Data Acquisition

The data-acquisition boards for the ARIANNA stations hold custom designed SST (*Synchronous Sampling and Triggering*) chips, which sample data on four channels at 2 Gsamples/s (HRA) or 1 Gsample/s (station X, Y, Z) into ring-buffers of 256 samples [152]. The absolute timing is based on the Iridium network and accurate to the order of a few microseconds. There is no time-synchronization between the stations since they are independent. After amplification, each LPDA is connected to one channel. The DAQ boards contain an

embedded *MBED micro-controller*, which can be remotely programmed and is capable of performing simple online analyses. Additionally to the real-time data transfer within a communication window the data is stored on a local 32 GB solid-state disk. The reconfiguration of the DAQ system during its normal operation is performed by adding a configuration file to a queue on the communication server. As soon as the station enters the next communication window, the file is transmitted and applied to the station. The configuration file contains, among other specifications, parameters to control the trigger thresholds and logic, the time between forced triggers, if and how to transmit data, the frequency between communication windows and the parameters for the application of the level 1 (L1) trigger.

Trigger System

The trigger system is set to a two of four channel majority logic, which means that at least two out of four antennas must receive a signal. The stations have a trigger threshold of about 100 mV. The signal for each channel is then read out and digitalized by an *analog-to-digital converter* (ADC). The received signal is bi-polar, meaning that it produces positive and negative voltages. Individual low and high voltage thresholds are set for each channel and the waveform has to exceed both within 5 ns in order for the channel to trigger. To trigger the system, two channels have to trigger within 32 ns. Details regarding the trigger system can be found in [178].

Typical background trigger rates are below 10^{-2} Hz. The only relevant anthropogenic background signals are narrow-band radio transmitters, namely a radio communication frequency at 140 MHz, air-traffic control at 220 MHz and a search and rescue channel at 400 MHz. The signals from any of these channels trigger the ARIANNA DAQ when they are in use, which is typically the case only for a few minutes per day. These signals are sinusoidal and maximize the trigger rate when they are active.

In order to suppress the events from this background, the (L1) trigger has been designed. Whenever the power in one frequency bin is higher than an adjustable fraction of typically 0.3 of the remaining spectrum, the event will be vetoed. The L1 trigger retains more than 99.99% of simulated neutrino signals. To collect background data for noise subtraction a *forced trigger* is applied every couple of minutes, depending on the configuration.

7.4 Directional Reconstruction

The reconstruction of the arrival direction of a neutrino signal is possible by using all antennas within a station. The positions of the LPDAs have to be well known and they are measured with a relative accuracy of about 10 cm for HRA [60]. The time the signals need to travel through the cables is equal for every

antenna with an accuracy in the sub-nanosecond range [65]. With this timing precision, the direction can be reconstructed accurately from cross correlation of the signals in the four antennas. The distance between two parallel antennas is 6 m. Cross-correlation is a method to compare the similarity of two signals with each other. In ARIANNA the signals received in two parallel downward pointing LPDAs are compared by sliding one waveform over the other until the *Pearson Correlation Coefficient* reaches a maximum value. The time delay between the two antennas reveals the arriving direction of the signal. For signals coming from the forward direction[12] the angular reconstruction has been shown to have a resolution between $0.14°$ and $0.17°$ [199].

---

[12]In this context forward direction means from below, towards the noses of the LPDAs.

8. Horizontal Propagation of Radio Waves in Firn and Ice

The term *Horizontal Propagation* (HP) describes the phenomenon of radio waves traveling horizontally through firn. To understand why this effect is important it is crucial to describe the predicted propagation of radio waves in firn.

8.1 The Shadowing Effect in Radio Wave Propagation
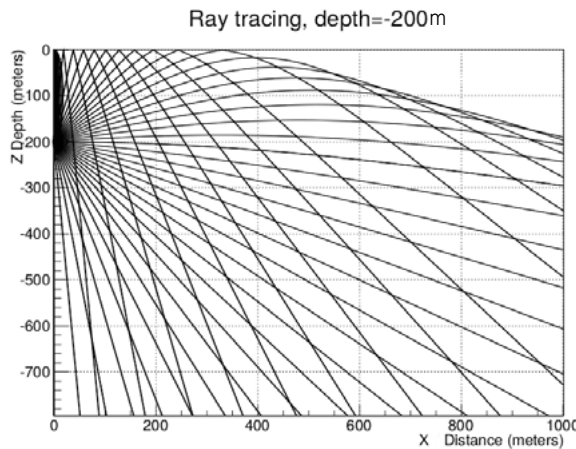
Figure 8.1. Simulation of individual rays emitted from a radio transmitter at the South Pole at a vertical depth of 200 m. The ray tracing in air above the firn is not simulated, and the simulation does not account for differences in power between partially and totally reflected rays. Adapted from paper [62].

At the surface, firn is lightly packed snow, but with depth the density increases until it reaches the density of ice ($\rho_{ice} = 0.9167$ g/cm^3). This leads to an index of refraction n increasing with depth. The relation between density ρ and n is described by the Schytt equation [205]:

$$n = 1 + 0.78 \cdot \frac{\rho}{\rho_{ice}}, \tag{8.1}$$

Laboratory measurements on solid glacier ice resulted in a refractive index of $n = 1.78$ [183], yielding the factor 0.78 in equation 8.1. Due to this gradient

in the refractive index, radio waves traveling through the firn will bend down. This leads to the existence of zones in which the rays should not be observable according to geometric optics. The effect is referred to as *shadowing* and these zones are correspondingly called *shadow zones*.

Figure 8.1 shows simulated radio waves traced from a transmitter at 200 m depth through the South Pole firn and ice assuming a smoothly varying *n* profile with depth *z*. This simulation illustrates the ray bending of radio waves in the simplest case and shows how the formation of shadow zones develops. The transition from firn to ice starts at the South Pole around 160 m, leading to a nearly constant refractive index below that depth. Due to the assumption of a smooth profile the transition is not distinct. Using Fermat's least-time principle and the principle of least action it can be shown that the shortest travel time between two points in the firn results in a parabolic path. If the velocity vector points down the rays have a straight path and if it is pointing up they experience a slight curvature in the trajectory after being reflected at the firn surface. Nearly horizontally emitted rays also show a curved trajectory. This behavior creates the shadow zone that can be seen in the upper right corner. The complete derivation of the formalism is described in [[62].
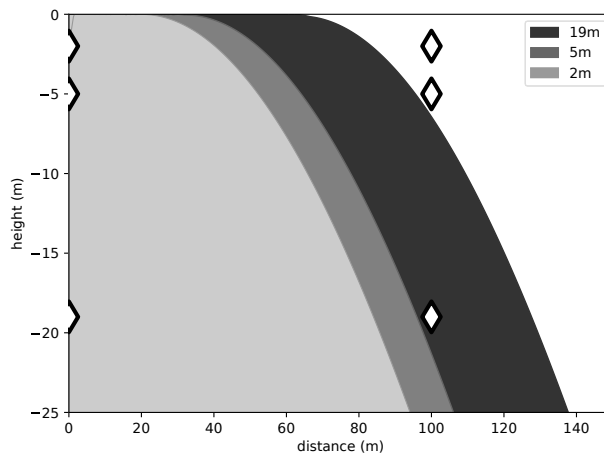
Figure 8.2. The shadowing effect at the Ross Ice Shelf. The diamonds represent different positions within the firn of the transmitter antenna (left) and the receiver antenna (right). The shaded areas show the regions below horizon visible to a receiver, where the light gray region indicates the horizon if the transmitter is at 2 m depth, the dark gray region represents the horizon with the transmitter at 5 m depth, and the black one shows it for 19 m depth. Adapted from [62].

Figure 8.2 shows the shadow zones calculated for the Moore's Bay site where ARIANNA is located. The transition from firn to ice is around 75 m at this

location. The receivers (right diamonds) at 2 m and 5 m depth and at a horizontal distance of 100 m from the transmitters (left diamonds) should not be able to receive any signals, independent of the transmitter depth (2 m, 5 m or 19 m). The receiver at 19 m should be able to receive only signals from the transmitter at 19 m, and not from the transmitters above. These calculations represent what we expected to observe during the ice studies, which will be described in the next sections in detail.

8.2 Measurements between Dipoles

The measurements between dipoles are the most basic ice studies which were performed, yet we will see that these essential tests lead to unexpected observations.

8.2.1 Experimental Setup
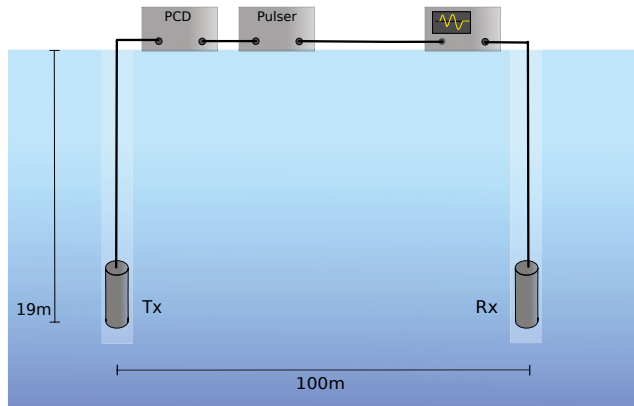
Figure 8.3. The experimental setup is shown schematically. The figure is not to scale.

In order to study the ice properties, two boreholes of 20 m depth each, with a distance of 100 m were drilled into the firn, see figure 8.3. Due to snow accumulating in the boreholes the lowest measurements were performed at 19 m. The transmitting antenna (Tx) and receiving antenna (Rx) were "fat dipoles" previously used by the RICE experiment. The dipoles are sensitive to frequencies between 200 MHz and 1000 MHz [147].

The signals generated by a *Pockels Cell Driver* (PCD) have a high amplitude (5 kV) and a short duration (20 ns). Due to the large power generated the signal is attenuated by 60 dB between the output of the PCD and the connected Tx.

The PCD is also connected to the input of a BNC Model 555 pulser, further referred to as pulser. The output of the pulser is connected to the external trigger of an oscilloscope. The pulser is responsible for triggering the PCD and oscilloscope simultaneously. The oscilloscope is connected to the receiver dipole in order to monitor the signals. Due to the connection between the pulser and the oscilloscope absolute timing was achieved. In order to calculate the absolute travel time of the pulse the delay of the complete setup was measured resulting in a *system time* of 268 ns. Throughout the measurements, 100 MHz high-pass filters were used.

To ensure that signals were not transmitted accidentally by the PCD itself, the transmitting antenna was disconnected at the PCD and an 50 Ω terminator was connected instead. No signals were measured. Furthermore, signal leakage from the cables was tested by disconnecting the Tx from the cables and measuring the signals emitted from the cables with the Rx. The cable pulses had different properties than the pulses transmitted by the dipole antenna. For all following analyses we selected pulses where the high-pass filter was connected between the PCD and the cable to the transmitter dipole. Furthermore, we present all waveforms with their absolute travel time.

8.2.2 Observations at Moore's Bay
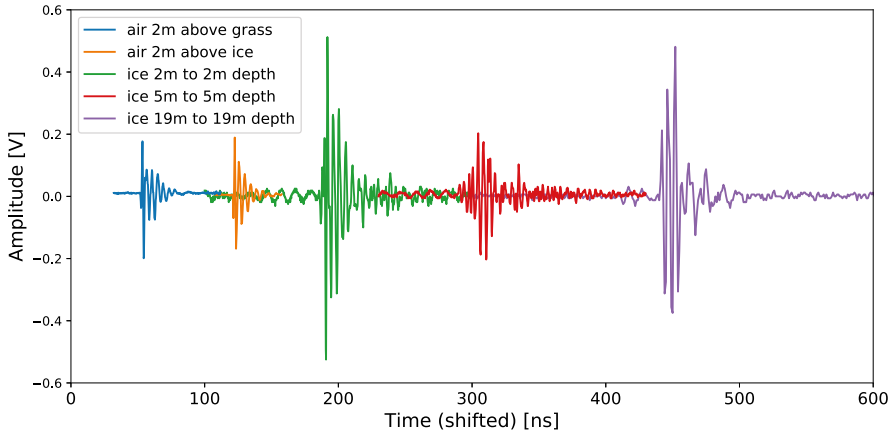
Figure 8.4. Comparison of pulses from transmitter dipole to receiver dipole in air and in firn at different symmetric depths at a 100 m distance. The pulses have been shifted in time for comparison. The above ice measurements were performed at Moore's Bay (orange) at 1.5 m height and those above grass were taken in a park (blue) in Irvine, California. In the park the conditions were good, flat area with dry ground, little conductivity and little high vegetation. The signals in firn (green, red) are horizontally propagating signals at different depths. The violate pulse lies within the classically allowed detection region. Figure credit: [62].

The prediction that for a horizontal distance of 100 m signals should be visible only when Tx and Rx were at 19 m depth (for the indicated test cases) was tested at Moore's Bay. The setup used is shown in figure 8.3. The observations show signal propagation for all configurations between the two dipoles. That means that the receivers at 2 m and 5 m depth, which are located in the shadow zone for the transmitters at the same depth, received signals. Figure 8.4 shows a comparison between the observations at Moore's Bay and a park in California. The comparison between the pulses above ground resulted in similar signal strength at the park, above grass (blue) and at Moore's Bay, above the firn (orange). The pulses above the firn will be further referred to as *air-pulses*. The reason why the pulse strength differs between the signals within the firn (green:2 m, red:5 m, violet:19 m) is probably due to multi-path effects which lead to constructive or destructive interference. As already mentioned only the violet signal should be observable according to the shadowing effect. However, as we will discuss later, the firn pulses shown in figure 8.4 have similar properties, regardless of if they are located in the shadow zone. Hence, we define horizontal propagation signals as pulses which reach the receiver in a time compatible with a direct path between Tx and Rx in firn. Another visible effect of these signals is the broadening of the waveform, which is likely due to interference and dispersion [62], which will be further discussed in section 8.3.1.

8.3 Horizontal Propagation of Radio Waves in a Medium with Varying Refractive Index

The unexpected observation of pulses in the shadow zone indicates that the model using a smooth gradient profile in the firn is not sufficient. In reality the firn shows deviations from the smooth profile, which can explain the HP effects. Over-densities and under-densities in the firn can arise due to yearly varying snow accumulation, sintering and in extreme warm periods even melting.

This phenomenon is demonstrated in figure 8.5 representing a detailed measurement of the density variation in the firn at depths between 0 m and ~ 170 m in southern Greenland[1]. Similar mechanisms resulting in density variations in the firn are also active in Antarctica. The conditions at the location in southern Greenland are similar to the ones at Moore's Bay. In the central parts of the Greenland ice sheet, the temperatures usually never get high enough to melt the top layer but they get high enough to sinter the snow, causing density variations. New layers of snow accumulate and the snow turns into firn

---

[1]Unfortunately, an equally extended measurement was not found for Moore's Bay, South Pole or Antarctica.
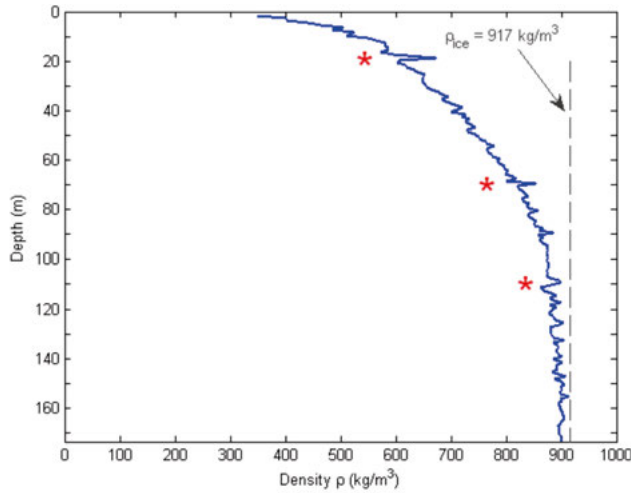
Figure 8.5. An illustration of rapid variations in a density profile. This density profile was measured from ice cores in southern Greenland [78]. The red asterisks indicate layers where the snow melted. The dashed line represents the density of ice.

when it gets buried under the new layers. The density increases with depth due to compression from the weight of the mass of snow above until it reaches the density of ice. When the firn reaches a density of about $0.8 \, \mathrm{g \, cm^{-3}}$ the connected air passages begin to close off and form separate air bubbles. At this stage the firn becomes impermeable to air flow. This point is defined as the transition from firn to ice. The firn cannot be further compressed and the ice density of $0.917 \, \mathrm{g \, cm^{-3}}$, at which the ice cannot be further compressed, is reached by compression of the air bubbles [131].

The depth at which the transition takes place depends on the temperature and snow accumulation rate of the location. As an example, figure 8.6 shows the detailed density measurements in the region of the transition depth at the Byrd Surface Camp in Antarctica[2]. The data shows variations in the layers at these depths and demonstrates that there is a several meters deep transition zone. The layers were tested for permeability to air to investigate when the air bubbles are closed off. The black squares show layers of ice and the white squares show layers of firn where air can still flow. At the Byrd Surface Camp the transition takes place at around 75 m [131], at Moores Bay on the Ross Ice Shelf the depth is also about 75 m, while at the South Pole it is about 160 m [4].

---

[2]No measurements showing the detailed transition region between firn and ice were found for Moore's Bay or South Pole.
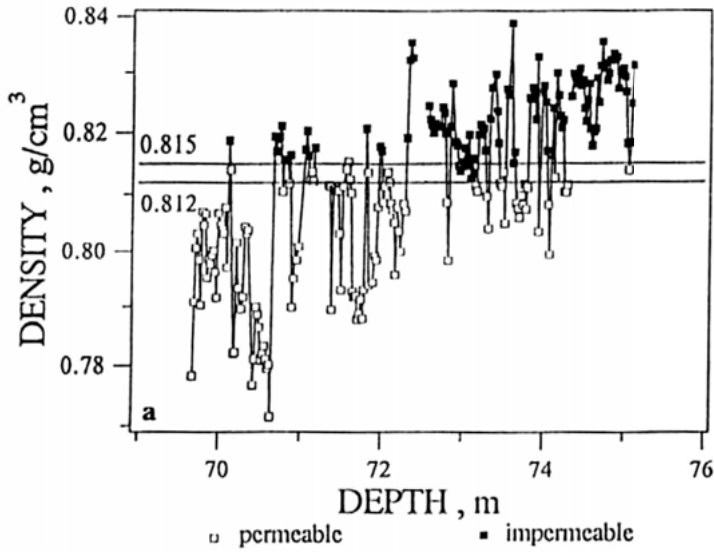
Figure 8.6. The density variations in the transition zone from firn to ice in dependency of depth are presented. These measurements were made at the Byrd Surface Camp, Antarctica. The transition zone is indicated by horizontal lines and lies between $0.812\,\mathrm{g\,cm^{-3}}$ and $0.815\,\mathrm{g\,cm^{-3}}$ at depths between $\sim 70\,\mathrm{m}$ and $\sim 75\,\mathrm{m}$. The squares at the peak values show the permeability to air of the respective layer, where white represents the permeable and black is for the impermeable layers [158].

Inhomogeneities in the firn influence correspondingly the index of refraction and therefore also the ray speed. Radio waves can get trapped by total internal reflections between under-density layers with a lower n and therefore a higher ray speed and can travel long distances. Groups of such layers will increase the effect of horizontal propagation [62]. Horizontal propagation can be compared to the principle behind optical fibers, where the electromagnetic waves are guided between under-density layers of firn instead of the fiber walls.

The theory derived in [62] is a starting point to understand the behavior of radio waves in the firn, but it can not explain all effects that have been observed. After discussing the observation of horizontal propagation within the community in the radio-astroparticle field it turned out that RICE [62], ARA and GNO, all saw similar signals after reanalyzing old data. The observations were initially disregarded. Recently GNO published a similar study, which was performed in 2013 at the Greenland Summit station and analyzed using extensive numerical modeling of the propagation with *Finite-Difference Time-Domain* (FDTD) simulation [91]. Three different models for depth-dependent firn profiles were used for the FDTD simulation. The timing and amplitude of the measured data was compared to the different simulated results. Within the uncertainties of the models, good agreement was found between measure-

ments and simulation regarding the signal travel times and waveform shapes. Also, a broadening of the observed pulses in the time domain was qualitatively reproduced. It is reasonable to believe that a similar numerical calculation could reproduce the results in [62]. The theory and modeling of the data as well as simulations are currently under development within the ARIANNA collaboration.

8.3.1 Interference
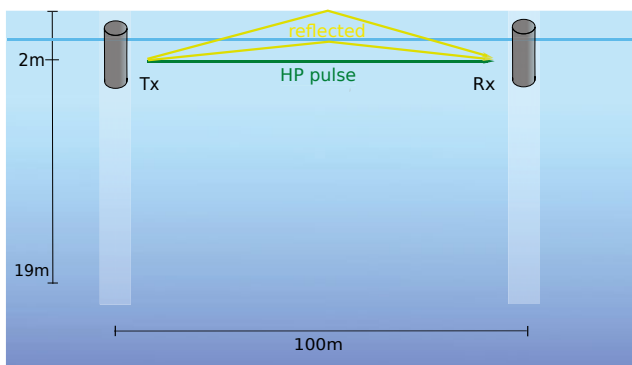
Figure 8.7. Schematic view of the three paths of interference at 2 m depth. The horizontally propagating signal (HP, green), a reflection off another firn layer and firn surface (yellow) are shown. The figure is not to scale.

Before going into the analyses of the measurements performed at Moore's Bay, we will discuss interference, because it is the most probable explanation for several observations. Figure 8.7 shows the same experimental setup as figure 8.3, but with the dipoles at 2 m depth. Additionally, it sketches possible interfering trajectories: the straight path from Tx to Rx (green) and paths going towards the firn/air interface or another firn layer, and being reflected (yellow). The pulses traveling along these paths have a time delay with respect to each other and will interfere constructively or destructively, depending on this time delay. In the ideal case the reflected pulses undergo total internal reflections before interfering at the receiver dipole. The radio pulse could reflect on any layer above or below Tx and Rx. Part of the pulse is likely also transmitted through the surface or the layers, depending on refractive index and angle of incidence. The lower firn, has a higher index of refraction, which makes pulses reflected by those layers slower.

When looking at the observations in figure 8.4 the amplitude of the green waveform, where Tx and Rx were at 2 m depth, is more than twice as high

as the amplitude of the air-pulses (blue and orange). The constructive interference of the HP pulse and several reflected pulses is likely the explanation for this observation. A full description of interference needs to take into account that the waves are still spherical when they interact with their close environment at inclined angles. A mathematical description of the reflection and transmission of spherical waves at an interface between two media with different refractive indices can be found in [209]. The far-field distance is the distance where a spherical wave front becomes a close approximation to the ideal planar phase front of a plane wave. For antennas physically larger than a half-wavelength of the radiation they emit, the far field distance r_{ff} is given by:

$$r_{ff} = \frac{2D^2}{\lambda},$$ (8.2)

where D represents the dimension of the antenna and λ is the wavelength. However the fat dipole is an electrically small antenna[3], meaning its dimensions are smaller than $\lambda/2$ for most emitted wavelengths. Hence this result may gives a too small far-field distance and the approximation

$$r_{ff} = 2\lambda = \frac{2c}{f}$$ (8.3)

is used instead [177], with c being the speed of light in vacuum and f is the frequency. For the frequency range important for the work within this thesis: $f = 150\,\text{MHz}$ - $250\,\text{MHz}$ (see section 8.8) the far-field distance results to 4 m - 2.5 m. Interference and the resulting amplitudes at different depths will be further discussed in section 8.4.2.

Another observation in figure 8.4 is that the air-pulses are shorter ($\sim$25 ns) than the waveforms within the firn ($\sim$50 ns with a tail above the noise level). When two pulses with a time shift between them interfere, the resulting waveform will have a longer duration than the waveforms of the separate pulses. The elongated structure of the received signals, compared to the emitted pulse in the time domain implies dispersion. Dispersion has the effect of stretching the signal in the time domain and by that reducing the amplitude[4]. Some dispersion effects are explained by the LPDA antenna response, which shows frequency and impact angle dependent group delays leading to dispersion [61, 42]. However, these effects are small compared to the time dispersion likely caused by the signals from one pulse taking different paths and arrive at the receiver with sufficient small time shifts, appearing as one stretched signal.

---

[3]The fat dipole has a length of 51.75 cm and an outer diameter of 7.62 cm.
[4]The amplitude reduction is not visible due to the interference effects.

8.4 Analyses of the Horizontal Propagation Pulses

Several analyses were performed to investigate the behavior of the observed pulses, and will be described in detail below.

8.4.1 Index of Refraction

Figure 8.8. A photograph of some cores retrieved from drilling the boreholes for the ice studies.

In order to perform the ice studies, two boreholes were drilled with an ice core drill and the cores were extracted, see figure 8.8. The volume and weight of the cores were measured and the density was determined. The core measurements are displayed in table 8.1. The index of refraction n was calculated using the Schytt equation 8.1 and deriving the density ρ from the measured mass m, length L and circumference C:

$$n_{density} = \frac{\rho}{0.9167} \cdot 0.78 + 1 = \frac{m}{V} \cdot \frac{0.78}{0.9167} + 1 = \frac{4\pi m}{LC^2} \cdot \frac{0.78}{0.9167} + 1 \quad (8.4)$$

The errors from the density measurements were estimated to be 5 mm for both the length and circumference. The uncertainties on the mass are neglected because the scale had a resolution of $\sim \pm 0.1$ g. The uncertainties were propagated according to the Gaussian error propagation. The uncertainties regarding the depth were estimated to be: 0.3 m.

In figure 8.9 the results (squares) were compared to the index of refraction determined by the timing measurements of the pulses between the boreholes at different depths when transmitter and receiver were at a symmetrical depth (circles), see table 8.2. The measurements resulting in a second value were taken on a different day. Due to absolute timing, the refractive index could
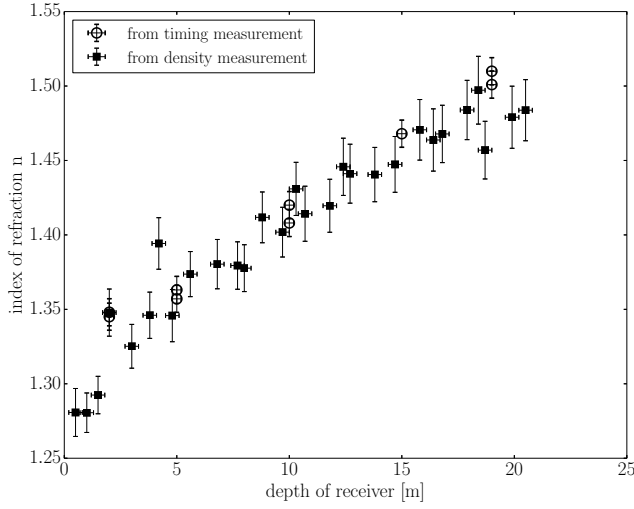
Figure 8.9. Comparison of the index of refraction n obtained from the density measurement while drilling the boreholes and the absolute time measurement while performing the pulse tests. The transmitter and receiver dipoles were lowered symmetrically, being always at the same depth when the measurements were taken. The density and timing measurement can be found in the tables 8.1 and 8.2 respectively.

simply be determined by:

$$n_{timeing} = \frac{ct}{r} \tag{8.5}$$

where c is the speed of light in vacuum, $r = 100\,\mathrm{m}$ is the distance between receiver and transmitter and t is the travel time of the pulse. The errors of the timing measurements are estimated to $\pm\ 3\,\mathrm{ns}$, because it is sometimes challenging to read off the exact starting position of the pulse. The distance does not have larger uncertainty than $0.1\,\mathrm{m}$. The errors regarding the dipole depth are estimated to be $0.2\,\mathrm{m}$. For the refractive index calculation the errors were also propagated with the Gaussian error propagation.

The data was further corrected for a systematic shift which was noticed when the setup was tested in air. The two dipoles were attached to bamboo sticks at $1.5\,\mathrm{m}$ hight and the rest of the setup remained the same as described in section 8.2.1. Instead of the expected refractive index of air $n_{air} = 1$, the measurement resulted in $n_{measured} = 1.016$, which indicates an instrumental systematic error. The *systematic delay* corresponds to $\delta t \approx 5\,\mathrm{ns}$.

8.4.2 Amplitudes of HP signals

Figure 8.10 shows the maximum amplitudes for the symmetrical measurements in dependence of depth. The amplitudes at $2\,\mathrm{m}$ are the highest indi-

Table 8.1. *Core measurements in dependency of their depth. Displayed are the weight m, length L and circumference C.*

depth [m]	m [g]	L [m]	C [m]
0.5	197	0.125	0.245
1.0	328	0.200	0.250
1.5	547	0.320	0.250
2.0	459	0.217	0.255
3.0	441	0.223	0.255
3.8	484	0.230	0.255
4.2	609	0.254	0.255
4.8	326	0.160	0.251
5.6	1065	0.465	0.256
6.8	613	0.265	0.255
7.7	773	0.335	0.255
8.0	886	0.395	0.252
8.8	969	0.390	0.254
9.7	892	0.365	0.255
10.3	964	0.365	0.256
10.7	589	0.232	0.256
11.8	791	0.310	0.255
12.4	759	0.280	0.255
12.7	617	0.230	0.255
13.8	1010	0.377	0.255
14.7	925	0.340	0.255
15.8	787	0.275	0.255
16.4	638	0.228	0.254
16.8	1138	0.400	0.255
17.9	1183	0.402	0.255
18.4	641	0.212	0.255
18.7	867	0.312	0.255
19.9	772	0.265	0.255
20.5	912	0.310	0.255

Table 8.2. *Dipole measurements at symmetrical depths of transmitter and receiver. These times are corrected with the systematic delay of $\delta t = 5$ ns.*

depth [m]	2	5	10	15	19
time [ns]	449	453	474	490	504
	450	455	470	-	501
amplitude [mV]	513	203	303	203	353
	556	197	309	-	359
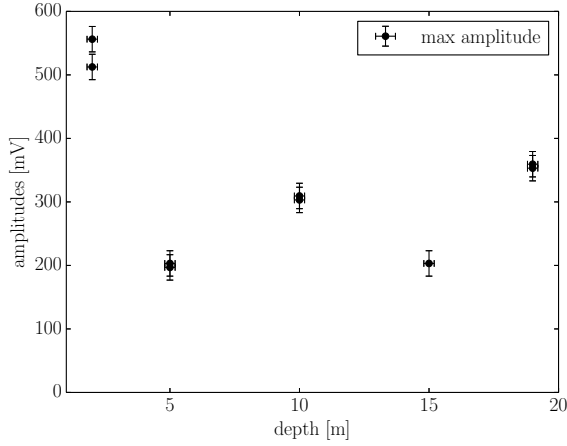
Figure 8.10. Maximum amplitude of the horizontal propagation pulses as a function of depth, when Tx and Rx were lowered symmetrically. The uncertainties are estimated to be $\pm$ 20 mV in amplitude and $\pm$ 0.2 m in depth.

cating constructive interference from several pulses. As also mentioned in section 8.3.1 these effects could be influenced by spherical waves interacting with their close environment. At 10 m and 19 m the amplitudes have higher values in comparison to the observations at 5 m and 15 m. However, even the lowest amplitudes measured in firn (at symmetrical depths) are about 200 mV, which is comparable to the amplitude observed in air, see figures 8.4 and 8.11. Note that the air-pulses also could be the result of two interfering signals, one with a direct flying path and one reflected off the grass or firn. The deeper the measurement was made, the higher is the probability for multi-path interference to occur, because more firn layers to be reflected on are added above the direct ray path. This might explain why deeper measurements are not likely to reach the same high amplitude as at 2 m depth. Below, in figure 8.14 an example of negative interference is shown. But first we estimate the geometrical conditions and time delays that would be needed for the seen interference.

We want to investigate the interference of the 2 m measurement closer. Assuming the two significant pulses which interfere are the horizontally propagating pulse and the reflection off the surface, we can calculate the time delay between the two signals, which results in t_{diff} =7.4 ns. For this calculation equation 8.5 was used, with the refractive index at 2 m, $n_{timing} = 1.35$ for the HP pulse and an average of $n = 1.29$ [128] in the upper firn and $n_{timing} = 1.35$ was taken for the reflected pulse: $n_{reflected} = 1.32$. The travel distance of the reflected pulse was determined by trigonometry taking the geometry from figure 8.7 into account:
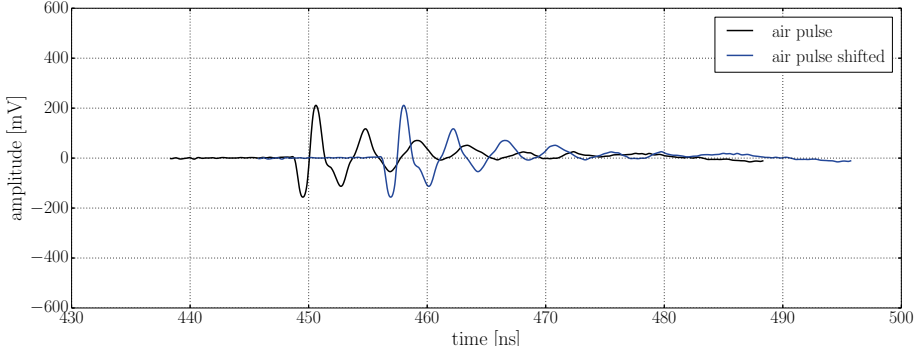
Figure 8.11. The air-pulse above ice is presented in black and the same pulse shifted by 7.4 ns in blue. The start of the pulses does not represent their absolute travel time, but the absolute flight time of the horizontally propagating pulse in the firn for later comparison.
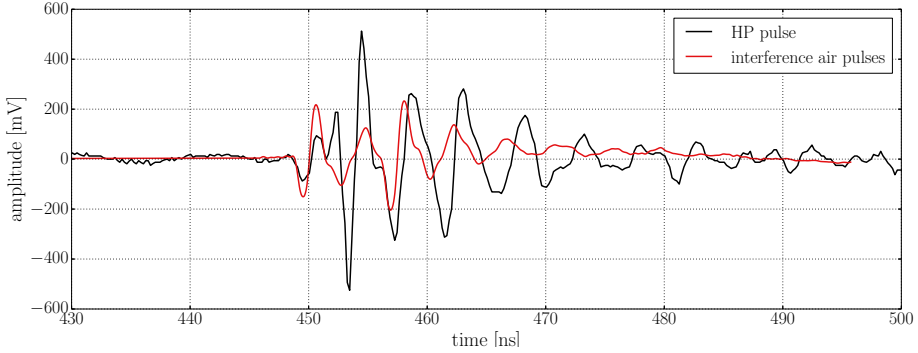
Figure 8.12. The black waveform is the horizontally propagating pulse where receiver and transmitter were 2 m deep in firn with absolute timing. The red signal is the interference of the two air waveforms from figure 8.11.

$$d = 2 \cdot \sqrt{(50\text{m})^2 + (2\text{m})^2} = 100.08\text{m} \qquad (8.6)$$

where the square root represents the path from transmitter to surface, and since we assume symmetry this way is doubled. Under these conditions the reflected pulse would arrive earlier ($t_{reflected} = 442$ ns) than the horizontal propagation signal ($t_{HP} = 449$ ns). The observations agree rather with the horizontal propagation arrival time as can be seen in figure 8.12. However, no proper ray tracing was applied[5] and these calculations are performed to make estimates of first order regarding the possible interference paths. To cross-check the result-

---

[5]Technically it would not even be possible to apply classical ray tracing because these signals lie within the shadow-zone.
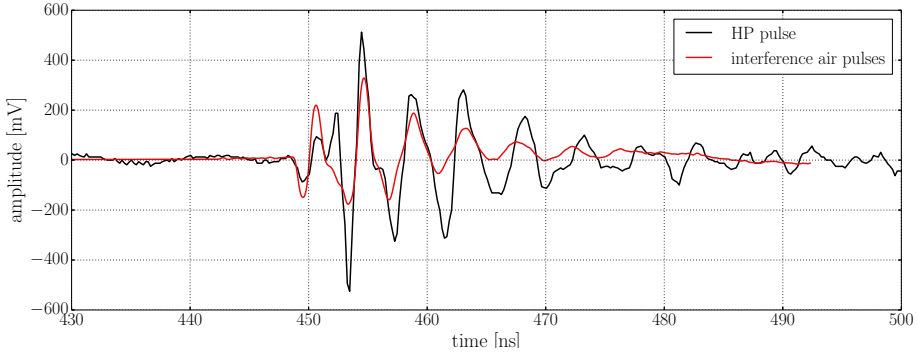
Figure 8.13. Same as figure 8.12, but the interfered air-pulses had a time difference of 4 ns, resulting into the red waveform above.

ing interference an air-pulse was used and shifted by t_{diff} as shown in figure 8.11. For this cross-check we assume that the signals in air and upper firn do not differ significantly. The result of the interference of these two waveforms can be viewed in figure 8.12 in red in comparison to the HP pulse at 2 m depth from figure 8.4. The interfered waveform shows a similar behavior as the horizontal propagation pulse in the beginning of the pulse (449 ns - 457 ns), but then an obvious time shift becomes visible. Furthermore, the two maximum peaks (at 453 ns and 465 ns) cannot be reproduced and the waveform shows destructive rather than constructive interference. This leads to the conclusion that the time delay between these two paths is too large to explain the observation by an interference of two signals propagating along the respective paths.

Assuming now that the reflected pulse was reflected off a firn layer[6] and arriving at the receiver with a time delay of 4 ns, the interfered pulse would look like in figure 8.13. Although the negative maximum peak still cannot be reproduced the positive maximum peak shows constructive interference. Overall the two waveforms show a better agreement and an obvious time shift starts at about 467 ns. As already mentioned, the received HP pulses are the result of several interferences, and which paths were taken is depending on the firn properties.

Besides the experiments where the two antennas were at symmetrical depths, also other measurements were performed where the transmitter dipole was at a fixed depth of 10 m and the receiver dipole was moved from 8 m to 12 m with 0.5 m steps. The measured signals looked similar to the signals obtained at symmetrical depths of Tx and Rx. The amplitudes of these measurements are shown in figure 8.14. We can observe how the amplitudes have their low-

---

[6]For this calculation no assumptions regarding the depth of the firn layer and the refractive index and the taken path were made.
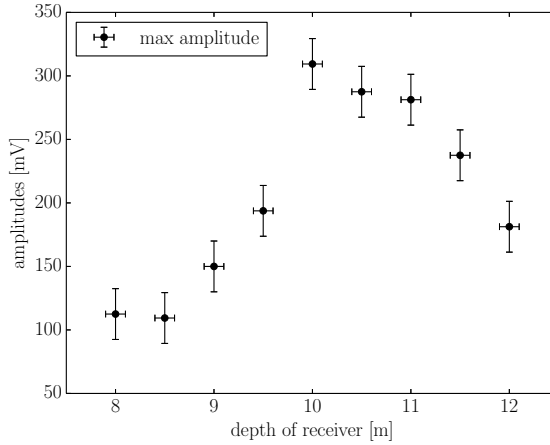
Figure 8.14. Maximum amplitude of the HP pulses in dependence of depth. The transmitter was at a fixed depth of 10 m while the receiver was moved. The uncertainties are estimated to $\pm$ 20 mV in amplitude and $\pm$ 0.2 m in depth.

est values around 110 mV at 8 m and 8.5 m. With lower depths the amplitudes increase steep until they reach a maximum at 10 m. Then the amplitudes decrease again with depth reaching 170 mV at 12 m. This behavior shows a strong indication for destructive and constructive interference, comparing these values to the amplitude of the air-pulse of about 200 mV. The rather irregular rise and fall shows how strong the firn environment influence is. It can be concluded that the amplitudes can vary strongly depending on the structure of the firn and therefore the opportunity to interfere.

8.5 Pre-Pulses

Additionally to the horizontally propagating pulses, ARIANNA observed low frequency signals which arrived even before the HP signals. These early signals are referred to as *pre-pulses* within this thesis. Figure 8.15 shows a zoom in on the time before the HP pulse arrives. The red highlighted pulse with low amplitude is seen approximately 100 ns before the horizontal propagation pulse. The dipole depth was 2 m for both Tx and Rx when this trace was recorded. This signal was registered under the same conditions as the HP pulse at 2 m depth (green) in figure 8.4, in which the pre-pulse is also visible in the beginning of the signal[7]. The pre-pulse has a lower frequency (around 100 MHz) compared to the HP pulse and a seemingly higher speed. Exam-

---

[7]The two pulses were recorded on different days, which means that the depth of the dipoles might not be exactly the same, which explains the amplitude difference of $\sim$ 7 mV between the pre-pulses. In figure 8.4 the amplitude is $\sim$ 20 mV in and figure 8.15 it is $\sim$ 13 mV.
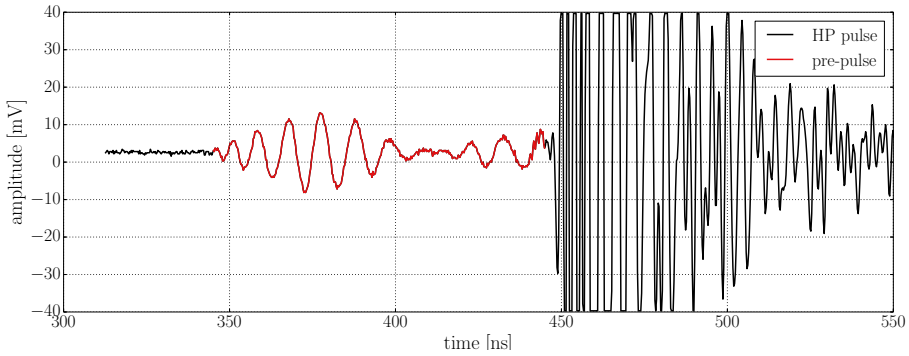
Figure 8.15. Zoom in of the pre-pulse (red) arriving before the horizontal propagation pulse with absolute timing. This signal was recored when Tx and Rx were at 2 m depth.

ining the waveforms in figure 8.4 closer, it can be seen that all signals in firn show a low frequency component before the main pulse. The pre-pulses have not been observed when the antennas were in air. This phenomenon was also not previously observed with ARIANNA data. It was verified that these signals were emitted from the antenna due to their disappearance when a 50 Ω terminator was connected to the PCD, see section 8.2.1.

Table 8.3 shows the arrival times of the HP- and pre-pulses in dependency of depth. The time difference between the arrival times decreases with depth form ~ 100 ns to 35 ns. It is interesting that the pre-pulses disappear at a depth around 10 m.

Table 8.3. *Time measurements of HP- and pre-pulses. If available the values are averaged over several measurements and rounded to three significant numbers.*

depth [m]	2	5	10	15	19
HP time [ns]	450	454	472	490	503
pre time [ns]	349	365	-	440	468

When performing the measurements, when Tx was at a fixed depth of 10 m and Rx was moved from 8 m to 12 m in 0.5 m steps, the pre-pulses were visible above 9.5 m. This measurement series was designed to investigate the horizontal propagating pulses and therefore, the recorded waveforms included the complete HP signals but only about 30 ns of the earlier arriving pre-pulses. These waveforms are adequate to identify the pre-pulses, but not sufficient to determine their arrival time or maximum amplitude. However, due to the small steps in depth it was possible to observe that the pre-pulses decreased

in amplitude as the receiver was moved down. At a depth of 9.5 m it was not possible to identify a pre-pulse anymore, because the amplitude decreased to noise level. It was furthermore not possible to observe the pre-pulses down to 12 m. However, as shown in figure 8.9 the amplitude increased so that the pre-pulse could be identified again at 15 m and 19 m. Since the amplitudes decreased steadily between 8 m and 10 m we surmise that at these depths destructive interference must have taken place.

8.6 Surface Propagation between Snow and Air

The pre-pulses are unlikely taking a direct path like the horizontally propagating pulses. The most likely explanation for the pre-pulses is that they traveled up and traversed along the air/firn interface. There are two possible propagation modes which allow waves to behave like that: *surface waves* and *lateral waves*. Both waves are a special solution of Maxwell equations and will be described briefly, starting with the surface waves.

In general a surface wave is a wave which propagates in two media along the interface. The easiest example are waves which develop on a smooth water surface when a stone is thrown in. For electromagnetic waves a surface wave is "trapped" on a two dimensional surface between two media with different dielectric constants. The theory was formulated by Jonathan Zenneck for metal-dielectric boundaries [8] [216].

An electromagnetic wave can be trapped in a surface when the incident angle is close to the polarization angle, also called the Brewster angle [1]. The Brewster angle is the angle of incidence at which the parallel component of light (regarding the plane of incidence) is not reflected. The orthogonally component is reflected and linear polarized. This also means, that electromagnetic radiation that is purely parallel polarized with regard to the plane of incidence would be perfectly transmitted. At the Brewster angle the angle between the reflected and transmitted light is 90°. When considering the measured refractive index of the surface firn at Moore's Bay ($n_{surface} = 1.29$ [128]), the Brewster angle is calculated according to:

$$\theta_B = \tan^{-1}\left(\frac{n_{air}}{n_{surface}}\right) = 37.8°, \tag{8.7}$$

where $n_{air} = 1$. This formula is also known as Brewster's law and can be derived from Snell's law ($n_1 \sin\theta_1 = n_2 \sin\theta_2$). These waves are expected to propagate along the surface, even in case of a curved surface. The group velocity

---

[8]Later these kind of waves were also called after him: *Zenneck waves*. Sometimes these waves are also called Sommerfeld-Zenneck waves.

is expected to be of the lighter medium[9] (air) and they have phase velocities greater than the speed of light. In propagation direction they experience little attenuation, and in perpendicular direction they are damped exponentially [1]. The signals emitted by the transmitter dipole are vertically polarized, which means they are parallel polarized with respect to the plane of incidence, which leads to the conclusion that they should not be reflected. However, in practice no antenna is able to transmit perfectly linear polarized pulses. In addition, the polarization is assumed to get scrambled with distance due to reflections and scattering within the firn[10]. These could be possible reasons why the amplitude of the pre-pulses is small in comparison to HP signals.

Lateral waves are also "bound" to the surface, but travel along it in only one medium, in this case air. Lateral waves develop when electromagnetic waves hit the surface with exactly the critical angle. The critical angle is the angle of incidence above which total internal reflection occurs. In this case the angle of refraction corresponds to 90°. At the critical angle the waves are not reflected or transmitted, but travel along the surface instead [1]. The critical angle is calculated using Snell's law:

$$\theta_{crit} = \sin^{-1}\left(\frac{n_{air}}{n_{surface}}\right) = 50.8°. \tag{8.8}$$

Both surface and lateral waves propagate with the speed of light in air and are expected to experience little attenuation in propagation direction. Due to these similar expectations they are hard to differentiate. Therefore, we will continue to call these signals pre-pulses[11].

In general pulses propagating at an interface are expected to decrease in amplitude like $1/\sqrt{r}$, whereas the geometrically expected effect for propagation in three dimensions goes like $1/r$. If lateral waves do not encounter obstacles they would travel along the surface without attenuation due to scattering or absorption. According to [181] the attenuation length for surface pulses is a factor $2\sqrt{2}$ longer than that of bulk ice. Especially due to the long attenuation length it has been suggested that pre-pulses would be useful for radio neutrino astronomy increasing the effective area of a detector [181]. It was previously attempted to detect pre-pulses with ARIANNA, but the experiment was unsuccessful [128].

---

[9]Note that this usually applies for waves entering the interface from the lighter medium. It is possible that if the waves enters the interface from the heavier medium, the wave propagates with a group velocity corresponding to the heavier medium. This possibility however, was not observed or described before.

[10]In order to travel between Tx and Rx pre-pulses traverse the firn to and from the surface.

[11]In [62] the pre-pulses are referred to as air-pulses

8.7 Simple Pre-Pulse Model
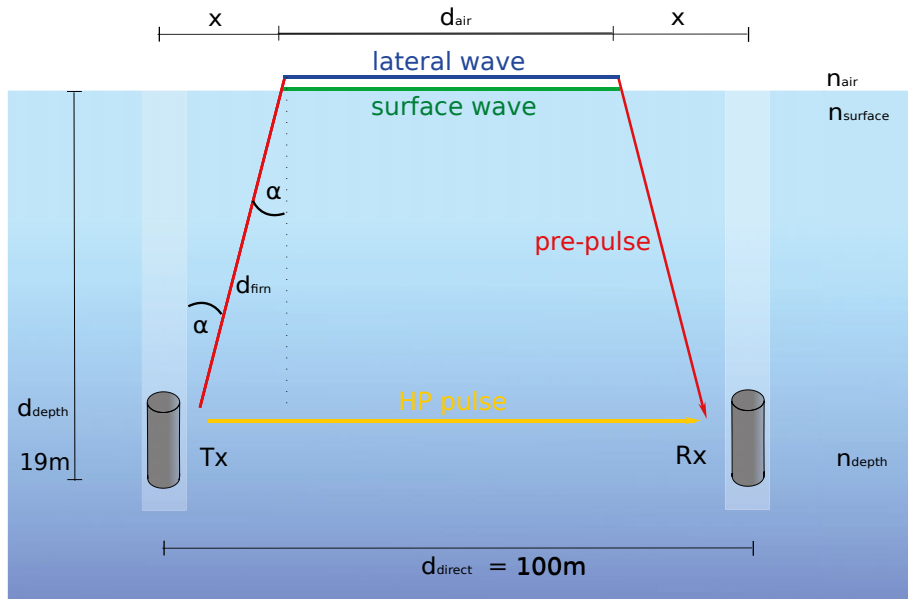
Figure 8.16. Schematic view of the conceptual HP pulse and pre-pulse. The yellow line shows the horizontal propagation path. The red paths are the firn components of the pre-pulse. When the ray reaches the surface there are two possibilities to propagate, either as a lateral wave (blue) or as a surface wave (green). The figure is not to scale.

In a simplified model we attempt to calculate the approximate path and incident angle of the pre-pulses. Figure 8.16 shows a sketch of the simplified symmetrical pre-pulse path: first it travels up (d_{firn}, red) and hits the firn/air interface at an incident angle α and moves then along the surface as either lateral- (blue) or surface- (green) wave (d_{air}). Then the pulse reenters the firn under the same angle α and traverses it (d_{firn}) until it reaches the receiver at the depth d_{depth}. For the distance covered in firn (d_{firn}) we assume an average refractive index:

$$n_{average} = \frac{n_{surface} + n_{depth}}{2}, \qquad (8.9)$$

where $n_{surface} = 1.29$ [128] and n_{depth} is the measured average refractive index at the corresponding depth, see figure 8.9. For the path along the surface, the refractive index of air $n_{air} = 1$ is used for both waves. For each depth, α was increased from $0°$ to $90°$ in a step size of $0.1°$ and d_{firn} and d_{air} were determined according to:

$$d_{firn} = \frac{d_{depth}}{\cos \alpha} \tag{8.10}$$

$$d_{air} = d_{direct} - 2d_{firn} \cdot \sin \alpha \tag{8.11}$$

With these values the flight time was calculated:

$$\begin{aligned}
t_{model} &= \frac{2n_{average} \cdot d_{firn}}{c} + \frac{n_{air} \cdot d_{air}}{c} \\
&= \frac{2n_{average} \cdot d_{depth}}{c \cdot \cos \alpha} + \frac{n_{air}}{c} \cdot \left(d_{direct} - 2d_{depth} \cdot \tan \alpha\right),
\end{aligned} \tag{8.12}$$

The model time was then compared to the average of the measured arrival time of the pre-pulse in table 8.4. When the two times agree with each other with an accuracy of 0.05 ns the model times were saved. Then, the model time with the best agreement was chosen and the corresponding angle is displayed in table 8.4. The table displays two angles $\alpha 1$ and $\alpha 2$, because equation 8.12 has two possible solutions, due to the competitive behavior of terms with $\cos \alpha$ and $\tan \alpha$.

Table 8.4. *Time measurements of the pre-pulse (corrected by $\delta t = 5$ ns), the average index of refraction and angle of incidence to the firn surface as calculated with the simple model are shown. Furthermore, the expected arrival times for lateral waves (t_{crit}) and surface waves (t_B) are calculated.*

depth [m]	2	5	15	19
time [ns]	349	365	440	468
$n_{average}$	1.32	1.33	1.38	1.4
α_1 [°]	10.5	32.1	24.2	27.1
α_2 [°]	71.2	61.3	62.3	59.5
t_B [ns]	345.50	363.84	430.71	459.82
t_{crit} [ns]	345.07	362.85	429.36	458.92

Compared to the Brewster angle ($\theta_B = 37.8°$) and the critical angle ($\theta_{crit} = 50.8°$) the incident angels from this calculation do not show a conclusive result. While the times t_B and t_{crit} at shallow depths are comparable with the measured times, they show an increasing discrepancy for deeper measurements.

We want to take a closer look at the measurements performed at 2 m depth. Using the simple pre-pulse model to calculate the necessary times one would expect the surface wave to arrive at $t_B = 345.50$ ns and the lateral wave at
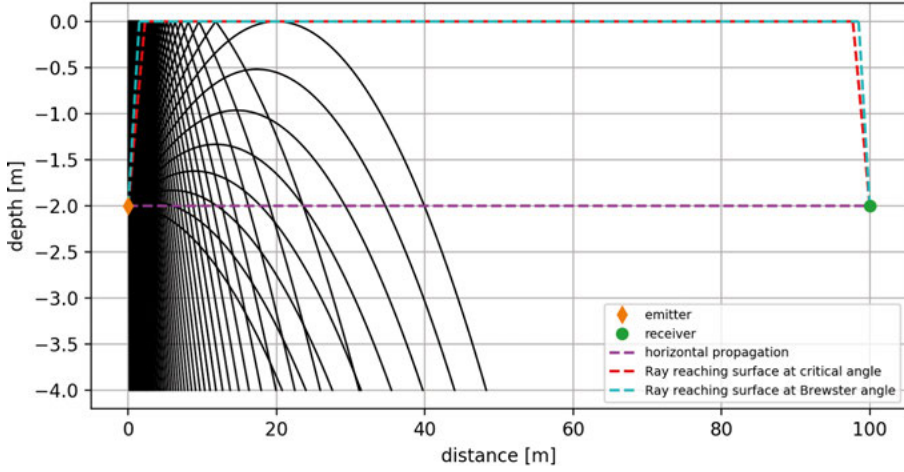
Figure 8.17. Simulated paths of various propagation models using ARIANNA ray tracing software. The black lines represent the classical ray traces. The purple dashed line represents the HP pulse with a calculated $t_{HP} = 448.95$ ns, which is in agreement with the measurement in table 8.2. The red and blue dashed lines show the paths a lateral wave ($t_{crit} = 345.33$ ns) and surface wave ($t_B = 345.80$ ns) respectively. Credit: ARIANNA collaboration.

$t_{crit} = 345.07$ ns. The time difference is vanishing and both times are only 4 ns apart from the measured time. Considering the estimated uncertainty of 349 ns $\pm$ 3 ns the theoretical times for surface and lateral waves are close to the measured value. It is important to stress that this calculation does not represent the true path and does not take the accurate ray tracing, which bends depending on refractive index, into account. Using ray tracing software developed within the ARIANNA collaboration the theoretical times were calculated to be $t_B = 345.80$ ns and $t_{crit} = 345.33$ ns, both are in agreement with the simple pre-pulse model. Furthermore, the applied paths can be viewed in figure 8.17.

An accurate firn model would be useful for this type of analysis. Firn models are hard to simulate because the firn accumulation varies from year to year, which results in layers with various densities.

The simple pre-pulse model is not able to explain the steady disappearance of the pre-pulses around 10 m, see section 8.5. Here, interference is most likely the explanation and could be due by rays, which were initially emitted under a different angle but then reflected[12] on firn layers towards the surface. Further

---

[12]The reflections could lead to the the Brewster or critical angle due previously refracted waves or effects of reflection of spherical waves.

investigations regarding pre-pulses are being performed within the ARIANNA collaboration with more data.

Pulses which arrived earlier than expected were also observed by RICE after reanalyzing previous data [62][13]. As already described in section 8.3, GNO observed and simulated horizontal propagation pulses. The observations and simulations also included pre-pulses, which have also been identified as surface- or lateral waves. GNO implemented a surface-mode for the pre-pulses in their simulations. Three different firn models were used, one of which was based on core density measurements. This model produced the best agreeing results compared to observations. The FDTD simulations and measurements for HP- and pre-pulses agreed well in flight times, waveform shapes and amplitudes [91].

8.8 Frequency Content of HP- and Pre-Pulses

Figure 8.18 shows the time (upper plot) and frequency (lower plot) domain of the air-pulse. The air-pulse was obtained with both dipoles 1.5 m above firn and otherwise the same setup as shown in figure 8.3. The *Discrete Fast Fourier Transformation* (DFFT) of this received pulse shows the largest contribution between 200 MHz and 300 MHz. Beyond 300 MHz the amplitude decays steadily until it reaches ~ 0 mV at around 800 MHz. Below 200 MHz the amplitude falls steeply and shows a flat behavior at ~ 10 mV to 30 mV between ~ 80 MHz and ~ 160 MHz. Below 80 MHz the amplitude decreases to ~ 0 mV due to the 100 MHz high-pass filter[14].

We want to compare the received air-pulse with the horizontally propagating pulse at 2 m depth, with the same setup as shown in figure 8.3. In figure 8.19 the time and frequency domain for the HP pulse is presented. The main peak of HP pulse is located slightly closer to 200 MHz compared to the air-pulse. At around 270 MHz to 300 MHz a signal loss is visible. At higher frequencies the spectrum shows the same general trend as for the air-pulse, with the exception of the valleys between 300 MHz and 450 MHz, which are signs of absorption.

Interesting is the new contribution at around 100 MHz, which was not observed in the DFFT of the air-pulse. The pre-pulse was also not observed in air, therefore, we separate it from the complete waveform and take the DFFT of the red highlighted waveform. Note that the starting time of the pre-pulse

---

[13]In this paper the pre-pulses are denoted as air-pulses, in this thesis air-pulses represent the signals measured in air, when both dipoles were 1.5 m above firn.

[14]The high-pass filter is not perfect and therefore frequencies below, but close to 100 MHz are observable.
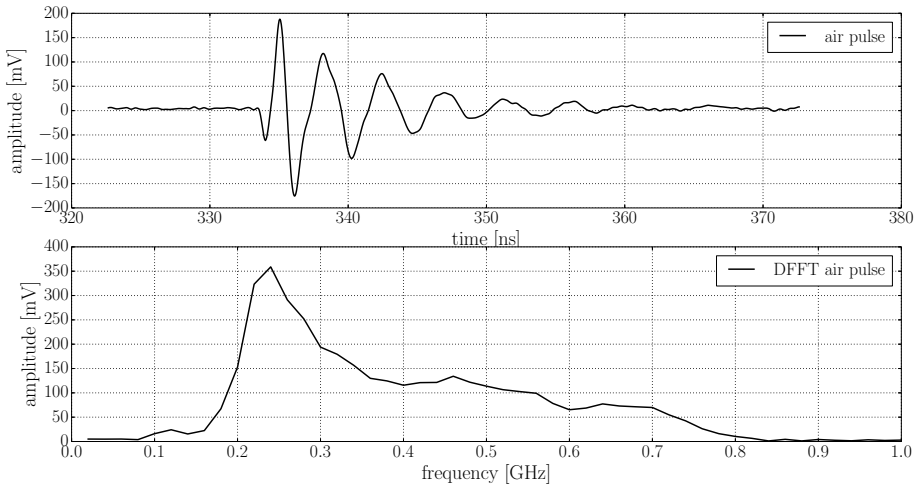
Figure 8.18. The upper plot presents the raw waveform recorded in air, with the two dipoles being separated by 100 m and attached to bamboo sticks 1.5 m above firn. The lower plot displays the DFFT of the waveform above.
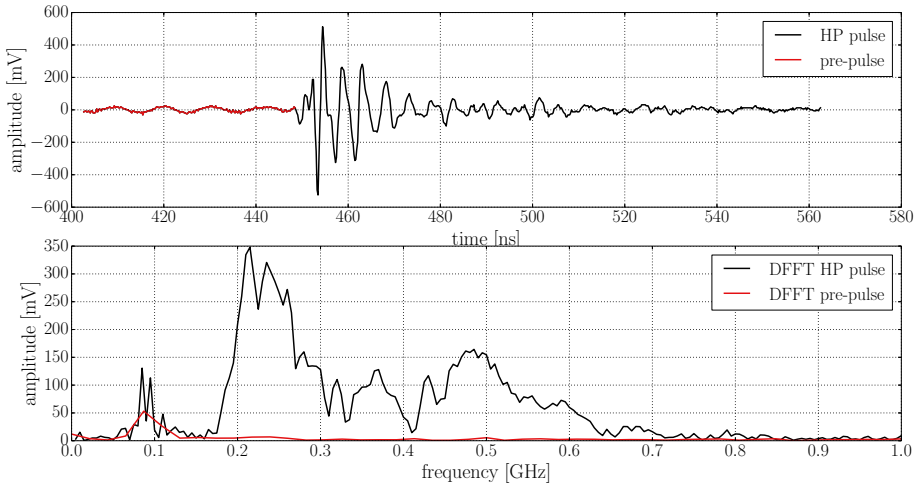
Figure 8.19. The upper plot shows the raw dipole to dipole wave form at 2 m depth and 100 m separation between Tx and Rx. This signal was observed with the same conditions as the signal in figure 8.15. The lower plot displays the DFFT of the waveform above. The pre-pulse, which beginning of the waveform is not completely recorded, is highlighted in red. Note that the DFFT of the pre-pulse was calculated using only the red region of the pulse, hence the resolution of the DFFT is lower.

is not recorded[15]. The DFFT of the pre-pulse reveals a low frequency contribution around 100 MHz.

When we compare the amplitude of the low frequency contribution in the frequency domain, we notice that the amplitude of the complete waveform (black) is higher ($\sim$ 125 mV) than the amplitude of the pure pre-pulse waveform (red, 50 mV). This indicates a 100 MHz component in the HP pulse. This could be a hint that the pre-pulse waveform extends further in time than visible, due to arrival of the HP pulse. If this assumption is correct, this would imply that the pre-pulse and HP pulse interfere with each other. However, the amplitude difference could also be explained by noise or by low frequency contents in the tail of the HP pulse. One effect that also has to be taken into account is that less points were used to determine the pre-pulse DFFT, which means it is more coarse and smeared compared to the complete waveform.
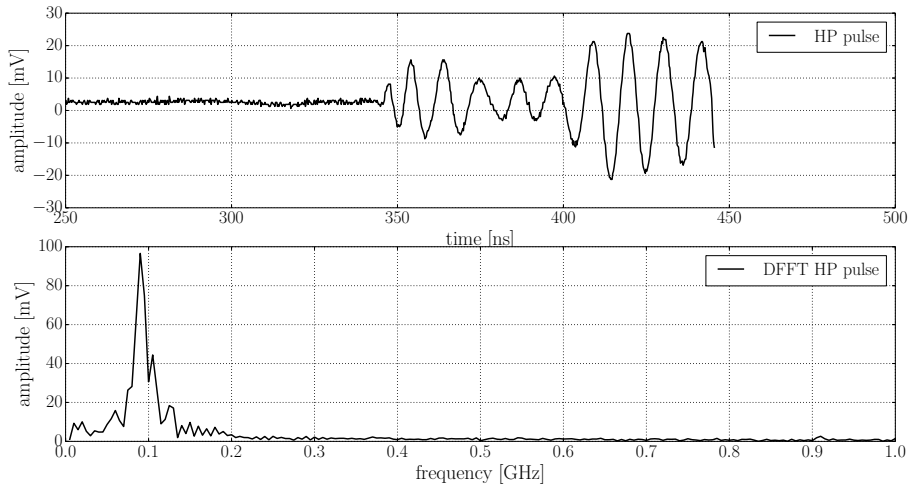
Figure 8.20. The upper plot shows a measurement of the pre-pulse received when Tx and Rx were both at 2 m depth with absolute timing. Lower plot displays the DFFT of the pulse above. The waveform in the time domain was cut right before the HP pulse starts.

Some pre-pulses were saved separately from the HP pulses and the pre-pulse at 2 m depth is displayed in figure 8.20. The DFFT of this waveform confirms that the pre-pulse has a frequency content of 100 MHz. The low frequency contribution of the pre-pulses was confirmed for all other depths, with the exception of 10 m where it disappears.

---

[15]Unfortunately we do not have a better recording where the waveforms of the pre-pulse and the HP pulse are visible completely together, because the measurements performed were focused on the horizontal propagation signal investigation.
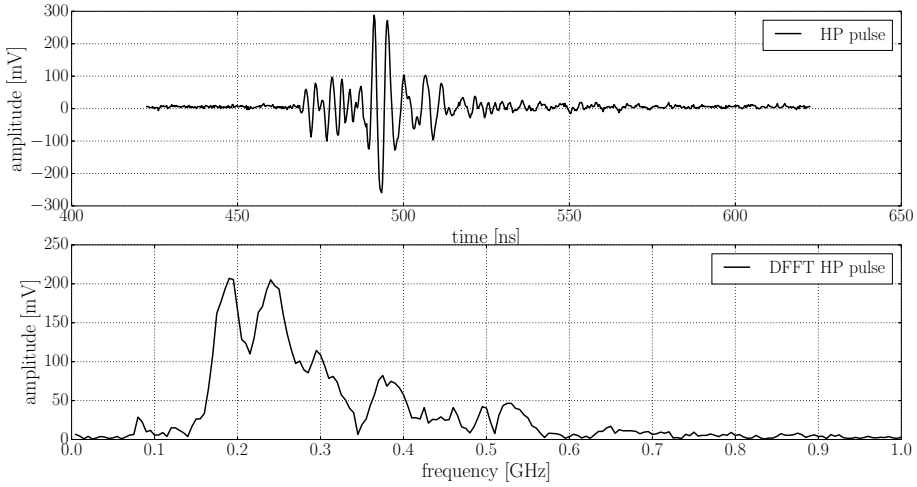
Figure 8.21. The upper plot shows the pulse received when Tx and Rx were both at 10.5 m depth with absolute timing. The lower plot displays the DFFT of the pulse above.

Figure 8.21 shows the complete waveform for the measurement at 10.5 m, where the pre-pulse is not observable. It cannot be differentiated from the noise by eye anymore. The frequency distribution also shows a small peak of about 25 mV below 100 MHz.

It has to be noted, that these measurements were performed with an 100 MHz high-pass filter. Taking this fact into account it is very likely that pre-pulses have more power than observed. Additionally we assume that the pre-pulses reach the receiver dipole rather from above. Dipoles follow a $\cos\theta$ field beam pattern and hence, the gain is depending on the arrival direction [147].

The observation of pre-pulses with this data was unexpected, and although the presented measurements were not designed to investigate these signals, we characterized their properties and found possible explanations of their origin and propagation. As already mentioned the pre-pulses are currently investigated with more data taken by ARIANNA, and the more we learn about them, the more important they become.

As suggested in [181] these pulses could be beneficial for radio neutrino experiments. Therefore, it might be worth while to take measurements with pre-pulses as focus.

If future measurements will be designed to investigate the pre-pulses, it would be interesting to send out different narrow frequency pulses and observe

them in dependency of depth and distance. That way it would be possible to find out to which extent the pre-pulses are frequency dependent, if dispersion influences these signals and how much of the interference is depth and location dependent. Preferably several boreholes in different directions and distances would need to be drilled. Another interesting experiment would be to see if the response is influenced by the diameter of the borehole, and therefore boreholes with different diameter would be needed.

Neutrino signals have a narrow Cherenkov emission cone, therefore not all effects observed with the dipoles will be relevant. One possibility to investigate the effects further would be to use a transmitter antenna which is able to emit radio waves which can mimic the pulses of neutrino signals. An antenna was developed with this purpose and tested with results that show very good agreement between the antenna radiation and Cherenkov radiation [132]. Currently a deployment of such an antenna in the firn is challenging, due to its large dimensions. However, with electric drills, which form could be designed for a desired antenna dimension, it would be possible to accommodate large dimension antennas at various depths in the firn. Such tools are currently under development.

8.9 The Bounce Pulse
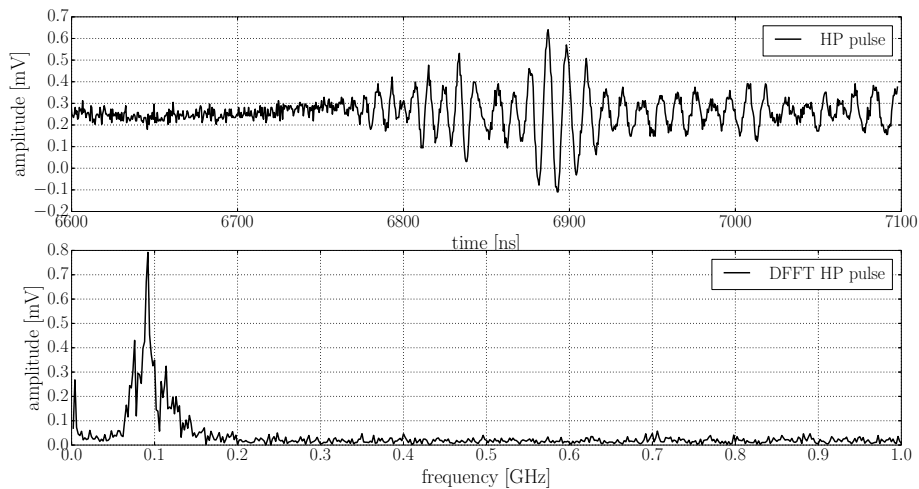
Figure 8.22. The bounce pulse which is observed when the dipoles are at 2 m. The top plot depicts the time domain and the bottom plot the frequency domain.

The bounce pulse travels from the transmitter antenna to the bottom of the ice and reflects on the ice/water interface via total internal reflection to traverse back up and reach the receiver antenna as shown in figure 8.22. It shows

a smaller amplitude compared to the horizontal propagation- and pre-pulses. Furthermore, it is very stretched, probably due to dispersion and interference from different pulses delayed by multi-paths. The frequency content shows that the main contribution is located at $100\,\text{MHz}$, which is expected because higher contributions are more likely to be absorbed faster.

Using a simplified model we can calculate the expected arrival time for the two dipoles in $d_{depth} = 2\,\text{m}$ depth and $d_{direct} = 100\,\text{m}$ distance. In this model the ray will travel in a straight path to the ice/water interface and reflect at half of the horizontal distance d_{direct} back up. We consider only the way from transmitter to the bottom:

$$d = \sqrt{(d_{direct}/2)^2 + d_d^2},\qquad(8.13)$$

where $d_d = d_s - d_{depth}$ is the difference between the shelf depth $d_s = 576\,\text{m}$ and the transmitter depth. Although ray tracing is not applied it is useful to consider that the first part of the path is in firn, d_{firn}, and the second part is in ice, d_{ice}, with the corresponding refractive indices. For $n_{average} = 1.55$ we take again the average between the refractive index at the transmitter depth ($n_{depth} = 1.32$) and $n_{ice} = 1.78$. In order to determine d_{firn} we use trigonometry:

$$d_{firn} = \frac{d_f - d_{depth}}{\cos(\alpha)},\qquad(8.14)$$

where $d_f = 75\,\text{m}$ is the vertical firn depth of the shelf and α is the radiated angle:

$$\alpha = \arctan\left(\frac{d_{direct}/2}{d_d}\right)\qquad(8.15)$$

The path in ice is then given by $d_{ice} = d - d_{firn}$ and we can calculate the time for the complete path according to:

$$t = \frac{n_{average} \cdot d_{firn}}{c} + \frac{n_{ice} \cdot d_{ice}}{c}\qquad(8.16)$$

If we now define the time from transmitter to the ice/water interface as t_1 and the path from the interface to the receiver as t_2, where both times can be calculated with the equations above, we can determine the expected time t_b for the bounce pulse:

$$t_b = t_1 + t_2 = 6726\text{ ns}.\qquad(8.17)$$

The calculated time is about 40 ns shorter than the observed 6765 ns, but considering that no ray tracing was applied the two times are consistent. The uncertainty for simplified models increases with the distance and the time spent in firn, because average refractive indices and straight paths become worse in describing the actual bent paths. Furthermore, the values for the shelf depth and firn are averaged as well.

9. Characterization of Events in an LPDA and ARIANNA Stations

How far can signals travel beyond the shadow zone? In chapter 8 we have learned that unexpected signals were received in all dipole configurations 100 m apart. The stations have horizontal distances between 350 m and 1450 m from the transmitter dipole. Therefore, they were in the shadow zone where no signals are expected to be observed.

When the bounce tests were performed in season 2011/1012, see section 7.2.4, the stations observed signals arriving much earlier than the expected bounce pulses. Such signals were discarded as artifacts of the measurement setup. These early signals were forbidden according to the shadowing effect [128]. In season 2016/2017 further tests were performed ruling out this explanation and introducing the concept of horizontal and surface propagation. During the ice studies presented in chapter 8 the stations registered the signals emitted from the transmitter dipole. The goal in this chapter is to understand which pulses triggered the stations and determine an attenuation length for these signals.

9.1 Measurements Between Dipole and Buried LPDA

Before investigating the observed signals from the stations, it is important to understand the response of an LPDA as a receiver antenna. The LPDA is the type of antenna which is used for all stations, see section 7.3.1. The LPDA was buried 2 m deep in the firn, nose pointing down. Larger depths were not possible within the time available for the campaign, because it is challenging to dig significantly deeper holes. The exchange of the receiver antenna from dipole to LPDA and the change of related cables resulted in a change of the absolute timing of the system from 268 ns to 348 ns. The rest of the setup remained the same as described in section 8.2.1. When performing air measurements between dipoles a systematic delay of $\delta t \approx 5$ ns was observed, see section 8.4.1. Since no air measurements were performed for a dipole transmitter and an LPDA receiver, the systematic delay for this measurement might have changed. Instead of correcting the absolute time with the known system delay between dipoles, we rather expand the uncertainty on the measurement

to $\pm\,10\,\text{ns}$. This number is the square root of the quadratic sum of the estimated error[1] of $\pm\,3\,\text{ns}$ and an arbitrary doubling of the systematic delay of $5\,\text{ns}$, from the dipole to dipole measurement.
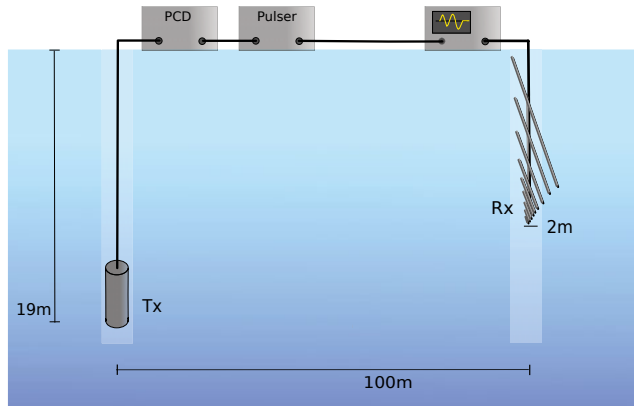
Figure 9.1. Setup for the measurements between the dipole transmitter Tx and the LPDA receiver Rx. The Tx was positioned at $19\,\text{m}$ depth and the LPDA was buried below the surface of the firn pointing down, with the tip at about $2\,\text{m}$ depth. The tines are set perpendicular to the signal direction. The rest of the setup was the same as in figure 8.3, with a distance of about $100\,\text{m}$ between the antennas. The figure is not to scale.

The measurements were taken with the transmitter dipole at $19\,\text{m}$ depth and the LPDA in two configurations: 1) with the tines of the LPDA perpendicular to the signal direction, see figure 9.1 (referred to as the perpendicular setup) and 2) with the tines parallel to the signal direction. Both configurations were needed, because most stations have their antennas in one of these positions relative to the signal direction[2]. The orientation of the LPDAs and received signals will be described in detail in section 9.2. The perpendicular setup gave stronger signals. Further analyses for the setup with $100\,\text{m}$ distance are therefore concentrated on the perpendicular configuration. With Tx at $19\,\text{m}$ and Rx at $2\,\text{m}$ no signals are expected due to the shadowing effect, see figure 8.2. However, even in this asymmetric depth configuration between transmitter and receiver, signals were observed.

Figure 9.2 shows the registered pulse at the LPDA (upper plot) in comparison to a waveform received by a dipole (lower plot). Comparing the two signals the LPDA registers a waveform which is smaller in amplitude. The signal

---

[1] See section 8.4.1.

[2] The exact positions of the stations, the transmitter and receiver holes can be viewed in figure 9.5.
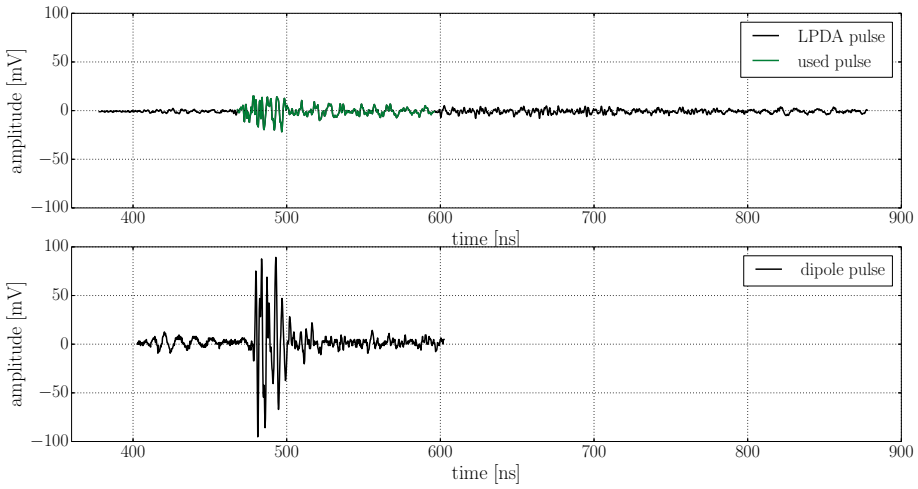
Figure 9.2. Comparison of waveforms received by an LPDA in the perpendicular configuration (upper plot) and a dipole (lower plot). The transmitter was at 19 m depth and the receivers were at 2 m depth. The green part of the pulse received with the LPDA is used for the analyses. It corresponds to the length of 128 ns, which is the time that HRA stations are recording. Both the pulse received by the LPDA and the dipole show a pre-pulse around 410 ns and a HP-pulse at ~ 480 ns. The pulses displayed are raw and not amplified.

transmitted from the dipole has a vertical polarization. A dipole receiver in the same configuration is optimal to receive these signals, it is *co-polarized*. It should be noted that the optimal configuration to observe signals with the LPDA would be with the nose in direction of the signal and the tines aligned with the polarization, in this case in vertical orientation. When the tines of the antenna are oriented orthogonal to the polarization of the signal the antenna setup is *cross-polarized*. Cross-polarized signals are always suppressed and the perpendicular setup as displayed in figure 9.1 is cross-polarized. Considering the parallel setup, more signal suppression is expected compared to the perpendicular setup, because the tine length projected on a plane perpendicular to the wave to register pulses corresponds to ~ 17 cm for a 1 m tine. Theoretically, cross-polarized signals should not be observed but in reality antennas are not perfect which means they never emit perfectly polarized radiation in one direction. Additionally, our setup is within firn and due to scattering and reflections in the firn the polarization gets scrambled, increasing with distance[3]. To quantify the exact amount of suppression one would require the knowledge of the precise arrival direction and the precise polarization of the signal in firn.

---

[3]As also mentioned in section 8.5

We estimate arrival times of ~ 410 ns for the pre-pulse and ~ 480 ns for the HP-signal. For the pre-pulse the time was calculated using the simple pre-pulse model, see section 8.7, considering the different depths of Tx and Rx. For the HP-pulse the direct path between Tx and Rx was assumed using an average $n = 1.4$. The actual path of the ray was more likely directed towards the surface and then trapped in upper layers of the firn before reaching the receiver antenna. The pulse arrival times found in the measurements are consistent with the expectations and with each other within the uncertainties, see figure 9.2 for measured arrival times. No records with focus on the pre-pulse have been made with the LPDA. The waveforms received by both the LPDA and the dipole show a long, noisy and slowly decaying tail. The LPDA pulse shows that the tail does not return to noise level (< 410 ns) for the complete recording window, ending ~ 400 ns after the pulse. It is known that the LPDAs are responsible for some dispersion because of their construction [61]. These effects are not sufficient to explain the dispersion of the signals observed. Dispersion of radio waves has the negative effect of stretching the signals in the time domain, which leads to reduction of the amplitude, as mentioned in section 8.3.1. At the same time, dispersion can be used to extract information on the relation of distance and vertex for neutrino events in a detector, by using the relative arrival times of different frequencies. On the other hand, interference enlarges signals in the time domain as well. Furthermore, it has a much larger effect on the amplitude of the signals.
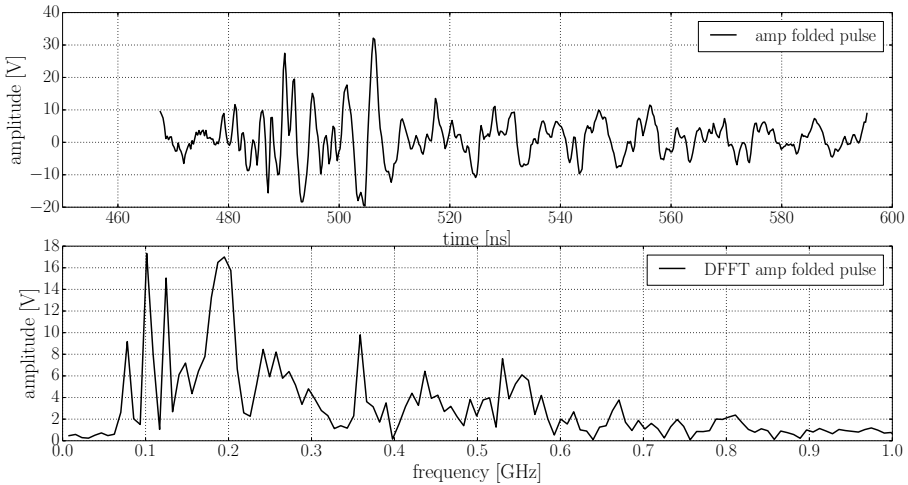
Figure 9.3. Frequency content of the green waveform in figure 9.2, after folding in the amplifier response. Note that the amplifier response is frequency dependent and therefore, the resulting pulse does not look exactly the same as the original.

In order to make the LPDA oscilloscope pulse comparable with the station data, the measurements have to be cut in time to match the station's record, and folded with the amplifier response of the stations. The wave form is cut down to the station's record length of 128 ns, represented in green in figure 9.2. The start and stop values of the time window are chosen to cut away the pre-pulse and start at the HP-pulse. The stations register the first 30 ns before the trigger. For the receiver LPDA in this scenario any noise right before the HP pulse is effectively masked by the pre-pulse. This is why this period was cut out. The amplifier response is frequency dependent and leads on average to an increased amplitude of about 60 dB, disregarding saturation effects. Another possibility for comparison would be to unfold the station data from the amplifier response to the original signal, but that method is more sensitive to the impact of noise and therefore less favorable for this analysis. The resulting waveform and the corresponding frequency content are displayed in figure 9.3. It shows a main contribution around 200 MHz, an equally high but narrow peak at 100 MHz, a few other peaks around 100 MHz, as well as smaller contributions at higher frequencies beyond ~ 240 MHz.
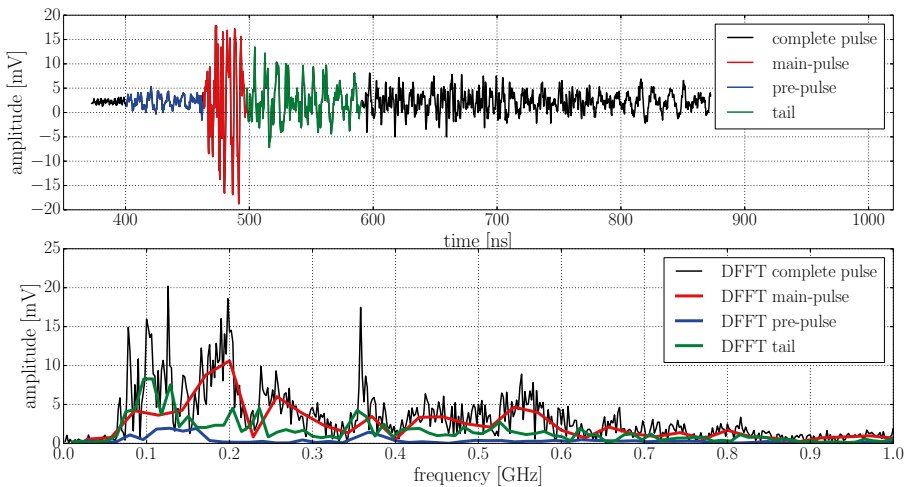
Figure 9.4. The pulse presented is the same (upper) pulse registered at the LPDA from figure 9.2. The waveform is divided into three parts, pre-pulse (blue), main pulse (red) and tail (green). The frequency content of these parts are compared to the frequency content of the complete waveform (black). The green highlighted pulse in figure 9.2 corresponds to the red and green highlighted parts in this waveform. The pulse displayed is raw and not amplified.

To get a better understanding for the frequency content described above, figure 9.4 shows the original waveform divided into three parts: the pre-pulse in blue, the main pulse in red, and the tail in green. The main pulse and the tail are the

parts which represent the used HP pulse (green) in figure 9.2. This is the waveform that was folded with the amplifier and displayed in figure 9.3. The lower plot in figure 9.4 shows the frequency content of these parts in comparison to the complete waveform in black. The pre-pulse shows main contributions between 80 MHz and 160 MHz, the main pulse has a main contribution between 150 MHz and 240 MHz and the tail shows its maximum around 100 MHz. All three parts show a distinct contribution at around 350 MHz. Obviously the LPDA has a different antenna response than the dipole. It is evident that the pre-pulse has a small contribution to the low frequency content of the waveform. The differences in the frequency domain between figure 9.3 and figure 9.4 can be explained by the frequency dependent amplifier response and the different resolution due to the amount of given data points in the time domain.

9.1.1 Various Pulse Definitions

In chapter 8 we have described three different signals: the horizontal propagation pulse, the pre-pulse and the bounce pulse. ARIANNA is designed to detect neutrinos with both bounced pulses and pulses traveling directly from the vertex. In addition, the discovered horizontal propagation allows for detection of neutrino events in the shadow zone. Of the signals investigated with dipole tests in chapter 8 we found that the HP pulse carried the most power, in comparison to the pre-pulse and bounce pulse. All pulses have different arrival time expectations, with the pre-pulse arriving first, then the HP pulse and lastly the bounce pulse. Considering the frequency content it has been shown, that the pre- and bounce pulse both have their main contribution around 100 MHz, while the frequency spectrum of the HP pulse shows a widely distributed content with the highest contribution around 200 MHz. Considering the LPDA response, the frequency content is spread wider, but the main contributions of the pre-pulse and HP pulse are still located close to 100 MHz and 200 MHz respectively. The bounce pulse was also observed with the LPDA. It arrived at the expected time of ~ 6800 ns and had a maximum amplitude of about 2 mV, which is ~ 10 times lower than the HP amplitude and ~ 2.5 times lower than the pre-pulse amplitude. The bounce pulse showed a very distinct main contribution around 100 MHz, without other significant contributions at higher frequencies. We will use these pulse properties to identify the signals in the stations.

9.2 Measurements between Dipole and ARIANNA Stations
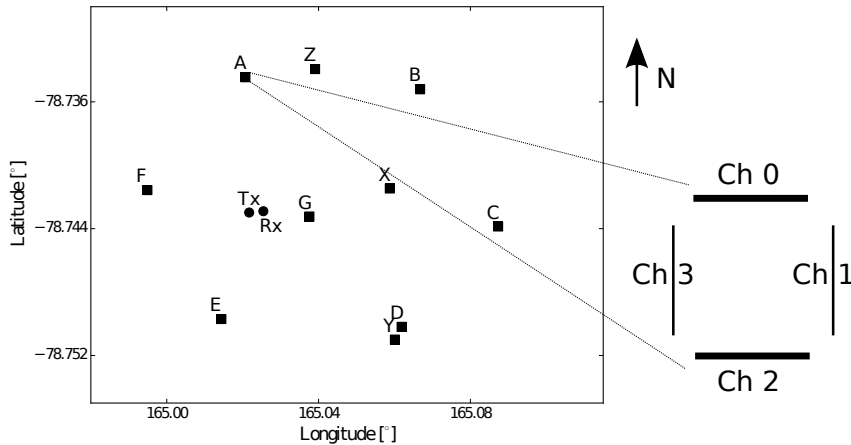
Figure 9.5. The detector layout in season 2016/2017 is presented with the top view of station A. The stations are shown as squares (A-Z) and the circles represent the position of the transmitter (Tx) borehole and receiver (Rx) borehole. The top view shows that the LPDA channel 0 (ch 0) is facing North, which is the case for all stations. Since the stations received the most power in LPDAs with tines oriented perpendicular to the signal direction, these channels are depicted with a solid thick line (ch 0 and ch 2) for station A. For other stations these channels can be determined by looking at the arrival direction from Tx.

All stations, except for the horizontal cosmic ray station (HCR or Z) register signals from the transmitter dipole, see figure 9.5 and chapter 7. There are several reasons why the HCR does not observe any pulses. The antennas are high above the snow (> 1.5 m), oriented towards North and therefore least sensitive towards the signal direction. Furthermore, the waves propagating along the firn surface have most likely too low amplitudes to trigger the station, especially in this configuration. Table 9.1 displays the stations, their horizontal distance to the transmitter borehole and their nose depth. The approximate nose depth depends on the year in which the stations were deployed. The older the deployment, the deeper the station. The stations X, Y and Z are separated due to their different configuration and sampling record.

Table 9.1. *The distances of the stations to the transmitter dipole Tx in the season 2016/2017 are displayed, including the approximate nose depth of the LPDAs and comments regarding special stations.*

station	distance to Tx [m]	~ nose depth	comments
A	953	4	
B	1311	2.5	
C	1433	4	
D	1189	2.5	
E	767	2.5	
F	606	2.5	
G	347	4	
X	825	2.5	CR
Y	1225	1.5	CR
Z	1079	-	HCR

When a station triggers on an arriving signal a 128 ns waveform for each antenna is recorded on the SST, see chapter 7. From this recorded waveform the channel specific *Fixed Pattern Noise* (FPN) is subtracted. This is an average of the noise events which a station registers when the forced trigger is applied. It is stable within one antenna system and therefore can be subtracted easily. Furthermore, a gain calibration for the amplifiers was determined before each station box was deployed. These gain calibration corrections are also applied to the data.

9.2.1 What did the Stations Trigger on?

The stations have a trigger threshold of about 100 mV and need two channels to observe a signal above this threshold before an event is triggered, see section 7.3.2. After an event was registered within a readout window of 128 ns, the dead time of an ARIANNA station is 13.33 ms [174], which means that the observed signal could be any of the three defined pulses, assuming the trigger criteria are fulfilled. Due to timing one would expect that the stations would trigger on the pre-pulses, because they arrive first. The stations are far enough from the Tx that they would register pre-pulses and HP-pulses as separate signals. With the simple models derived in chapter 8 the approximate arrival times at selected stations were calculated, see table 9.2. The time differences between the pre-pulses calculated with the Brewster- and critical angle are so small that these two scenarios are indistinguishable. Although the time differences between the pre-pulses, horizontally propagating pulses and bounce pulses are distinct, they are much shorter than the station's dead time. Unfortunately, there is no absolute timing on the stations, so that the question if the

observed events were pre-, HP- or bounce signals could be answered by their exact arrival time. However, we do have other methods to determine which signals were recorded.

Table 9.2. *Stations with standard antenna setup and the calculated arrival times of four pulse hypotheses. The pre-pulse times were calculated using the simple pre-pulse model, see section 8.7, assuming the Brewster angle (pre t B) and critical angle (pre t c). The HP times (HP t) were calculated using a straight path between transmitter and the stations, and the bounce times (bounce t) were calculated using the model in section 8.9. The depth of the transmitter dipole was* 19 m *and the depth of the stations was estimated from their nose depths (see table 9.1) subtracted by* 1 m.*

station	pre t B [ns]	pre t c [ns]	HP t [ns]	bounce t [ns]
A	3236	3231	3857	8686
B	4426	4421	5338	10205
C	4837	4832	5800	10762
D	4019	4014	4842	9664
E	2611	2606	3123	8019
F	2074	2069	2468	7517
G	1214	1210	1405	6905

Figure 9.6 shows a typical event from the transmitter, received by station A. Similar events were observed by most other stations and we will discuss them in the next section. The signal was registered by all four antennas, but was especially strong in channel 0 and 2 (ch0 & ch2). These LPDAs have their tines perpendicular to the signal direction, while the tines of the antennas connected to channel 1 and 3 have their tines parallel with regard to the signal direction, as shown in figure 9.5. Considering the orientation of the LPDAs, we expect the signal to arrive first in ch2; ch1 and ch3 should receive it at the same time; and ch0 should register it last. Looking at the time domain this is exactly what we observe.

This order of arrival would be theoretically true for all three pulses characterized in section 9.1.1. However, the time difference in two parallel channels, Δt, is different for each of those pulses due to the arrival direction of the signals: from above, horizontal or from below. There are six meters between two parallel LPDAs. We take station A as an example and present the time differences between ch2, where the pulse arrives first, and ch0, where the pulse arrives last. The HP signal would have the largest time difference, corresponding to $\Delta t \approx 26$ ns. The bounce pulse would arrive from below with a direction determined from the distance to the transmitter dipole and the ice thickness, corresponding to $\Delta t \approx 15$ ns. Pre-pulses would be incident from above. Assuming the Brewster angle the time difference corresponds to $\Delta t \approx$ 16 ns, while using the critical angle the difference results in $\Delta t \approx 20$ ns. The
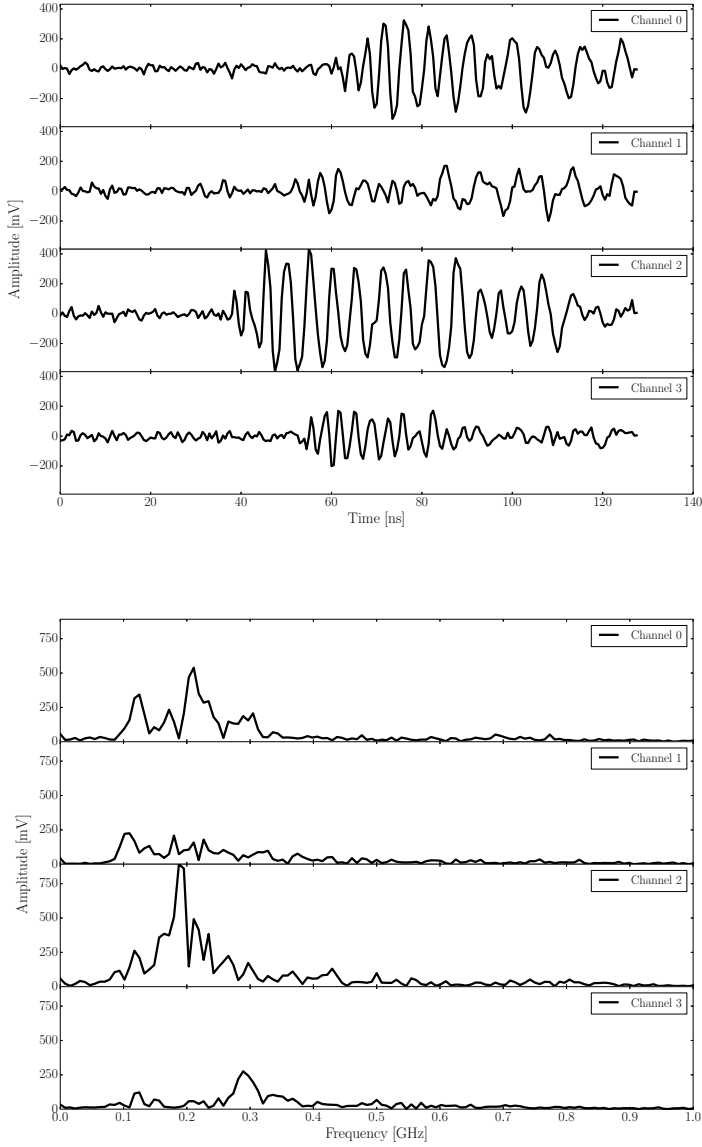
Figure 9.6. Station A: a typical received event, divided in the signals which each channel recorded (upper plots) and the corresponding DFFTs (lower plots). This signal arrived from the transmitter dipole, it is strong and visible in all four channels. The signals arrive in the expected time sequence: [1] ch2; 2) ch1 & ch3; 3) ch0].

bounce time differences vary depending on the station's distances, pre-pulse time differences depend entirely on the incident angle from above and the time differences for HP pulses are expected to be the same for stations with the perpendicular setup. For stations at an angle to the beam the values are somewhat different. To determine if the observed signals were bounce- or HP-pulses the times between the antennas were compared for all stations to the expected time differences. The result was compatible with the HP-hypothesis and disfavored the bounce hypothesis, see figure 12 in paper [62] for details. Note that the pre-pulse hypothesis is not represented in the figure, because those pulses were not characterized at that time.

The frequency domain of station A in figure 9.6 shows major contributions between 100 MHz and 400 MHz. All channels have peaks at $\sim$ 100 MHz. The two strongest signals (ch 0 and ch2) display a main peak close to 200 MHz. The frequency content of these signals is compatible with the horizontally propagating pulses as characterized in section 9.1.1. Channel 1 shows various peaks with similar signal strength at 100 MHz and close to 200 MHz, while channel 3 has a main peak at around 300 MHz. Due to the geometry of ch1 and ch3 these LPDAs are expected to receive a weaker signal, see figure 9.5. The frequency content of these channels can be explained by a combination of the signal that gets scattered and reflected towards the direction of these antennas and the tines which managed to picked up the signal. For the antennas in the parallel configuration the pulses show the expected behavior for the pulse start time and amplitudes but the details of the time and frequency distributions are not fully understood. Another effect has to be also mentioned: as soon as the signal reaches the first LPDA, the signal received by all other channels is influenced by this antenna. This effect continues when the next LPDA(s) is(are) reached by the signal due to the cross-talk of antennas. This effect should be negligible for the stronger signal in perpendicular oriented LPDAs but it may influence the antennas in the parallel configuration more.

The pre- and bounce-pulses had much smaller amplitudes compared to the HP-pulses in the dipole to dipole and dipole to LPDA measurements. The stations have a trigger threshold of about 100 mV, which means that the amplitudes of the pulses must reach this threshold in two channels in order to be recorded. The possibility to record a pre-pulse is thus dependent on distance, therefore, close stations have a better possibility to observe the pre-pulse than distant stations. We will discuss the observations of the two closest stations G and F, starting with station F, the second closest station with a distance of 606 m.

Figure 9.7. Station F, typical observed event. Upper plot: time domain divided by channels. Lower plot: frequency domain (DFFT) divided by channels.
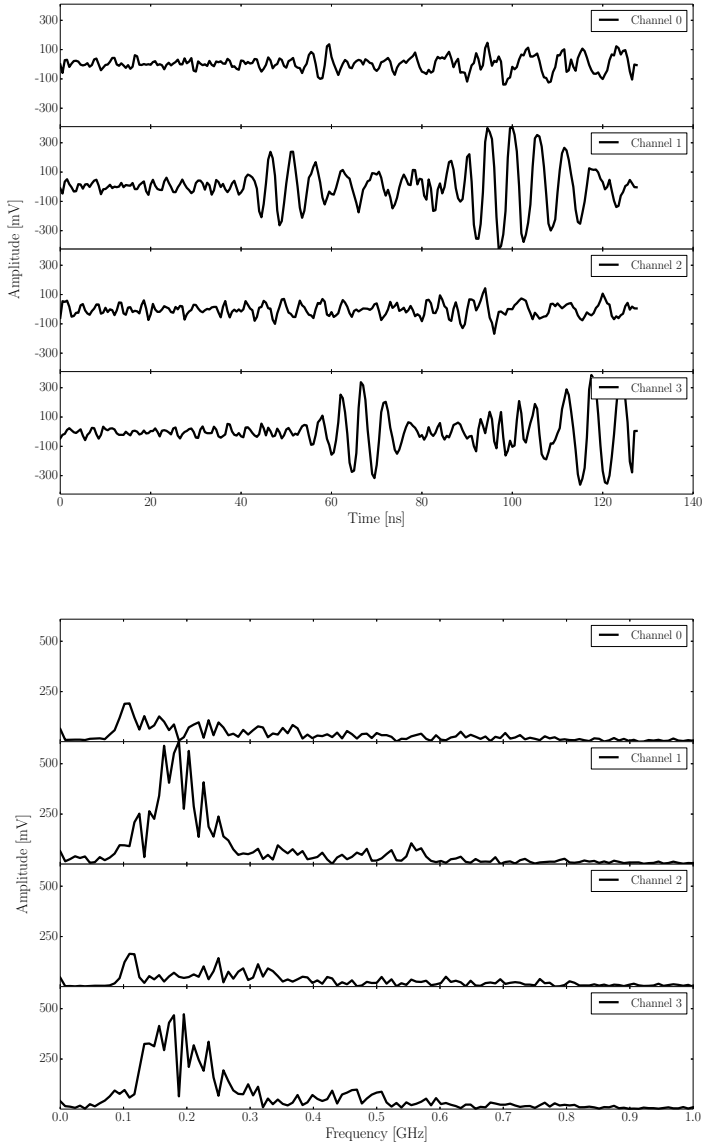
Figure 9.8. Station F: event recorded with 6 dB attenuator on PCD. Otherwise the conditions were the same as above. Upper plot: time domain divided by channels. Lower plot: frequency domain (DFFT) divided by channels. The signals arrive close to the expected time sequence: [1] ch1; 2) ch0 & ch2; 3) ch3].
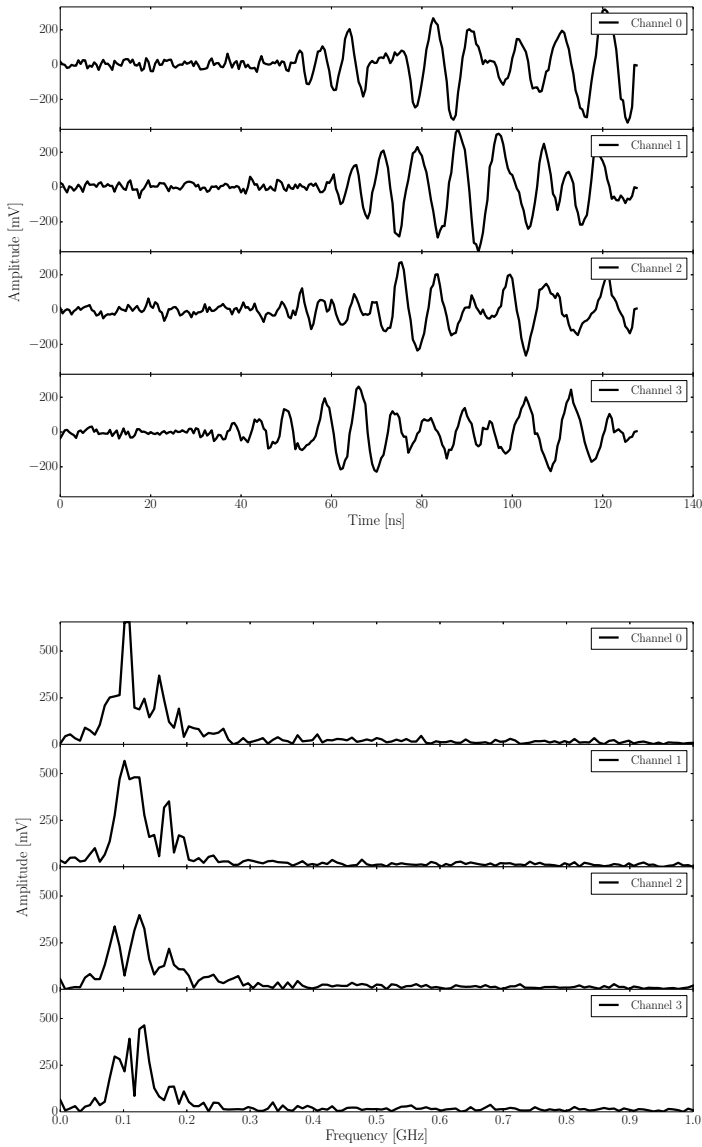
Figure 9.9. Station G: typical event, exclusive occurrence. This event is not consistent with HP events because of its low frequency content. Upper plot: time domain divided by channels. Lower plot: frequency domain (DFFT) divided by channels. Station distance: 347 m.

Station F recorded two different types of pulses, depending on the attachment of a 6 dB attenuator on the PCD. In the time window without the attenuator[4] station F showed typical events with significant frequency contributions at low frequencies around 100 MHz only, see figure 9.7. The amplitudes of these events was very low ($\sim$ 150 mV) compared to station A ($\sim$ 350 mV) and other stations, see section 9.3. These pulses are comparable with the characteristics of pre-pulses or bounce pulses, see section 9.1.1. It is hard to determine the arrival order of the signals in figure 9.7, which is another argument that these events arrived either from above or from below.

When the 6 dB attenuator was connected to the PCD the low frequency signals were suppressed and events with high amplitudes, comparable to the ones in station A, are observed, see figure 9.8. The main frequency content is close to 200 MHz in the two LPDAs perpendicular to the Tx signal (ch1 & ch3), which is comparable with the HP-pulse characterization. Interesting is the double pulse structure, which is likely due to reflections and interferences. The appearance of the double structure in the stronger signal indicates that the two pulses traveled different paths.

Station G is the closest station to the transmitter dipole and triggered exclusively on low frequency events and a typical event is displayed in figure 9.9. The frequency domain shows a main contribution around 100 MHz. The pulses are strong in amplitude (300 mV), which can be explained with the close distance of 347 m to the Tx. These pulses are consistent with either pre-pulses or bounce pulses. When the 6 dB attenuator was attached, it was not enough attenuation to suppress the low frequency signals, so they just reduced in amplitude. The signal arrival order was consistent with pulses from the transmitter direction [1) ch3, 2) ch0 & ch2, 3) ch1].

It is unlikely that the low frequency events are a bounce pulses, because the pre-pulses reach the stations first, and due to the close distance they have enough power to trigger the stations.

Low frequency events, besides other unusual events, were occasionally observed by other stations as well and are presented in the appendix A. Especially the behavior of station F is further confirmation for the hypothesis that the typically recorded signals in the other stations are horizontally propagating pulses.

---

[4]This refers to one of the time windows which is used for the event selection and the following analyses.

9.3 Station and Event Selection for the Determination of the HP Attenuation Length

The setup of the LPDAs and channels is the same for each station, see figure 9.5 for setup and location of the stations. The stations A, C, E, G, F and X have LPDAs with the perpendicular configuration regarding the signal direction, which we are interested in. The LPDAs of the station B, D and Y have a less fortunate angle of about $45°$ to the transmitter direction. However, even for these stations, all four channels registered pulses from the transmitter.

Table 9.3. *Selected stations for the determination of the horizontal propagation attenuation length with the number of used events.*

station	events
A	231
B	501
C	366
D	221
E	341

The stations X and Y have a different antenna layout and a different sampling rate of $1\,\mathrm{GHz}$[5], see section 7.1. For this reason they are excluded for the determination of the horizontal propagation attenuation length. The two closest stations G and F triggered on pulses which did not fit the HP-profile during the pulser time windows selected for the following analyses, see figure 9.9 and figure 9.7. These signals are compatible with pre-pulses because of the amplitude and the frequency content. In section 9.2.1 it was discussed that station F observed HP signals when a $6\,\mathrm{dB}$ attenuator was attached. Although station F was initially discussed to be included, it was decided to exclude it due a different time window and the need of an attenuator correction. Station G was not taken into account because it did not register HP events. The remaining stations are summarized in table 9.3 including the number of selected events. The number of events depends on the event selection, described below, but is also limited if a station happened to be in communication mode when the pulses were emitted.

Only events which agreed with the criteria of horizontal propagation events were selected. Typical events are displayed and described for station A (figure 9.6), B (figure 9.10), C (figure 9.11), D (figure 9.12) and E (figure 9.13). For the determination of the attenuation length for horizontal propagation we selected events which were observed when the transmitter dipole was at $19\,\mathrm{m}$

---

[5]This sampling rate leads to the time record of $256\,\mathrm{ns}$, as compared to the HRA stations with a sampling rate of $2\,\mathrm{GHz}$ and a record of $128\,\mathrm{ns}$.
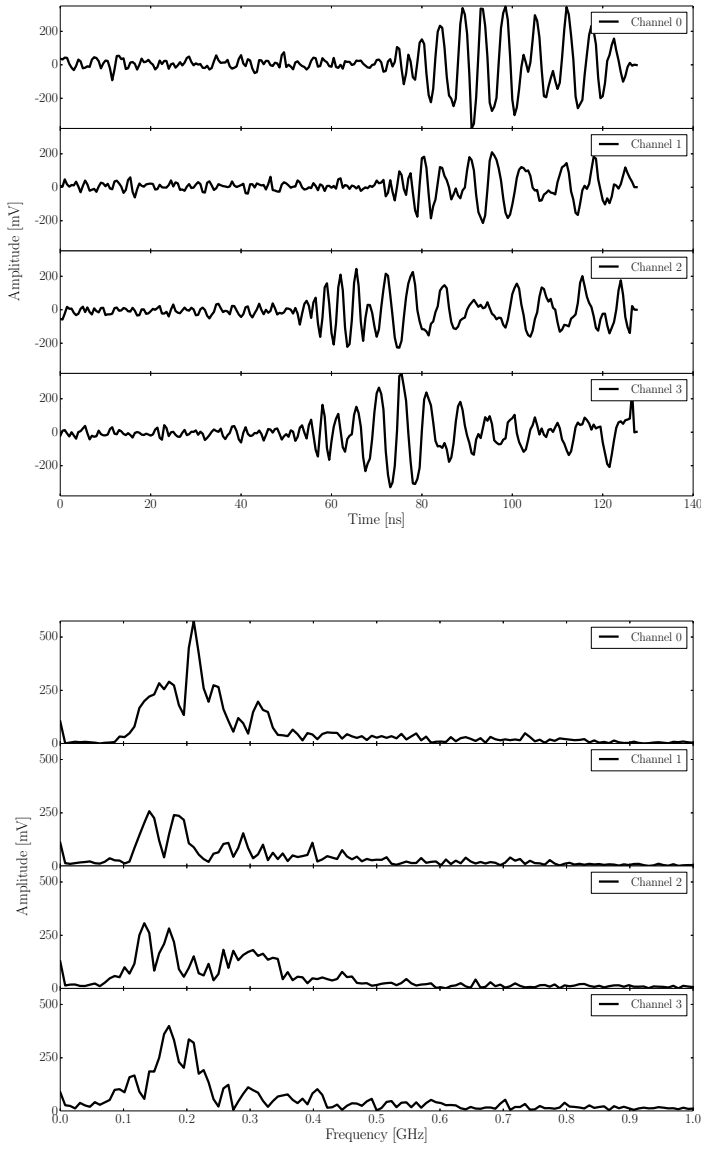
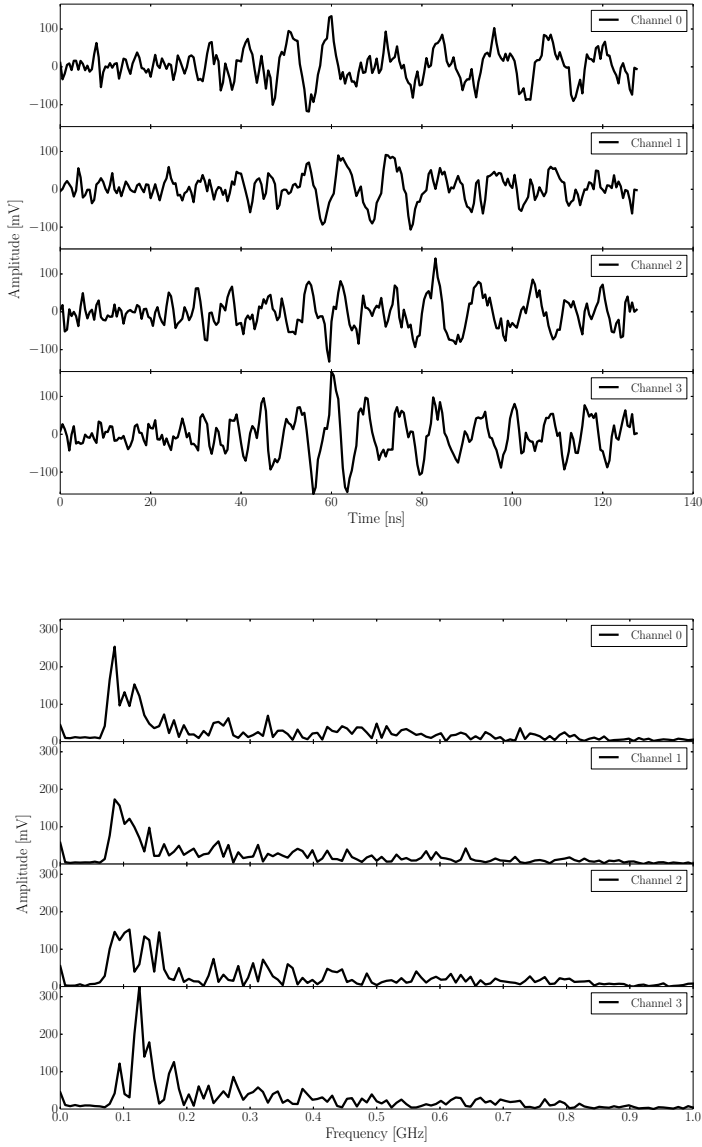*Figure 9.10.* Station B: typical event. Upper plot: time domain divided by channels. Lower plot: frequency domain (DFFT) divided by channels. The signals arrive in the expected time sequence: [1) ch2 & ch3 2) ch 0 & ch1]. There is a strong contribution close to 200 MHz in ch0 and ch3. The other two channels show peaks close to 200 MHz as well. A double pulse structure can be observed, likely due to reflections and interference. These events are identified as HP events.
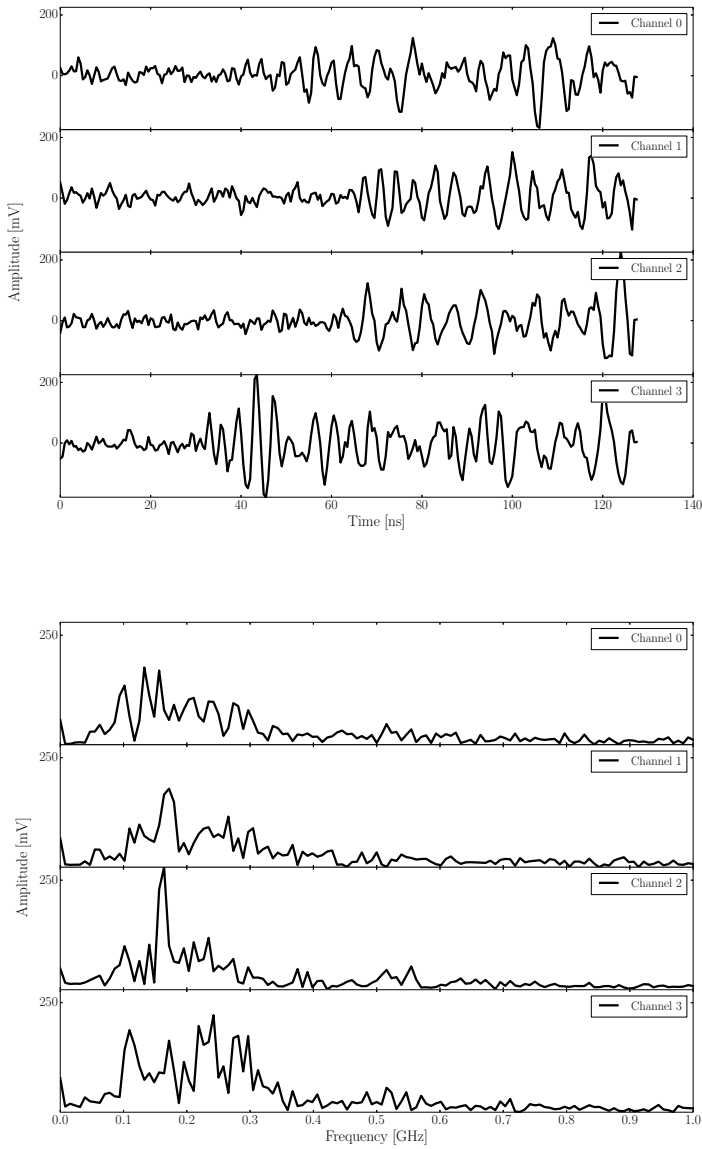
Figure 9.11. Station C: typical event. Upper plot: time domain divided by channels. Lower plot: frequency domain (DFFT) divided by channels. It is the furthest station. Most signals arrive close to the expected time sequence: [1) ch3; 2) ch0 & ch2; 3) ch1]. Contributions in the frequency domain are close to 200 MHz in all channels. These signals are compatible with HP-pulses.
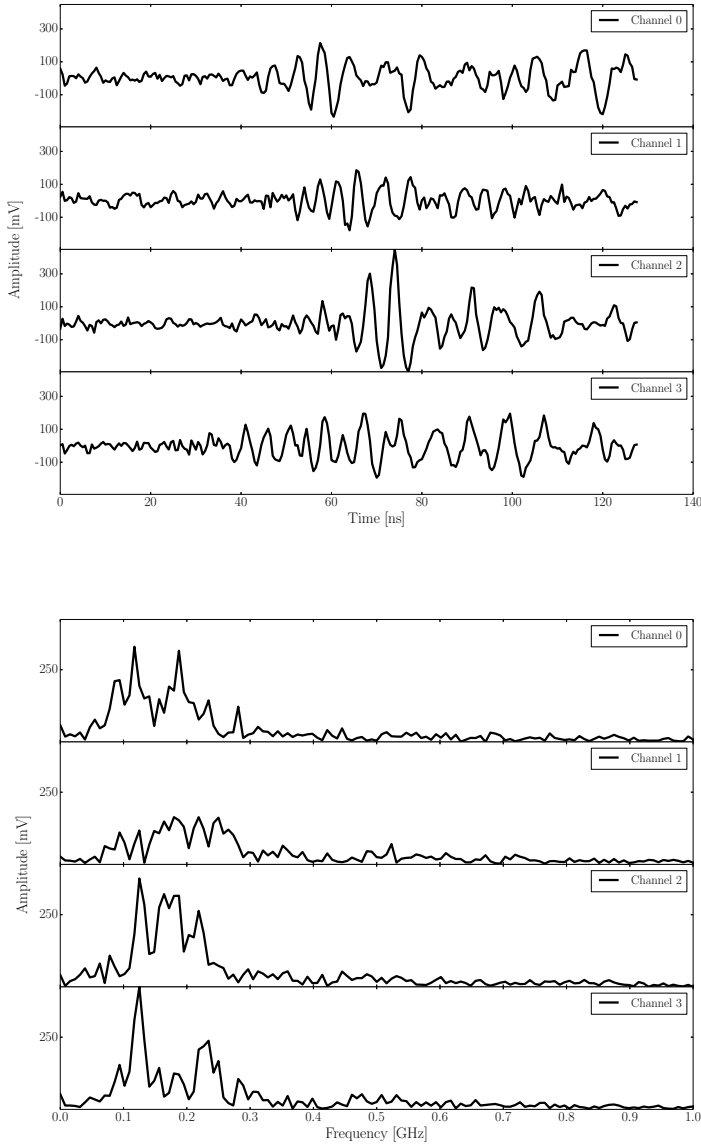
Figure 9.12. Station D: typical event. Upper plot: time domain divided by channels. Lower plot: frequency domain (DFFT) divided by channels. The signals arrive close to the expected time sequence [1) ch3 & ch0; 2) ch1 & ch2]. Although the peaks around 100 MHz exceed the peaks at 200 MHz, the contribution close to 200 MHz is clearly visible. These signals can be compared to the pulse from the oscilloscope, see figure 9.4, which also had major contributions around 100 MHz. Pre- and bounce pulses never showed high frequency contributions, which makes these consistent with HP-pulses.
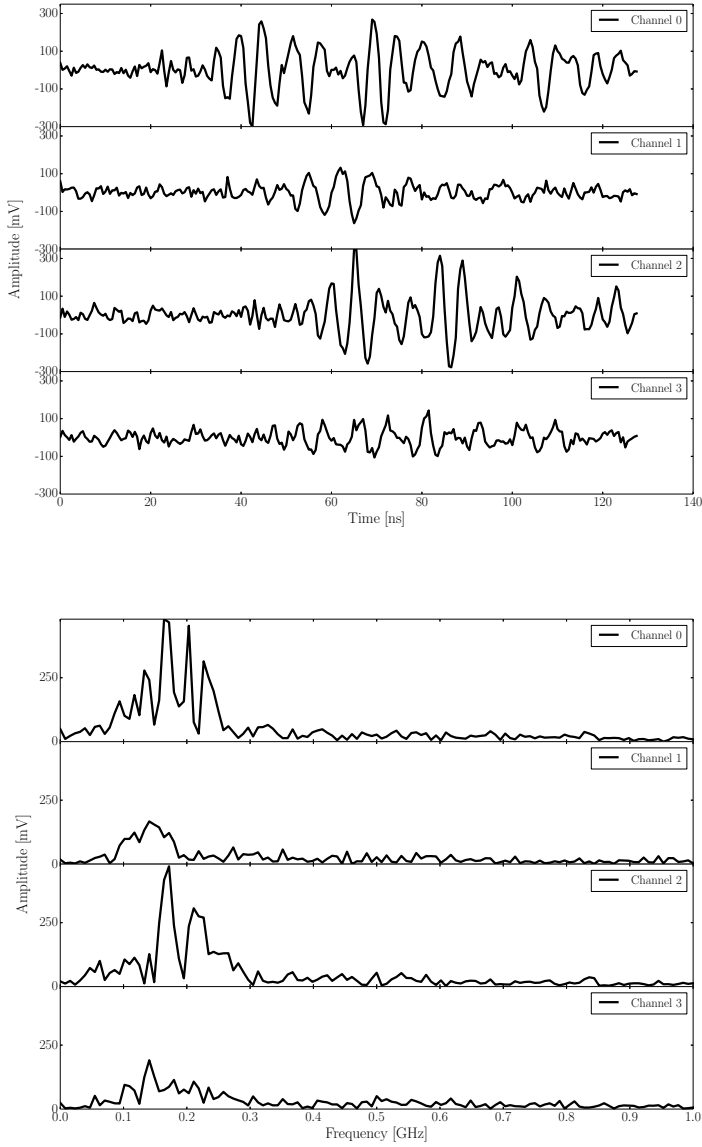
Figure 9.13. Station E: typical event. Upper plot: time domain divided by channels. Lower plot: frequency domain (DFFT) divided by channels. The signals arrive close to the expected time sequence: [1] ch0; 2) ch1 & ch3; 3) ch2]. There is a strong contribution close to 200 MHz in ch0 and ch2. The other two channels show contributions around 200 MHz as well, with peaks at lower frequencies. A double pulse structure can be observed in ch0 and ch2, likely due to reflections and interference. These events are identified as HP event.

depth. All forced-trigger waveforms were removed from the samples. The pulser was set to send out signals every 2 s and to ensure to select only these events, only signals with a time difference of 2 s were chosen. It has to be noted that several stations observed events which were not compatible with HP-signals but certainly originated from the transmitted dipole. These events are discussed in appendix A for all stations.

For stations with a perpendicular setup with regard to the Tx such as A, C and E the requirement was that both perpendicular channels had their main frequency contribution between 150 MHz and 250 MHz. For the stations which have the LPDAs at a 45° angle to the signal direction (B and D) it was sufficient if one channel had its peak in this frequency range. This extended frequency range was chosen because the main peaks vary within this range from channel to channel. The analyses performed with this selection are described in chapter 10.

10. Result: Attenuation Lengths for Horizontal Propagation

Analyses are performed under two different hypotheses in order to determine the electric field attenuation length and to investigate the impact of dispersion. The results will be presented and discussed below.

10.1 Attenuation Lengths

Table 10.1. *Chosen stations with their horizontal distance to the Tx borehole (dist) and the number of selected events. The S stands for the oscilloscope measurement and the numbers were rounded to two significant digits. The average of the maximum amplitude (peak) and the sum of amplitudes between* $150\,\text{MHz}$ *and* $250\,\text{MHz}$ *in the frequency domain (sum) and their uncertainties (err) are presented.*

station	dist [m]	events	peak [mV]	± err [mV]	sum [mV]	± err [mV]
S	100	1	$32 \cdot 10^3$	$2 \cdot 10^3$	$640 \cdot 10^3$	$39 \cdot 10^3$
A	953	231	370	12	4128	157
B	1311	501	394	13	3418	136
C	1433	366	183	14	1412	80
D	1189	221	330	16	2389	98
E	767	341	302	16	2866	117

For each event in one station, the maximum amplitudes (peaks) of every channel are determined. The next step depends on the station location. For stations with LPDAs in the perpendicular setup (A, C and E), there are two main channels with a strong signal. The peaks of these two channels are averaged, while the other two channels are ignored. For stations with LPDAs at $\sim 45°$ regarding the signal direction (B and D), the peaks of all channels are averaged. After an average peak amplitude is established for every event, the distribution of all these peak amplitudes for all events within one station is evaluated by fitting a Gaussian curve through the distribution. The mean and sigma of this distribution correspond to the peak and error presented in table 10.1.

In the frequency domain the amplitudes of the DFFT were summed between $150\,\text{MHz}$ and $250\,\text{MHz}$, which corresponds to 12 bins in every channel. The

resulting summed amplitudes were then treated in the same way as the peak evaluation. These summed amplitudes were averaged within one event over the appropriate channels, and the sum and uncertainties correspond to the mean and σ of the Gaussian fit through the distribution of the sums in every station.

We have only one measurement from the oscilloscope, and the same method of determining the peak, the sum and the respective uncertainties cannot be applied. As an educated guess it is reasonable to choose an uncertainty which corresponds approximately to the stations' uncertainties, which are between 4% and 5% of their peak or sum values. We choose a slightly larger value of 6% for the oscilloscope measurement to be conservative.

It was investigated how large the contribution of the sum in the 150 MHz - 250 MHz range is compared to the total summed amplitude of the DFFT. Both the channels and the oscilloscope DFFT had a total of 128 bins and the signal frequency range consisted of 12 bins. The total summed amplitudes were treated in the same way as described above and the result was compared to the signal sum in every station. The values range between 30% to 45%. The exception is the pulse registered with the oscilloscope with 21%. This pulse has larger contributions outside the signal frequency band in comparison to the stations, which explains the discrepancy.

The first hypothesis we investigate assumes that the amplitude of horizontally propagating signals should fall like $1/r$. That means that the voltages V for the peaks and sums in table 10.1 should follow:

$$V = \frac{V_{ff}r_{ff}}{r} \cdot e^{C-\frac{r}{\lambda}} \tag{10.1}$$

where r is the station distance, λ is the attenuation length, C is a constant and V_{ff} is the amplitude at the far-field distance r_{ff} from the transmitter dipole, which is about 3 m for 200 MHz, see equation 8.3. Since we do not have these measurements the amplitudes were normalized to the values obtained at station A for the sum- and peak-analysis respectively. In order to determine the attenuation length for horizontal propagation we want to perform a linear regression and hence transform equation 10.1 to:

$$\ln\left(\frac{Vr}{V_A r_A}\right) = s \cdot r + C \tag{10.2}$$

where V_A is the voltage in station A, r_A is the distance of station A to the transmitter dipole, and $s = -1/\lambda$. The linear regression was performed for the peaks (triangles) and sums (circles), assuming the values in table 10.1 are exact and the results are displayed in figure 10.1. The first data points at 100 m distance are the values derived from the oscilloscope pulse. The oscilloscope
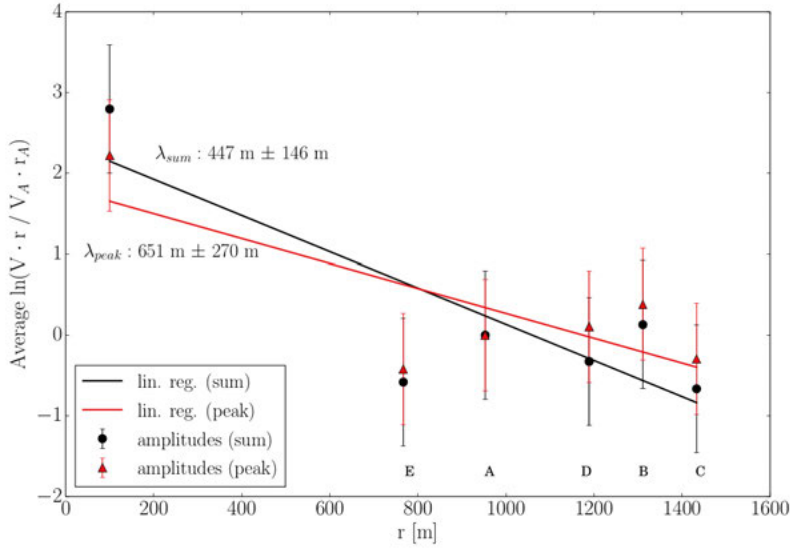
Figure 10.1. This plot represents the electric field attenuation of the horizontal propagation events measured by the selected stations under the hypothesis that the amplitude reduces with distance like $1/r$. Two different analyses are applied using the peak of the waveforms (triangles) and the summed DFFT amplitudes between 150 MHz and 250 MHz (circles). The first points at 100 m represent the oscilloscope measurements. Linear regressions were performed through the data, resulting in attenuation lengths of 447 m for the sum analysis (black line) and 651 m for the peak analysis (red line). The uncertainties shown are estimated from the residuals obtained in the regression.

signal was folded with the station's amplifier response to be able to compare the observed signals, see section 9.1. No corrections in adjustments of the amplitudes regarding varying firn properties, like constructive or destructive interference depending on station depths, or inconvenient geometry of the LP-DAs were applied to the data, due to lack of exact measurements and models.

The results of the linear regression are shown in table 10.2 and the resulting attenuation lengths are 447 m $\pm$ 146 m for the sum calculation and 651 m $\pm$ 270 m for the peak calculation. The uncertainties on the attenuation lengths were propagated with the Gaussian error propagation. The attenuation lengths are consistent within the uncertainties. The error bars of the data points in figure 10.1 were estimated based on the performed regression using an ideal reduced χ^2-test value ($\chi^2_{red} = 1$) to compensate for the unknown systematic effects.

For the sum-analysis it has been investigated how much the frequency borders influence the results, by shifting the boundaries to various lower and

higher frequencies, keeping 200 MHz central. The changes yielded no significant change of the attenuation length, within the uncertainties. The results for both analyses are driven by the oscilloscope measurement, which shows much higher amplitudes than the stations. This measurement was treated to be as comparable to the stations' measurements as possible. However, it was obtained and handled differently, considering that the amplifier response was folded in and no noise reduction was performed as it has been for the stations, see section 9.2. In paper [62] the sum-analysis was called integrated analysis[1] and the data points were not normalized, which does not influence the linear regression.
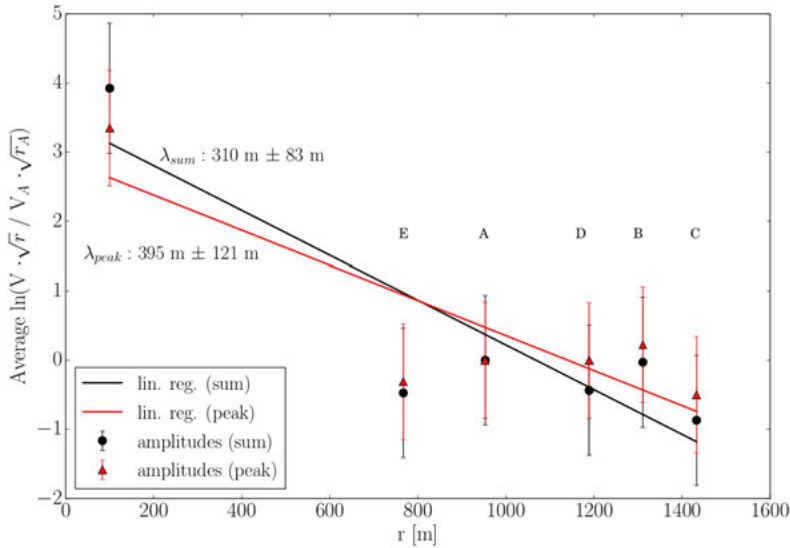
Figure 10.2. This plot represents the electric field attenuation of the horizontal propagation events measured by the selected stations under the hypothesis that the amplitude reduces with distance like $1/\sqrt{r}$. Two different analyses are applied using the peak of the waveforms (triangles) and the summed DFFT amplitudes between 150 MHz and 250 MHz (circles). The first points at 100 m represent the oscilloscope measurements. Linear regressions were performed through the data, resulting in attenuation lengths of 310 m for the sum analysis (black line) and 395 m for the peak analysis (red line). The uncertainties shown are estimated from the residuals obtained in the regression.

The second hypothesis we consider is the assumption that horizontal propagation pulses decrease in amplitude geometrically like $1/\sqrt{r}$. This hypothesis is based on the idea that HP signals could move along a layer within the firn, similar to pre-pulses along the surface. The analyses to obtain the attenuation

---

[1]It was only named integrated analysis, the procedure of deriving the data was the same.

lengths remained the same and the result can be seen in figure 10.2. These attenuation lengths are shorter: $\lambda_{sum_{1/\sqrt{r}}} = 310\,\text{m} \pm 83\,\text{m}$ for the sum analysis and $\lambda_{peak_{1/\sqrt{r}}} = 395\,\text{m} \pm 121\,\text{m}$ for the peak calculation. Within the uncertainties also these values are compatible with each other. The regression parameters can be found in table 10.2.

Both hypotheses $1/r$ and $1/\sqrt{r}$ give reasonable results. The attenuation lengths without the oscilloscope measurement would lead to much larger values, hence, the results presented are conservative for both hypotheses, representing lower limits on the attenuation length. The $1/\sqrt{r}$ assumption leads to more conservative attenuation lengths in comparison to the $1/r$ hypothesis. However, the $1/r$ expectation has larger uncertainties which cover the attenuation lengths of the $1/\sqrt{r}$ hypothesis. We have to conclude that more data is needed in order to identify the correct hypothesis.

Table 10.2. *Linear regression results for slope and offset for the attenuation length for the sum- and peak-analysis respectively.*

hypothesis	parameter	sum	peak
$1/r$	slope s [1/m] $\times 10^{-3}$	-2.239 $\pm$ 0.731	-1.537 $\pm$ 0.637
$1/r$	offset C	2.37 $\pm$ 0.77	1.80 $\pm$ 0.67
$1/\sqrt{r}$	slope s [1/m] $\times 10^{-3}$	-3.231 $\pm$ 8.662	-2.529 $\pm$ 0.773
$1/\sqrt{r}$	offset C	3.45 $\pm$ 0.91	2.88 $\pm$ 0.82

The attenuation length for horizontally propagating pulses can also be derived from RICE data [62]. It turns out that RICE also did observe signals in the classically forbidden zone at a distance of over 3 km which results in an attenuation length of $542\,\text{m} \pm 16\,\text{m}$, compatible with the $1/r$ result of ARIANNA. However, one must consider that attenuation lengths are in general larger at the South Pole, due to colder temperatures. RICE also saw pulses which arrived faster than the expected HP signals, denoted as air pulses in paper [62].

The detectability of horizontally propagating signals leads to an increased effective detector volume. A preliminary estimation of the additional volume for ARIANNA was performed in [174] and results in about 40% for Moore's Bay and around 90% for the South Pole. For both sites a substantial part of the expected neutrino signals arrive at angles close to the horizon. The reason why the relative gain in volume is smaller for Moore's Bay is because the effective volume is larger from the outset, given the sensitivity for downgoing neutrinos, due to the radio signals being reflected at the ice/water interface, besides the sensitivity for the near horizon band.

10.2 Summary and Conclusions

Observations from ice studies performed with ARIANNA on the Ross Ice Shelf in the season 2016/2017 were described in detail and analyzed. Propagation effects of radio waves from dipole to dipole and dipole to LPDA were classified and identified as pre-pulses, horizontal propagation pulses, and bounce pulses.

The signals emitted by the transmitter dipole were observed in all stations with antennas below the firn surface. These signals were identified to be most likely horizontally propagating pulses. A station and event selection was performed and the chosen events were used, together with the oscilloscope measurements with an LPDA receiver, to perform analyses under two hypotheses. Attenuation lengths for horizontally propagating signals in the Ross Ice Shelf were derived. The fist hypothesis was that the signal amplitude of HP pulses decreases with distance like $1/r$. The attenuation length derived with the average maximum peak values of the selected events resulted in $\lambda_{peak} = 651\,\text{m} \pm 270\,\text{m}$ and the analysis summing over the signal frequency range, resulted in $\lambda_{sum} = 447\,\text{m} \pm 146\,\text{m}$. The second hypothesis assumed an amplitude reduction as $1/\sqrt{r}$ and resulted in $\lambda_{sum_{1/\sqrt{r}}} = 310\,\text{m} \pm 83\,\text{m}$ and $\lambda_{peak_{1/\sqrt{r}}} = 395\,\text{m} \pm 121\,\text{m}$. Within each hypothesis the two results are compatible with each other considering their uncertainties. With the given data it is not possible to differentiate which hypothesis is correct. The results under the $1/r$ expectation are comparable with the HP attenuation length of $542\,\text{m} \pm 16\,\text{m}$ determined by RICE for the South Pole. However, it has to be considered, that attenuation lengths at the South Pole are in general expected to be longer than at Moore's Bay. These results provide evidence for horizontally propagating electromagnetic waves far beyond the classically shadowed zones. The HP attenuation lengths are in agreement with the vertical attenuation lengths determined at Moore's Bay for bounce pulses ($300\,\text{m}$ to $500\,\text{m}$). The obtained attenuation lengths with these analyses are guided by the oscilloscope measurement and can therefore be considered as conservative lower limits.

HP implies a gain in effective volume for radio neutrino observatories working with antenna receivers below the firn. To estimate the exact impact, further data and investigations are needed. It is important to understand how much power these horizontally propagating events carry if observed with an LPDA receiver in optimal configuration regarding the signal direction. Therefore, it would be necessary to investigate the polarization of these pulses, and how much of it is preserved over distance, since it is expected it may be scrambled due to reflections and scattering in the firn.

Besides the HP-signals, the pre-pulses were characterized and two possible explanations regarding their nature were found, they could be either surface

waves or lateral waves. Both waves travel along the surface with the speed of light in air. With the performed measurements it is not possible to differentiate them. However, the measurement of these pulses is in itself a great achievement, because it is experimentally challenging to observe them between firn and air. Only after ARIANNA discussed the observation of horizontally propagating signals and pre-pulses, other experiments like RICE and GNO reanalyzed their previously taken data with respect to these signals, observing both HP- and pre-pulses.

Many ARIANNA stations occasionally observed events, which could not be classified as horizontally propagating signals, but originated from the transmitter dipole. These events are summarized in appendix A. Some of these events can be categorized as either pre-pulses or bounce pulses. With absolute timing it would be possible to identify these events, but considering that the pre-pulses arrived faster and carried more power than the bounce pulses in the dipole-to-dipole measurements it is likely that these signals were pre-pulses. If the hypothesis that the stations successfully observed pre-pulses can be confirmed in future, this would be the first observation characterizing the pre-pulses. Data from RICE and GNO suggest observation of pre-pulses as well, but no emphasis was given to these signals. The successful observation of pre-pulses would confirm the proposal that these waves can be used for neutrino astronomy and therefore increase the sensitivity of observing the expected neutrino flux at the highest energies of the spectrum [181].

10.3 Outlook

Further measurements were taken in the seasons 2017/2018 and 2018/2019 at Moore's Bay and with the stations at the South Pole. These measurements are currently analyzed. The new data is taken with variations of transmitter and receiver antenna to analyze the signal properties and propagation. Different depths and distances are being used to investigate the effect of changing firn conditions. The limitations due to lack of absolute timing for the ARIANNA stations are overcome by using an oscilloscope that can be triggered on distances of up to 1 km by using a long cable. This setup allows to study the full time interval from the emission of the signal until the last signals reflected on the ice/water interface have been detected in stations with distances up to 1 km. Reachable depths for LPDA antennas are still limited by the necessity to manually shuffle snow but tools using electric power from a portable generator are being developed and will allow for more variations in antenna orientations and depths. Additionally, models and simulations of the various signal propagation modes are developed and compared to the data, gaining accuracy with accumulated data.

The pre-pulses were "discovered" as a byproduct of measurements designed to investigate horizontal propagation. Analyses with the available data were performed, but more measurements are needed. These signals could be used for neutrino detection and are further investigated by the ARIANNA collaboration.

The radiation pattern of Askaryan signals is rather different from that of dipole antennas. It would thus be of interest to verify that the model for propagation as obtained from studies using dipoles can be applied to Askaryan pulses. This could be achieved by using an antenna which was designed to mimic Askaryan radiation [133].

For the future of in ice radio detection of neutrinos important conclusions from both the ARA and ARIANNA projects are being drawn. Both were prototype projects that allowed testing of the concept and learning important lessons, backgrounds, triggering, technical implementation and reliability as well as e.g. the existence of horizontal propagating signals which are described in this thesis. The groups are investigating the best way towards a large scale in ice radio-based neutrino detector, the discussion is ongoing.

The future of extreme high energy neutrino astronomy is bright and hopefully we will be able to build successful detectors to observe cosmogenic neutrinos, further investigate them and come closer to the answers to long asked questions regarding the acceleration processes, the GZK mechanism and maybe even discover new physics.

Appendices

A. Unusual Events Seen at ARIANNA Stations

The stations also triggered on pulses which were not forced noise triggers and inconsistent with horizontally propagating pulses as defined in this thesis. See section 9.1.1 for the HP- pre- and bounce-pulse definitions, section 9.2.1 for the derivation of the conclusion that the stations triggered on HP signals, and section 9.3 for a visualization of typical HP events in selected stations (A-E). The signals described below are not understood yet and we can only speculate about their classification, however for the future it is important to describe and report them. For easier understanding of this Appendix we will call events consistent with HP-pulses *usual* and all other signals *unusual*. For a single station events can be *typical*, due to their main occurrence, and *untypical*, because of their rare occurrence, however, both event classes can be unusual for ARIANNA, because most events observed in most stations were usual HP-events. Furthermore, main channels always refer to the two antennas of one station with the perpendicular setup[1] to the signal direction, where the most power is registered for the usual events.

Before describing the events in more detail, it should be noted that these events arrived within the time window which was used for the HP attenuation length determination. That means, that the transmitter dipole was at 19 m depth sending out radio pulses every 2 seconds. For stations which observed mainly HP events every 2 s, that means that sometimes unusual signals were observed instead of HP-signals. Due to this event "replacement" and because no signals were detected when the PCD was off, it can be assumed that these unusual events originated from the dipole transmitter. Some stations detected only unusual events. All unusual events were excluded from the event selection for the HP attenuation length analyses. Some of the unusual events barely triggered the stations, which have a trigger threshold of about 100 MHz.

Station A

Station A detected mostly HP events as shown in figure 9.6. The untypical signals were characterized by a substantial contribution at high frequencies between 500 MHz and 800 MHz, while the frequency contributions around 100 MHz and 200 MHz were rather consistent with noise ($\sim$ 50 MHz), see figure A.1. The arrival order in the channels was consistent with the expected

---

[1]See section 9.1.

Figure A.1. Station A: untypical event, occurred occasionally. This event is unusual because of its high frequency content and low amplitude. Upper plot: time domain divided by channels. Lower plot: frequency domain (DFFT) divided by channels. Station distance: 953 m.
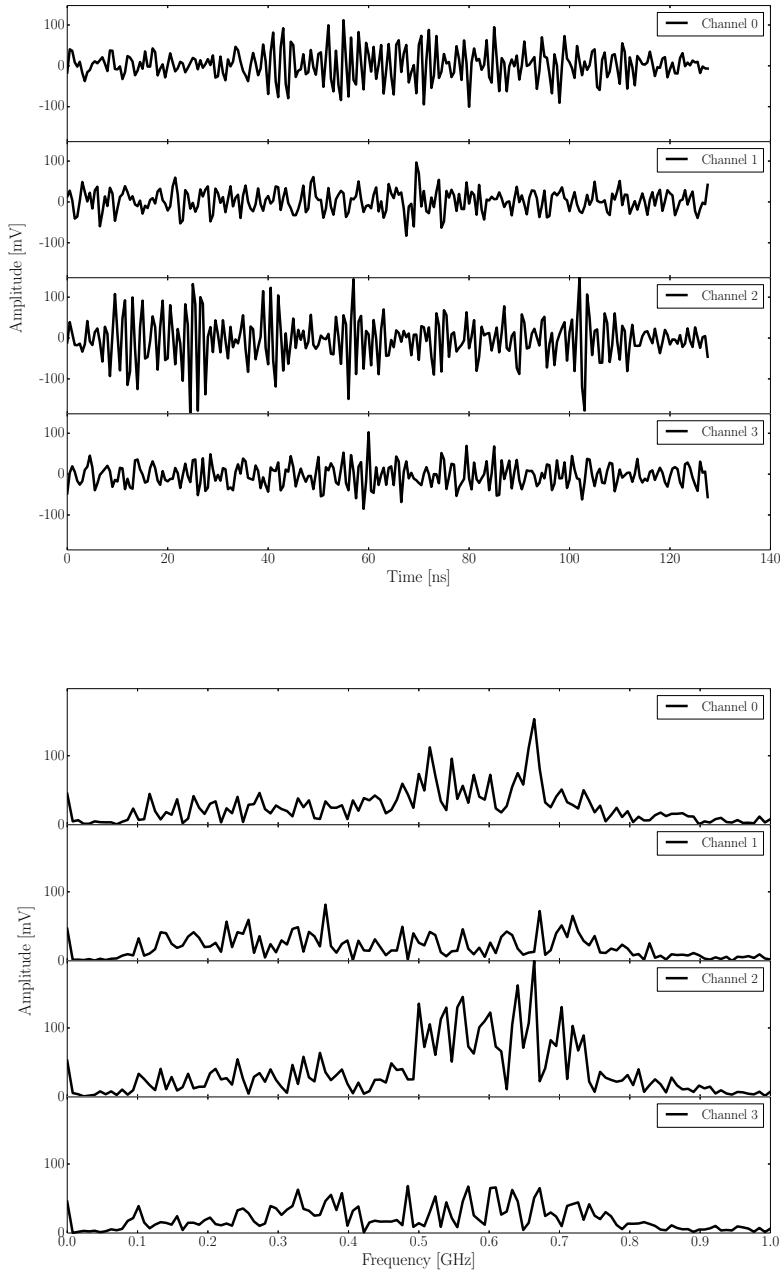
Figure A.2. Station E: untypical event, occurred occasionally. This event is unusual because of its low frequency content and low amplitude. Upper plot: time domain divided by channels. Lower plot: frequency domain (DFFT) divided by channels. Station distance: 767 m.

order from a signal arriving from the transmitter dipole direction [1] ch2, 2) ch1 & ch3, 3) ch0] in the two main channels (ch2 & ch3). For ch1 and ch3 it was hard to determine if a signal was picked up and the start of the waveform. These pulses had a much lower amplitude ($\sim 130\,\text{mV}$) than the HP pulses ($\sim 450\,\text{mV}$). Due to their small amplitude it is suspected that they arrived before the HP signals, otherwise the station would exclusively trigger on the HP pulses. These events have been noticed in station A in previous ice studies as well. Station A was the only station which triggered on signals with such high frequency content. The untypical signals are inconsistent with any pulse definition in section 9.1.1. No low frequency events (with a main contribution at 100 MHz) were observed.

Station B
Station B triggered exclusively on HP signals. Station distance: 1311 m.

Station C
Station C triggered exclusively on HP signals. Station distance: 1433 m.

Station D
Station D triggered exclusively on HP signals. Station distance: 1189 m.

Station E
Station E triggered mostly on HP events as shown in figure 9.13. The untypical events for this station were characterized due to low main frequency contributions and low amplitudes in comparison to the HP events, as presented in figure A.2. The main frequency distribution was located around 100 MHz and the amplitudes were around 100 mV, barely triggering the station. For HP signals the amplitudes were $\sim 300\,\text{mV}$ and the signal arrival order was consistent with pulses from the transmitter direction [1] ch0, 2) ch1 & ch3, 3) ch2]. For these unusual pulses it is hard to identify the beginning of the wave form, which makes it challenging to determine an approximate arrival direction. These pulses show characteristics of pre-pulses and bounce-pulses, see section 9.1.1. Due to the lack of absolute timing it is not possible to determine the exact time of arrival and because of the dead time of 13.33 ms only one of the three pulses could be detected. Because HP pulses have shown to have the most power they should trigger the stations, unless pre-pulses had enough power to trigger a station first. It is unlikely that an HP pulse was skipped, which would allow the possibility that the station triggered on the bounce-pulse. It is more likely that some pre-pulses had enough power to trigger the station prior to the arrival of the HP pulse. These events are comparable to the potentially observed pre-pulses in stations F and G as seen in figure 9.7 and discussed in section 9.2.1.

Station F

Station F triggered exclusively on unusual events during the HP attenuation length analyses time window. Typical events were displayed in figure 9.7 and have the characteristics of pre-pulses. When a 6 dB attenuator was used (in a different time window), the potential pre-pulses had not enough power to trigger the station and signals consistent with HP pulses were observed. The events of station F are discussed in more detail in section 9.2.1. Station distance: 606 m.

Station G

Station G triggered exclusively on unusual events during the HP attenuation length analyses time window. These events were strong and had a low frequency contribution. They were identified to be likely pre-pulses. Station G is discussed in section 9.2.1. Station distance: 347 m.

Station X

As described in section 7.1 station X was a CR station in the season 2016/17 with two antennas pointing up at an angle of $45°$ relative to the surface in direction North (ch0) and West (ch3), respectively. The other two LPDAs were pointing straight down. In comparison to HRA stations (A-G) this station had a record time of 256 ns (1 Gsamples/s)[2], see section 7.3.2.

Typical events in station X showed a double pulse structure with large amplitudes (~ 400 mV), see figure A.3, comparable to the double pulse structures in stations F. The signal amplitude height is comparable to the heights of HP pulses detected in other stations, however the frequency domain shows a main contribution at 100 MHz with a decaying tail up to 200 MHz, rather comparable to pre- or bounce-pulses. This frequency behavior is present in all channels regardless of geometry. The signal arriving order is inconsistent with the expectation for an horizontally propagating signal from the transmitter dipole direction: [1) ch3, 2) ch2 & ch0, 3) ch1]. Although ch3 detects the signal first, it seems that ch1 is the second channel to register the pulse, while it should be the last. It is not excluded that ch0 and ch1 detected the signal at the same time, but ch2 observes it last. Station X was the only station detecting unusual events with these properties, which are not consistent with any pulse definitions presented in section 9.1.1.

Occasionally station X observed untypical events with low main frequency content and low amplitudes, consistent with pre- and bounce-pulses, see figure A.4[3]. For these pulses it is hard to determine the start of the waveform. Also here it is more likely that these signals are pre-pulses, applying the same argumentation as for stations E, F and G. When the 6 dB attenuator was used,

---

[2]In comparison to usual stations with 128 ns time record due to 2 Gsample/s.

[3]Although ch2 detects an amplitude which is always above trigger threshold, a second channel has to be above the threshold for the event to trigger the station. Occasionally ch1 reaches the demanded amplitude.

Figure A.3. Station X: typical event, main occurrence. This event is not consistent with HP events because of its mainly low frequency content. Upper plot: time domain divided by channels. Lower plot: frequency domain (DFFT) divided by channels. Station distance: 825 m.
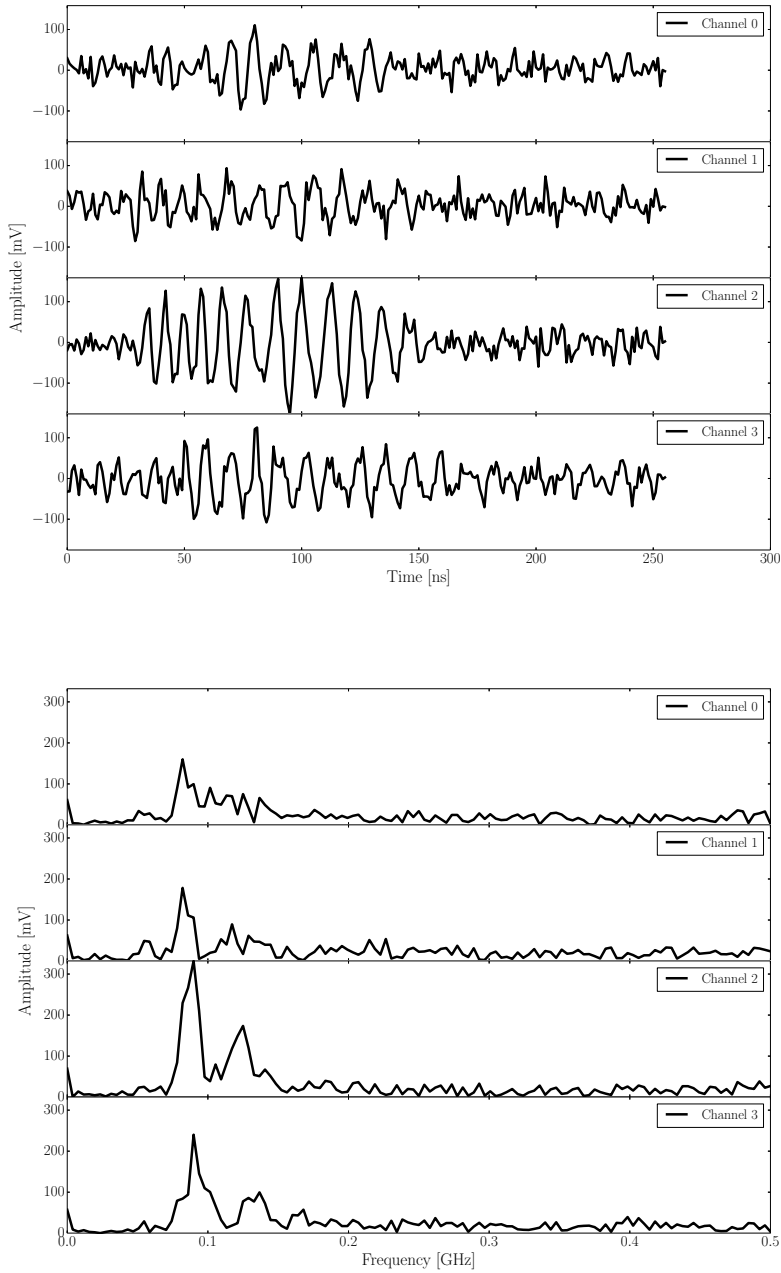
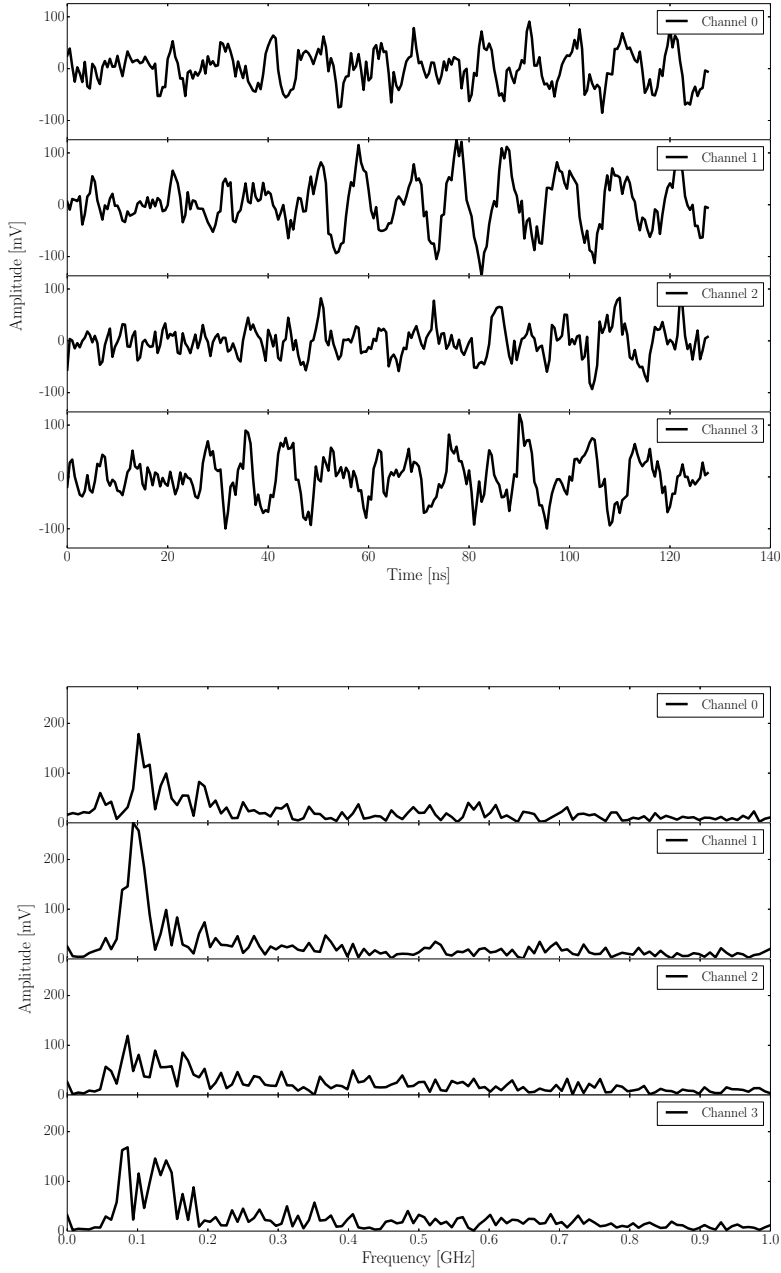*Figure A.4.* Station X: unusual event, occurred occasionally. This event is not consistent with HP events because of its mainly low frequency content. Upper plot: time domain divided by channels. Lower plot: frequency domain (DFFT) divided by channels. Station distance: 825 m.

station X registered exclusively the typical pulses with a decreased amplitude, which supports the hypothesis, that the low frequency signals were pre-pulses, which did have enough power to trigger the station after attenuation.

Station Y

Station Y, also a cosmic ray station like X but with all four antennas pointing up, typically registered pulses consistent with HP signals, see figure A.5. The peak values in the frequency domain of the first hit channels (ch0 & ch3) were around 200 MHz. The signal arrival order is consistent with the expected order [1) ch0 & ch3, 2) ch2 & ch1]. This station was excluded from the analyses because it has a different antenna configuration and record time (256 ns).

Occasionally station Y detected signals peaking at 100 MHz, see figure A.6. These events were consistent with the properties of pre- and bounce-pulses and are comparable to the low frequency events in the stations E, F, G and Y. We apply the same argumentation that these events are more likely pre-pulses, which makes station Y the furthest station to detect potential pre-pulses. We suspect this is possible due to the upward facing antennas, because the highest gain is registered at the nose of an LPDA.
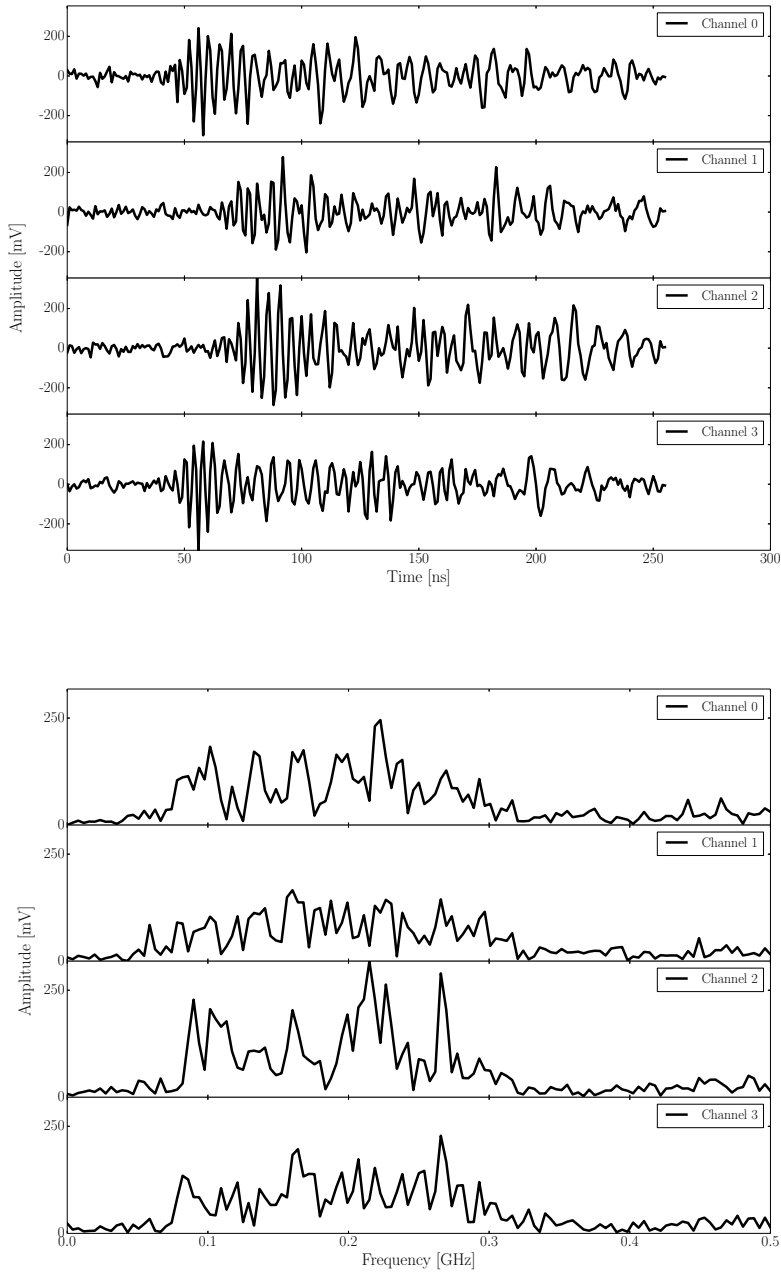
Figure A.5. Station Y: typical and usual event, main occurrence. This event is consistent with HP events. Upper plot: time domain divided by channels. Lower plot: frequency domain (DFFT) divided by channels. Station distance: 1225 m.
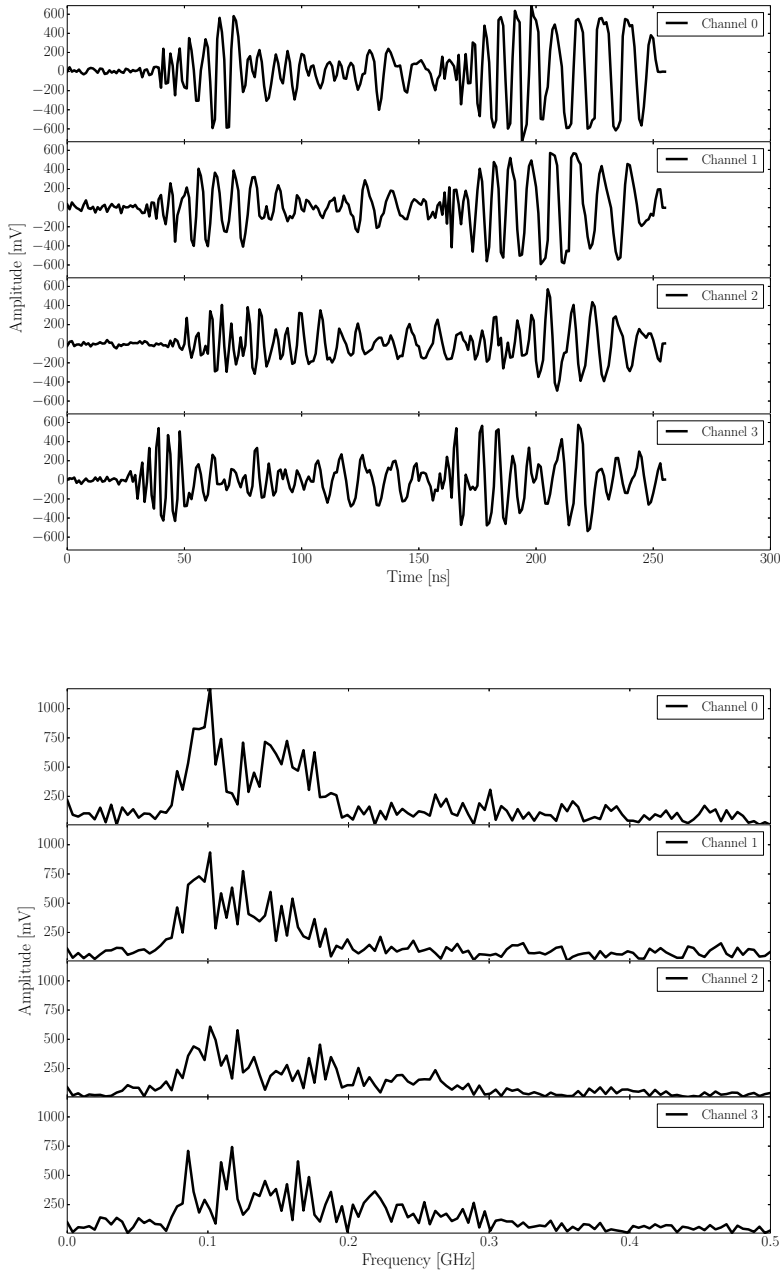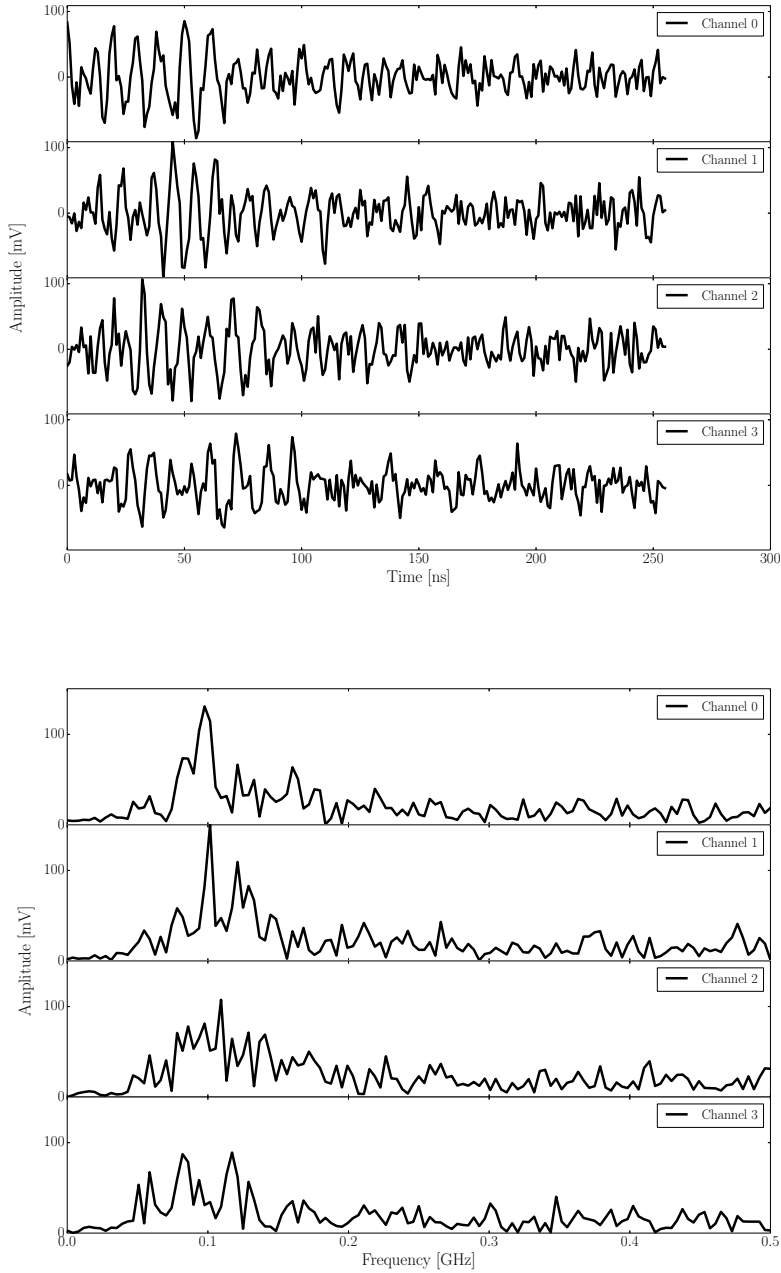
Figure A.6. Station Y: untypical event, occurred occasionally. This event is not consistent with HP events because of its mainly low frequency content. Upper plot: time domain divided by channels. Lower plot: frequency domain (DFFT) divided by channels. Station distance: 1225 m.

Summary in Swedish
Sammanfattning på Svenska

Avhandlingens titel:

Neutrinoastronomins extrempunkter
Från Fermi-Bubblor med IceCube till isstudier med ARIANNA

Att förstå universum är en av mänsklighetens största utmaningar. Genom historien har nyfikna individer vänt blicken mot skyn för att observera astronomiska objekt såsom stjärnor och galaxer - deras ljus och hur de rör sig. Ögat var det första verktyg som användes till sådana observationer, men med teknologiska framsteg har en uppsjö av nya instrument utvecklats för den ständigt pågående upptäcktsresan. Idag kan vi undersöka ett brett spektrum av elektromagnetisk strålning, från radiovågor till gammastrålar (γ-strålning) med olika typer av teleskop. Förutom fotoner har andra budbärare visat sig vara användbara för att studera universum: Kosmisk Strålning (KS), gravitationsvågor och neutriner. KS är laddade partiklar och utgörs till 90% av protoner, 9% heliumkärnor och därutöver elektroner, positroner och tyngre kärnor upp till järn. Gravitationsvågor är det senaste tillskottet till astrofysikens budbärarfamilj. Dessa är vågor i rumtiden som orsakas av accelererade massiva objekt och rör sig med ljusets hastighet. Neutriner, elementarpartiklar med en extremt liten massa och utan elektrisk laddning, är de budbärare som är av störst intresse för denna avhandling.

Denna avhandling

Denna avhandling är uppdelad i två huvudsakliga delar. Den första delen ägnas åt undersökningar av ett möjligt neutrinoflöde från Fermi-bubblorna med IceCube, medan den andra delen behandlar isegenskaper vid Ross Shelf-is som studerats med radiovågor i ARIANNA.

Del I:
Undersökning av neutriner från Fermi-bubblorna med IceCube

Fermibubblorna (FB) är utsträckta regioner ovan- och nedanför centrum i vår galax som avger gammastrålning. De är vardera 25 000 ljusår tvärsöver och

upptäcktes med hjälp av data från Fermi-LAT (Large Area Telescope), ett instrument på rymdfarkosten Fermi Gamma Ray Space Telescope. För att förklara denna γ-strålnings ursprung har olika teorier framlagts. I en klass av modeller, som kallas hadronmodeller, antas det att de observerade γ-strålarna genereras av accelererade KS som interagerar med interstellär materia, vilket även skulle generera neutriner. I detta arbete har en hadronmodell valts där KS produceras och accelereras i sjärnbildningsregionen nära galaxens centrum. Galaxvindar för sedan med sig KS till FB-regionen där de fastnar i magnetfält i cirka 10^{10} år. Man har tidigare trott att Fermibubblorna utsänder ett hårt γ-spektrum där formen på flödet, Φ, ges av ett potensförhållande $\Phi \propto E^{-2}$, men resultat från Fermi-LAT-kollaborationen tyder på att en logaritmisk-paraboliskt formel passar bättre när hela spektrumet (100 MeV - 500 GeV) tas i beaktande. Denna formel har här använts för att härleda ett möjligt neutrinoflöde från Fermi-bubblorna.

För att mäta det eventuella neutrinoflödet från FB har neutrinoobservatoriet IceCube nyttjats. IceCube är en neutrinodetektor på Antarktis, nära den geografiska sydpolen. Den består ett nät av Digitala Optiska Moduler (DOMs), med 86 strängar utspridda över en kubikkilometer av den extremt klara glaciärisen mellan 1.45 och 2.45 kilometers djup, samt ett s.k. luftkursnät vid ytan som täcker en kvadratkilometer. Åtta av de 86 strängarna är förlagda mellan de mest centrala övriga IceCube-strängarna och har en tätare sträng- och DOM-fördelning. Dessa åtta, tillsammans med de intilliggande IceCube-strängarna utgör tillsammans deldetektorn DeepCore. Tack vare den tätare DOM-fördelningen i DeepCore sänks energitröskeln för neutrinodetektion till 10 GeV, vilket tillåter undersökningar av neutrinooscillationer och astrofysikaliska neutrinoflöden vid låga energier, till exempel flödet från Fermi-bubblorna.

Syftet med analysen i denna avhandling är att undersöka det möjliga neutrinoflödet från FB vid de energier där γ-strålar tidigare mätts, mellan 10 GeV och 200 GeV. Alla neutrinotyper har likartade sfäriska händelsesignaturer (kaskader) i DeepCore vid dessa låga energier. Ett existerande händelseurval, som ursprungligen optimerades för att söka efter neutriner från mörk materia-annihilationer i Vintergatans halo, valdes till den här analysen. Urvalet är bra eftersom det är optimerat för lågenergikaskader. Analysen som framläggs i denna avhandling utvidgar detta händelseurval till att omfatta nästan sex år av data.

Monte Carlo -simuleringar av den förväntade FB-signalen användes för att generera statistiska täthetsfunktioner (TF) över hela himlavalvet. För att generera bakgrundens TF användes verklig data. Datahändelserna blandades i rektascension för att bevara blindhet gällande deras verkliga inkommande riktning. En utjämningsprocedur applicerades också till både signalens och bakgrundens TF, för att undvika oavsiktliga systematiska fel. En analys för maxi-

mal sannolikhet applicerades på signalens och bakgrundens TF för att ta fram en känslighet för FB-neutrinoflödet. Eftersom verklig data används för den förväntade bakgrunden tog analysmetoden hänsyn till en möjlig signalkontaminering i bakgrundens TF genom att inkludera en blandad signal-TF i den. Känsligheten, som visar hur känslig detektorn är för den förväntade signalen, var nästan två storleksordningar högre än den förväntade FB-signalen. Detta innebär att neutrinoflödet från Fermi-bubblorna skulle behöva vara cirka två storleksordningar högre än förväntat för att kunna observeras i den här analysen.

Efter att känsligheten bestämts och IceCube-kollaborationen granskat analysen gavs godkännande för att avslöja de verkliga händelseriktningarna, och dessa användes för att beräkna en övre gräns för neutrinoflödet från Fermibubblorna för de tre neutrino-arom-typerna med energier mellan 10 GeV och 200 GeV. Denna övre gräns ligger 0.86 standardavvikelser över känsligheten och är just nu den enda gränsen för FB-neutrinoflödet vid de energier där gammaflödet från Fermi-bubblorna ursprungligen mättes.

Studier av systematiska felfaktorer genomfördes för att uppskatta hur känsligheten påverkas av dessa faktorer. Detektor- och ismodells-relaterade osäkerheter studerades genom att variera en parameter i taget i Monte Carlo-simuleringar. Analysrelaterade osäkerheter bestämdes genom att öka utjämningen av TF. Systematiskt fel på grund av parametriseringen av Fermibubblornas γ-flöde undersöktes genom att byta potensförhållande som det förväntade flödet baserades på och sedan applicera samma analysmetod. Den största felkällan visade sig vara flödesparametriseringen, som ledde till en 60-procentig försämring av känsligheten. Den totala systematiska osäkerheten är dock ändå mindre än den statistiska osäkerheten. Den sistnämnda är stor på grund av att vinkelupplösningen för lågenergihändelser är låg.

Till sist gjordes en jämförelse med de övre gränserna för neutrinoflöden från Fermi-bubblorna som satts av ANTARES, ett neutrinoobservatorium i Medelhavet. Analysmetoderna var väldigt olika. ANTARES använde flera zoner formade som FB på himlavalvet. En lades över FBs position (sedermera kallad signal-zonen) och de andra zonerna fördelades över resten av himlen (bakgrunds-zonerna). Därefter räknades antalet neutrino-händelser som kom ifrån signal-zonen respektive bakgrunds-zonerna, och antalen jämfördes med varandra. Data från ungefär 6 år av datainsamling användes. ANTARES antog att formen på neutrinoflödet beskrivs av ett potensförhållande med avbrott vid energier i TeV-området. Det bör tilläggas att de övre gränserna som tagits fram vid ANTARES är giltiga i ett annat energiområde ($\sim$ 2 TeV - 1 PeV) än gränserna från analysen med IceCube-data Gränsen från ANTARES ligger ungefär en tiopotens över den förväntade signalen, medan IceCubes övre gräns ligger nästan två tiopotenser över det förväntade neutrinoflödet från FB. Dock

har gränsen från denna analys härletts för det lägsta energiintervallet (10 GeV och 200 GeV) som något neutrinoteleskop kan uppnå. Det bör även noteras att i det energiområdes som ANTARES undersökt har det inte heller setts ett γ-flöde från Fermibubblorna, dvs inget flöde som skulle motivera närvaron av ett neutrino-flöde.

Del II:
Undersökning av isegenskaper med hjälp av radiovågor i ARIANNA

Medan analysen som beskrivits i Del I gjordes vid de lägsta energier som IceCube kan nå har experimenten vid ARIANNA (Antarctic Ross Ice-shelf ANtenna Neutrino Array) målet att detektera neutriner med extremt hög energi (EHE), mellan 100 PeV och 100 EeV. Dessa neutriner, som också kallas kosmogeniska neutriner, härrör från KS-interaktioner med den kosmiska bakgrundsstrålningen, en rest från Big Bang. ARIANNAs koncept bygger på mätning av radiovågor som produceras genom Askaryan-effekten då EHE-neutriner växelverkar i isen.

För närvarande är huvudsaken med ARIANNA att testa detektor-konceptet. ARIANNA består av tolv av varandra oberoende stationer (säsongen 2018/2019). Av dessa befinner sig tio på Ross Shelf-is, med 1 km avstånd sinsemellan, och två vid den geografiska sydpolen. Sju av de tio stationerna på Ross Shelf-is utgör den s.k. Hexagonal Radio Array (HRA). Varje station består av fyra nedåtpekande LPDA-antenner (Log Periodic Dipole Array), som är utplacerade i en kvadrat och kopplade till en elektroniklåda. Elektroniklådan innehåller hårdvaran som behövs för att registrera signaler från antennerna. Dessutom finns elektronik som reglerar strömmen från solpanelerna och elektronik för kommunikationen över satellit med en server på norra halvklotet. Lådan och antennerna är grunt nedgrävda under snöytan, medan solpanelerna är fästa på ett torn. Ross Shelf-is ger en utmärkt miljö för detta projekt på grund av sin stora mängd is och sina få bakgrundsradiokällor. Dess istäcke är i genomsnitt cirka 580 m tjockt, varav de översta $\sim$ 70 m är firn. Dock behöver radiovågsutbredningen genom isen och firnen (hårt packad snö) undersökas.

Enligt klassisk fysik borde den varierande densiteten, och därmed det varierande brytningsindexet, leda till att radiosignalernas väg genom firn böjs av, vilket ger upphov till en skuggnings-effekt. Mätningar mellan två dipol-antenner, separerade med 100 m och placerade på flera olika djup mellan 2 m och 19 m, genomfördes. Vid symmetriskt djup hos sändardipolen (Tx) och mottagardipolen (Rx) på 2 m och 5 m förväntades ingen signal, då Rx borde ligga i den skuggade zonen för Tx. Dock borde man observera signal vid symmetriskt djup på

19 m för Tx och Rx, då detta faller utanför den skuggade zonen. Förvånansvärt nog observerades signal vid alla djupkombinationer. Detta kan förklaras med att radiovågorna färdats horisontellt i firn där brytningsindexet varierar, vilket nedan kallas horisontell propagering (HP).

Klassiskt antas det att firndensiteten ökar kontinuerligt med djupet tills den möter isen och når isens densitet. Firnen uppvisar dock ojämnheter som leder till lager med högre och lägre brytningsindex, vilket påverkar radiovågornas utbredningshastighet. Radiovågor kan färdas långa sträckor i firnen då de kan fångas av inre reflektion mellan lager med högre täthet, och därmed högre brytningsindex och lägre strålhastighet. Grupper av sådana lager ökar effekten av horisontell propagering [I]. Horisontell propagering, där radiovågor leds mellan skikt av högre täthet i firn, kan jämföras med principen bakom optiska fibrer, där ljusstrålar leds mellan fiberns väggar.

Tätheten hos firnen mättes i samband med att hål borrades för att sänka ner dipoler. Resultaten användes för att beräkna det djupberoende brytningsindexet och jämfördes med brytningsindex från mätningarna med dipoler. De överensstämde väl. HP-pulserna mellan dipoler undersöktes vidare och deras egenskaper karaktäriserades. Huvudegenskapen hos HP-pulserna är att de verkar färdas direkt mellan Tx och Rx med den ljushastighet som ges av firnens djup. De syns främst runt 200 MHz, men har även bidrag vid andra frekvenser. Bidragen vid andra frekvenser är dock hårt dämpade om man jämför med mätningar som gjorts i luft, 1.5 m ovanför firnen. I luft ses ett jämnt och brett och spektrum mellan 150 MHz och 800 MHz, som är som högst vid 230 MHz.

Utöver de horisontellt propagerande pulserna observerades även oväntade signaler. De inkom före HP-pulserna, med lägre amplitud samt innehåll av lägre frekvenser (∼ 100 MHz). Dessa tidiga signaler kallas här för förpulser. Den mest sannolika förklaringen till förpulserna är att de färdats uppåt och sedan längs luft/firn-ytan. Det finns två möjliga propageringsmoder som låter vågor utbredas på det sättet: ytvågor och laterala vågor. Dock kan vi i nuläget inte särskilja dessa. Förpulser har tidigare föreslagits som en möjlig detektionsmetod för EHE-neutriner när det gäller neutrinoteleskop som använder sig av is och firn, men har aldrig uppmätts vid firnytan. Mätningarna som presenteras i denna avhandling togs fram med avsikten att undersöka HP-pulser, men en del av datan har även analyserats med syfte att karakterisera förpulserna. En förenklad modell av förpulsernas utbredning har därmed härletts.

Det huvudsakliga fokuset i Del II av detta arbete ligger på att bestämma den karaktäristiska sträckan över vilken horisontellt propagerande signaler i firn försvagas. Detta eftersom HP-pulser observerades långt in i skuggzonen hos samtliga ARIANNA-stationer på horisontella avstånd upp till 1.4 km. För detta syfte genomfördes mätningar mellan en sändardipolantenn och en LPDA-

mottagarantenn. Dipolen var placerad på 19 meters djup och LPDAn var begravd under 2 m firn, pekandes nedåt med spetsarna vinkelrätt mot signalens utbredningsriktning, för att få en liknande placering som i stationens LPDA-konfigurationer. Signalen som observerades med denna uppställning, vidare hänvisad till som oscilloskop-pulsen, faltades med stationernas förstärkarsvar och jämfördes med de signaler som uppmätts vid stationerna. Ett stations- och händelseurval gjordes och man drog slutsatsen att stationerna sannolikt aktiveras av HP-pulser snarare än förpulser.

Slutligen undersöktes två hypoteser angående den geometriska dämpningen av HP-pulser – att amplituden minskar proportionerligt med $1/r$ eller $1/\sqrt{r}$, där r är avståndet till sändaren. Inom ramen för vardera hypotes gjordes två analyser för att ta fram den karaktäristiska dämpningslängden för HP-pulser. Två separata analyser gjordes för att ta hänsyn till spridningseffekter. Den första analysen byggde på den högsta uppmätta amplituden för varje händelse, och den andra analysen gjordes genom summering av amplituderna i frekvensdomänen från 150 MHz till 250 MHz. Resultaten gav dämpningslängder mellan $310\,\text{m} \pm 83\,\text{m}$ och $651\,\text{m} \pm 270\,\text{m}$, beroende på vilken av hypoteserna som antagits och vilken analys som utförts. Inom ramen för vardera hypotes är resultaten för de två analyserna kompatibla.

Efter att ARIANNA-kollaborationen diskuterat observationen av horisontellt propagerande signaler och förpulser inom fältet valde andra kollaborationer, RICE (Radio Ice Cherenkov Experiment) och GNO (Greenland Neutrino Observatory), att återanalysera sina data med dessa signaler i åtanke. Både HP-pulser och förpulser observerades då. Man kan därmed dra slutsatsen att radiovågor kan färdas långa sträckor horisontellt, vilket leder till en förstoring av den effektiva volymen för radiobaserade neutrinodetektorer i firn.

Avslutning

Denna avhandling baseras på energi-extremfallen inom neutrino-astronomi. Här behandlas neutriner med de lägsta energierna som IceCube kan observera för att undersöka Fermi-Bubblorna kring Vintergatans centrum. Här behandlas även de radiovågs-egenskaper som kommer att tillåta framtida undersökningar av kosmiska neutriner med de högsta möjliga energierna med ARIANNA.

References

[1] ELECTRICAL SCIENCE: A Series of Monographs and Texts. In: G. Tyras, editor, Radiation and Propagation of Electromagnetic Waves. Academic Press (1969). ISBN 978-0-12-705650-0. doi: https://doi.org/10.1016/B978-0-12-705650-0.50001-2.
URL `http://www.sciencedirect.com/science/article/pii/B9780127056500500012`

[2] South Pole glacial climate reconstruction from multi-borehole laser particulate stratigraphy. *Journal of Glaciology*, 59(218):1117–1128 (2013). doi:10.3189/2013JoG13J068.

[3] A. Romero-Wolf for the EVA Collaboration. The ExaVolt Antenna Mission Concept and Technology Developments. In: Proceedings, 34th International Cosmic Ray Conference (ICRC2015) (20168).
URL `https://doi.org/10.22323/1.236.1151`

[4] Huege, Tim and Besson, Dave. Radiowave Detection of Ultra-High Energy Neutrinos and Cosmic Rays. *ArXiv Astrophysics - Instrumentation and Methods for Astrophysics e-prints* (2017). `1701.02987`.
URL `https://arxiv.org/abs/1701.02987`

[5] J. van Santen for the The IceCube-Gen2 Collaboration. IceCube-Gen2: the next-generation neutrino observatory for the South Pole. In: Proceedings, 35th International Cosmic Ray Conference (ICRC2017) Bexco, Busan, Korea (2018). doi:doi.org/10.22323/1.301.0991.
URL `https://doi.org/10.22323/1.301.0991`

[6] A. Nelles and C. Persichilli for the ARIANNA Collaboration. Livetime and sensitivity of the ARIANNA Hexagonal Radio Array. In: 34th International Cosmic Ray Conference, vol. 1087. ICRC (2015).
URL `arXiv:1509.00115`

[7] M. Aartsen, R. Abbasi, Y. Abdou, et al. Measurement of South Pole ice transparency with the IceCube LED calibration system. *Nuclear Instruments and Methods in Physics Research Section A: Accelerators, Spectrometers, Detectors and Associated Equipment*, 711:73 – 89 (2013). ISSN 0168-9002. doi:https://doi.org/10.1016/j.nima.2013.01.054.
URL `http://www.sciencedirect.com/science/article/pii/S0168900213001460`

[8] M. Aartsen, R. Abbasi, Y. Abdou, et al. Improvement in fast particle track reconstruction with robust statistics. *Nuclear Instruments and Methods in Physics Research Section A: Accelerators, Spectrometers, Detectors and Associated Equipment*, 736:143 – 149 (2014). ISSN

0168-9002. doi:https://doi.org/10.1016/j.nima.2013.10.074.
URL http://www.sciencedirect.com/science/article/pii/S0168900213014654

[9] M. Aartsen, K. Abraham, M. Ackermann, et al. All-flavour search for neutrinos from dark matter annihilations in the Milky Way with Ice-Cube/DeepCore. *European Physical Journal C*, 76(10) (2016). ISSN 1434-6044. doi:10.1140/epjc/s10052-016-4375-3.

[10] M. Aartsen, M. Ackermann, J. Adams, et al. The IceCube Neutrino Observatory: instrumentation and online systems. *Journal of Instrumentation*, 12(03):P03012 (2017).
URL http://stacks.iop.org/1748-0221/12/i=03/a=P03012

[11] M. G. Aartsen, R. Abbasi, M. Ackermann, et al. Search for a diffuse flux of astrophysical muon neutrinos with the IceCube 59-string configuration. *Phys. Rev. D*, 89:062007 (2014). doi:10.1103/PhysRevD.89.062007.
URL https://link.aps.org/doi/10.1103/PhysRevD.89.062007

[12] M. G. Aartsen, K. Abraham, M. Ackermann, et al. A Combined Maximum-likelihood Analysis of the High-energy Astrophysical Neutrino Flux Measured with IceCube. *The Astrophysical Journal*, 809(1):98 (2015).
URL http://stacks.iop.org/0004-637X/809/i=1/a=98

[13] M. G. Aartsen, K. Abraham, M. Ackermann, et al. PINGU: a vision for neutrino and particle physics at the South Pole. *Journal of Physics G: Nuclear and Particle Physics*, 44(5):054006 (2017).
URL http://stacks.iop.org/0954-3899/44/i=5/a=054006

[14] M. G. Aartsen, M. Ackermann, J. Adams, et al. Differential limit on the extremely-high-energy cosmic neutrino flux in the presence of astrophysical background from nine years of IceCube data. *Phys. Rev. D*, 98:062003 (2018). doi:10.1103/PhysRevD.98.062003.
URL https://link.aps.org/doi/10.1103/PhysRevD.98.062003

[15] M. G. Aartsen and et. al. Erratum: Constraints on Ultrahigh-Energy Cosmic-Ray Sources from a Search for Neutrinos Above 10 PeV with IceCube [Phys. Rev. Lett. 117, 241101 (2016)]. *Phys. Rev. Lett.*, 119:259902 (2017). doi:10.1103/PhysRevLett.119.259902.
URL https://link.aps.org/doi/10.1103/PhysRevLett.119.259902

[16] M. G. Aartsen et al. IceCube-Gen2: A Vision for the Future of Neutrino Astronomy in Antarctica (2014). 1412.5106.

[17] M. G. Aartsen et al. The IceCube Neutrino Observatory - Contributions to ICRC 2017 Part II: Properties of the Atmospheric and Astrophysical Neutrino Flux (2017). 1710.01191.

[18] M. G. e. a. Aartsen. Letter of Intent: The Precision IceCube Next Generation Upgrade (PINGU). *arXiv:1401.2046* (2014). 1401.2046.

[19] K. N. Abazajian and M. Kaplinghat. Detection of a gamma-ray source

in the Galactic Center consistent with extended emission from dark matter annihilation and concentrated astrophysical emission. *Phys. Rev. D*, 86:083511 (2012). doi:10.1103/PhysRevD.86.083511.
URL `https://link.aps.org/doi/10.1103/PhysRevD.86.083511`

[20] R. Abbasi, Y. Abdou, T. Abu-Zayyad, M. Ackermann, and et al. The design and performance of IceCube DeepCore. *Astroparticle Physics*, 35(10):615 – 624 (2012). ISSN 0927-6505. doi: https://doi.org/10.1016/j.astropartphys.2012.01.004.
URL `http://www.sciencedirect.com/science/article/pii/S0927650512000254`

[21] R. Abbasi, Y. Abdou, T. Abu-Zayyad, et al. Calibration and characterization of the IceCube photomultiplier tube. *Nuclear Instruments and Methods in Physics Research Section A: Accelerators, Spectrometers, Detectors and Associated Equipment*, 618(1):139 – 152 (2010). ISSN 0168-9002. doi:https://doi.org/10.1016/j.nima.2010.03.102.
URL `http://www.sciencedirect.com/science/article/pii/S0168900210006662`

[22] R. Abbasi and Y. Abdou and et al. IceTop: The surface component of IceCube. *Nuclear Instruments and Methods in Physics Research A*, 700:188–220 (2013). doi:{10.1016/j.nima.2012.10.067}.

[23] R. Abbasi, M. Ackermann, J. Adams, et al. The IceCube data acquisition system: Signal capture, digitization, and timestamping. *Nuclear Instruments and Methods in Physics Research Section A: Accelerators, Spectrometers, Detectors and Associated Equipment*, 601(3):294 – 316 (2009). ISSN 0168-9002. doi: https://doi.org/10.1016/j.nima.2009.01.001.
URL `http://www.sciencedirect.com/science/article/pii/S0168900209000084`

[24] B. P. Abbott, R. Abbott, T. D. Abbott, et al. Observation of Gravitational Waves from a Binary Black Hole Merger. *Phys. Rev. Lett.*, 116:061102 (2016). doi:10.1103/PhysRevLett.116.061102.
URL `https://link.aps.org/doi/10.1103/PhysRevLett.116.061102`

[25] A. Abeysekara, R. Alfaro, C. Alvarez, et al. Sensitivity of the high altitude water Cherenkov detector to sources of multi-TeV gamma rays. *Astroparticle Physics*, 50-52:26 – 32 (2013). ISSN 0927-6505. doi:https://doi.org/10.1016/j.astropartphys.2013.08.002.
URL `http://www.sciencedirect.com/science/article/pii/S0927650513001230`

[26] A. U. Abeysekara, A. Albert, R. Alfaro, et al. Search for Very High-energy Gamma Rays from the Northern Fermi Bubble Region with HAWC. *The Astrophysical Journal*, 842(2):85 (2017). doi:10.3847/1538-4357/aa751a.
URL `https://doi.org/10.3847%2F1538-4357%2Faa751a`

[27] J. Abraham, M. Aglietta, I. Aguirre, et al. Properties and performance of the prototype instrument for the Pierre Auger Observatory. *Nuclear Instruments and Methods in Physics Research Section A: Accelerators, Spectrometers, Detectors and Associated Equipment*, 523(1):50 – 95 (2004). ISSN 0168-9002. doi: https://doi.org/10.1016/j.nima.2003.12.012.
URL `http://www.sciencedirect.com/science/article/pii/S0168900203033497`

[28] M. Ackermann, M. Ajello, A. Albert, et al. The Spectrum of Isotropic Diffuse Gamma-Ray Emission between 100 MeV and 820 GeV. *The Astrophysical Journal*, 799(1):86 (2015).
URL `http://stacks.iop.org/0004-637X/799/i=1/a=86`

[29] M. Ackermann, M. Ajello, A. Albert, et al. TheFermiGalactic Center GeV Excess and Implications for Dark Matter. *The Astrophysical Journal*, 840(1):43 (2017). doi:10.3847/1538-4357/aa6cab.
URL `https://doi.org/10.3847%2F1538-4357%2Faa6cab`

[30] M. Ackermann, A. Albert, W. B. Atwood, et al. The Spectrum and Morphology of the Fermi Bubbles. *The Astrophysical Journal*, 793(1):64 (2014).
URL `http://stacks.iop.org/0004-637X/793/i=1/a=64`

[31] M. Ackermann, H.-J. Arends, X. Bai, et al. Optical properties of deep glacial ice at the South Pole. *Journal of Geophysical Research*, 111 (2006).
URL `icecube.berkeley.edu/~bprice/publications/Optical.properties.deep.ice.South.Pole.pdf`

[32] J. H. Adams et al. White paper on EUSO-SPB2 (2017). `1703.04513`.

[33] S. Adrian-Martinez, M. Ageron, F. Aharonian, et al. Letter of intent for KM3NeT 2.0. *Journal of Physics G: Nuclear and Particle Physics*, 43(8):084001 (2016).
URL `http://stacks.iop.org/0954-3899/43/i=8/a=084001`

[34] AFAR Communications, Inc. AFAR Communications (2018).
URL `http://afar.net/`

[35] M. Ageron, J. Aguilar, I. A. Samarai, et al. ANTARES: The first undersea neutrino telescope. *Nuclear Instruments and Methods in Physics Research Section A: Accelerators, Spectrometers, Detectors and Associated Equipment*, 656(1):11 – 38 (2011). ISSN 0168-9002. doi:https://doi.org/10.1016/j.nima.2011.06.103.
URL `http://www.sciencedirect.com/science/article/pii/S0168900211013994`

[36] M. Ahlers and F. Halzen. Opening a new window onto the universe with IceCube. *Progress in Particle and Nuclear Physics*, 102:73 – 88 (2018). ISSN 0146-6410. doi:https://doi.org/10.1016/j.ppnp.2018.05.001.
URL `http://www.sciencedirect.com/science/article/pii/S0146641018300346`

196

[37] M. Ahlers and K. Murase. Probing the Galactic origin of the IceCube excess with gamma rays. *Phys. Rev. D*, 90:023010 (2014). doi:10.1103/PhysRevD.90.023010.
URL `https://link.aps.org/doi/10.1103/PhysRevD.90.023010`

[38] Q. R. Ahmad, R. C. Allen, T. C. Andersen, et al. Measurement of the Rate of $\nu_e + d \rightarrow p + p + e^-$ Interactions Produced by ^8B Solar Neutrinos at the Sudbury Neutrino Observatory. *Phys. Rev. Lett.*, 87:071301 (2001). doi:10.1103/PhysRevLett.87.071301.
URL `https://link.aps.org/doi/10.1103/PhysRevLett.87.071301`

[39] S. Aiello et al. Sensitivity of the KM3NeT/ARCA neutrino telescope to point-like neutrino sources (2018). `1810.08499`.

[40] M. Akita, J. Kataoka, M. Arimoto, et al. Diffuse X-Ray Emission from the Northern Arc of Loop I Observed with Suzaku. *The Astrophysical Journal*, 862(1):88 (2018). doi:10.3847/1538-4357/aacd08.
URL `https://doi.org/10.3847%2F1538-4357%2Faacd08`

[41] J. Aleksic et al. Performance of the MAGIC stereo system obtained with Crab Nebula data. *Astroparticle Physics*, 35:435–448 (2012). doi:{10.1016/j.astropartphys.2011.11.007}.

[42] Alexander Burgman, Elisabeth Unger. Characterizing LPDA Antennas. Uppsala University (2015). ARIANNA internal document.

[43] Allard, D., Parizot, E., Olinto, A. V., Khan, E., and Goriely, S. UHE nuclei propagation and the interpretation of the ankle in the cosmic-ray spectrum. *Astronomy and Astrophysics*, 443(3):L29–L32 (2005). doi:10.1051/0004-6361:200500199.
URL `https://doi.org/10.1051/0004-6361:200500199`

[44] P. Allison, R. Bard, J. J. Beatty, et al. Performance of two Askaryan Radio Array stations and first results in the search for ultrahigh energy neutrinos. *Phys. Rev. D*, 93:082003 (2016). doi:10.1103/PhysRevD.93.082003.
URL `https://link.aps.org/doi/10.1103/PhysRevD.93.082003`

[45] R. Aloisio. Ultra High Energy Cosmic Rays: A Short Review. In: Proceedings, 9th Workshop on Science with the New Generation of High Energy Gamma-ray Experiments (SciNeGHE 2012): Lecce, Italy, June 20-22, 2012 (2012). `1211.2004`.

[46] J. Alvarez-Muñiz, A. Romero-Wolf, and E. Zas. Čerenkov radio pulses from electromagnetic showers in the time domain. *Phys. Rev. D*, 81:123009 (2010). doi:10.1103/PhysRevD.81.123009.
URL `https://link.aps.org/doi/10.1103/PhysRevD.81.123009`

[47] J. Alvarez-Muñiz et al. The Giant Radio Array for Neutrino Detection (GRAND): Science and Design (2018). `1810.09994`.

[48] L. ANCHORDOQUI, T. PAUL, S. REUCROFT, and J. SWAIN. ULTRAHIGH ENERGY COSMIC RAYS: THE STATE OF THE ART BEFORE THE AUGER OBSERVATORY. *International Jour-*

nal of Modern Physics A, 18(13):2229–2366 (2003). doi:10.1142/S0217751X03013879.
URL https://doi.org/10.1142/S0217751X03013879

[49] C. Andreopoulos et al. The GENIE Neutrino Monte Carlo Generator. *Nucl. Instrum. Meth.*, A614:87–104 (2010). doi:10.1016/j.nima.2009.12.009. 0905.2517.

[50] W. D. Apel, J. C. Arteaga-Velázquez, K. Bekk, et al. Kneelike Structure in the Spectrum of the Heavy Component of Cosmic Rays Observed with KASCADE-Grande. *Phys. Rev. Lett.*, 107:171104 (2011). doi:10.1103/PhysRevLett.107.171104.
URL https://link.aps.org/doi/10.1103/PhysRevLett.107.171104

[51] G. Askaryan. EXCESS NEGATIVE CHARGE OF AN ELECTRON-PHOTON SHOWER AND THE COHERENT RADIO EMISSION FROM IT. *Zhur. Eksptl'. i Teoret. Fiz.*, Vol: 41 (1961).

[52] G. A. Askaryan. Excess Negative Charge of an Electron-Photon Shower And Its Coherent Radio Emission. *Soviet Journal of Experimental and Theoretical Physics*, 14:441–444 (1962).

[53] G. A. Askaryan. Coherent Radio Emission from Cosmic Showers in Air and in Dense Media. *Soviet Phys. JETP*, 21:658 (1965).

[54] W. B. Atwood, A. A. Abdo, and M. Ackermann and et al. The Large Area Telescope on the Fermi Gamma-Ray Space Telescope Mission. *The Astrophysical Journal*, 697(2):1071–1102 (2009). doi:{10.1088/0004-637X/697/2/1071}.
URL https://doi.org/10.1088%2F0004-637x%2F697%2F2%2F1071

[55] J. Avva, J. M. Kovac, C. Miki, D. Saltzberg, and A. G. Vieregg. An in situ measurement of the radio-frequency attenuation in ice at Summit Station, Greenland. *Journal of Glaciology*, 61(229):1005–1011 (2015). doi:10.3189/2015JoG15J057.

[56] V. Aynutdinov, A. Dmitrievich Avrorin, A. Valentinovich Avrorin, et al. Status of the Baikal-GVD experiment - 2017. In: Proceedings, 35th International Cosmic Ray Conference (ICRC2017) Bexco, Busan, Korea, page 1034 (2017). doi:10.22323/1.301.1034.

[57] B. Balaji, I. Cholis, P. J. Fox, and S. D. McDermott. Analyzing the gamma-ray sky with wavelets. *Phys. Rev. D*, 98:043009 (2018). doi:10.1103/PhysRevD.98.043009.
URL https://link.aps.org/doi/10.1103/PhysRevD.98.043009

[58] T. Barrella, S. Barwick, and D. Saltzberg. Ross Ice Shelf (Antarctica) in situ radio-frequency attenuation. *Journal of Glaciology*, 57(201):61–66 (2011). doi:10.3189/002214311795306691.

[59] P. H. Barrett, L. M. Bollinger, G. Cocconi, Y. Eisenberg, and K. Greisen. Interpretation of Cosmic-Ray Measurements Far Underground. *Rev. Mod. Phys.*, 24:133–178 (1952). doi:10.1103/RevModPhys.24.133.

URL `https://link.aps.org/doi/10.1103/RevModPhys.24.133`

[60] S. Barwick, E. Berg, D. Besson, et al. A first search for cosmogenic neutrinos with the ARIANNA Hexagonal Radio Array. *Astroparticle Physics*, 70:12 – 26 (2015). ISSN 0927-6505. doi: https://doi.org/10.1016/j.astropartphys.2015.04.002.
URL `http://www.sciencedirect.com/science/article/pii/S0927650515000638`

[61] S. Barwick, E. Berg, D. Besson, et al. Time-domain response of the ARIANNA detector. *Astroparticle Physics*, 62:139 – 151 (2015). ISSN 0927-6505. doi:https://doi.org/10.1016/j.astropartphys.2014.09.002.
URL `http://www.sciencedirect.com/science/article/pii/S0927650514001315`

[62] S. Barwick, E. Berg, D. Besson, et al. Observation of classically 'forbidden' electromagnetic wave propagation and implications for neutrino detection. *Journal of Cosmology and Astroparticle Physics*, 2018(07):055–055 (2018). doi:10.1088/1475-7516/2018/07/055.
URL `https://doi.org/10.1088%2F1475-7516%2F2018%2F07%2F055`

[63] S. Barwick, D. Besson, A. Burgman, et al. Radio detection of air showers with the ARIANNA experiment on the Ross Ice Shelf. *Astroparticle Physics*, 90:50 – 68 (2017). ISSN 0927-6505. doi: https://doi.org/10.1016/j.astropartphys.2017.02.003.
URL `http://www.sciencedirect.com/science/article/pii/S0927650516302134`

[64] S. Barwick, D. Besson, P. Gorham, and D. Saltzberg. South Polar in situ radio-frequency ice attenuation. *Journal of Glaciology*, 51(173):231–238 (2005). doi:10.3189/172756505781829467.

[65] S. W. Barwick, E. C. Berg, D. Z. Besson, et al. Design and Performance of the ARIANNA HRA-3 Neutrino Detector Systems. *IEEE Transactions on Nuclear Science*, 62(5):2202–2215 (2015). ISSN 0018-9499. doi:10.1109/TNS.2015.2468182.

[66] J. K. Becker. High-energy neutrinos in the context of multimessenger astrophysics. *Physical Reports*, 458:173–246 (2008).

[67] A. R. Bell. The acceleration of cosmic rays in shock fronts - I. *Monthly Notices of the Royal Astronomical Society*, 182(2):147–156 (1978). doi:10.1093/mnras/182.2.147.
`/oup/backfile/content_public/journal/mnras/182/2/10.1093/mnras/182.2.147/2/mnras182-0147.pdf`.
URL `http://dx.doi.org/10.1093/mnras/182.2.147`

[68] V. Berezinsky, A. Gazizov, and S. Grigorieva. On astrophysical solution to ultrahigh energy cosmic rays. *Phys. Rev. D*, 74:043005 (2006). doi: 10.1103/PhysRevD.74.043005.
URL `https://link.aps.org/doi/10.1103/PhysRevD.74.043005`

[69] V. Berezinsky, A. Gazizov, and S. Grigorieva. On the status of the dip

in UHECR spectrum. In: Proceedings, 30th International Cosmic Ray Conference (ICRC2007) Merida, Mexico (2007).

[70] V. S. Berezinsky and S. I. Grigor'eva. A bump in the ultra-high energy cosmic ray spectrum. *Astronomy and Astrophysics*, 199:1–12 (1988).

[71] Berezinsky, V. UHECR: Signatures and models. *EPJ Web of Conferences*, 53:01003 (2013). doi:10.1051/epjconf/20135301003.
URL https://doi.org/10.1051/epjconf/20135301003

[72] P. L. Biermann. The origin of the highest energy cosmic rays. *Journal of Physics G: Nuclear and Particle Physics*, 23(1):1 (1997).
URL http://stacks.iop.org/0954-3899/23/i=1/a=002

[73] D. J. Bird, S. C. Corbató, H. Y. Dai, et al. Evidence for correlated changes in the spectrum and composition of cosmic rays at extremely high energies. *Phys. Rev. Lett.*, 71:3401–3404 (1993). doi:10.1103/PhysRevLett.71.3401.
URL https://link.aps.org/doi/10.1103/PhysRevLett.71.3401

[74] J. Bland-Hawthorn and M. Cohen. The Large-Scale Bipolar Wind in the Galactic Center. *The Astrophysical Journal*, 582(1):246–256 (2003). doi:10.1086/344573.
URL https://doi.org/10.1086%2F344573

[75] S. Blot. IceCube Upgrade and Gen-2. http://www.cd-corp.com/eng/cma/clp5130.pdf (2018).
URL https://indico.desy.de/indico/event/18204/session/14/contribution/264/material/slides/0.pdf

[76] R. Bordoloi, A. J. Fox, F. J. Lockman, et al. MAPPING THE NUCLEAR OUTFLOW OF THE MILKY WAY: STUDYING THE KINEMATICS AND SPATIAL EXTENT OF THE NORTHERN FERMI BUBBLE. *The Astrophysical Journal*, 834(2):191 (2017). doi:10.3847/1538-4357/834/2/191.
URL https://doi.org/10.3847%2F1538-4357%2F834%2F2%2F191

[77] N. E. Bramall, R. C. Bay, K. Woschnagg, R. A. Rohde, and P. B. Price. A deep high-resolution optical log of dust, ash, and stratigraphy in South Pole glacial ice. *Geophysical Research Letters*, 32(21) (2005). doi:10.1029/2005GL024236. https://agupubs.onlinelibrary.wiley.com/doi/pdf/10.1029/2005GL024236.
URL https://agupubs.onlinelibrary.wiley.com/doi/abs/10.1029/2005GL024236

[78] S. Buchardt. Densification. [Online].
URL http://www.iceandclimate.nbi.ku.dk/research/flowofice/densification/

[79] Carretti Ettore, Crocker Roland M., Staveley-Smith Lister, et al. Giant magnetized outflows from the centre of the Milky Way. *Nature*, 493:66 (2013). doi:https://doi.org/10.1038/nature1173410.1038/nature11734.
URL https://www.nature.com/articles/nature11734#

`supplementary-information`

[80] D. Chirkin. Evidence of optical anisotropy of the South Pole ice. In: Proceedings, 33th International Cosmic Ray Conference (ICRC2013) Rio de Janero (2013).

[81] D. Chirkin. Photon tracking with GPUs in IceCube. *Nuclear Instruments and Methods in Physics Research Section A Accelerators Spectrometers Detectors and Associated Equipment*, 725:141–143 (2013).

[82] D. Chirkin and W. Rhode. Muon Monte Carlo: A High-precision tool for muon propagation through matter (2004). `hep-ph/0407075`. URL `https://arxiv.org/abs/hep-ph/0407075`

[83] C. L. Cowan Jr., F. Reines, F. B. Harrison, H. W. Kruse, and A. D. McGuire. Detection of the Free Neutrino: a Confirmation. *Science*, 124:103–104 (1956). doi:10.1126/science.124.3212.103.

[84] Creative Design Corporation. Log Periodic Antenna - CLP5130-x CLP3100. `http://www.cd-corp.com/eng/cma/clp5130.pdf` (2018-03-02).

[85] R. M. Crocker and F. Aharonian. Fermi Bubbles: Giant, Multibillion-Year-Old Reservoirs of Galactic Center Cosmic Rays. *Phys. Rev. Lett.*, 106:101102 (2011). doi:10.1103/PhysRevLett.106.101102. URL `http://link.aps.org/doi/10.1103/PhysRevLett.106.101102`

[86] R. M. Crocker, G. V. Bicknell, A. M. Taylor, and E. Carretti. A UNIFIED MODEL OF THE FERMI BUBBLES, MICROWAVE HAZE, AND POLARIZED RADIO LOBES: REVERSE SHOCKS IN THE GALACTIC CENTER'S GIANT OUTFLOWS. *The Astrophysical Journal*, 808(2):107 (2015). doi:10.1088/0004-637x/808/2/107. URL `https://doi.org/10.1088%2F0004-637x%2F808%2F2%2F107`

[87] D. Finkbeiner et al. Fermi data reveal giant gamma-ray bubbels. NASA (2010). URL `https://www.nasa.gov/mission_pages/GLAST/news/new-structure.html`

[88] R. Davis et al. Measurement of the solar electron neutrino flux with the Homestake Chlorine Detector. *The Astrophysical Journal*, 496:505–526 (1998).

[89] D. De Marco and T. Stanev. On the shape of the ultrahigh energy cosmic ray spectrum. *Phys. Rev. D*, 72:081301 (2005). doi:10.1103/PhysRevD.72.081301. URL `https://link.aps.org/doi/10.1103/PhysRevD.72.081301`

[90] De Paolis, F., Gurzadyan, V. G., Nucita, A. A., et al. Planck confirmation of the disk and halo rotation of M. *A&A*, 565:L3 (2014). doi:10.1051/0004-6361/201423849. URL `https://doi.org/10.1051/0004-6361/201423849`

[91] C. Deaconu, A. G. Vieregg, S. A. Wissel, et al. Measurements and modeling of near-surface radio propagation in glacial ice and implica-

tions for neutrino experiments. *Phys. Rev. D*, 98:043010 (2018). doi:10.1103/PhysRevD.98.043010.
URL `https://link.aps.org/doi/10.1103/PhysRevD.98.043010`

[92] G. Dobler. A LAST LOOK AT THE MICROWAVE HAZE/BUBBLES WITHWMAP. *The Astrophysical Journal*, 750(1):17 (2012). doi:10.1088/0004-637x/750/1/17.
URL `https://doi.org/10.1088%2F0004-637x%2F750%2F1%2F17`

[93] G. Dobler, D. P. Finkbeiner, I. Cholis, T. Slatyer, and N. Weiner. THEFERMIHAZE: A GAMMA-RAY COUNTERPART TO THE MICROWAVE HAZE. *The Astrophysical Journal*, 717(2):825–842 (2010). doi:10.1088/0004-637x/717/2/825.
URL `https://doi.org/10.1088%2F0004-637x%2F717%2F2%2F825`

[94] C. D. Donato and G. Medina-Tanco. Experimental constraints on the astrophysical interpretation of the cosmic ray Galactic–extragalactic transition region. *Astroparticle Physics*, 32(5):253 – 268 (2009). ISSN 0927-6505. doi:https://doi.org/10.1016/j.astropartphys.2009.09.004.
URL `http://www.sciencedirect.com/science/article/pii/S092765050900139X`

[95] R. Enberg, M. H. Reno, and I. Sarcevic. Prompt neutrino fluxes from atmospheric charm. *Phys. Rev. D*, 78(4):043005 (2008). doi:10.1103/PhysRevD.78.043005.
URL `http://link.aps.org/doi/10.1103/PhysRevD.78.043005`

[96] S. Euler. Observation of oscillations of atmospheric neutrinos with the IceCube Neutrino Observatory. Ph.D. thesis, RWTH Aachen University (2014).

[97] B. Falkenburg and W. Rhode and editors. From Ultra Rays to Astroparticles: A Historical Introduction to Astroparticle Physics. Springer (2012). ISBN 9400754213.

[98] G. J. Feldman and R. D. Cousins. Unified approach to the classical statistical analysis of small signals. *Phys. Rev. D*, 57:3873–3889 (1998). doi:10.1103/PhysRevD.57.3873.
URL `http://link.aps.org/doi/10.1103/PhysRevD.57.3873`

[99] E. Fermi. On the Origin of the Cosmic Radiation. *Phys. Rev.*, 75:1169–1174 (1949). doi:10.1103/PhysRev.75.1169.
URL `https://link.aps.org/doi/10.1103/PhysRev.75.1169`

[100] D. P. Finkbeiner. Microwave Interstellar Medium Emission Observed by theWilkinson Microwave Anisotropy Probe. *The Astrophysical Journal*, 614(1):186–193 (2004). doi:10.1086/423482.
URL `https://doi.org/10.1086%2F423482`

[101] A. J. Fox, R. Bordoloi, B. D. Savage, et al. Probing the Fermi Bubbles in Ultraviolet Absorption: A Spectroscopic Signature of the Milky Way's Biconical Nuclear Outflow. *The Astrophysical Journal*, 799(1):L7 (2015). doi:10.1088/2041-8205/799/1/l7.
URL `https://doi.org/10.1088%2F2041-8205%2F799%2F1%2Fl7`

[102] Y. Fujita, Y. Ohira, and R. Yamazaki. THE FERMI BUBBLES AS A SCALED-UP VERSION OF SUPERNOVA REMNANTS. *The Astrophysical Journal*, 775(1):L20 (2013). doi:10.1088/2041-8205/775/1/l20.
URL `https://doi.org/10.1088%2F2041-8205%2F775%2F1%2Fl20`

[103] Y. Fujita, Y. Ohira, and R. Yamazaki. A HADRONIC-LEPTONIC MODEL FOR THE FERMI BUBBLES: COSMIC-RAYS IN THE GALACTIC HALO AND RADIO EMISSION. *The Astrophysical Journal*, 789(1):67 (2014). doi:10.1088/0004-637x/789/1/67.
URL `https://doi.org/10.1088%2F0004-637x%2F789%2F1%2F67`

[104] Y. Fukuda, T. Hayakawa, E. Ichihara, et al. Evidence for Oscillation of Atmospheric Neutrinos. *Phys. Rev. Lett.*, 81:1562–1567 (1998). doi:10.1103/PhysRevLett.81.1562.
URL `https://link.aps.org/doi/10.1103/PhysRevLett.81.1562`

[105] T. K. Gaisser. Cosmic Rays and Particle Physics. Cambridge University Press (1990).

[106] T. K. Gaisser. Origin of cosmic radiation. In: AIP Conference Proceedings, vol. 558, 27 (2001). doi:https://doi.org/10.1063/1.1370778.

[107] T. K. Gaisser and T. Stanev. Neutrinos and cosmic rays. *arXiv:1202.0310v1* (2012).

[108] A. Gazizov and M. Kowalski. ANIS: High energy neutrino generator for neutrino telescopes. *Computer Physics Communications*, 172(3):203 – 213 (2005). ISSN 0010-4655. doi:https://doi.org/10.1016/j.cpc.2005.03.113.
URL `http://www.sciencedirect.com/science/article/pii/S0010465505004194`

[109] S. L. Glashow. Resonant Scattering of Antineutrinos. *Phys. Rev.*, 118:316–317 (1960). doi:10.1103/PhysRev.118.316.
URL `https://link.aps.org/doi/10.1103/PhysRev.118.316`

[110] M. Glück, E. Reya, and A. Vogt. Dynamical parton distributions revisited. *The European Physical Journal C*, 5:461–470 (1998).

[111] L. Goodenough and D. Hooper. Possible Evidence For Dark Matter Annihilation In The Inner Milky Way From The Fermi Gamma Ray Space Telescope (2009). `0910.2998`.

[112] P. Gorham, P. Allison, S. Barwick, et al. The Antarctic Impulsive Transient Antenna ultra-high energy neutrino detector: Design, performance, and sensitivity for the 2006–2007 balloon flight. *Astroparticle Physics*, 32(1):10 – 41 (2009). ISSN 0927-6505. doi:https://doi.org/10.1016/j.astropartphys.2009.05.003.
URL `http://www.sciencedirect.com/science/article/pii/S0927650509000838`

[113] P. Gorham, F. Baginski, P. Allison, et al. The ExaVolt Antenna: A large-aperture, balloon-embedded antenna for ultra-high energy

particle detection. *Astroparticle Physics*, 35(5):242 – 256 (2011). ISSN 0927-6505. doi:https://doi.org/10.1016/j.astropartphys.2011.08.004. URL `http://www.sciencedirect.com/science/article/pii/S0927650511001629`

[114] P. W. Gorham, S. W. Barwick, J. J. Beatty, et al. Observations of the Askaryan Effect in Ice. *Phys. Rev. Lett.*, 99:171101 (2007). doi:10.1103/PhysRevLett.99.171101. URL `https://link.aps.org/doi/10.1103/PhysRevLett.99.171101`

[115] P. W. Gorham, D. Saltzberg, R. C. Field, et al. Accelerator measurements of the Askaryan effect in rock salt: A roadmap toward teraton underground neutrino detectors. *Phys. Rev. D*, 72:023002 (2005). doi:10.1103/PhysRevD.72.023002. URL `https://link.aps.org/doi/10.1103/PhysRevD.72.023002`

[116] K. M. Górski, E. Hivon, A. J. Banday, et al. HEALPix: A Framework for High-Resolution Discretization and Fast Analysis of Data Distributed on the Sphere. *Ap.J.*, 622:759–771 (2005). doi:10.1086/427976. `arXiv:astro-ph/0409513`.

[117] E. Grashorn, J. de Jong, M. Goodman, et al. The atmospheric charged kaon/pion ratio using seasonal variation methods. *Astroparticle Physics*, 33(3):140 – 145 (2010). ISSN 0927-6505. doi:https://doi.org/10.1016/j.astropartphys.2009.12.006. URL `http://www.sciencedirect.com/science/article/pii/S0927650509001947`

[118] K. Greisen. End to the cosmic-ray spectrum? *Phys. Rev. Lett.*, 16(17):748–750 (1966).

[119] D. Griffiths. Introduction to Elementary Particles. RWiley-VCH, Berlin (2008). ISBN 978-3-527-40601-2.

[120] J. E. Grindlay, H. F. Helmken, R. H. Brown, J. Davis, and L. R. Allen. Evidence for the detection of gamma rays from Centaurus A at gamma-ray energies above 300 GeV. *apjl*, 197:L9–L12 (1975). doi:10.1086/181764.

[121] D. E. GROOM, N. V. MOKHOV, and S. I. STRIGANOV. MUON STOPPING POWER AND RANGE TABLES 10 MeV–100 TeV. *Atomic Data and Nuclear Data Tables*, 78(2):183 – 356 (2001). ISSN 0092-640X. doi:https://doi.org/10.1006/adnd.2001.0861. URL `http://www.sciencedirect.com/science/article/pii/S0092640X01908617`

[122] F. Guo and W. G. Mathews. THE FERMI BUBBLES. I. POSSIBLE EVIDENCE FOR RECENT AGN JET ACTIVITY IN THE GALAXY. *The Astrophysical Journal*, 756(2):181 (2012). doi:10.1088/0004-637x/756/2/181. URL `https://doi.org/10.1088%2F0004-637x%2F756%2F2%2F181`

[123] C. Haak and C. Wiebush. A measurement of the diffuse astrophysical

muon neutrinoux using eight years of IceCube data. In: Proceedings, 35th International Cosmic Ray Conference (ICRC2017) Bexco, Busan, Korea (2017). doi:https://doi.org/10.22323/1.301.1005.

[124] S. Hallmann. Neutrinos from the Fermi Bubbles with ANTARES. In: 35th International Cosmic Ray Conference. ICRC (2017).
URL `https://pos.sissa.it/301/1001/`

[125] F. Halzen and D. Hooper. High-energy neutrino astronomy: the cosmic ray connection. *Reports on Progress in Physics*, 65(7):1025 (2002).
URL `http://stacks.iop.org/0034-4885/65/i=7/a=201`

[126] F. Halzen and S. R. Klein. Invited Review Article: IceCube: An instrument for neutrino astronomy. *Review of Scientific Instruments*, 81(8):081101 (2010). doi:10.1063/1.3480478. `https://doi.org/10.1063/1.3480478`.
URL `https://doi.org/10.1063/1.3480478`

[127] J. Hanson, S. W. Barwick, E. Berg, et al. Radar absorption, basal reflection, thickness and polarization measurements from the Ross Ice Shelf, Antarctica. *Journal of Glaciology*, 61:438–446 (2015). doi:10.3189/2015JoG14J214.

[128] J. C. Hanson. The Performance and Initial Results of the ARIANNA Prototype. Ph.D. thesis, University of California, Irvine (2013).

[129] D. Heck, J. Knapp, J. Capdevielle, G. Schatz, and T. Thouw. CORSIKA: A Monte Carlo Code to Simulate Extensive Air Showers. *Forschungszentrum Karlsruhe, Wissenschaftliche Berichte FZKA 6019* (1998).

[130] L. Herold and D. Malyshev. Hard and bright gamma-ray emission at the base of the Fermi bubbles (2019). `1904.01454`.

[131] M. Herron and C. C. Langway. Firn Densification: An Empirical Model. *Journal of Glaciology*, 25:373–385 (1980). doi:10.3189/s0022143000015239.

[132] T. Hertel and G. Smith. Pulse radiation from an insulated antenna: An analog of Cherenkov radiation from a moving charged particle. *Antennas and Propagation, IEEE Transactions on*, 48:165 – 172 (2000).

[133] T. W. Hertel and G. S. Smith. Pulse radiation from an insulated antenna: an analog of Cherenkov radiation from a moving charged particle. *IEEE Transactions on Antennas and Propagation*, 48(2):165–172 (2000). ISSN 0018-926X. doi:10.1109/8.833065.

[134] G. C. Hill and K. Rawlins. Unbiased cut selection for optimal upper limits in neutrino detectors: the model rejection potential technique. *Astroparticle Physics*, 19(3):393 – 402 (2003). ISSN 0927-6505. doi:http://dx.doi.org/10.1016/S0927-6505(02)00240-2.
URL `http://www.sciencedirect.com/science/article/pii/S0927650502002402`

[135] A. M. Hillas. The Origin of Ultra-High-Energy Cosmic Rays. *Annual review of astronomy and astrophysics*, 22(13):425–444 (1984). doi:

10.1146/annurev.aa.22.090184.002233.
URL `https://www.annualreviews.org/doi/10.1146/annurev.aa.22.090184.002233`

[136] A. M. Hillas. Cosmic Rays: Recent Progress and some Current Questions. *arXiv:astro-ph/0607109v2* (2006).

[137] J. A. Hinton. The status of the HESS project. *New Astronomy Reviews*, 48:331–337 (2004). doi:{10.1016/j.newar.2003.12.004}.

[138] M. Honda, T. Kajita, K. Kasahara, S. Midorikawa, and T. Sanuki. Calculation of atmospheric neutrino flux using the interaction model calibrated with atmospheric muon data. *Phys. Rev. D*, 75(4):043006 (2007). doi:10.1103/PhysRevD.75.043006.
URL `http://link.aps.org/doi/10.1103/PhysRevD.75.043006`

[139] M. Honda et al. Calculation of the flux of atmospheric neutrinos. *Physics Review D*, 52(9):4985 (1995).

[140] J. R. Hörandel. Models of the knee in the energy spectrum of cosmic rays. *Astroparticle Physics*, 21(3):241 – 265 (2004). ISSN 0927-6505. doi:https://doi.org/10.1016/j.astropartphys.2004.01.004.
URL `http://www.sciencedirect.com/science/article/pii/S0927650504000209`

[141] IceCube Collaboration. DCorsika releases. IceCube internal document.
URL `https://wiki.icecube.wisc.edu/index.php/DCorsika_releases`

[142] IceCube Collaboration. Evidence for High-Energy Extraterrestrial Neutrinos at the IceCube Detector. *Science*, 342(6161) (2013). ISSN 0036-8075. doi:10.1126/science.1242856. `http://science.sciencemag.org/content/342/6161/1242856.full.pdf`.
URL `http://science.sciencemag.org/content/342/6161/1242856`

[143] IceCube Collaboration. Evidence for High-Energy Extraterrestrial Neutrinos at the IceCube Detector. *Science*, 342(6161) (2013). ISSN 0036-8075. doi:10.1126/science.1242856. `http://science.sciencemag.org/content/342/6161/1242856.full.pdf`.
URL `http://science.sciencemag.org/content/342/6161/1242856`

[144] T. Kajita. Atmospheric neutrinos. *New Journal of Physics*, 6:194–194 (2004). doi:10.1088/1367-2630/6/1/194.
URL `https://doi.org/10.1088%2F1367-2630%2F6%2F1%2F194`

[145] K.-H. Kampert and M. Unger. Measurements of the cosmic ray composition with air shower experiments. *Astroparticle Physics*, 35(10):660 – 678 (2012). ISSN 0927-6505. doi:https://doi.org/10.1016/j.astropartphys.2012.02.004.
URL `http://www.sciencedirect.com/science/article/pii/S0927650512000382`

[146] M. T. Karim, A. J. Fox, E. B. Jenkins, et al. Probing the Southern Fermi

Bubble in Ultraviolet Absorption Using Distant AGNs. *The Astrophysical Journal*, 860(2):98 (2018). doi:10.3847/1538-4357/aac167.
URL `https://doi.org/10.3847%2F1538-4357%2Faac167`

[147] I. Kavchenko, S. Hussain, D. Seckel, et al. Updated results from the RICE experiment and future prospects for ultra-high energy neutrino detection at the South Pole. *Faculty Publications, Department of Physics and Astronomy*, 97 (2012).
URL `http://digitalcommons.unl.edu/physicsfacpub/97`

[148] H. Kawai, S. Yoshida, H. Yoshii, et al. Telescope Array Experiment. *Nuclear Physics B - Proceedings Supplements*, 175-176:221 – 226 (2008). ISSN 0920-5632. doi: https://doi.org/10.1016/j.nuclphysbps.2007.11.002. Proceedings of the XIV International Symposium on Very High Energy Cosmic Ray Interactions.
URL `http://www.sciencedirect.com/science/article/pii/S0920563207007992`

[149] J. Kelley. Searching for Quantum Gravity with High-energy Atmospheric Neutrinos and AMANDA-II. Ph.D. thesis, University of Wisconsin, Madison (2008).

[150] U. Keshet and I. Gurwich. Fermi bubbles: high-latitude X-ray supersonic shell. *Monthly Notices of the Royal Astronomical Society*, 480(1):223–235 (2018). ISSN 0035-8711. doi:10.1093/mnras/sty1533. `http://oup.prod.sis.lan/mnras/article-pdf/480/1/223/25230261/sty1533.pdf`.
URL `https://doi.org/10.1093/mnras/sty1533`

[151] S. A. Kleinfelder. Design of the second-generation ARIANNA ultra-high-energy neutrino detector systems. In: 2015 IEEE Nuclear Science Symposium and Medical Imaging Conference (NSS/MIC), pages 1–4 (2015). doi:10.1109/NSSMIC.2015.7581856.

[152] S. A. Kleinfelder, E. Chiem, and T. Prakash. The SST Multi-G-Sample/s Switched Capacitor Array Waveform Recorder with Flexible Trigger and Picosecond-Level Timing Accuracy. *ArXiv* (2015). `1508.02460`.

[153] J.-H. Koehne, K. Frantzen, M. Schmitz, et al. PROPOSAL: A tool for propagation of charged leptons. *Computer Physics Communications*, 184(9):2070 – 2090 (2013). ISSN 0010-4655. doi: https://doi.org/10.1016/j.cpc.2013.04.001.
URL `http://www.sciencedirect.com/science/article/pii/S0010465513001355`

[154] A. Kouchner and J. Coelho. Measuring the Neutrino Mass Ordering and other oscillation parameters with KM3NeT-ORCA. *PoS*, ICRC2017:1027 (2018). doi:10.22323/1.301.1027.

[155] I. Kravchenko, G. Frichter, D. Seckel, et al. Performance and simulation of the RICE detector. *Astroparticle Physics*, 19(1):15 – 36 (2003). ISSN 0927-6505. doi:https://doi.org/10.1016/S0927-6505(02)00194-9.

URL http://www.sciencedirect.com/science/article/pii/S0927650502001949

[156] F. Krennrich, I. Bond, P. Boyle, et al. VERITAS: the Very Energetic Radiation Imaging Telescope Array System. *New Astronomy Reviews*, 48(5):345 – 349 (2004). ISSN 1387-6473. doi:https://doi.org/10.1016/j.newar.2003.12.050. 2nd VERITAS Symposium on the Astrophysics of Extragalactic Sources.
URL http://www.sciencedirect.com/science/article/pii/S1387647303003610

[157] B. C. Lacki. The Fermi bubbles as starburst wind termination shocks. *Monthly Notices of the Royal Astronomical Society: Letters*, 444(1):L39–L43 (2014). doi:10.1093/mnrasl/slu107. http://mnrasl.oxfordjournals.org/content/444/1/L39.full.pdf+html.
URL http://mnrasl.oxfordjournals.org/content/444/1/L39.abstract

[158] C. C. Langway, H. Shoji, A. Mitani, and H. B. Clausen. Transformation process observations of polar firn to ice. *Annals of Glaciology*, 18:199–202 (1993). doi:10.3189/S0260305500011502.

[159] M. J. Larson. Simulation and Identification of Non-Poissonian Noise Triggers in the IceCube Neutrino Detector. Master's thesis, University of Alabama, Tuscaloosa (2013).

[160] M. J. Larson. A Search for Tau Neutrino Appearance with IceCube-DeepCore. Master's thesis, Niels Bohr Institute, University of Copenhagen (2018).

[161] M. Lemoine. Extragalactic magnetic fields and the second knee in the cosmic-ray spectrum. *Phys. Rev. D*, 71:083007 (2005). doi:10.1103/PhysRevD.71.083007.
URL https://link.aps.org/doi/10.1103/PhysRevD.71.083007

[162] J.-T. Li, E. Hodges-Kluck, Y. Stein, et al. Detection of Nonthermal Hard X-Ray Emission from the "Fermi Bubble" in an External Galaxy. *The Astrophysical Journal*, 873(1):27 (2019). doi:10.3847/1538-4357/ab010a.
URL https://doi.org/10.3847%2F1538-4357%2Fab010a

[163] C. Lunardini, S. Razzaque, K. T. Theodoseau, and L. Yang. Neutrino events at IceCube and the Fermi bubbles. *Phys. Rev. D*, 90:023016 (2014). doi:10.1103/PhysRevD.90.023016.
URL https://link.aps.org/doi/10.1103/PhysRevD.90.023016

[164] mbed Microcontrollers. mbed Microcontrollers (2019).
URL https://os.mbed.com/handbook/mbed-Microcontrollers

[165] P. Mertsch and S. Sarkar. Fermi Gamma-Ray "Bubbles" from Stochastic Acceleration of Electrons. *Phys. Rev. Lett.*, 107:091101 (2011). doi:10.1103/PhysRevLett.107.091101.
URL http://link.aps.org/doi/10.1103/PhysRevLett.107.091101

[166] M. J. Miller and J. N. Bregman. THE INTERACTION OF THE FERMI BUBBLES WITH THE MILKY WAY'S HOT GAS HALO. *The Astrophysical Journal*, 829(1):9 (2016). doi:10.3847/0004-637x/829/1/9.
URL `https://doi.org/10.3847%2F0004-637x%2F829%2F1%2F9`

[167] T. Miller, R. Schaefer, and H. B. Sequeira. PRIDE (Passive Radio [frequency] Ice Depth Experiment): An instrument to passively measure ice depth from a Europan orbiter using neutrinos. *Icarus*, 220(2):877 – 888 (2012). ISSN 0019-1035. doi: https://doi.org/10.1016/j.icarus.2012.05.028.
URL `http://www.sciencedirect.com/science/article/pii/S0019103512002102`

[168] G. Mou, D. Sun, and F. Xie. The Bending Feature of the Fermi Bubbles: A Presumed Horizontal Galactic Wind and Its Implication on the Bubbles' Age. *The Astrophysical Journal*, 869(1):L20 (2018). doi: 10.3847/2041-8213/aaf421.
URL `https://doi.org/10.3847%2F2041-8213%2Faaf421`

[169] G. Mou, F. Yuan, D. Bu, M. Sun, and M. Su. FERMI BUBBLES INFLATED BY WINDS LAUNCHED FROM THE HOT ACCRETION FLOW IN SGR A∗. *The Astrophysical Journal*, 790(2):109 (2014). doi: 10.1088/0004-637x/790/2/109.
URL `https://doi.org/10.1088%2F0004-637x%2F790%2F2%2F109`

[170] G. Mou, F. Yuan, Z. Gan, and M. Sun. THE ACCRETION WIND MODEL OF FERMI BUBBLES. II. RADIATION. *The Astrophysical Journal*, 811(1):37 (2015). doi:10.1088/0004-637x/811/1/37.
URL `https://doi.org/10.1088%2F0004-637x%2F811%2F1%2F37`

[171] NASA's Goddard Space Flight Center. Fermi bubble art labels. NASA (2010).
URL `https://www.nasa.gov/mission_pages/GLAST/news/new-structure.html`

[172] C. S. Neal. The Dynamics of the Ross Ice Shelf Revealed by Radio Echo-Sounding. *Journal of Glaciology*, 24(90):295–307 (1979). doi: 10.3189/S0022143000014817.

[173] A. F. Nelles. Radio emission of air showers, The perspective of LOFAR and AERA. Ph.D. thesis, Radboud Universiteit Nijmegen (2014).

[174] C. R. Persichilli. Performance and Simulation of the ARIANNA Pilot Array, with Implications for Future Ultra-high Energy Neutrino Astronomy. Ph.D. thesis, University of California, Irvine (2018).

[175] Pierre Auger. The Pierre Auger Observatory: Contributions to the 34th International Cosmic Ray Conference (ICRC 2015) (2015). 1509.03732.
URL `http://lss.fnal.gov/archive/2015/conf/fermilab-conf-15-396-ad-ae-cd-td.pdf`

[176] Planck Collaboration:, Ade, P. A. R., Aghanim, N., et al. Planck intermediate results - IX. Detection of the Galactic haze with Planck. *A&A*,

554:A139 (2013). doi:10.1051/0004-6361/201220271.
URL https://doi.org/10.1051/0004-6361/201220271

[177] D. M. Pozar. Microwave Engineering, 4th edition. John Wiley and Sons, Inc. (2012). ISBN 978-0-470-63155-3.

[178] T. Prakah. A Fully-Synchronous Multi-GHz Analog Waveform Recording And Triggering Circuit. Ph.D. thesis, University of California, Irvine (2017).
URL https://escholarship.org/uc/item/5bt060dn

[179] M. S. Pshirkov, V. V. Vasiliev, and K. A. Postnov. Evidence of Fermi bubbles around M31. *Monthly Notices of the Royal Astronomical Society: Letters*, 459(1):L76–L80 (2016). ISSN 1745-3925. doi:10.1093/mnrasl/slw045. http://oup.prod.sis.lan/mnrasl/article-pdf/459/1/L76/8010272/slw045.pdf.
URL https://doi.org/10.1093/mnrasl/slw045

[180] V. S. Ptuskin, S. I. Rogovaya, V. N. Zirakashvili, et al. Diffusion and drift of very high energy cosmic rays in galactic magnetic fields. *Astronomy and Astrophysics*, 268:726–735 (1993). ISSN 0004-6361.

[181] J. P. Ralston. Radio surf in polar ice: A new method of ultrahigh energy neutrino detection. *Phys. Rev. D*, 71:011503 (2005). doi:10.1103/PhysRevD.71.011503.
URL https://link.aps.org/doi/10.1103/PhysRevD.71.011503

[182] M. Richman. A Search for Muon Neutrinos Coincident with Northern Gamma-Ray Bursts using IceCube. Ph.D. thesis, University of Maryland (2015).

[183] G. d. Q. Robin, S. Evans, and J. T. Bailey. Interpretation of radio echo sounding in polar ice sheets. *Philosophical Transactions of the Royal Society of London, Ser. A*, 265(1166):437–505 (1970).

[184] G. I. Rubtsov and Y. Zhezher. Spatial structure of the WMAP-Planck haze (2018). 1812.05228.

[185] R. S. Fletcher, T. K. Gaisser, P. Lipari, and T. Stanev. SIBYLL: An event generator for simulation of high energy cosmic ray cascades. *Physical review D: Particles and fields*, 50:5710–5731 (1994).

[186] D. Saltzberg, P. Gorham, D. Walz, et al. Observation of the Askaryan Effect: Coherent Microwave Cherenkov Emission from Charge Asymmetry in High-Energy Particle Cascades. *Phys. Rev. Lett.*, 86:2802–2805 (2001). doi:10.1103/PhysRevLett.86.2802.
URL https://link.aps.org/doi/10.1103/PhysRevLett.86.2802

[187] S. I. Sinegovsky, A. A. Kochanov, and T. S. Sinegovskaya. High-energy atmospheric neutrinos. *ArXiv e-prints*, 1010.2336 (2010).

[188] S. L. Snowden, R. Egger, M. J. Freyberg, et al. ROSATSurvey Diffuse X-Ray Background Maps. II. *The Astrophysical Journal*, 485(1):125–135 (1997). doi:10.1086/304399.
URL https://doi.org/10.1086%2F304399

[189] C. Spiering. Towards high-energy neutrino astronomy. *The European Physical Journal H*, 37(3):515–565 (2012). ISSN 2102-6467. doi:10.1140/epjh/e2012-30014-2.
URL `https://doi.org/10.1140/epjh/e2012-30014-2`

[190] T. Stanev. High Energy Cosmic Rays. Springer (2004). ISBN 3540406530. Springer Praxis Books / Astronomy and Planetary Sciences.

[191] R. Ström. Exploring the universe using neutrinos. Ph.D. thesis, Uppsala University (2015).

[192] M. Su and D. P. Finkbeiner. Evidence for Gamma-Ray Jets in the Milky Way. *The Astrophysical Journal*, 753(1):61 (2012).
URL `http://stacks.iop.org/0004-637X/753/i=1/a=61`

[193] M. Su, T. R. Slatyer, and D. P. Finkbeiner. Giant Gamma-ray Bubbles from Fermi-LAT: Active Galactic Nucleus Activity or Bipolar Galactic Wind? *The Astrophysical Journal*, 724(2):1044 (2010).
URL `https://iopscience.iop.org/article/10.1088/0004-637X/724/2/1044/meta`

[194] H. Taavola. Dark Matter in the Galactic Halo. Ph.D. thesis, Uppsala University (2015).

[195] M. Tahara, J. Kataoka, Y. Takeuchi, et al. SUZAKUX-RAY OBSERVATIONS OF THE FERMI BUBBLES: NORTHERNMOST CAP AND SOUTHEAST CLAW DISCOVERED WITH MAXI-SSC. *The Astrophysical Journal*, 802(2):91 (2015). doi:10.1088/0004-637x/802/2/91.
URL `https://doi.org/10.1088%2F0004-637x%2F802%2F2%2F91`

[196] M. Takeda, N. Sakaki, K. Honda, et al. Energy determination in the Akeno Giant Air Shower Array experiment. *Astroparticle Physics*, 19(4):447 – 462 (2003). ISSN 0927-6505. doi:https://doi.org/10.1016/S0927-6505(02)00243-8.
URL `http://www.sciencedirect.com/science/article/pii/S0927650502002438`

[197] A. Tamburro. Measurements of Cosmic Rays with IceTop/IceCube: Status and Results. *Modern Physics Letters A*, 27:1230038 (2012). doi:{10.1142/S0217732312300388}.

[198] M. Tanabashi, K. Hagiwara, K. Hikasa, et al. Review of Particle Physics. *Phys. Rev. D*, 98:030001 (2018). doi:10.1103/PhysRevD.98.030001.
URL `https://link.aps.org/doi/10.1103/PhysRevD.98.030001`

[199] J. E. Tatar. Performance of Sub-Array of ARIANNA Detector Stations during First Year of Operation. Ph.D. thesis, University of California, Irvine (2013).

[200] The CTA Consortium, M. Actis, G. Agnetta, et al. Design concepts for the Cherenkov Telescope Array CTA: an advanced facility for ground-based high-energy gamma-ray astronomy. *Experimental Astronomy*, 32(3):193–316 (2011). ISSN 1572-9508. doi:10.1007/

s10686-011-9247-0.
URL `https://doi.org/10.1007/s10686-011-9247-0`

[201] The KM3NeT collaboration, S. Adrián-Martínez, M. Ageron, et al. Intrinsic limits on resolutions in muon- and electron-neutrino charged-current events in the KM3NeT/ORCA detector. *Journal of High Energy Physics*, 2017(5):8 (2017). ISSN 1029-8479. doi:10.1007/ JHEP05(2017)008.
URL `https://doi.org/10.1007/JHEP05(2017)008`

[202] The LIGO Scientific Collaboration and The Virgo Collaboration. Binary Black Hole Population Properties Inferred from the First and Second Observing Runs of Advanced LIGO and Advanced Virgo. *ArXiv High Energy Physics - Phenomenology e-prints* (2018). `1811.12940`.
URL `https://arxiv.org/abs/1811.12940`

[203] S. Todor. High Energy Cosmic Rays. Springer-Verlag (2010).

[204] E. Unger. Investigations of the atmospheric neutrino flux with IceCube data. Master's thesis, Ruhr-Universität Bochum, Germany (2013).

[205] V. Schytt et al. Scientific results (Norwegian-British-Swedish Antarctic Expedition (1949-1952)). Oslo : Norsk Polarinstitutt (1958-1963).

[206] F. L. Villante and F. Vissani. How precisely can neutrino emission from supernova remnants be constrained by gamma ray observations? *Phys. Rev. D*, 78:103007 (2008). doi:10.1103/PhysRevD.78.103007.
URL `http://link.aps.org/doi/10.1103/PhysRevD.78.103007`

[207] C. Wiebusch et al. Physics Capabilities of the IceCube DeepCore Detector. *ArXiv e-prints* (2009).

[208] C. WILEMAN. The Spread in the Arrival Times of Particles in Air-Showers for Photon and Anisotropy Searches above 10 EeV (2008).

[209] D. R. Williams. The Askaryan Effect and Detection of Extremely High Energy Neutrinos in the Lunar Regolith and Salt. Ph.D. thesis, University of California, Los Angeles (2004).

[210] K. Woschnagg. Optical Properties of South Pole Ice at Depths from 140 to 2300 Meters. In: 26th International Cosmic Ray Conference, vol. 2, page 200. ICRC (1999).
URL `http://adsabs.harvard.edu/abs/1999ICRC....2..200W`

[211] H.-Y. K. Yang and M. Ruszkowski. The Spatially Uniform Spectrum of the Fermi Bubbles: The Leptonic Active Galactic Nucleus Jet Scenario. *The Astrophysical Journal*, 850(1):2 (2017). doi:10.3847/1538-4357/ aa9434.
URL `https://doi.org/10.3847%2F1538-4357%2Faa9434`

[212] H.-Y. K. Yang, M. Ruszkowski, and E. Zweibel. The Fermi bubbles: gamma-ray, microwave and polarization signatures of leptonic AGN jets. *Monthly Notices of the Royal Astronomical Society*, 436(3):2734–2746 (2013). ISSN 0035-8711. doi:10.1093/mnras/ stt1772. `http://oup.prod.sis.lan/mnras/article-pdf/436/3/ 2734/4090845/stt1772.pdf`.

URL `https://doi.org/10.1093/mnras/stt1772`

[213] H.-Y. K. Yang, M. Ruszkowski, and E. G. Zweibel. Unveiling the Origin of the Fermi Bubbles. *Galaxies*, 6(1) (2018). ISSN 2075-4434. URL `http://www.mdpi.com/2075-4434/6/1/29`

[214] L. Yang and S. Razzaque. Constraints on very high energy gamma-ray emission from the Fermi bubbles with future ground-based experiments. *Phys. Rev. D*, 99:083007 (2019). doi:10.1103/PhysRevD.99.083007. URL `https://link.aps.org/doi/10.1103/PhysRevD.99.083007`

[215] Yang, Rui-zhi, Aharonian, Felix, and Crocker, Roland. The Fermi bubbles revisited. *A&A*, 567:A19 (2014). doi:10.1051/0004-6361/201423562. URL `https://doi.org/10.1051/0004-6361/201423562`

[216] J. Zenneck. Über die Fortpflanzung ebener elektromagnetischer Wellen längs einer ebenen Leiterfläche und ihre Beziehung zur drahtlosen Telegraphie. *Annalen der Physik*, 328(10):846–866 (1907). doi: 10.1002/andp.19073281003. `https://onlinelibrary.wiley.com/doi/pdf/10.1002/andp.19073281003`. URL `https://onlinelibrary.wiley.com/doi/abs/10.1002/andp.19073281003`

Acta Universitatis Upsaliensis
Uppsala Dissertations from the Faculty of Science
Editor: The Dean of the Faculty of Science

1–11: 1970–1975

12. *Lars Thofelt*: Studies on leaf temperature recorded by direct measurement and by thermography. 1975.

13. *Monica Henricsson*: Nutritional studies on Chara globularis Thuill., Chara zeylanica Willd., and Chara haitensis Turpin. 1976.

14. *Göran Kloow*: Studies on Regenerated Cellulose by the Fluorescence Depolarization Technique. 1976.

15. *Carl-Magnus Backman*: A High Pressure Study of the Photolytic Decomposition of Azoethane and Propionyl Peroxide. 1976.

16. *Lennart Källströmer*: The significance of biotin and certain monosaccharides for the growth of Aspergillus niger on rhamnose medium at elevated temperature. 1977.

17. *Staffan Renlund*: Identification of Oxytocin and Vasopressin in the Bovine Adenohypophysis. 1978.

18. *Bengt Finnström*: Effects of pH, Ionic Strength and Light Intensity on the Flash Photolysis of L-tryptophan. 1978.

19. *Thomas C. Amu*: Diffusion in Dilute Solutions: An Experimental Study with Special Reference to the Effect of Size and Shape of Solute and Solvent Molecules. 1978.

20. *Lars Tegnér*: A Flash Photolysis Study of the Thermal Cis-Trans Isomerization of Some Aromatic Schiff Bases in Solution. 1979.

21. *Stig Tormod*: A High-Speed Stopped Flow Laser Light Scattering Apparatus and its Application in a Study of Conformational Changes in Bovine Serum Albumin. 1985.

22. *Björn Varnestig*: Coulomb Excitation of Rotational Nuclei. 1987.

23. *Frans Lettenström*: A study of nuclear effects in deep inelastic muon scattering. 1988.

24. *Göran Ericsson*: Production of Heavy Hypernuclei in Antiproton Annihilation. Study of their decay in the fission channel. 1988.

25. *Fang Peng*: The Geopotential: Modelling Techniques and Physical Implications with Case Studies in the South and East China Sea and Fennoscandia. 1989.

26. *Md. Anowar Hossain*: Seismic Refraction Studies in the Baltic Shield along the Fennolora Profile. 1989.

27. *Lars Erik Svensson*: Coulomb Excitation of Vibrational Nuclei. 1989.

28. *Bengt Carlsson*: Digital differentiating filters and model based fault detection. 1989.

29. *Alexander Edgar Kavka*: Coulomb Excitation. Analytical Methods and Experimental Results on even Selenium Nuclei. 1989.

30. *Christopher Juhlin*: Seismic Attenuation, Shear Wave Anisotropy and Some Aspects of Fracturing in the Crystalline Rock of the Siljan Ring Area, Central Sweden. 1990.

31. *Torbjörn Wigren*: Recursive Identification Based on the Nonlinear Wiener Model. 1990.
32. *Kjell Janson*: Experimental investigations of the proton and deuteron structure functions. 1991.
33. *Suzanne W. Harris*: Positive Muons in Crystalline and Amorphous Solids. 1991.
34. *Jan Blomgren*: Experimental Studies of Giant Resonances in Medium-Weight Spherical Nuclei. 1991.
35. *Jonas Lindgren*: Waveform Inversion of Seismic Reflection Data through Local Optimisation Methods. 1992.
36. *Liqi Fang*: Dynamic Light Scattering from Polymer Gels and Semidilute Solutions. 1992.
37. *Raymond Munier*: Segmentation, Fragmentation and Jostling of the Baltic Shield with Time. 1993.

Prior to January 1994, the series was called *Uppsala Dissertations from the Faculty of Science*.

Acta Universitatis Upsaliensis
Uppsala Dissertations from the Faculty of Science and Technology
Editor: The Dean of the Faculty of Science

1–14: 1994–1997. 15–21: 1998–1999. 22–35: 2000–2001. 36–51: 2002–2003.
52. *Erik Larsson*: Identification of Stochastic Continuous-time Systems. Algorithms, Irregular Sampling and Cramér-Rao Bounds. 2004.
53. *Per Åhgren*: On System Identification and Acoustic Echo Cancellation. 2004.
54. *Felix Wehrmann*: On Modelling Nonlinear Variation in Discrete Appearances of Objects. 2004.
55. *Peter S. Hammerstein*: Stochastic Resonance and Noise-Assisted Signal Transfer. On Coupling-Effects of Stochastic Resonators and Spectral Optimization of Fluctuations in Random Network Switches. 2004.
56. *Esteban Damián Avendaño Soto*: Electrochromism in Nickel-based Oxides. Coloration Mechanisms and Optimization of Sputter-deposited Thin Films. 2004.
57. *Jenny Öhman Persson*: The Obvious & The Essential. Interpreting Software Development & Organizational Change. 2004.
58. *Chariklia Rouki*: Experimental Studies of the Synthesis and the Survival Probability of Transactinides. 2004.
59. *Emad Abd-Elrady*: Nonlinear Approaches to Periodic Signal Modeling. 2005.
60. *Marcus Nilsson*: Regular Model Checking. 2005.
61. *Pritha Mahata*: Model Checking Parameterized Timed Systems. 2005.
62. *Anders Berglund*: Learning computer systems in a distributed project course: The what, why, how and where. 2005.
63. *Barbara Piechocinska*: Physics from Wholeness. Dynamical Totality as a Conceptual Foundation for Physical Theories. 2005.
64. *Pär Samuelsson*: Control of Nitrogen Removal in Activated Sludge Processes. 2005.

65. *Mats Ekman*: Modeling and Control of Bilinear Systems. Application to the Activated Sludge Process. 2005.
66. *Milena Ivanova*: Scalable Scientific Stream Query Processing. 2005.
67. *Zoran Radovic´*: Software Techniques for Distributed Shared Memory. 2005.
68. *Richard Abrahamsson*: Estimation Problems in Array Signal Processing, System Identification, and Radar Imagery. 2006.
69. *Fredrik Robelius*: Giant Oil Fields – The Highway to Oil. Giant Oil Fields and their Importance for Future Oil Production. 2007.
70. *Anna Davour*: Search for low mass WIMPs with the AMANDA neutrino telescope. 2007.
71. *Magnus Ågren*: Set Constraints for Local Search. 2007.
72. *Ahmed Rezine*: Parameterized Systems: Generalizing and Simplifying Automatic Verification. 2008.
73. *Linda Brus*: Nonlinear Identification and Control with Solar Energy Applications. 2008.
74. *Peter Nauclér*: Estimation and Control of Resonant Systems with Stochastic Disturbances. 2008.
75. *Johan Petrini*: Querying RDF Schema Views of Relational Databases. 2008.
76. *Noomene Ben Henda*: Infinite-state Stochastic and Parameterized Systems. 2008.
77. *Samson Keleta*: Double Pion Production in dd→απ Reaction. 2008.
78. *Mei Hong*: Analysis of Some Methods for Identifying Dynamic Errors-invariables Systems. 2008.
79. *Robin Strand*: Distance Functions and Image Processing on Point-Lattices With Focus on the 3D Face-and Body-centered Cubic Grids. 2008.
80. *Ruslan Fomkin*: Optimization and Execution of Complex Scientific Queries. 2009.
81. *John Airey*: Science, Language and Literacy. Case Studies of Learning in Swedish University Physics. 2009.
82. *Arvid Pohl*: Search for Subrelativistic Particles with the AMANDA Neutrino Telescope. 2009.
83. *Anna Danielsson*: Doing Physics – Doing Gender. An Exploration of Physics Students' Identity Constitution in the Context of Laboratory Work. 2009.
84. *Karin Schönning*: Meson Production in pd Collisions. 2009.
85. *Henrik Petrén*: η Meson Production in Proton-Proton Collisions at Excess Energies of 40 and 72 MeV. 2009.
86. *Jan Henry Nyström*: Analysing Fault Tolerance for ERLANG Applications. 2009.
87. *John Håkansson*: Design and Verification of Component Based Real-Time Systems. 2009.
88. *Sophie Grape*: Studies of PWO Crystals and Simulations of the $\bar{p}p \to \bar{\Lambda}\Lambda, \bar{\Lambda}\Sigma^0$ Reactions for the PANDA Experiment. 2009.
90. *Agnes Rensfelt*. Viscoelastic Materials. Identification and Experiment Design. 2010.
91. *Erik Gudmundson*. Signal Processing for Spectroscopic Applications. 2010.
92. *Björn Halvarsson*. Interaction Analysis in Multivariable Control Systems. Applications to Bioreactors for Nitrogen Removal. 2010.
93. *Jesper Bengtson*. Formalising process calculi. 2010.
94. *Magnus Johansson*. Psi-calculi: a Framework for Mobile Process Calculi. Cook your own correct process calculus – just add data and logic. 2010.
95. *Karin Rathsman*. Modeling of Electron Cooling. Theory, Data and Applications. 2010.

96. *Liselott Dominicus van den Bussche*. Getting the Picture of University Physics. 2010.

97. *Olle Engdegård*. A Search for Dark Matter in the Sun with AMANDA and IceCube. 2011.

98. *Matthias Hudl*. Magnetic materials with tunable thermal, electrical, and dynamic properties. An experimental study of magnetocaloric, multiferroic, and spin-glass materials. 2012.

99. *Marcio Costa*. First-principles Studies of Local Structure Effects in Magnetic Materials. 2012.

100. *Patrik Adlarson*. Studies of the Decay $\eta \to \pi^+\pi^-\pi^0$ with WASA-at-COSY. 2012.

101. *Erik Thomé*. Multi-Strange and Charmed Antihyperon-Hyperon Physics for PAN-DA. 2012.

102. *Anette Löfström*. Implementing a Vision. Studying Leaders' Strategic Use of an Intranet while Exploring Ethnography within HCI. 2014.

103. *Martin Stigge*. Real-Time Workload Models: Expressiveness vs. Analysis Efficiency. 2014.

104. *Linda Åmand*. Ammonium Feedback Control in Wastewater Treatment Plants. 2014.

105. *Mikael Laaksoharju*. Designing for Autonomy. 2014.

106. *Soma Tayamon*. Nonlinear System Identification and Control Applied to Selective Catalytic Reduction Systems. 2014.

107. *Adrian Bahne*. Multichannel Audio Signal Processing. Room Correction and Sound Perception. 2014.

108. *Mojtaba Soltanalian*. Signal Design for Active Sensing and Communications. 2014.

109. *Håkan Selg*. Researching the Use of the Internet — A Beginner's Guide. 2014.

110. *Andrzej Pyszniak*. Development and Applications of Tracking of Pellet Streams. 2014.

111. *Olov Rosén*. Parallel Stochastic Estimation on Multicore Platforms. 2015.

112. *Yajun Wei*. Ferromagnetic Resonance as a Probe of Magnetization Dynamics. A Study of FeCo Thin Films and Trilayers. 2015.

113. *Marcus Björk*. Contributions to Signal Processing for MRI. 2015.

114. *Alexander Madsen*. Hunting the Charged Higgs Boson with Lepton Signatures in the ATLAS Experiment. 2015.

115. *Daniel Jansson*. Identification Techniques for Mathematical Modeling of the Human Smooth Pursuit System. 2015.

116. *Henric Taavola*. Dark Matter in the Galactic Halo. A Search Using Neutrino Induced Cascades in the DeepCore Extension of IceCube. 2015.

117. *Rickard Ström*. Exploring the Universe Using Neutrinos. A Search for Point Sources in the Southern Hemisphere Using the IceCube Neutrino Observatory. 2015.

118. *Li Caldeira Balkeståhl*. Measurement of the Dalitz Plot Distribution for $\eta \to \pi^+\pi^-\pi^0$ with KLOE. 2015.

119. *Johannes Nygren*. Input-Output Stability Analysis of Networked Control Systems. 2016.

120. *Joseph Scott*. Other Things Besides Number. Abstraction, Constraint Propagation, and String Variable Types. 2016.

121. *Andrej Andrejev*. Semantic Web Queries over Scientific Data. 2016.

122. *Johan Blom*. Model-Based Protocol Testing in an ERLANG Environment. 2016.
123. *Liang Dai*. Identification using Convexification and Recursion. 2016.
124. *Adriaan Larmuseau*. Protecting Functional Programs From Low-Level Attackers. 2016.
125. *Lena Heijkenskjöld*. Hadronic Decays of the ω Meson. 2016.
126. *Delphine Misao Lebrun*. Photonic crystals and photocatalysis. Study of titania inverse opals. 2016.
127. *Per Mattsson*. Modeling and identification of nonlinear and impulsive systems. 2016.
128. *Lars Melander*. Integrating Visual Data Flow Programming with Data Stream Management. 2016.
129. *Kristofer Severinsson*. Samarbete = Samverkan? En fallstudie av AIMday vid Uppsala universitet. 2016.
130. *Nina Fowler*. Walking the Plank of the Entrepreneurial University. The little spin-out that could? 2017.
131. *Kaj Jansson*. Measurements of Neutron-induced Nuclear Reactions for More Precise Standard Cross Sections and Correlated Fission Properties. 2017.
132. *Petter Bertilsson Forsberg*. Collaboration in practice. A multiple case study on collaboration between small enterprises and university researchers. 2018.
133. *Andreas Löscher*. Targeted Property-Based Testing with Applications in Sensor Networks. 2018.
134. *Simon Widmark*. Causal MMSE Filters for Personal Audio. A Polynomial Matrix Approach. 2018.
135. *Damian Pszczel*. Search for a new light boson in meson decays. 2018.
136. *Joachim Pettersson*. From Strange to Charm. Meson production in electron-positron collisions. 2018.
137. *Elisabeth Unger*. The Extremes of Neutrino Astronomy. From Fermi Bubbles with IceCube to Ice Studies with ARIANNA. 2019.